SMRA 2018

www.society4MRA.org

30th Annual International Conference

A SuperCool MRA Experience

Glasgow
Kelvin Gallery | University of Glasgow

Pre-Conference Educational Workshop
Tuesday, August 28th

Main Conference
Wednesday, August 29th
Thursday, August 30th
Friday, August 31st

President :
Richard Frayne

Organizer:
Giles Roditi

Scientific Program Chair:
Aleksandra Radjenovic

Table of Contents

Program at a Glance

Pre-Conference Educational Workshop

Tuesday, August 28th

08:45 Welcome and Opening Remarks
09:00 Session 1: Introduction to MRA and basic techniques
10:40 Break
11:00 Session 2: Advanced MRA techniques
12:40 Lunch
13:30 Session 3: Applications: above diaphragm
15:10 Break
15:30 Session 4: Applications: below diaphragm
17:10 Closing address
19:00 Welcome Reception @ Hunterian Museum

Main Conference Scientific Sessions and Poster Exhibition

Wednesday, August 29th

08:30 Opening Session - Welcome from President/organising committee
09:00 Session 1: Cardiothoracic MRA (Proffered talks & Clinical Challenge)
10:00 Break and Poster Setup
10:30 Session 2: Quantitative Flow MRI (Proffered talks)
12:10 Gold Sponsor Presentation - Siemens Healthineers
12:20 Lunch
13:40 Keynote - David Lurie: Fast Field-Cycling MRI: Technology, Methods and First Patient Studies
14:15 Session 3: Contrast MRA (Proffered talks)
15:10 Break / Posters
15:40 Session 4: Peripheral MRA (Proffered talks, Technical & Clinical Challenges)
16:40 Gold Sponsor Presentation - Guerbet
17:10 Session 5: 'Power-Pitch: rapid fire poster session' (1/2)
18:30 Evening Social Event @ Kelvingrove Art Gallery & Museum

Thursday, August 30th

08:50 Announcements
09:00 Keynote - Matthias Stuber: A Sound (♪) Approach to Fully Self-Gated Cardiac Imaging
09:30 Session 6: Coronary MRA (Proffered talks)
10:30 Gold Sponsor Presentations - GE Healthcare & Bracco
10:50 Break / Posters
11:20 Session 7: Cardiac MRI (Proffered talks)
13:00 Lunch
14:15 Keynote - Nicole Seiberlich: Cardiac MR Fingerprinting
14:50 Gold Sponsor Presentation - Philips
15:00 Session 8: Vessel Wall MRI (1/2) (Proffered talks)
15:50 Break / Posters
16:20 Session 9: Vessel Wall MRI (2/2) (Proffered talks)
17:10 Session 10: 'Power-Pitch: rapid fire poster session' (2/2)
19:00 Evening Social Event @ Glasgow Old Fruitmarket, Whisky Tasting and Ceilidh with Jiggered

Friday, August 31st

08:50 Announcements
09:00 Keynote - Tim Leiner: New Developments in Machine Learning for Cardiovascular Imaging
09:30 Session 11: Emerging Techniques in MRA (1/2) (Proffered talks)
10:20 Break / Posters
10:50 Session 12: Emerging Techniques in MRA (2/2) (Proffered talks)
11:40 Session 13: Head & Neck MRA (Proffered talks)
12:30 Clinical challenge and round table discussion on the future of carotid MRA
13:00 Lunch
14:15 Keynote - David Newby: The Magnetism of Antimatter: Lesson from PET-MRI
14:50 Session 14: Ferumoxytol MRA (Proffered talks)
15:45 Break / Posters
16:15 Session 15: Abdominal MRA (Proffered talks & Clinical Challenges)
17:15 Awards and closing session
19:00 Evening Social Event @ Oran Mor, President's Address, Dinner & Magic

Conference Venue

Click this *Link for Venue Room Map*

This will display a map of the building then click 'Current Location' for map and directions from wherever you are

Walking route Hillhead Subway to conference venue

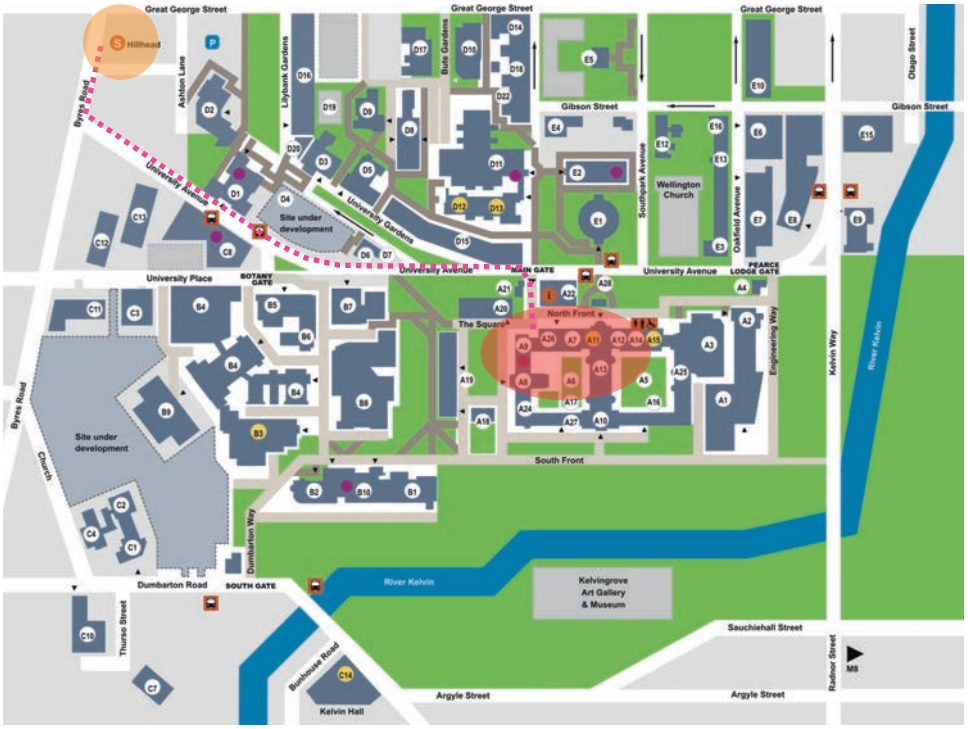

céad míle fáilte

Welcome to Glasgow and to the 30th Annual Meeting of the Society for Magnetic Resonance Angiography (SRMA). We should all be proud of this annual meeting – over the past 30 years we have grown from a group that met somewhat informally to discuss advances in the field to become the pre-eminent gathering of scientists, clinicians, corporate partners, trainees and others who are interested in MRA. Many innovations in this field were first presented and discussed at one of our meetings; many of these advances are now impacting healthcare worldwide.

A special welcome is extended to those who are attending their first meeting. I hope that you find our meeting to be a stimulating and enriching experience. I would wholeheartedly encourage you to participate fully in the discussion that occurs during the scientific sessions, lunches and breaks, and that often continue into the evening social events. The poster sessions and engaging with our exhibitors are always another highlight.

This year Giles Roditi and Aleksandra Radjenovic and their local team have done a fabulous job of developing an innovative program. We will meet in the historic Kelvin Gallery at the University of Glasgow, one of Scotland's four ancient universities and founded in 1451. The Kelvin Gallery is a delightful meeting space and is named after one of the university's illustrious faculty, Lord Kelvin (1824-1907), who was a Professor of Natural Philosophy for 53 years! The core of the meeting consists of presentations given by many of you. I am pleased that the pace and quality of innovation in our field remains high. It is especially reassuring to see the number of talented young investigators who will again be competing for the Potchen and Passariello Awards (best oral presentation and best poster, respectively). These awards appropriately recognize the early contributions to the SMRA of James Potchen and Roberto Passariello.

contd.

Giles and Sasha have invited many international experts to speak, with a special emphasis on distinguished colleagues from the British Isles. The one-day educational program, now entering its eighth year at our meeting, will be a highpoint. They have also instituted some new "challenge'' based sessions at this year's meeting. The social events are often a highlight of the meeting – this year a series of events that highlight Glaswegian culture have been selected. The local organizing team and our hosts at the University of Glasgow deserve our hearty thanks for their creative and diligent meeting organization. Our society secretariat also has played an invaluable role keeping track of the many details, both big and small, associated with the meeting; a special thank you goes out to Donna Lyons, Kevin Henley, Johanne Langford and Janette Wallace.

Our corporate sponsors are essential to the continued success of this meeting. Through their generous support, they allow us to develop and put on the annual meeting. Please stop by their exhibits and thank them for their ongoing support. I send a sincere thank you to all of our sponsors. Having trainees and others starting their career in MRA attend the meeting has been critical to our success. I speak first hand of this culture as I was first exposed to the meeting as a PhD student in 1992 (wow!). This year, we are pleased to acknowledge the considerable support provided by both the US National Institute of Health, as well at the Martin R Prince Charitable Foundation who together have helped fund the attendance of over 30 trainees at this meeting.

The society continues to evolve. Over the past three years we have continued on the path to becoming a professionally run, not-for-profit society. Thanks to all who have put us on (and kept us on) this path. At the 2018 meeting I will continue in this tradition and am pleased to announce an open competition to find a new SMRA logo! Enjoy this year's meeting, as Giles is fond of saying, have a "Super Cool MRA Experience." Enjoy your week in Glasgow and perhaps you can find some time to venture a little further afield. During this year's meeting I will pass the Presidential Gavel onto Michael Markl. Michael has been invaluable in helping organize this year's meeting and is now working hard with Jean-Michel Serfaty and others to arrange the 2019 meeting. I look forward to seeing you again at next year's meeting in Nantes, France.

Sincerely,

Richard Frayne, PhD

Your Society of Magnetic Resonance Angiography (SMRA)

"An international group of scientists and clinicians devoted to the development, application and promotion of MR imaging techniques to visualise the cardiovascular system and to improve patient care"

The Society for Magnetic Resonance Angiography (SMRA) was founded in 1989 as the MR Angio Club to bring together scientists, clinicians and industry with a common interest in MR Angiography (MRA). The society's annual conference is widely recognised as the premier international conference in MR Angiography. Each year, prominent researchers and clinicians come from all over the world to attend this event and present their most up to date research results and exchange ideas. MR-related vendors also showcase their state-of-the-art products, technical advances, and clinical applications in an engaging environment intended to foster new connections and collaborations.

Executive Committee

- Richard Frayne: President
- Michael Markl: President Elect
- Charles (Chuck) Dumoulin: Secretary
- Kevin DeMarco: Treasurer
- James Carr: Past-President
- Jeffrey Maki: Past-past-President
- Elizabeth Hecht
- Giles Roditi
- David Saloner

Organizing Committee

SMRA Secretariat
- Janette Wallace
- Johanne Langford
- Donna Lyons
- Kevin Henley

Local Organiser
- Giles Roditi

Scientific Program Chair
- Aleksandra (Sasha) Radjenovic

Local Team
- Alison Riach
- Peter Douglas
- Alfie Tan
- Alexander Vesey
- Pauline Hall-Barrientos

Volunteers - We would like to gratefully acknowledge the volunteers for contributing their time and energy into making this event a success! Especially Alexa Roditi, Luka Radjenovic & Mark Frayne who have no interest in MRI whatsoever, it wouldn't have been possible without you — thank you!

Trainee Educational and Travel Support

Funding for this conference was made possible (in part) by 1R13HL144016-01 from the National Heart, Lung and Blood Institute. The views expressed in written conference materials or publications and by speakers and moderators do not necessarily reflect the official policies of the NIH; nor does mention by trade names, commercial practices, or organisations imply endorsement by the U.S. Government.

Trainee education has also been generously supported (in part) by The Martin R Prince Charitable Foundation.

For the 2018 SMRA Meeting, Trainee Education and Travel Support Awards were made to the following individuals:

Maria Aristova	Northwestern University, Chicago
Lionel Arn	Department of Radiology, University Hospital Lausanne (CHUV)
Li Chen	University of Washington
Louise Collins	Northwestern University
Teresa Correia	King's College London
Emeline Darçot	Lausanne University Hospital (CHUV)
Laura Eisenmenger	University of California, San Francisco
Mohammed Elbaz	Northwestern University
Sebastian Flassbeck	German Cancer Research Center (DKFZ)
Giulia Ginami	King's College London
Daniel Gordon	Northwestern University
Hualu Han	Tsinghua University
Henrik Haraldsson	University of California, San Francisco
John Heerfordt	Lausanne University Hospital (CHUV)
Kelly Jarvis	Radiology, Northwestern University, Chicago
Hao Li	Department of Radiology, University of Cambridge and Addenbrooke's Hospital
Patrick Liebig	Friedrich-Alexander Universität Erlangen-Nürnberg
Liliana Ma	Northwestern University, Chicago
Christian Meixner	Institute of Radiology, Friedrich-Alexander Universität Erlangen-Nürnberg
Giorgia Milotta	King's College London
Camila Munoz	King's College London
Pascal Ruetten	University of Cambridge, Department of Radiology
Roberto Sarnari	Northwestern University
Simon Schmidt	German Cancer Research Center (DKFZ)
Felicia Seemann	Lund University, Sweden
Zhang Shi	Changhai hospital of Shanghai
Eddie, Po Tao Sho	Singapore General Hospital
Roberto Souza	University of Calgary, Canada
Ammara Usman	University of Cambridge
Pim van Ooij	Academic Medical Center
Martin Wagner	University of Wisconsin
Michelle Walkden	University Hospital Southampton NHS foundation trust
Yan Wen	Cornell University
Clarissa Wink	Physikalisch-Technische Bundesanstalt (PTB)
Jiayi Wu	Institute of Artificial Intelligence and Robotics, Xian Jiaotong University

Abstract Reviewers

The scientific side would not of course have been possible without our team of abstract reviewers and their rigorous selection. We would therefore like to thank the following -

James Carr
Jeremy Collins
Kevin DeMarco
Charles Dumoulin
Petter Dyverfeldt
Robert Edelman
Zhaoyang Fan
Paul Finn
Christopher Francois
Peter Gatehouse
Pauline Hall Barrientos
Martin Hennesy
Michael Hope
John Huston
Ioannis Koktzoglou
Jing Liu
Jeffrey Maki
Michael Markl
Aleksandra Radjenovic
John Ridgway
Giles Roditi
David Saloner
Mark Schiebler
Jean-Michel Serfaty
Alex Vesey
Jonathan Weir-McCall
Oliver Wieben
Winfried Willinek

Amazing job, well done !

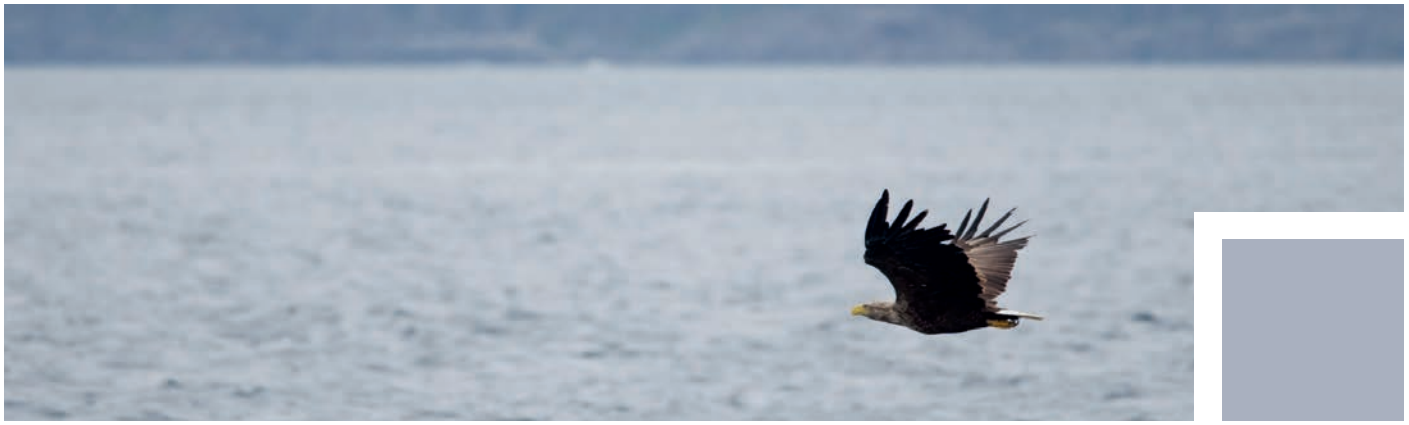

Educational Workshop Program

Tuesday, August 28th

08:45 **Welcome** - Opening remarks & brief history of SMRA
Richard Frayne (University of Calgary and Foothills Medical Centre, Calgary, Alberta, Canada), SMRA President

Session 1: Introduction to MRA and basic techniques

09:00 **W1** Fundamental MRA Techniques – Phase-Contrast
Charles Dumoulin (Cincinnati Children's Hospital, Ohio, USA)
09:20 **W2** Fundamental MRA Techniques – Time-of-Flight
Martin Graves (Cambridge University Hospitals, UK)
09:40 **W3** Introduction to k-space and Parallel imaging
Nicole Seiberlich (Case Western Reserve University, Cleveland, USA)
10:00 **W4** Gadolinium-based Contrast Agents
Tim Leiner (Utrecht University Medical Center, Netherlands)
10:20 **W5** Contrast-enhanced MRA and Background Suppression Methods
Eric Stinson (Mayo Clinic, Rochester, Minnesota, USA)

10:40 **Break**

Session 2: Advanced MRA techniques

11:00 **W6** Dynamic CE-MRA
Christopher J. Francois (University of Wisconsin – Madison, Wisconsin, USA)
11:20 **W7** Ferumoxytol MRA
Paul Finn (UCLA, Los Angeles, California)
11:40 **W8** 4D MRA
Michael Markl (Northwestern University Feinberg School of Medicine, Chicago)
12:00 **W9** Advanced Non-Contrast MRA Techniques
Robert Edelman (Northwestern University, Chicago, USA)
12:20 **W10** Imaging microcirculation
Aleksandra Radjenovic (University of Glasgow, Scotland, UK)

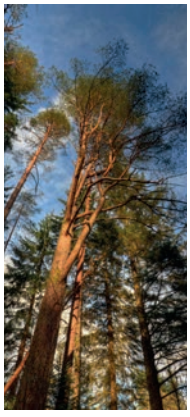

12:40 **Lunch** (12:40 - 13:30)

Educational Workshop Program

Tuesday, August 28th

Session 3: Applications: above diaphragm

13:30 **W11** Carotid & Intracranial MRA for Stroke Assessment
James Meaney (St. James's Hospital, Dublin, Ireland)
13:50 **W12** Intracranial MRA for Aneurysms & AVMs
Kevin DeMarco (Walter Reed National Military Medical Center and Uniformed Services University of the Health Sciences, USA)
14:10 **W13** Vessel Wall & Plaque imaging
Rene Botnar (King's College, London, UK)
14:30 **W14** Coronary MRA
Matthias Stuber (University of Lausanne, Switzerland)
14:50 **W15** Thoracic Aorta
James Carr (Northwestern University, Chicago, USA)

15:10 **Break**

Session 4: Applications: below diaphragm

15:30 **W16** Renal MRA
Giles Roditi (University of Glasgow, Scotland, UK)
15:50 **W17** Liver MRA
Elizabeth Hecht (New York Presbyterian, New York, USA)
16:10 **W18** Peripheral extremities MRA
Jeff Maki (University of Colorado, USA)
16:30 **W19** Whole Body MRA
Jonathan Weir-McCall (Ninewells Hospital, Dundee, Scotland, UK)
16:50 **W20** MRA of the Skin including AVMs
Martin Prince (Cornell and Columbia Universities, New York, USA)

17:10 **Closing address** - Motion-resolved quantitative CMR: Applications for plaque characterization and MRA
Debiao Li (Cedars Sinai, Los Angeles, California, USA)

19:00 Welcome Reception @ Hunterian Museum

Scientific Program

Wednesday, August 29th morning

08:30 Opening Session - Welcome from President and Organising Committee

Scientific Session 1: Cardiothoracic MRA (Proffered talks & Clinical Challenge)

Moderators: James Carr & Hideki Ota

09:00		**Introduction**
09:05	**A01**	Adaptive Navigator-Corrected, Breath-Hold Single-Shot Pulmonary MRA - Robert Edelman, NorthShore University HealthSystem
09:14	**A02**	4D flow MRI for Chronic Thromboembolic Pulmonary Hypertension: Hemodynamic Findings before and after Balloon Pulmonary Angioplasty - Hideki Ota, Tohoku University Graduate School of Medicine
09:23	**A03**	Accelerated, Navigator-Triggered, Noncontrast Relaxation Enhanced Angiography with Compressed SENSE at 1.5T - Hui Wang, Philips Healthcare
09:32	**A04**	Lung Perfusion Assessed without Exogenous Contrast via Arterial Spin Labeling - Mark DiFrancesco, Cincinnati Children's Hospital Medical Center
09:41	**A05**	Direct signs of Pulmonary Embolism at MRA: Intra Reader Agreement - Mark Schiebler, University of Wisconsin - Madison
09:50		**Clinical Challenge 1 - Thoraco-Abdominal Aorta and Major Branches in Suspected Large Vessel Vasculitis**

10:00 Break and Poster Set-up

⁕ Potchen Award Competitor

Scientific Program

Wednesday, August 29th morning

Scientific Session 2: Quantitative Flow MRI (Proffered talks)

Moderators: Michael Markl & Christopher Francois

10:30		**Introduction**
10:35	**A06**	Mapping of reversed flow and wall shear stress in aortas with bicuspid aortic valves - Pim van Ooij, Academic Medical Center, Amsterdam
10:44	**A07**	4D Flow vCath: 3D Virtual Catheter for Volumetric Time-varying Aortic Hemodynamic Analysis from 4D Flow MRI - Mohammed Elbaz, Northwestern University ⁕
10:53	**A08**	Directional Flow and Stasis Maps from 4D flow MRI to Characterize Aortic Dissection - Kelly Jarvis, Northwestern University ⁕
11:02	**A09**	Ultra Low Dose CT Fluoroscopy: A new tool for CT-guided Vascular Intervention. - Martin Wagner, University of Wisconsin - Madison
11:11	**A10**	Slice following in the era of feature-tracking: Pilot study to improve accuracy of trans-valvular flow - Felicia Seemann, Lund University ⁕
11:20	**A11**	4D Flow Imaging with Reduced Field-Of-Excitation - Clarissa Wink, Physikalisch-Technische Bundesanstalt, Berlin ⁕
11:29	**A12**	Non-invasive Assessment of Splanchnic Flow in Patients Suspected of Mesenteric Ischaemia using MRI 4D Flow - Pilot Study - Pauline Hall Barrientos, NHS Glasgow
11:38	**A13**	Reduction of Flow Jets following Lumbar Puncture in Patients with Pulsatile Tinnitus - Henrik Haraldsson, UCSF
11:47	**A14**	Augmenting 4D Flow MRI in Cerebral Aneurysms with High-resolution PIV and CFD Data - Sean Rothenberger, Purdue University ⁕
11:56	**A15**	Preoperative 4D Flow Analysis of Renal Cell Carcinoma - Christopher Francois, University of Wisconsin Madison

12:10 Gold Sponsor Presentation Siemens Healthineers - 'Advances in Time-of-Flight Imaging' - presented by Jianing Pang

12:20 Lunch

⁕ **Potchen Award Competitor**

Scientific Program

Wednesday, August 29th afternoon

13:40 Keynote - David Lurie: Fast Field-Cycling MRI: Technology, Methods and First Patient Studies, University of Aberdeen, UK

Scientific Session 3: Contrast MRA (Proffered talks)

Moderators: Catherine Ludman & Eric Stinson

14:15		**Introduction**
14:20	**A16**	Modeling to Better Understand Bolus Shaping Effects in Contrast-Enhanced MRA - Jeffrey Maki, University of Colorado
14:29	**A17**	Next Generation Gd-Free T1 MRI Contrast Agents for Angiography: High Relaxivity, Remarkable Stability and Tunable Pharmacokinetics - Xiao-an Zhang, University of Toronto
14:38	**A18**	Assessment of Pulmonary Hypertension using Time Resolved MRA and 4D flow MRI - Daniel Gordon, Northwestern University
14:47	**A19**	18F-Fluoride PET MR in valvular and coronary heart disease; A pilot investigational study - Jack Andrews, University of Edinburgh ⁕
14:56	**A20**	Efficacy of gadoterate meglumine enhanced MRA in evaluating vascular diseases compared with gadobutrol enhanced MRA. - Louise Collins, Northwestern University

15:10 Break/Posters

⁕ **Potchen Award Competitor**

Scientific Program

Wednesday, August 29th afternoon

15:40 Gold Sponsor Presentation Guerbet - 'Gadolinium Deposition' - presented by Jean-Sébastien Raynaud

Session 4: Peripheral MRA (Proffered talks)

Moderators: Jeff Maki & Giles Roditi

15:50		**Introduction**
15:55	**A21**	Flow-MRF: a novel way of quantifying blood velocities in combination with tissue relaxation parameters - Sebastian Flassbeck, German Cancer Research Center, Heidelberg ❋
16:04	**A22**	Submillisecond water excitation for flow-independent noncontrast-enhanced peripheral angiography at 3T - Nolwenn Leveque, University Hospital Lausanne ❋
16:13	**A23**	Contrast Free MRI Methods for Vascular Assessment in Diabetic Lower Extremities - Jie Zheng, Washington University School of Medicine
16:22	**A24**	Magnetic Resonance Imaging of Diabetic Feet – Going with the Flow - Jie Zheng, Washington University School of Medicine
16:31	**A25**	Non-invasive lower limb angiography in a large health board – how low a radiation dose is achievable? Audit Update - Peter Douglas, NHS Glasgow ❋
16:40		**Clinical Challenge 2 - Critical Lower Limb Ischaemia** **Technical Challenge: PAVES**

❋ **Potchen Award Competitor**

Scientific Program

Wednesday, August 29th afternoon

Session 5: 'Power-Pitch: rapid fire poster session'

Moderator: Jim Meaney

17:10	**A26**	Ferumoxytol MRA in Haemodialysis Access Assessment : Pre- and Post-Surgical Findings - A Pictorial Review - Alfred Tan, NHS Greater Glasgow and Clyde ❂
17:13	**A27**	Safety profile of ferumoxytol as contrast for MR angiography in patients with chronic kidney disease - Sokratis Stoumpos, University of Glasgow ❂
17:16	**A28**	Protocol time optimization: Institutional experience in clinically applied high-resolution intracranial vessel wall MRI - Laura Eisenmenger, University of California, San Francisco ❂
17:19	**A29**	A Morphology aided Diagnosis Network for Discrimination between Normal and Atherosclerotic Carotid Arteries on Black-Blood Vessel Wall MRI - Jiayi Wu, Xian Jiaotong University ❂
17:22	**A30**	An optimised subtraction approach for subtractive NCE-MRA techniques based on robust regression using the deviation angle - Hao Li, University of Cambridge and Addenbrooke's Hospital ❂
17:25	**A31**	Simultaneous Multi-VENC Imaging with Dual-Echo Acquisition - Simon Schmidt, German Cancer Research Center, Heidelberg ❂
17:28		**Group Discussion**

❂ **Passariello Award Competitor**

19:00 Evening Social Event @ Kelvingrove Art Gallery & Museum

Scientific Program

Thursday, August 30th morning

08:50 Announcements

09:00 Keynote - Matthias Stuber: A Sound (♪) Approach to Fully Self-Gated Cardiac Imaging, University of Lausanne, Switzerland

Session 6: Coronary MRA (Proffered talks)

Moderators: Debiao Li & Claudia Prieto

09:30		**Introduction**
09:35	**A32**	Motion-corrected coronary magnetic resonance angiography and myocardial positron emission tomography: initial clinical experience - Camila Munoz, King's College London ⁕
09:44	**A33**	XD-ORCCA: Optimized Respiratory-resolved 3D Cartesian Coronary MRA - Teresa Correia, King's College London
09:53	**A34**	Quantitative myocardial perfusion using multi-echo Dixon for combined motion and T2* correction - Markus Henningsson, King's College London
10:02	**A35**	Particle swarm optimization for simultaneous T2 preparation and robust broadband fat suppression for coronary magnetic resonance angiography at 3T - Lionel Arn, University Hospital Lausanne ⁕
10:11	**A36**	Flexible, Semi-Projective MR Angiography using Cine FISS ASL for Combined Flow Quantification and Optimal Display of Arterial Anatomy - Robert Edelman, NorthShore University HealthSystem

10:30 Gold Sponsor Presentation GE Healthcare - 'Recent Advances in Magnetic Resonance Angiography' - presented by Kabasawa Hiroyuki

10:40 Gold Sponsor Presentation Bracco - 'Contrast-enhanced MR angiography: how do changing EU regulations impact daily practice?' - presented by Günther Schneider

10:50 Break/Posters

⁕ Potchen Award Competitor

Scientific Program

Thursday, August 30th morning

Session 7: Cardiac MRI (Proffered talks)

Moderators: Matthias Stuber & Aleksandra Radjenovic

11:20		Introduction
11:25	**A37**	Altered Biventricular Myocardial Velocities in Patients During Year 1 After Heart Transplantation - Roberto Sarnari, Northwestern University
11:34	**A38**	A multimodality quantification of the influence of cardiac allograft vasculopathy on the coronary arteries and the myocardium - Ruud van Heeswijk, Lausanne University Hospital
11:43	**A39**	Quantitative 4D CT DSA: A New tool for CT-guided Vascular Diagnosis and Intervention. - Martin Wagner, University of Wisconsin - Madison
11:52	**A40**	Assessment of myocardial microvascular pathology using ferumoxytol-enhanced MRI and 3-compartment model of capillary level water exchange in patients with chronic kidney disease: comparison with healthy controls - Aleksandra Radjenovic, University of Glasgow
12:01	**A41**	Non-Contrast Enhanced Simultaneous Bright- and Black-Blood 3D Whole-Heart MRI in Patients with Congenital Heart Disease - Giulia Ginami, King's College London ⁕
12:10	**A42**	Native T1-rho mapping: An alternative to ECV for detection of diffuse myocardial fibrosis? A Clinical Study in 219 patients - Martijn Froeling, Utrecht University Medical Center
12:19	**A43**	Left ventricle in Idiopathic Pulmonary Arterial Hypertension. Longitudinal, circumferential and radial strain and dyssynchrony. - Geeshath Jayasekera, University of Glasgow ⁕
12:28	**A44**	Cardiac Quantitative Susceptibility Mapping at 3T: a Comparison between Breathhold and Freebreathing Approaches - Yan Wen, Cornell University ⁕
12:37	**A45**	Peak velocity across the aortic valve using same-day Doppler echocardiography and 4D flow MRI - Hyungkyu Huh, Radiology Northwestern University ⁕
12:46	**A46**	Simultaneous 3D whole-heart bright-blood anatomy and black blood wall assessment with interleaved T2prep-IR - Giorgia Milotta, King's College London ⁕

13:00 Lunch

⁕ **Potchen Award Competitor**

Scientific Program

Thursday, August 30th afternoon

14:15 Keynote - Nicole Seiberlich: Cardiac MR Fingerprinting, Case Western Reserve University, Cleveland, USA

14:40 Gold Sponsor Presentation Philips - 'Advances in Cardiovascular MR' presented by Marc Kouwenhoven

Session 8: Vessel Wall MRI (1/2) (Proffered talks)

Moderators: Chun Yuan & Martin Graves

15:00		**Introduction**
15:05	**A47**	Maximizing the Conspicuity and Characterizing Signal Generation of Fluorine-19 MRI for the Quantification of Inflammation in Atherosclerosis - Emeline Darçot, Lausanne University Hospital ⁕
15:14	**A48**	Simultaneous T1 and T2 Mapping of Plaque (SIMPLE) with T2 and Inversion Recovery Prepared 3D Radial Imaging - Huijun Chen, Tsinghua University
15:23	**A49**	Vascular Deformation Mapping (VDM) for Assessment of Thoracic Aortic Growth Using Magnetic Resonance Angiography: Preliminary Results - Nicholas Burris, University of Michigan
15:32	**A50**	Comparison of Qualitative and Quantitative Methods for Vessel Wall Imaging MRI Evaluation of Intracranial Atherosclerosis - Matthew Alexander, University of Utah
15:41	**A51**	Cardiovascular black-blood imaging using Volume ISotropic Turbo spin echo Acquisition (VISTA) in patients with congenital heart disease - Markus Henningsson, King's College London

15:50 Break/Posters

⁕ **Potchen Award Competitor**

Scientific Program

Thursday, August 30th afternoon

Session 9: Vessel Wall MRI (2/2) (Proffered talks)

Moderators: Chun Yuan & Martin Graves

16:20	**A52**	Simultaneous Water-Fat Separation and Quantitative Susceptibility Mapping of the Carotid Artery Wall: Sequence and Processing Considerations - Pascal Ruetten, University of Cambridge ⁕
16:29	**A53**	Comparison of Multiple Normal Reference Structures for Vessel Wall Imaging MRI Sequences - Matthew Alexander, University of Utah
16:38	**A54**	Vessel Wall Imaging using 3T MRI in Perforating Artery Infarction - Difference between LSA and PPA - Keiji Igase, Washokai Sadamoto Hospital
16:47	**A55**	Added Value of Femoral Artery Atherosclerosis for Determining Severity of White Matter Lesions: A 3D MR Vessel Wall Imaging Study - Xihai Zhao, Tsinghua University
16:56	**A56**	Visualizing the Lumen and Wall of Intracranial Artery Stenosis Before and After Stenting Using High Resolution MRI Vessel Wall Imaging - Bing Tian, Changhai Hosiptal of Shanghai

⁕ Potchen Award Competitor

Scientific Program

Thursday, August 30th afternoon

Session 10: 'Power-Pitch: rapid fire poster session' (2/2)

Moderator: Martin Prince

17:10	**A57**	3D Radial Free-breathing Variable Flip Angle Whole Heart Myocardial T1 Mapping - Orhan Unal, University of Wisconsin - Madison
17:13	**A58**	Combined Low-dose time-resolved and single-phase high-resolution contrast-enhanced MRA: effectiveness in detection of spinal vascular diseases - Bum-soo Kim, Seoul St. Mary's Hospital, The Catholic University of Korea
17:16	**A59**	Development of a targeted contrast agent for MR molecular imaging of EDB-FN - Zheng-Rong Lu, Case Western Reserve University
17:19	**A60**	Using non-contrast navigator MRA to decrease scan times of MR aorta - Michelle Walkden, University Hospital Southampton ❂
17:22	**A61**	Hemodynamics assessed with Dual-Venc 4D flow MRI in patients with cerebral aneurysms - Susanne Schnell, Northwestern University
17:25	**A62**	Quantitative Analysis of Plaque Enhancement on Vessel Wall Imaging MRI Sequences for Intracranial Atherosclerosis - Matthew Alexander, University of Utah
17:28		**Group Discussion**

❂**Passariello Award Competitor**

19:00 Evening Social Event @ Glasgow Old Fruitmarket, Whisky Tasting and Ceilidh with Jiggered

Scientific Program

Friday, August 31st morning

08:50 Announcements

09:00 Keynote - Keynote - Tim Leiner: New Developments in Machine Learning for Cardiovascular Imaging, Utrecht University Medical Centre, Netherlands

Session 11: Emerging Techniques in MRA (1/2) (Proffered talks)

Moderators: Tim Leiner & Jianing Pang

09:30		Introduction
09:35	**A63**	Highly accelerated 4D flow with compressed sensing for evaluation of aortic hemodynamics - Liliana Ma, Northwestern University ⁕
09:44	**A64**	Quantitative 3D Dynamic Contrast Enhanced (DCE) MR Imaging of Carotid Vessel Wall by Fast T1 Mapping Using Multitasking - Nan Wang, Cedars-Sinai Medical Center ⁕
09:53	**A65**	Dynamic Fast Spin Echo Single Image Super-resolution Using Generative Adversarial Network - Roberto Souza, Uni of Calgary ⁕
10:02	**A66**	Deep Learning for Automated Reference-Free Image Quality Assessment of Whole-Heart Magnetic Resonance Images - Davide Piccini, Siemens Healthcare Switzerland
10:11	**A67**	Identification of high-risk intracranial atherosclerotic plaque features in intracranial atherosclerosis: initial experience using a radiomic approach by high resolution MRI - Zhang Shi, Changhai Hospital of Shanghai

10:20 Break/Posters

⁕ Potchen Award Competitor

Scientific Program

Friday, August 31st morning

Session 12: Emerging Techniques in MRA (2/2) (Proffered talks)

Moderators: Tim Leiner & Jianing Pang

10:50	**A68**	Carotid Artery Localization and Lesion Detection on 3D-MERGE MRI through Online Learning - Li Chen, University of Washington ❋
10:59	**A69**	Deep Learning meets Compressed Sensing: Image Quality-Regularized Coronary MRA - John Heerfordt, Lausanne University Hospital ❋
11:08	**A70**	Clinical Feasibility of High-Resolution Prospective Compressed Sensing Time-of-Flight Angiography at 7 Tesla - Patrick Liebig, Friedrich-Alexander Universität Erlangen-Nürnberg ❋
11:17	**A71**	High Resolution Time-of-Flight Angiography of Human Brain at 7 Tesla with VERSE Saturation and Compressed Sensing - Christian Meixner, Friedrich-Alexander Universität Erlangen-Nürnberg ❋
11:26	**A72**	Intracranial Vessel Wall Segmentation on 3D black-blood MRI using Convolutional neural network - Huijun Chen, Center for Biomedical Imaging Research, Tsinghua University

Session 13: Head & Neck MRA (Proffered talks)

Moderators: Kevin DeMarco & Alex Vesey

11:40		**Introduction**
11:45	**A73**	Network-based 4D Flow MRI quantification in healthy neurovasculature and arteriovenous malformation - Maria Aristova, Northwestern University ❋
11:54	**A74**	Association between Cerebrovascular Large Artery Atherosclerosis and Cerebral Perfusion - Hualu Han, Tsinghua University ❋
12:03	**A75**	Assessment of the Hemodynamic Impact of Intracranial Atherosclerosis Disease - Alireza Vali, Radiology, Northwestern University ❋
12:12	**A76**	Automatic Segmentation of Carotid Vessel Wall in Multi-Contrast Blackblood Images using Deep Learning - Rui Li, Tsinghua University
12:21	**A77**	Utility of Combining Positron Emission Tomography and Magnetic Resonance Imaging of Carotid Plaque: Review and Early Experience - Alex Vesey, Edinburgh University
12:30		**Clinical Challenge 3 - Carotid and Vertebral MRA in Suspected Dissection** **Round table discussion on the future of carotid MRA including address by Rhian Touyz Director of Research Institute/Professor (Institute of Cardiovascular and Medical Sciences)**

13:00 Lunch

❋Potchen Award Competitor

Scientific Program

Friday, August 31st afternoon

14:15 Keynote - David Newby: The Magnetism of Antimatter: Lesson from PET-MRI, University of Edinburgh, UK

Session 14: Ferumoxytol MRA (Proffered talks)

Moderators: Paul Finn & Giles Roditi

14:50		**Introduction**
14:55	**A78**	Safety for the Off-label Use of Ferumoxytol in Magnetic Resonance Imaging: Early Results from the FeraSafe Multi-Center Registry™ - Kim-Lien Nguyen, UCLA
15:04	**A79**	Ferumoxytol-Enhanced MRI for Intramyocardial Vascular Reactivity Mapping: Early Pre-Clinical Results - Kim-Lien Nguyen, UCLA
15:13	**A80**	CT angiography (CTA) vs ferumoxytol-enhanced MR angiography (FeMRA) for the assessment of potential kidney transplant recipients - Sokratis Stoumpos, University of Glasgow ❋
15:22	**A81**	Utility of Ferumoxytol-enhanced 3-Dimensional Magnetic Resonance Imaging in the assessment of carotid atheroma inflammation - Ammara Usman, University of Cambridge
15:31	**A82**	3D high resolution Black Blood(BB) Multi-Echo(ME) T2* Imaging Technique for Quantitative Superparamagnetic Iron Nanoparticle Uptake into Intracranial Atherosclerosis - Seong-Eun Kim, University of Utah

15:45 Break/Posters take-down

❋Potchen Award Competitor

Scientific Program

Friday, August 31st afternoon

Session 15: Abdominal MRA (Proffered talks)

Moderators: Elizabeth Hecht & Robert Edelman

16:15		Introduction
16:20	**A83**	4D Flow MRI of the Uterine and Ovarian Vessels in the 2nd Trimester in Healthy Subjects - Oliver Wieben, University of Wisconsin - Madison
16:29	**A84**	Simultaneous quantitative assessment of cardio-renal perfusion and glomerular filtration rate using dual-bolus DCE-MRI - Matthew Lee, University of Glasgow ❋
16:38	**A85**	Comparison of renal split function using 1.5T DCE-MRI and Nuclear Medicine - Sau Lee Chang, NHS Glasgow ❋
16:47	**A86**	Use of kZ-Space for Providing Sub-Millimeter Through-Plane Resolution in 2D Multislice Imaging - Soudabeh Kargar, Mayo Clinic
16:56	**A87**	Comparison of GFR measurements using 1.5T DCE-MRI and Nuclear Medicine - Rosario Lopez Gonzalez, NHS Galsgow
17:05		**Clinical Challenges 4 & 5 - Potential Living Kidney Donors & Vasculature of the Skin**

17:15 Awards and Closing Session

Richard Frayne (President), James Carr (Past President) and Michael Markl (President-elect)

- Acknowledgement and thanks to SMRA Secretariat and Local Organizing Committee – Richard Frayne, Aleksandra Radjenovic and Giles Roditi
- Presentation of the Potchen Award and Passariello Awards – James Carr
- Introduction of new Board Member and President – Richard Frayne
- Announcement of and Invitation to the 2019 SMRA Meeting, Michael Markl with Jean-Michel Serfaty
- Closing Remarks – Michael Markl

19:00 Evening Social Event @ Oran Mor, President's Address, Dinner & Magic

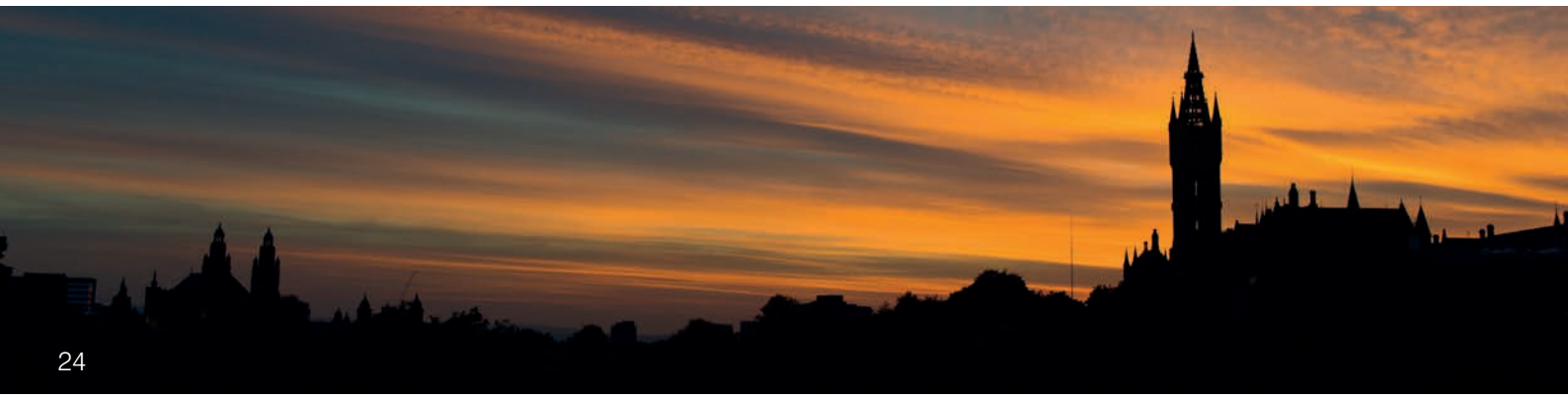

Poster Exhibition

Wednesday, August 29th - Friday, August 31st

A26	Ferumoxytol MRA in Haemodialysis Access Assessment : Pre- and Post-Surgical Findings - A Pictorial Review - Alfred Tan, NHS Greater Glasgow and Clyde ❂
A27	Safety profile of ferumoxytol as contrast for MR angiography in patients with chronic kidney disease - Sokratis Stoumpos, University of Glasgow ❂
A28	Protocol time optimization: Institutional experience in clinically applied high-resolution intracranial vessel wall MRI - Laura Eisenmenger, University of California, San Francisco ❂
A29	A Morphology aided Diagnosis Network for Discrimination between Normal and Atherosclerotic Carotid Arteries on Black-Blood Vessel Wall MRI - Jiayi Wu, Xian Jiaotong University
A30	An optimised subtraction approach for subtractive NCE-MRA techniques based on robust regression using the deviation angle - Hao Li, University of Cambridge and Addenbrooke's Hospital ❂
A31	Simultaneous Multi-VENC Imaging with Dual-Echo Acquisition - Simon Schmidt, German Cancer Research Center, Heidelberg ❂
A57	3D Radial Free-breathing Variable Flip Angle Whole Heart Myocardial T1 Mapping - Orhan Unal, University of Wisconsin - Madison
A58	Combined Low-dose time-resolved and single-phase high-resolution contrast-enhanced MRA: effectiveness in detection of spinal vascular diseases - Bum-soo Kim, Seoul St. Mary's Hospital, The Catholic University of Korea
A59	Development of a targeted contrast agent for MR molecular imaging of EDB-FN - Zheng-Rong Lu, Case Western Reserve University
A60	Using non-contrast navigator MRA to decrease scan times of MR aorta - Michelle Walkden, University Hospital Southampton ❂
A61	Hemodynamics assessed with Dual-Venc 4D flow MRI in patients with cerebral aneurysms - Susanne Schnell, Northwestern University
A88	Bright venous and/or sinus signals on arterial spin labeling MRI for identifying cerebral venous thrombosis, comparing with MRA findings - Dong Woo Park, Hanyang University Guri Hospital, South Korea
A89	Results of Contrast Enhanced Magnetic Resonance Angiography (MRA) of the Hand – A Retrospective Evaluation - Manuela Aschauer, LKH Graz
A90	Fractional flow reserve in the femoral arteries derived through computational fluid dynamics: a non-invasive diagnostic tool for stenotic diseases - Simeon Skopalik, University of Glasgow ❂
A91	Experimental Assessment of MEDIC and ToF Imaging Accuracy - Conor MacDonald, University of Dundee ❂
A92	Evaluate the Characteristics of Spontaneous Intracranial Artery Dissection using High Resolution MRI Vessel Wall Imaging - Bing Tian, Changhai Hospital of Shanghai
A93	Design of a phantom to validate the accuracy of 4D flow MRI velocity measurements and derived bio-markers - Marco Castagna, Université de Nantes - Ecole Centrale Nantes ❂
A94	Contrast-enhanced Magnetic Resonance Angiographic (ceMRA) in Evaluation of Vascular Stents - Ability of Assessment and Artefacts in Dependence of Stent Material and Field Strength - Manuela Aschauer, LKH Graz, Austria
A95	Diffusion-Weighted Magnetic Resonance Imaging of Acute Lower Extremity Deep Vein Thrombosis - Zeynep Tekin, Medeniyet University Göztepe Training And Research Hospital
A96	Influence of Intracranial Aneurysms on Volume Flow Rate Measurement using Magnetic Resonance Fluid Dynamics - Haruo Isoda, Brain & Mind Research Center, Nagoya University
A97	Contrast enhanced MRA in Thoracic Outlet Syndrome: Indications and Technical Considerations - Soh Eddie Po Tao, Singapore General Hospital
A98	Use of Time Resolved Imaging of Contrast Kinetics (TRICKS) MRA sequences in complex arteriovenous malformation (AVM) assessment – pictorial review - Mark Lewis, Norfolk and Norwich University Hospitals NHS Trust

❂ Passariello Award Competitor

Sponsor Presentations

This year 5 of our Gold Sponsors will have presentations as follows -

Wednesday, August 29th

12:10 Gold Sponsor Presentation Siemens Healthineers - 'Advances in Time-of-Flight Imaging' - presented by Jianing Pang

15:40 Gold Sponsor Presentation Guerbet - 'Gadolinium Deposition' - presented by Jean-Sébastien Raynaud

Thursday, August 29th

10:30 Gold Sponsor Presentation GE Healthcare - 'Recent Advances in Magnetic Resonance Angiography' - presented by Kabasawa Hiroyuki

10:40 Gold Sponsor Presentation Bracco - 'Contrast-enhanced MR angiography: how do changing EU regulations impact daily practice?' - presented by Günther Schneider

14:40 Gold Sponsor Presentation Philips - 'Advances in Cardiovascular MR' presented by Marc Kouwenhoven

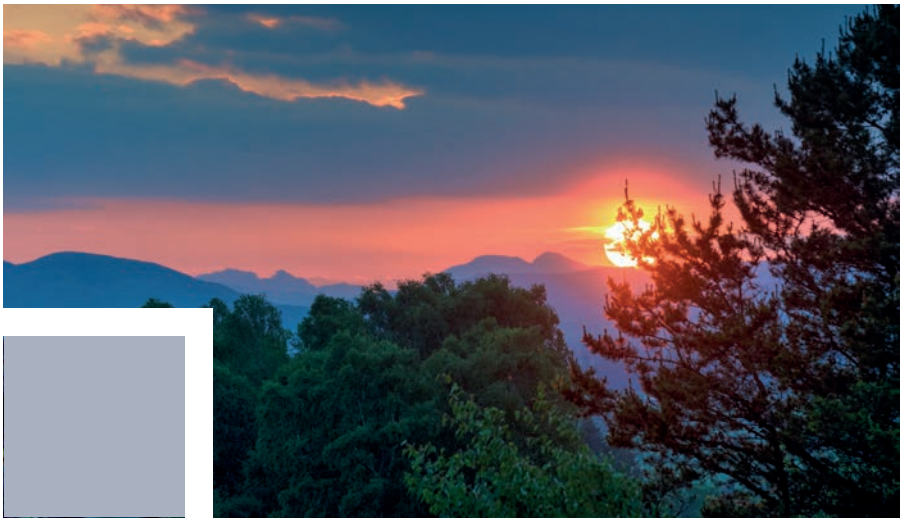

Adaptive Navigator-Corrected, Breath-Hold Single-Shot Pulmonary MRA

Robert R. Edelman[1,2], Jianing Pang[3], Amit Pursnani[4], Ioannis Koktzoglou[1,5]
[1]Radiology, NorthShore University HealthSystem, Evanston, Illinois, United States, [2]Radiology, Feinberg School of Medicine, Northwestern University, Chicago, Illinois, United States, [3]Siemens Medical Solutions USA Inc, Chicago, Illinois, United States, [4]Medicine, NorthShore University HealthSystem, [5]Radiology, Pritzker School of Medicine, University of Chicago, Chicago, Illinois, United States

Purpose: MR angiography offers a potentially useful alternative to CT angiography for arterial evaluation in suspected pulmonary embolism and venous evaluation prior to pulmonary vein isolation procedures. Compared with contrast-enhanced 3D MRA, nonenhanced techniques such as single-shot radial QISS [1] are markedly less sensitive to artifacts from respiratory and cardiac motion. However, several breath-holds are usually required to provide sufficient anatomical coverage of the pulmonary vessels, which introduces the likelihood of image misregistration both within and across breath-holds due to variations in diaphragm position. We hypothesized that navigator-based monitoring of diaphragm position, in conjunction with adaptive correction of slice position and end-expiratory breath-holding, would minimize slice misregistration and thereby optimize image quality and diagnostic utility.

Methods: Imaging was performed in healthy volunteers and patients at 1.5 Tesla (MAGNETOM Avanto, Siemens Healthcare, Erlangen, Germany). For evaluation of the pulmonary arteries, single-shot radial QISS images were acquired in a coronal plane using 2 or 3-mm slices (1 slice per RR interval). For evaluation of the pulmonary veins, single-shot radial bSSFP images were acquired in an axial plane using 2-mm slices thickness with ECG gating for subjects in normal sinus rhythm and without ECG gating for those in atrial fibrillation. A cross-pair navigator was positioned over the antero-medial aspect of the right hemidiaphragm to avoid saturation of the right pulmonary veins. Initially, several end-expiratory breath-holds were acquired with monitoring of the navigator to determine an average breath-hold diaphragm position, which was then used as the baseline for subsequent scans as well as to determine a comfortable breath-hold duration. For image acquisition, real-time navigator data were monitored during each breath-hold; the scan was interrupted, and the breath-hold repeated if the diaphragm was observed to be more than 5-mm from baseline. Any residual drift within a breath-hold was corrected via shifting the acquisition slice according to the diaphragm position with a correction factor of 0.6.

Results: Navigator-corrected breath-hold images of the pulmonary arteries and veins demonstrated excellent spatial registration of images acquired within the same breath-hold as well as across breath-holds (Fig. 1). Image registration and MIP image quality were substantially improved compared with uncorrected breath-hold scans as well as free-breathing navigator-gated scans.

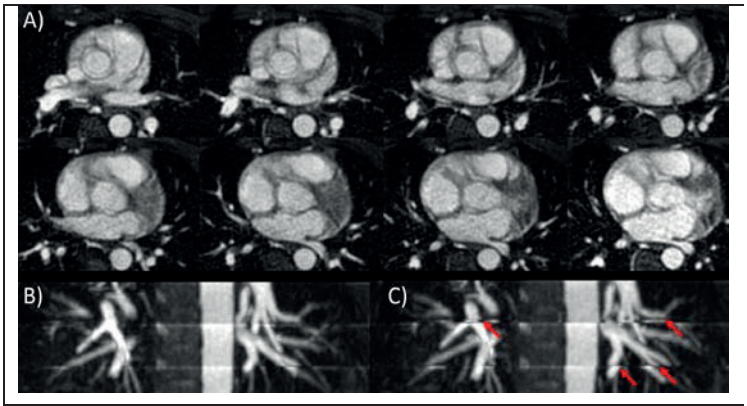

Fig. 1. *A) Navigator-corrected axial radial bSSFP images (8 shown of 45 acquired in 3 breath-holds). B) Corresponding 12-mm coronal MIP shows excellent image registration. C) 12-mm MIP from images acquired without navigator correction shows misregistration artifacts (arrows).*

Discussion: We found that navigator-based real-time monitoring and adaptive correction can be easily translated to breath-hold single-shot radial QISS and bSSFP scans of the pulmonary vessels, thereby ensuring optimal quality and image registration. An additional benefit is that the navigator tracing provides real-time feedback regarding breath-hold capability, thereby permitting the number of slices per group to be optimized and for breath-holds with inconsistent diaphragm position to be interrupted and repeated.

References: [1] Edelman RR, et al. J Cardiovasc Magn Reson. 2017 June 19(1):48.

Funding: NIH grants R01 HL137920, R01 HL130093, and R21 HL126015.

4D flow MRI for Chronic Thromboembolic Pulmonary Hypertension: Hemodynamic Findings before and after Balloon Pulmonary Angioplasty

Hideki Ota[1], Wenyu Sun[1] Koichiro Sugimura[2], Haruka Sato[2], Yuta Urushibata[3], Yoshiaki Komori[3], and Kei Takase[1].
[1]Diagnostic Radiology and [2]Cardiovascular Surgery, Tohoku University Hospital, Sendai, Japan.
[3]Siemens Japan K.K., Tokyo, Japan.

Purpose: Chronic thromboembolic pulmonary hypertension (CTEPH) is caused by obstruction of pulmonary artery with organized clot and secondary vasculopathy. It is diagnosed with characteristic catheter angiographic or CT angiographic findings and sustained pulmonary hypertension (mean pulmonary arterial pressure [mPAP] > 25 mmHg) for more than six months. Recently, balloon pulmonary angioplasty (BPA) procedure was recognized for treatment of inoperable CTEPH resulting in improved right ventricular (RV) function and prognosis[1]. Past studies indicated conventional cardiac and 4D flow MR imaging parameters were correlated with mPAP[2,3]. Odagiri et al. demonstrated that low wall shear stress (WSS) measured with 4D flow MRI was observed in PH patients[4]. Therefore, we hypothesized that improvement of PH after BPA may be evaluated by cardiac MR including 4D flow MRI. The purpose of this study was to examine whether MR parameters are correlated with the change of mPAP after BPA for patients with CTEPH.

Methods: This study included a total of 30 patients (mean age, 68.4 ± 7.9 year old, M/F=5/25,) with inoperable CTEPH scheduled for BPA. All patients underwent serial MR scans using a 3.0T whole body scanner before and after BPA procedures. MR scan protocols included standard cardiac cine MR imaging and 4D flow MR imaging of the pulmonary trunk. 4D flow MR imaging parameters were in the following: 3-dimensional phase-contrast MR imaging with 3-directional velocity encoding in transverse acquisition; ECG-gating; respiratory-gating; TR/TE, 52.4ms/3.43ms; flip angle, 15 degrees; VENC, 50-110cm/sec; matrix size, 2.4mm x 1.8mm x 3.5mm.

Cine MRI measurements included left ventricular ejection fraction (LVEF), LV cardiac index (LVCI), RVEF, RVCI, RV end-diastolic and end-systolic volume index (RVEDVI, RVESVI) and pulmonary trunk diameter to ascending aortic diameter ratio (PA/AA ratio). 4D flow MR images were analysed with postprocessing software (CVI[42], Circle Cardiovascuar Imaging, Calgary, Canada). On 4D flow MRI, peak and mean PA flow velocities, maximum energy loss (EL) and maximum wall shear stress (WSS) maps in the pulmonary trunk were evaluated.

Individual data were compared before and after BPA procedures. Pearson's correlation coefficients between MR imaging parameters and catheter-driven parameters (mPAP). A $p<0.05$ was used to designate statistical significance.

Results: The mean of mPAP was significantly improved after BPA in all patients (39.0 ± 9.3 mmHg vs 25.0±6.8 mmHg, p<0.01). Significant correlations with pre-BPA mPAP were observed in PA/AA diameter ratio (0.39, p=0.035) and maximal WSS (r= -0.37, p=0.045). RVEF (-0.33, p=0.07), RVESVI (r=0.30, p=0.10) and peak PA flow velocity (r=-0.35, p=0.062) showed trends towards correlation with mPAP. No other MR imaging parameter was correlated with mPAP.

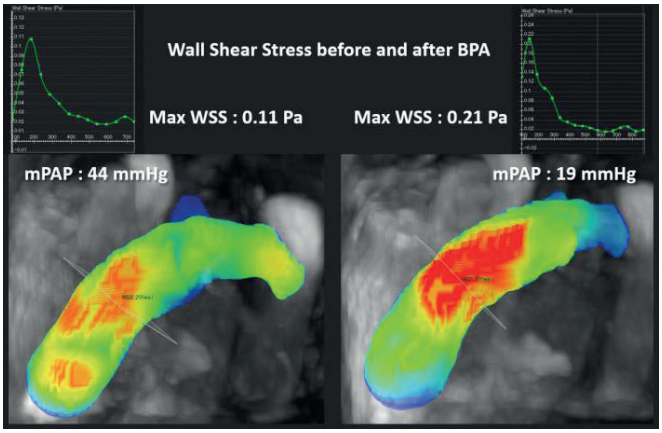

All MR parameters except for LVEF demonstrated significant improvement after BPA. The difference of mPAP before and after BPA were significantly correlated with the differences of RVESVI (r=0.38, p=0.05), PA/AA ratio (r=0.42, p=0.02), maximum EL (r=0.38, p=0.04) and maximum WSS (r=-0.47, p<0.01) (Figure). On multivariate linear regression analysis, the difference of maximum WSS remained significantly correlated with the difference of mPAP (p<0.016).

Discussion: Cardiac MR parameters demonstrated improvement after BPA for CTEPH. Negative correlation between mPAP and maximum WSS was in line with the previous study demonstrating low WSS in PH patients. Moreover, the changes of WSS observed after BPA may reflect the treatment effect on CTEPH.

Conclusion: Findings on cardiac MR including 4D flow MRI can reflect improvement of mPAP after effective BPA and can be used for the management of patients with CTEPH.

References:

1. Galiè N, Humbert M, Vachiery J-L, et al. 2015 ESC/ERS Guidelines for the diagnosis and treatment of pulmonary hypertension. European Heart Journal. 2016;37:67-119. doi:10.1093/eurheartj/ehv317
2. Swift AJ, Rajaram S, Hurdman J, et al. Noninvasive Estimation of PA Pressure, Flow, and Resistance With CMR Imaging: Derivation and Prospective Validation Study From the ASPIRE Registry. J Am Coll Cardiol Img. 2013;6:1036-1047. doi:10.1016/j.jcmg.2013.01.013
3. Reiter G, Reiter U, Kovacs G, Olschewski H, Fuchsjäger M. Blood Flow Vortices along the Main Pulmonary Artery Measured with MR Imaging for Diagnosis of Pulmonary Hypertension. Radiology. 2014;275:71-79. doi:10.1148/radiol.14140849
4. Odagiri K, Inui N, Hakamata A, et al. Non-invasive evaluation of pulmonary arterial blood flow and wall shear stress in pulmonary arterial hypertension with 3D phase contrast magnetic resonance imaging. Springerplus. 2016;5. doi:10.1186/s40064-016-2755-7

Accelerated, Navigator-Triggered, Noncontrast Relaxation Enhanced Angiography with Compressed SENSE at 1.5T

Hui Wang[1, 2], Matthew Lanier[1], Masami Yoneyama[3], Jean Tkach[1], Brynne Williams[1], Lacey Haas[1], Kaley Bridgewater[1], Marty Jones[1], Jonathan R. Dillman[1], and Charles Dumoulin[1]

[1]Radiology, Cincinnati Children's Hospital Medical Center, Cincinnati, OH, United States, [2]Philips Healthcare, Cincinnati, OH, United States, [3]Philips Healthcare, Tokyo, Japan

Purpose

Non-contrast MR angiography (MRA) is a promising technique to diagnose and follow-up vascular diseases, especially in children, a population where gadolinium contrast material administration should be minimized given recent concerns with gadolinium retention in the body. Relaxation Enhanced Angiography without Contrast and Triggering (REACT) [1-3] has been proposed to acquire noncontrast MRA for uniform fat suppression at large field-of-view (FOV). REACT with navigator-triggering could compensate for respiratory motion and improve image quality. However, navigator-triggering prolongs scan time. In this study, we propose an accelerated, navigator-triggered, relaxation-enhanced angiography sequence with compressed SENSE.

Methods

Fig. 1 shows the pulse sequence diagram. It is an improved mDIXON gradient echo sequence (mDIXON XD), with T2 preparation (T2prep) prep-pulse and non-selective short tau inversion recovery (STIR). To compensate respiratory motion, a navigator echo is used to trigger the scan in the beginning of expiration. The T2prep pulse can be used to differentiate arteries and veins. The STIR pre-pulse is to increase the contrast between blood and background signals such as muscle. mDixon XD (water image) provides robust fat suppression. Compressed SENSE [4] undersampling and iterative reconstruction are used to reduce scan time. Specifically, the center of k-space is measured using a standard Cartesian sampling pattern with SENSE acceleration factor=2, while the sampling density in the outer part of k-space is further decreased by a factor of 2 or 3 through the use of a pseudo-random sampling pattern.

All imaging was performed on a Philips Ingenia™ 1.5T scanner, using anterior and posterior phased array coils. Five healthy volunteers were imaged for this feasibility study. The scan parameters were: TR = 5.8ms; TE1/TE2 = 1.73/3.8ms; FA = 10°; T2 prep time = 50ms, FOV = 400x510x117mm, coronal plane, voxel size = 1.37x1.37x2mm, turbo factor = 100, SENSE factor = 2, total acquisition time = 6 min 27 s. Using the accelerated approach with compressed SENSE, total scan time is reduced to 3 min 8 s or 2 min 6 s with additional CS factor of 2 or 3, respectively.

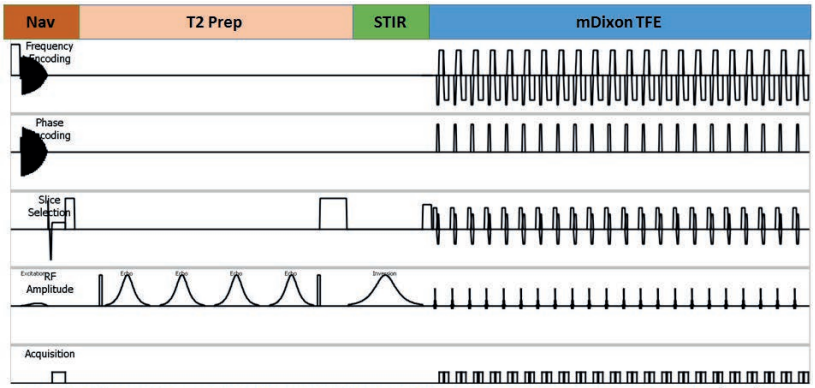

Fig 1: Sequence diagram. It consists of a navigator, T2 preparation, short time inversion recovery (STIR), and mDixon TFE readout.

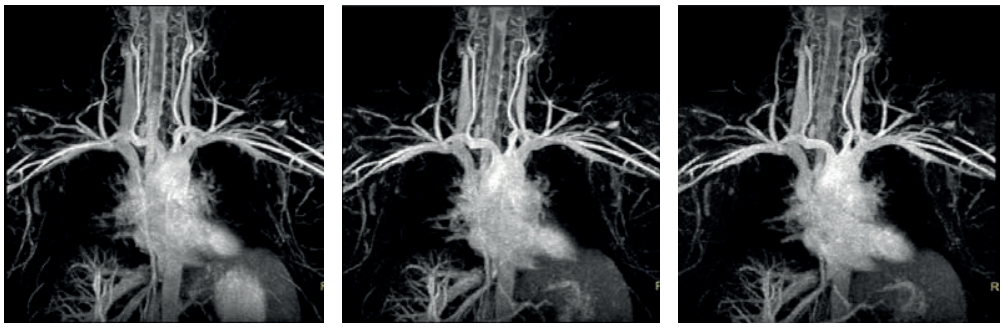

Fig. 2: MIP of REACT without CS (left), CS factor = 2 (middle), CS factor = 3 (right)

Results

In all subjects, all scans were acquired successfully. Fig 2 shows an MIP of one volunteer with regular REACT (left), REACT with CS extras reduction factor = 2 (middle) and 3 (right). The image quality is comparable between all the scans.

Discussion

We have demonstrated the feasibility of using compressed SENSE to speed up an mDixon-based noncontrast MRA acquisition. This could provide navigator-triggered high-quality MRA with robust fat suppression in large FOVs. The next step is to validate this technique in pediatric and adult patients.

References

[1] – Yoneyama, M et al. Proc. Intl. Soc. Mag. Reson. Med. 24, 2252 (2016). [2] – Toyonari, N et al. Proc. Intl. Soc. Mag. Reson. Med. 24, 2684 (2016). [3] – Pokorney, A et al. Proc. Intl. Soc. Mag. Reson. Med. 25, 0335 (2017). [4] Lustig M, et al. Magn Reson Med, 58(6):1182-95, 2007.

Lung Perfusion Assessed without Exogenous Contrast via Arterial Spin Labeling

Mark DiFrancesco, Raouf Amin, Jason Woods, Robert Fleck, Alister Bates, Chamindu Gunatilaka, Gautham Mylavarapu, Gregory Lee
Cincinnati Children's Hospital Medical Center, Cincinnati, OH USA

Purpose:

Regional measures of blood perfusion in the lungs is critical for assessment of pulmonary conditions including cystic fibrosis and pulmonary hypertension. Methods that are noninvasive and that do not require exogenous contrast [1] are particularly important for longitudinal studies and disease tracking, especially in children [2]. We report results of applying pseudocontinuous arterial spin labeling (pCASL) MRI to measure regional lung perfusion.

Methods:

Imaging was conducted on a 3T MR scanner (Philips Achieva, Eindhoven, The Netherlands) with ECG triggering. The pCASL approach included labeling, by inversion, blood flowing through a plane crossing the main pulmonary artery (MPA) at systole (Figure 1). The labeling plane was positioned to avoid lung tissue as much as possible. We employed a labeling duration of 400 ms to capture the period of peak flow in the MPA [3]. Following a delay, the lungs are imaged using a turbo spin echo sequence covering a single 15 mm coronal slice (matrix 96 x 96, FOV 288 mm x 288 mm, effective TE=22 ms, shot duration = 86 ms). This sequence was repeated without labeling. Subtraction of labeled from unlabeled images produced an image with perfusion weighting. The pCASL sequence ran continuously, with TR=3 s, while the participant's breathing was coached by a paradigm running under Presentation (Neurobehavioral Systems, Inc., San Francisco). Imaging acquired during 15 s periods of end-expiration breath-hold was used for processing.

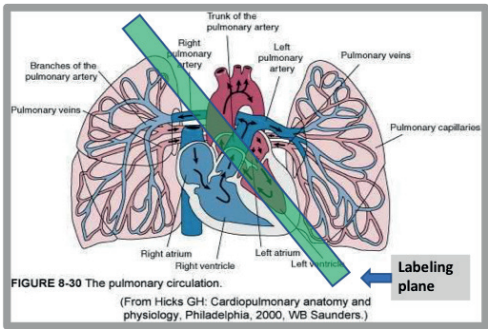

Figure 1: Schematic of pCASL labeling strategy.

To demonstrate the time course of blood inflow, we performed this procedure for a range of post-label delays.

Results:

Example perfusion-weighted maps in a coronal lung slice in an adult female volunteer are shown in Figure 2 for post-label delays ranging from 100 ms to 1500 ms. The frames demonstrate mainly large vessels in the early phase with eventual perfusion to the periphery of the lung by 600 ms. This is followed by wash-out and subsequent signal decay for longer delays.

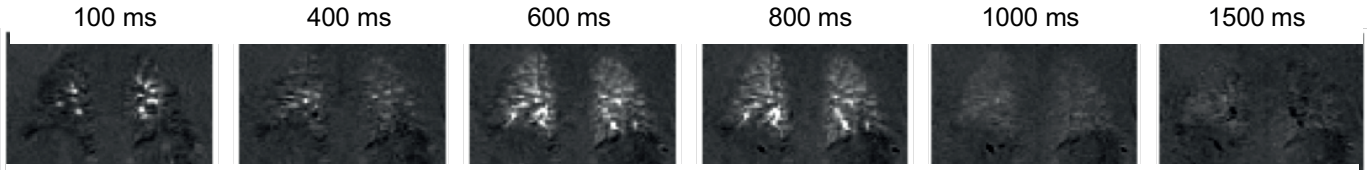

Figure 2: Perfusion-weighted coronal lung images for a series of post-label delays, indicated above each image.

Discussion:

We demonstrate a feasible method for obtaining regional lung perfusion-weighted images without exogenous contrast. Remaining challenges include optimal modeling for accurate perfusion quantification in the lung and to reduce dependence on breath-holds to allow application in the youngest patients.

References:

1. Henderson AC, Prisk GK, Levin DL, Hopkins SR, Buxton RB. Characterizing pulmonary blood flow distribution measured using arterial spin labeling. NMR Biomed. 2009;22(10):1025-35.
2. Ciet P, Tiddens HA, Wielopolski PA, Wild JM, Lee EY, Morana G, Lequin MH. Magnetic resonance imaging in children: common problems and possible solutions for lung and airways imaging. Pediatr Radiol. 2015;45(13):1901-15.
3. Martirosian P, et al., Measurement of lung perfusion using optimized pseudo-continuous arterial spin labeling of pulmonary arteries and fast True-FISP imaging at 3 Tesla. Proceedings of Annual Meeting ISMRM, 2017.

Direct signs of Pulmonary Embolism at MRA: Intra Reader Agreement

Mark L. Schiebler, M.D.(1), Nanae Tsuchiya, M.D., PhD (1,2) , Colin Longhurst, M.S.(3), Christopher Francois, M.D. (1), Lindsay Griffin, M.D. (1), Karl Vigen, PhD (1), Donald Benson, M.D., PhD (1)

1. Department of Radiology, UW-Madison School of Medicine and Public Health, Madison, WI
2. Department of Radiology, Graduate School of Medical Science, University of the Ryukyus, Okinawa, Japan
3. Department of Biostatistics and Medical Informatics, University of Wisconsin-Madison

Purpose: To determine which direct imaging signs for pulmonary embolism (PE) at MRA have the highest intra –reader agreement.

Materials and Methods: This was an IRB approved and HIPAA compliant retrospective analysis. From a database of over 600 pulmonary MRA (1) performed for the primary diagnosis of PE cases with a final read of positive for PE were re-examined. From these, 93 positive cases were included. Two readers interpreted all of these cases on two separate occasions to prevent recall bias. Reader 1 had two years' experience with MRA for PE and Reader 2 had 6 weeks of experience. Each reader recorded the presence or absence of the following direct findings of PE at MRA: Non-occlusive thrombus, Occlusive thrombus, vessel cut off, double bronchus, central dot, ghost vessel, and high T1 signal of PE. Cohen's kappa statistic (k) determined the intra- observer agreement. A p value of 0.05 determined statistical significance.

Direct findings	Intra-Reader 1 Cohen's kappa [p value] {95% C.I.}	Reader 1 N cases (Prevalence at Time 1, Time 2)	Intra-Reader 2 Cohen's kappa [p value] {95% C.I.}	Reader 2 N cases (Prevalence at Time 1, Time 2)
Non-Occlusive thrombus	0.84 [0.0001] {0.727,0.954}	93 (35,36)	0.46 [0.0001] {0.27,0.646}	93 (30,35)
Occlusive Thrombus	0.84 [0.0001] {0.73,0.96}	93 (57,56)	0.55 [0.0001] {0.378,0.725}	93 (56,56)
Vessel cutoff	0.48 [0.0001] {0.297,0.654}	93 (56,50)	0.49 [0.0001] {0.312,0.68}	93 (46,56)
Double Bronchus	0.43 [0.0001] {0.248,0.617}	93 (41,41)	0.70 [0.0001] {0.505,0.893}	93 (14,18)
Central Dot	0.40 [0.0001] {0.204,0.589}	93 (35,26)	0.61 [0.0001] {0.453,0773}	93 (50,46)
Ghost Vessel	0.51 [0.0001] {0.364,0.719}	93 (35,26)	0.53 [0.0001] {0.355,0.713}	92 (59,57)
High T1 signal of PE	0.52 [0.0001] {0.333,0.718}	88 (29,20)	0.63 [0.0001] {0.46,0.811}	87 (20,29)

Table 1: Intra-reader agreement for interpretation of the direct signs of PE at MRA.

Results: There was variability in the intra-reader kappa scores for the direct signs of PE at MRA (Table 1). The two most consistent signs for Reader 1 were the non-occlusive thrombus and occlusive thrombus (k- 0.84, p 0.0001 for both signs), while for Reader 2 the double bronchus and high signal intensity PE sign were the two most consistently observed signs (k- 0.70 and 0.63 respectively; both p values 0.0001).

Discussion: The intra reader kappa scores shows that experience interpreting these exams matters. The occlusive and non-occlusive thrombi had the highest intra- reader reproducibility for Reader 1; while Reader 2 was best at recognizing the direct signs of the double bronchus followed by the high T1 signal intensity in the PE on the pre-contrast enhanced exams. Experience and careful training helps to insure correct interpretation of these exams.

References:(1)Schiebler ML, Nagle SK, Francois CJ, et al. Effectiveness of MR angiography for the primary diagnosis of acute pulmonary embolism: clinical outcomes at 3 months and 1 year. Journal of magnetic resonance imaging : JMRI. 2013;38(4):914-25.

Mapping of reversed flow and wall shear stress in aortas with bicuspid aortic valves

Pim van Ooij[1], Emile S. Farag[2], S. Matthijs Boekholdt[3], Aart J. Nederveen[1], R. Nils Planken[1]
[1]Radiology & Nuclear Medicine, [2]Cardiothoracic Surgery, [3]Cardiology, Academic Medical Center, Amsterdam

Purpose: Since the direction of blood flow and wall shear stress (WSS) are important biomarkers in aortic disease[1,2], the purpose was to visualize and quantify abnormal velocity and WSS direction in subjects with bicuspid aortic valves.

Methods: Forty five subjects (38±12 years old, 18 women) with bicuspid aortic valves (BAV) and 25 controls (37±13 years old, 10 women) underwent 4D flow MRI (3 Tesla Philips, Best, NL) with temporal and isotropic spatial resolution of ±42 ms and 2.5 mm, with TE/TR/FA of 2.1 ms/3.4 ms/8° and k-t PCA acceleration of 8. The data was corrected for eddy currents and velocity aliasing. The thoracic aorta was segmented (Mimics, Materialize, Leuven, Belgium) from time-averaged phase contrast MRA images created by multiplication of the magnitude with the absolute velocity images. Peak systole was defined as the time frame with the highest velocity averaged over the segmentation and was used for WSS calculation[3]. Peak systolic velocity and WSS atlases were created from the control subjects with a previously published methodology modified for vectors, i.e. the scaling factor (the diagonal of the rotation matrix) in affine registration was set to zero for vector registration (figure 1a and b)[4]. After registration of the atlas to the BAV subjects (figure 1c), regions where BAV velocity or WSS vectors deviated more than 120° from the control atlas were mapped in red, between 120° and 60° in yellow and below 60° in green (figure 1d and e). Quantification consisted of velocity voxels or WSS points with abnormal direction (red or yellow) as a percentage of the total number of velocity voxels or WSS points in the inner and outer curvature of the aorta. Differences in abnormally directed flow and WSS between the inner and outer curvature were assessed with a Wilcoxon rank sum test where $P<0.05$ was considered significant. Mid-ascending aortic diameters were measured on contrast-enhanced MRA. Peak velocities and valve morphology were assessed with echocardiography. Linear regression was performed between abnormal direction percentages, aortic diameter and peak velocity with R^2 reported and $P<0.05$ considered significant. Additional maps were created to show the incidence of abnormal WSS and velocity direction combining all BAV subjects[5].

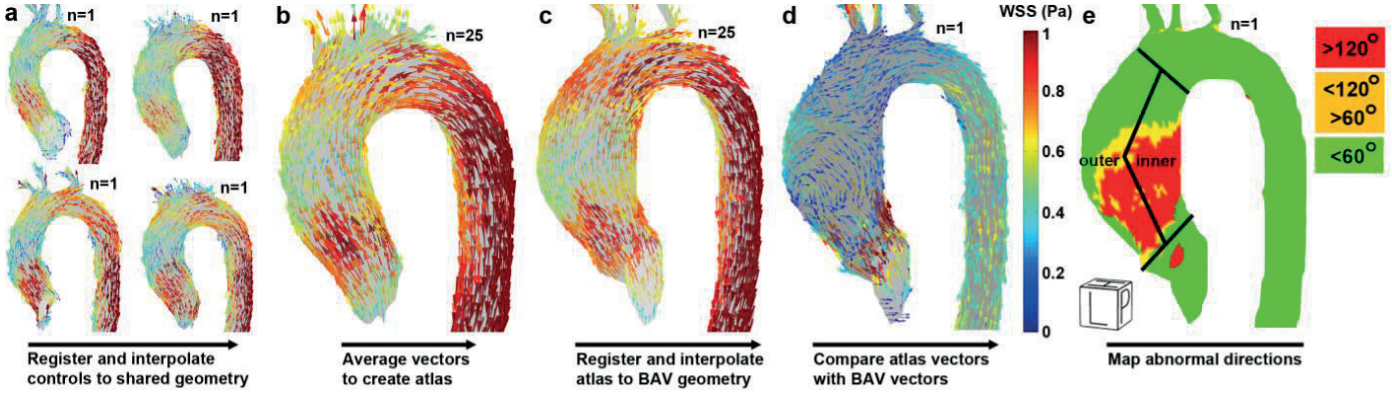

Figure 1. The pipeline for mapping of reversed WSS vectors in subjects with BAV. The pipeline for velocity is identical.

Results: The mean percentages of abnormal WSS and velocity direction were significantly higher at the aortic inner as compared to the outer curvature (table 1). Significant correlations between percentages of abnormal flow and WSS direction and aortic diameter were found, as well as with echocardiographic peak velocity (table 2). No differences in abnormal flow and WSS direction were found between right-left (n=36) and right-noncoronary fusion (n=7). For BAV, 69% and 56% had WSS and velocity directions deviating by more than 120° in the inner curvature (figure 2).

Table 1. Percentage with abnormal WSS and velocity direction

	WSS			Velocity		
	Inner	Outer	P*	Inner	Outer	P*
%>120°	18±14	8±7	<0.001	15±13	5±5	<0.001
60°>%<120°	22±13	12±9	<0.001	24±12	16±11	<0.05

**Wilcoxon rank sum test, P<0.05 significant*

Table 2. Regression correlation coefficient R^2

	WSS		Velocity	
Diameter	Inner	Outer	Inner	Outer
%>120°	0.13*	0.07	0.13*	0.15*
60°>%<120°	0.12*	0.10*	0.28*	0.18*
Peak velocity				
%>120°	0.36*	0.16*	0.37*	0.29*
60°>%<120°	0.11*	0.15*	0.25*	0.28*

**Significant correlation with P<0.05*

Discussion: In this study, a methodology based on 4D flow MRI was used to show that peak systolic blood flow and WSS were reversed in the inner curvature of the aorta in a large number of BAV subjects. We found that altered direction of hemodynamics correlated with peak velocity. Aortic stenosis may therefore lead to abnormal directions of hemodynamics and different expression of WSS on the endothelial cells, potentially leading to aortic dilation. The methodology presented may be useful for the usually semi-quantitative assessment of helical and vortical flow[6], which have been implicated in aortic diseases such as aneurysms, regurgitation and stroke[1].

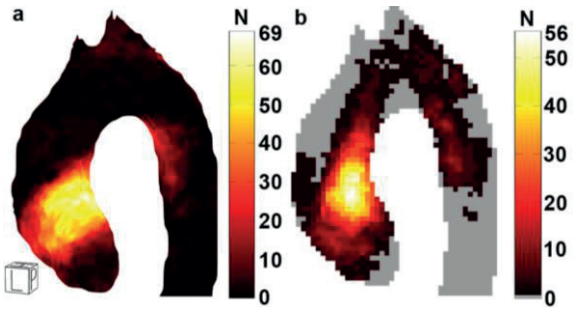

Figure 2. Incidence maps for abnormal direction (>120° from controls) of a) WSS and b) velocity

References: [1]Shen et al. JMRI 2017, [2]Sotelo et al. MRM 2018, [3]Potters et al. JMRI 2015, [4]van Ooij et al. MRM 2015, [5]van Ooij et al. ISMRM 2017, [6]Meierhofer et al. Eur Heart J CV Imaging 2012

4D Flow vCath: 3D Virtual Catheter for Volumetric Time-varying Aortic Hemodynamic Analysis from 4D Flow MRI

Mohammed S.M. Elbaz[1], Michael B. Scott[1], Alex J Barker[1], Patrick McCarthy[2], Chris Malaisrie[2], Jeremy D Collins[1], James Carr[1], Michael Markl[1,3]

[1]Department of Radiology, [2]Cardiac Surgery, Northwestern University Feinberg School of Medicine, Chicago, IL, USA
[3]Department of Biomedical Engineering, Northwestern University, Evanston, IL, USA

Purpose: 4D Flow MRI has emerged as a useful technique for the detection and quantification of altered aortic blood flow in patients with aortic valve disease such as congenitally abnormal Bicuspid Aortic Valve (BAV). However, current 4D flow data analysis frameworks are 1) often cumbersome and time-consuming and 2) adopt a multi 2D plane analysis approach, not fully utilizing the 4D nature (3D + time) of the data. Here, we propose a novel 3D virtual catheter (vCath) method that robustly utilizes the volumetric 4D Flow data for assessing 3D time-varying aortic hemodynamics with a high degree of automation. The goals of the study were to 1) demonstrate the feasibility of vCath to study longitudinal changes in volumetric time-varying kinetic energy (KE) and viscous energy loss rate (EL) in a large cohort of BAV patients, and 2) investigate its potential for automated analysis with minimal user interaction.

Methods: ***Study Cohort and MR Imaging:*** Baseline and follow-up aortic 4D Flow MRI at 1.5T MRI (Siemens, Germany) were performed in 44 BAV patients (age: 45±12 years, follow-up scan at 2.6±0.7 years). 26 healthy controls (age: 47±12 years, n=9 with follow-up 4D Flow MRI at 2.7±0.5 years) were also included. 4D Flow MRI was acquired during free breathing with respiratory navigator gating (spatial resolution = 2-3mm^3, temporal resolution = 33–43ms, total scan time 8-12 minutes, venc = 150–450 cm/s).

vCath analysis: **1)** 4D Flow MRI preprocessing included corrections for eddy currents, velocity aliasing and the calculation of a 3D phase-contrast angiography (PCMRA) employed for 3D segmentation of the aorta (Mimics, Materialise, USA). **2)** Automated 3D aortic centerline curve detection was performed using the fast marching method [1]. **3)** Aortic branch segments were excluded from the detected centerline when present. **4)** A virtual catheter vCath was constructed as a tube with a fixed radius R_{vCath} centered around the aortic centerline. To account for inter-individual differences in aortic dimensions, R_{vCath} was individually determined automatically for each aorta based on the 75th percentile (P75) of aortic lumen radii along the entire aorta centerline, derived by 3D distance transform, (R_{vCath} = *P75/3*). **5)** Within the vCath mask, for each acquired time point, hemodynamic metrics of KE and EL were quantified over the total vCath volume, resulting in time-evolution curves [2]. **6)** Systolic vCath peak KE (KE_{vcath_peak}) and peak EL rate (EL_{vcath_peak}) were calculated and normalized by the total vCath volume (Fig. 1).

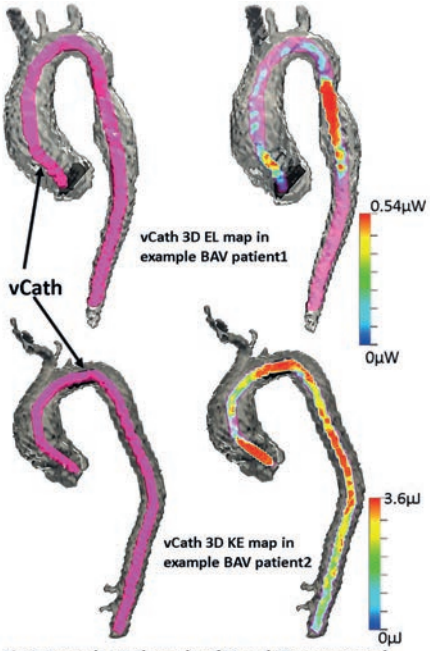

Fig.1: Example vCath results of EL and KE maps at peak Systole in two different BAV patients

Results (Table 1): For all 123 4D flow scans, automated aortic centerline detection was successful. Automated branch exclusion was successful in 106 cases (86%) and manually corrected in the rest. Automatically-derived vCath radius (R_{vCath}) and volume were not significantly different between BAV patients at baseline and follow-up (p=0.51; p=0.70) or in the sub-cohort (n=9) of follow-up volunteers (p=0.60; p=0.87) indicating reliability of the method. Compared to the total 26 volunteers, BAV patients had significantly larger vCath radius and volume (p<0.001). Volume normalized systolic KE_{vcath_peak} was significantly lower (p=0.03) while EL_{vcath_peak} was significantly higher (p=0.04) in follow-up BAV patients compared to baseline. Interestingly, while no significant differences were found in KE_{vcath_peak} between healthy controls (n=26) and BAV patients at baseline (p=0.40) or follow-up (p=0.67), EL_{vcath_peak} was significantly higher in both BAV patient groups compared to controls (p<0.001 in both). Meanwhile, none of the parameters showed significant differences between baseline and follow-up in the sub-cohort of follow-up controls indicating excellent reproducibility of the automated methods (p>0.22).

Table 1: vCath results

	Baseline BAV (n=44)	Follow-up BAV (n=44)	Controls (n=26)	Sub-cohort follow-up controls	
				Baseline (n=9)	Follow-up (n=9)
vCath radius R_{vCath} (mm)	4.6±0.6	4.5[4.2,4.8]	3.7±0.4	3.7±0.4	3.8±0.5
vCath volume (cm^3)	25.7[22.0, 32.7]	26.9[21.4,33.8]	18.8 ±4.7	19.6±5.03	19.9±4.3
KE_{vcath_peak} (J/m3)	350.1[228.1,434.1]	306.9[235.1,415.5]	330.0±153.6	333.8±139.7	236.0[208.1,369.9]
EL_{vcath_peak} (W/m3)	26.2[18.1,59.6]	28.2[20.8,60.1]	19.5±7.5	20.4±8.4	14.8±6.4

Data presented as mean ± std or median[IQR] where appropriate based on Shapiro-Wilk normality test. Wilcoxon signed-rank or rank-sum and paired or unpaired t-test were used for comparison where appropriate. P<0.05 considered significant.

Discussion: This study presents a novel 3D virtual catheter approach for studying aortic hemodynamics in a 3D time-varying manner that utilizes the volumetric nature of 4D Flow MRI and with a high degree of automation. The quantitative time-varying volumetric information enabled by the vCath identified longitudinal aortic hemodynamic changes in BAV patients while showing consistent non-significant differences in the follow-up healthy volunteers. This indicates robustness and sensitivity of the method. Notably, vCath is patient-specific as it automatically adjusts to the patient's aortic shape based on its centerline (Fig.1) and is extendable to other hemodynamic metrics besides energetics. Automated R_{vCath} definition makes vCath centrally located with enough marginal distance from the aortic boundary over the cardiac cycle therefore mitigating potential errors due to time-varying aortic geometry. A limitation was needing manual identification of aortic branch segments for exclusion in 17 (out of 123) cases. In future studies, we will work on developing a better automated approach to handle such cases and on evaluating the method in various large patient cohorts. **References**: [1] Hassouna, M. S. et.al. IEEE PAMI (2007). [2] Elbaz MSM et.al. MRM 2017. **Acknowledgments**: Grant support by R01HL115828 and R01HL133504

Directional Flow and Stasis Maps from 4D flow MRI to Characterize Aortic Dissection

Kelly Jarvis, PhD[1], Bradley D. Allen, MD[1], Alex J. Barker, PhD[1], Emilie Bollache, PhD[3], Hyungkyu Huh, PhD[1], Alireza Vali, PhD[1], S. Chris Malaisrie, MD[2], Patrick M. McCarthy, MD[2], James C. Carr, MD[1], Jeremy D. Collins, MD[1], Michael Markl, PhD[1]

[1]Radiology, [2]Cardiac Surgery, Northwestern University, Chicago, USA; [3]Sorbonne Université, CNRS, INSERM

Purpose: Patients with Stanford type B aortic dissections present with acute and time-sensitive complications (e.g. aortic rupture, dilatation and aneurysm). The decision to treat surgically versus manage medically is challenging and driven by both patient symptomatology and imaging findings. 4D flow MRI has the potential to help assess dissection severity through the characterization of blood flow (i.e. peak velocity and directional flow maps indicating hemodynamically active fenestrations, stasis maps to identify slow flow regions that may be more likely to thrombose) in the true (TL) and false (FL) lumens. The goal of this research was to explore the utility of these quantitative hemodynamic maps from longitudinal 4D flow MRI in aortic dissection.

Methods: Free-breathing 4D flow MRI was acquired in 3 aortic dissection patients at baseline and post-surgery [months after baseline] (55 y/o M [26 mo]: elephant trunk repair, 62 y/o F [3 mo] and 55 y/o M [2 mo]: thoracic endovascular aortic repair TEVAR) and 6 controls (3 females, age=48 +/- 17 [25-66] years) with spatial res. ~2-3 mm^3 and temporal res. ~40ms, venc=150-250 cm/s. A phase contrast MR angiogram was calculated and used to segment a mask of the aorta, separating the TL and FL. Directional flow (i.e. forward and reverse flow calculated using a 3D centerline), peak systolic velocity and stasis (i.e. percent of time velocity<0.1 m/s) were evaluated on a 3D voxel-wise basis and displayed as 2D projections. ROIs were positioned in the proximal descending thoracic aorta for quantification.

Results: See Figures 1-2. Patient 1 had a history of aortic valve replacement and root repair and after elephant trunk repair had a stable post-interventional outcome but developed irregular s-shaped flow from the trunk to the TL and FL. Patient 2 showed retrograde filling of FL after TEVAR repair, likely from fenestrations in the abdominal aorta. Patient 3 had unstable dissection involving a large fenestration and flow jet impinging on the vessel wall and after TEVAR developed partial thrombus in FL. The controls typically had values in the upper range for forward flow and in the lower range for reverse flow and stasis, compared to the patients, particularly for FL.

Discussion: These preliminary results indicate a variety of flow situations for patients prior to surgery (i.e. hemodynamically active fenestrations that may promote induced remodeling of FL, filling of FL, stasis regions) and as they were being monitored after surgery (i.e. changes in active fenestrations, altered reverse flow regions, stasis areas that may thrombose). For each unique and complex case, 4D flow MRI has the potential to provide a better characterization of aortic dissection hemodynamics which may improve risk stratification and treatment planning.

Funding Sources: Grant support by NIH, NHLBI T32 HL134633

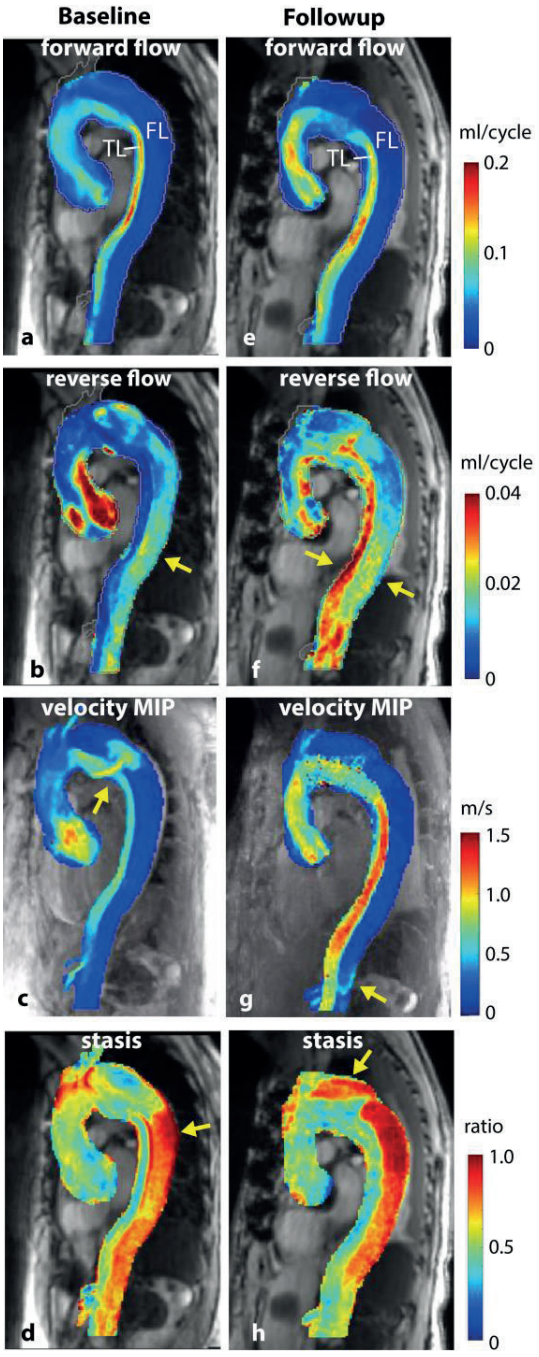

Figure 1 (above): Evaluation of blood flow from 4D flow MRI in 55 year old (patient 3) with aortic dissection at baseline (left) and after TEVAR at 2 months (right). a-b) forward flow in TL and reverse flow in FL (yellow arrow) are shown. c) A hemodynamically active intimal tear is indicated (yellow arrow). d) An area of stasis is evident in FL but no thrombus has formed. e-f) forward flow is shown in TL and elevated reverse flow in TL and FL (yellow arrows), likely due to hemodynamically active fenestration (yellow arrow shown in g). h) An area of stasis is evident in FL (yellow arrow) near location of an observed partial thrombus.

Figure 2 (below): Quantifications for 3 patients (baseline and post-surgery) and 6 controls in proximal descending thoracic aorta.

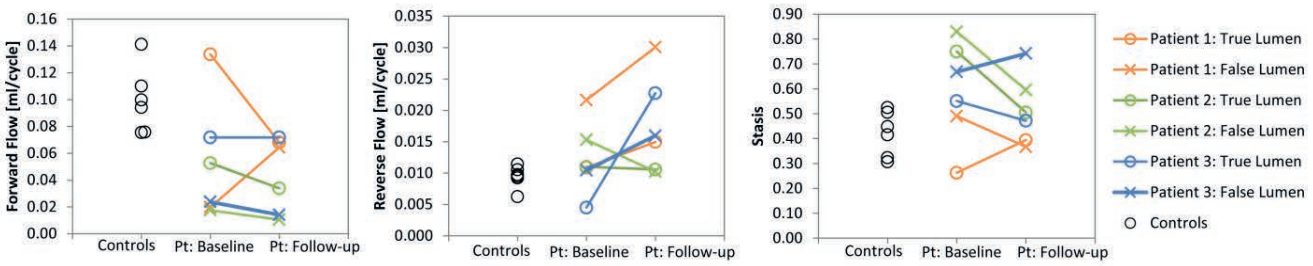

Ultra Low Dose CT Fluoroscopy: A new tool for CT-guided Vascular Intervention.

M Wagner, Y Wu, P Laeseke, F Lee, L Hinshaw, Y LI, M Speidel, T Szczykutowicz, G. Shaughnessy, CM Strother, and CA Mistretta
The University of Wisconsin Madison

Purpose Conventional time-resolved CT imaging techniques such as CT fluoroscopy require continuous CT acquisition during multiple gantry rotations. Each gantry rotation is used to reconstruct a single time point and commonly contains around 1000 projection images. Conventional CT fluoroscopy is seldom used due to the high radiation dose to both the patient and clinician. The purpose of this work is to introduce a new X-ray CT method that makes use of the sparseness of the reconstructed objects to reduce the number of images required to extract a single time point. This could be used to track intravascular devices such as catheters during minimally invasive procedures. The technique has the potential to increase the temporal resolution of conventional CTF while reducing radiation exposure by a factor of 250 by pulsing the x-ray tube only at selected angles during the gantry rotation.

Methods Vascular Ultra Low Dose CT Fluoroscopy (ULD CTF) can be implemented to provide, when used with the 4D-CT-DSA technique also reported at this meeting [1], an environment for performing quantitative vascular interventions using CT. The dose-reduced fluoroscopy is implemented using just 2 instead of 1000 CT projections to reconstruct a single time frame resulting in an image of the interventional device without filtered back projection (FBP) artifacts. Four projection images per gantry rotation were used for reconstruction of vascular fluoroscopy providing 8 frames per second for a gantry rotation time of 0.5 s and a 250 x dose reduction. An initial static CT angiogram is used as a roadmap and is motion corrected and combined with the ongoing interventional device reconstruction. Traditional roadmap and endovascular views are available for device guidance. Image SNR is considerably higher than achieved with traditional low mA CT fluoroscopy.

Results To compare the image quality of conventional CTF and the proposed dose reduced technique, the method was applied to acquisitions of percutaneous needle insertions. Figure 1 shows a series of time frames for conventional CTF in the first row and ULD CTF in the second row. In traditional CT Fluoroscopy there are significant needle artifacts and poor SNR relative to the new 500x dose reduced method (2 frames per second). Because the technique does not use conventional FBP reconstruction, the images are free of metal artifacts. To evaluate the accuracy of the intravascular device reconstruction a series of acquisitions was performed of a catheter guided through the aorta into the splenic artery. The localization error of the device tip was 2.70 ± 0.73 mm compared to conventional reconstruction. Figure 2 shows a semitransparent glass pipe view and a virtual endoscopic view of the catheter within the vascular reconstructed using ULD CTF.

Figure 1

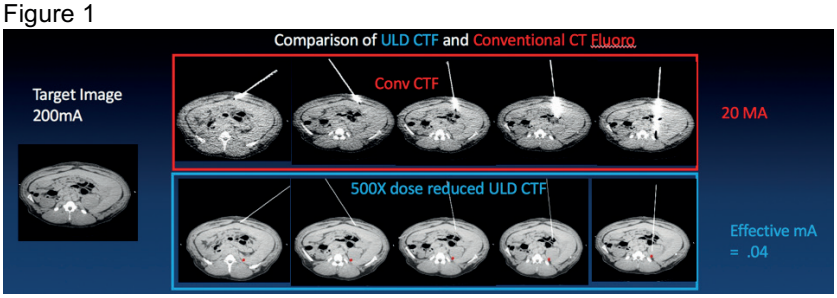

Figure 2

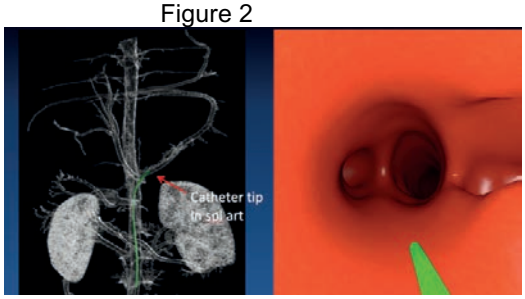

Discussion The availability of near zero dose CT fluoroscopy provides the opportunity for a new field of CT-guided vascular intervention. It can be used in combination with 4D CT DSA which provides quantitative blood flow estimates. These capabilities should reduce the need for combined c-arm and CT interventional suites, which are typically very expensive.

Synopsis The new tools we are reporting at this conference could significantly impact current vascular interventional practice. Estimates of flow, including coronary blood flow, could provide important new opportunities in interventional Radiology and Cardiology.

References

1. M Wagner*,**, Y Wu*, P Laeseke*, Y LI,* M Speidel*, S Leng#, Gabe Shaughnessy*, Fred Lee*,**,CM Strother*, and CA Mistretta*,**, Quantitative 4D CTA DSA : A New tool for CT Vascular Diagnosis and Intervention.

Preferred Presentation Oral

Slice following in the era of feature-tracking: Pilot study to improve accuracy of trans-valvular flow

Felicia Seemann[1,2], Maolin Qiu[2], Dana C. Peters[2]

1. Dept of Clinical Physiology, Skåne University Hospital, Lund University, Lund, Sweden
2. Dept of Radiology & Biomedical Imaging, Yale School of Medicine, Yale University, New Haven, USA

Purpose: Accurate measurement of trans-valvular flow is important, for example to quantify mitral and tricuspid regurgitation, or measure “E”, “A” and “e-prime” for characterization of diastolic function. Quantification of mitral regurgitation is increasingly important (1), as it is recognized that magnetic resonance imaging (MRI) outperforms echocardiography in therapeutic guidance for mitral valve repair. There is also an increasing awareness of the impact of diastolic function, due to its role in diseases such as atrial fibrillation and heart failure (2). Diastolic function can be assessed by MRI - although it rarely is.

The accuracy of trans-valvular flow quantification is impacted by the highly mobile valvular plane; this motion means that the depicted tissue in the imaged slice changes throughout the cardiac cycle, not showing the same tissue in all timeframes. To address this, methods with 4D flow have been investigated, to improve accuracy by retrospectively varying the slice-plane (3). Furthermore, methods have been developed for phase-contrast with prospective slice-following (4). Recently, a fast robust feature-tracking technique has been introduced for tracking the valve plane on long-axis cine (5). We employed this feature-tracking algorithm, in conjunction with slice-following, and compared it with static phase-contrast of the mitral valve.

Methods: Subjects were imaged on a 3T Siemens PRISMA scanner. The phase-contrast sequence used 2D GRE cine, with through-plane VENC of 180m/s, TR/TE/flip=5.2ms/3ms/15◦, a matrix of 192 x160, FOV=360mm, 8mm slice, 4 bipolar pairs per phase, 42ms temporal resolution. A 4-chamber cine was acquired, with temporal resolution and phases matched to the phase-contrast sequence. The 4-chamber cine was ported offline for analysis with Segment (Fig 1A) (6). The quantified slice displacements were saved to a file accessed by the phase-contrast sequence. Fig 1A shows the slice-following phase-contrast method, in which the slice was changed in real-time, based on the cardiac phase.

Results: Fig 1B,C shows differences in the max velocity vs. time for a slice at the valve, both with slice-following and with stationary slice phase-contrast. The magnitude images (Fig 1DE) show that the same slice is being sampled throughout the cardiac cycle, using slice-following, but not using a stationary slice.

Discussion: Slice-following phase-contrast from offline feature tracking of the mitral valve in a 4-chamber cine is feasible. Further study will focus on comparing differences in flow and velocity revealed by slice-following in a larger cohort.

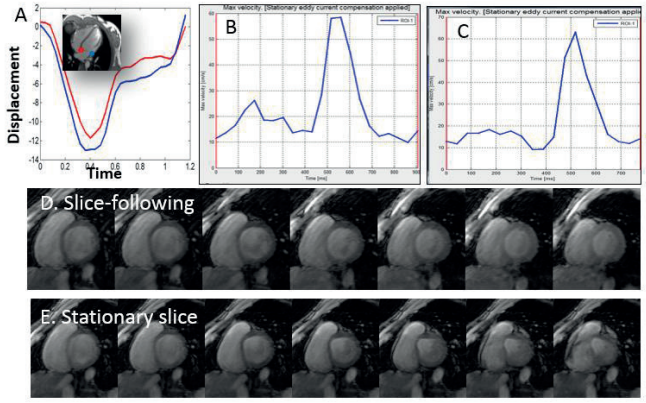

Figure 1: A) Feature-tracking of a 4-chamber cine generates a semi-automatic slice-displacement curve. Maximal through-plane velocity vs. time, using slice-following **(B)** and a stationary slice **(C)**. Magnitude images (shown from begin systole to early diastole) from the slice-following images **(D)** and stationary slice images **(E).** Slice-following allows the imaging of the same slice, while it moves during the cardiac cycle.

References: 1) Uretsky S et al. JACC 2015. **2)** Rosenberg MA et al. Circulation 2012. **3)** Westenberg JJM et al. Radiology. 2008. **4)** Kozerke S et al. Magn Reson Med 1999. **5)** Seemann F et al. BMC Med Imaging 2017. **6)** Heiberg E et al. BMC Med Imaging 2010.

4D Flow Imaging with Reduced Field-Of-Excitation

Clarissa Wink[1], Giulio Ferrazzi[1], Jean Pierre Bassenge[1], Sebastian Flassbeck[2], Simon Schmidt[2], Tobias Schaeffter[1], and Sebastian Schmitter[1]

[1]Physikalisch-Technische Bundesanstalt (PTB), Braunschweig and Berlin, Germany, [2]Medical Physics in Radiology, German Cancer Research Center (DKFZ), Heidelberg, Germany

Purpose

4D Flow Imaging[1] enables non-invasive quantification of time-resolved velocity vector fields in-vivo. However, it requires long acquisition times. 2D-selective excitation allows reducing the field-of-view (FOV) in both phase encoding directions to accelerate the acquisition. Here, we investigate the feasibility of using 2D-selective excitation in combination with reduced FOV imaging for fast 4D flow imaging with correct velocity quantification.

Methods

We designed a 2D-selective RF-Pulse according to Pauly[2] in the small flip angle regime with spiral k-space trajectory and bandwidth-time-product $\mathrm{BWTP} = 1.2$ exciting a $(6 \times 6 \times \infty)\mathrm{cm}^3$ field-of-excitation (FOX). The spiral starts at $k_{\max} = 2.51\,\mathrm{rad/cm}$ and spirals inwards to k-space centre in $n = 10$ turns and $T = 3.5\mathrm{ms}$. 2D-selective excitation pulses were calculated based on measured gradient waveforms and integrated into a GRE 4D flow sequence[1].

We performed a phantom and an in-vivo measurement at 3T (Siemens Verio). The flow phantom measurement with constant velocity served for non-time-resolved flow quantification validation. To this end we measured all four combinations of non-selective/ selective excitation with full/reduced FOV.

The volunteer was scanned according to an approved ethical protocol and with informed consent. We measured 4D flow of his cerebrum with 1D-slab-selective and 2D-$(6 \times 6 \times \infty)\mathrm{cm}^3$-selective excitation and correspondingly adjusted imaging FOV (Fig.2c). Read-out was placed along the non-selective axis (Anterior-Posterior) and both phase-encodings perpendicular to it (see Fig.2b bottom-right).

Results

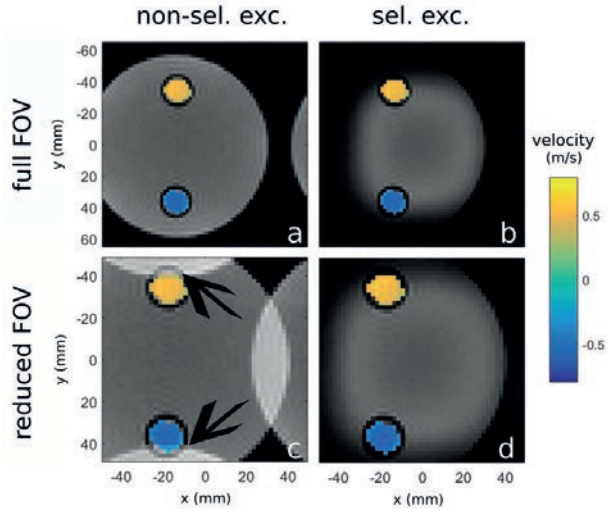

Fig.1: *Magnitude (grey) and through plane flow (colored) for all four scans performed in the flow phantom.*

With reduced FOV and non-selective excitation, velocities are underestimated by $\Delta v / v_{\mathrm{ref}} = 24 \pm 15\%$ when aliasing occurs in the phantom data (Fig.1c), whereas 2D-selective excitation is successful with no apparent aliasing and correct velocity quantification (Fig1d).

Figure 2a shows systolic flow velocities measured with 1D/2D-selective excitation in the Circle of Willis. Qualitatively, no apparent artifacts are observed and velocity quantification was successful (Fig.2a). Moreover, the time-resolved blood flow through the basilar artery and internal carotids agrees quantitatively (Fig.2b).

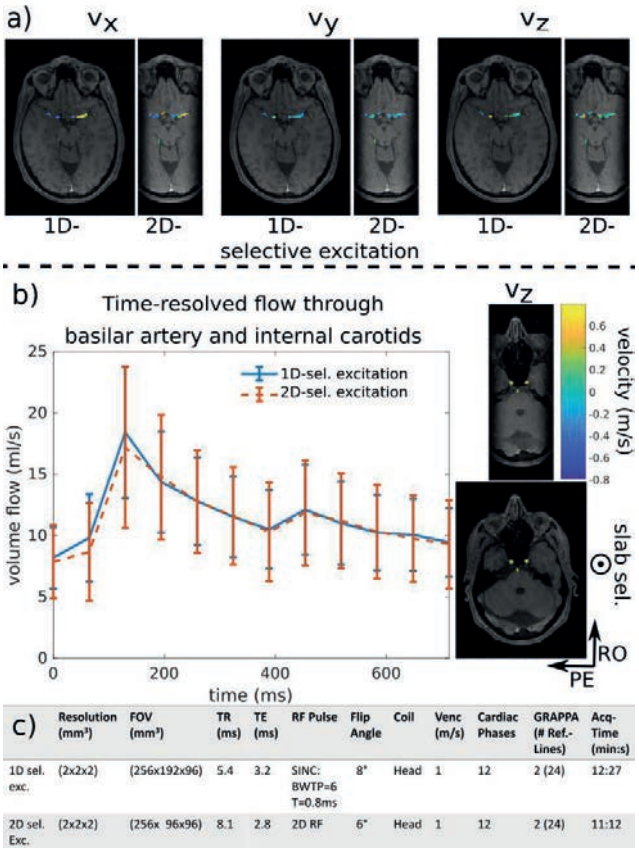

c)

	Resolution (mm^3)	FOV (mm^3)	TR (ms)	TE (ms)	RF Pulse	Flip Angle	Coil	Venc (m/s)	Cardiac Phases	GRAPPA (# Ref.-Lines)	Acq-Time (min:s)
1D sel. exc.	(2x2x2)	(256x192x96)	5.4	3.2	SINC: BWTP=6 T=0.8ms	8°	Head	1	12	2 (24)	12:27
2D sel. Exc.	(2x2x2)	(256x 96x96)	8.1	2.8	2D RF	6°	Head	1	12	2 (24)	11:12

Fig.2: ***(a)*** *Comparison between 1D/2D-selective excitation of magnitude (grey) and systolic velocities (colored) in the Circle of Willis.* ***(b)*** *Comparison of 1D/2D-selective excitation of time-resolved volume flow through basilar artery and internal carotids.* ***(c)*** *Table with scan parameters.*

Discussion

We demonstrate successful 4D flow imaging and quantification in a reduced FOX and FOV. Halving the FOV and applying the presented RF pulse, acquisition time can be maximally reduced to 75%. However, we aim for applying parallel transmission (pTX) that allows shortening the RF-pulse duration. Using pTX, any FOV reduction is expected to translate approximately into the same acquisition time reduction.

References

[1] Markl, M. ea.: 4D Flow MRI: JMRI, 36(5):1015–1036, 2012.

[2] Pauly, J. ea.: A k-space analysis of small-tip-angle excitation: JMR, 81(1):43 – 56, 1989.

Non-invasive Assessment of Splanchnic Flow in Patients Suspected of Mesenteric Ischaemia using MRI 4D Flow - Pilot Study

P Hall Barrientos[1], K Knight[2], D Black[2], A Radjenovic[3], A Vesey[2], G Roditi[2]
[1]Clinical Physics, NHS Greater Glasgow and Clyde, Glasgow, UK
[2]Academic Unit of Surgery, Glasgow Royal Infirmary, Glasgow, UK
[3]Radiology, Queen Elizabeth University Hospital, Glasgow, UK
[4]MRI, BHF Glasgow Cardiovascular Research Centre, Glasgow, UK

Purpose: The most common cause of chronic mesenteric ischaemia is atherosclerosis which results in limitation of blood flow to the gastrointestinal tract. This usually manifests as abdominal pain provoked by eating with accompanying weight loss. Although atherosclerosis is a common problem, true mesenteric angina is relatively rare due to the presence of 3 main arteries supplying the gastro-intestinal tract: the celiac axis, superior mesenteric and inferior mesenteric arteries. If one vessel is stenosed or even occluded, the remaining vessels often provide collateral supply, overcoming any deficit. Patients with abdominal pain and a diagnosis of atherosclerotic disease are increasingly being referred for imaging to rule out mesenteric vascular insufficiency.

This study aimed to evaluate a 4D flow work-in-progress package (Siemens) as a potential tool for the analysis of blood flow within the mesenteric vessels beyond the limitations of 2D single-slice based acquisitions.

Methods: The mesenteric vessels of seven people were scanned, 3 patients and 4 healthy volunteers. A baseline MRI was acquired after 6 hours of fasting followed by a post-meal MRI obtained 50 minutes after ingestion of 220ml EnsurePlus. Two 4D flow datasets were acquired, one focused over the superior mesenteric artery and the other over the portal vein. Standard 2D PC-MRI slices were acquired along the aorta (supra-coeliac, renal and infra-renal), portal vein (PV), splenic vessel (SV), superior mesenteric artery/vein (SMA/SMV).

Studies were performed on a 3 T Siemens Prisma with a body array coil and ECG gating. The sequences used were as follows: 4D flow: TR/TE 45.92/3.19 ms, spatial resolution 0.8 x 0.8 x 0.8 cm, flip angle = 7°, venc = 150-200 and 30-50 cm/s, ~ 20 cardiac phases and scan duration ~8 minutes. 2D: TR 51.9 ms, TE 5.1 ms, spatial resolution 0.8 x 0.8 x 5 mm, flip angle = 20°, venc 150 and 50 cm/s, ~30 cardiac phases and scan duration ~9 s. 4D flow datasets were analysed using a work-in-progress package supplied by Siemens. 2D datasets were analysed using Argus by Siemens. Paired two-tailed Student p-values were calculated to detect the differences between 2D and 4D peak velocities and net flow, and pre- and post-meal net flow in the PV.

Results: In the volunteer cohort, there was a marked increase in blood flow post-meal within the portal vein ($p=0.018$). This was not seen in the patient cohort ($p=0.1835$). When 2D and 4D peak velocities, in both aorta and PV, were compared it was found that 4D technique over estimated peak velocities ($p<0.05$). However, there was a good agreement between 2D and 4D net flow measurements ($p=0.2$).

Discussion:
The 4D flow software has enabled measurement of flow parameters within the mesenteric vessels. The software has also enabled 3D visualisation of blood flow within the PV, SMV and SV, a shown in figure 1, which could enhance the current clinical diagnostic assessment methods. 2D flow acquisition of the smaller vessels such as the SV and IMV was challenging and time-consuming. It was crucial to determine the correct venc setting for the portal vein, as high venc settings created poorly visualised vessels. This study has given the ground work for a larger cohort study to be undertaken, as there is much interest in translating 4D flow imaging into clinical practice.

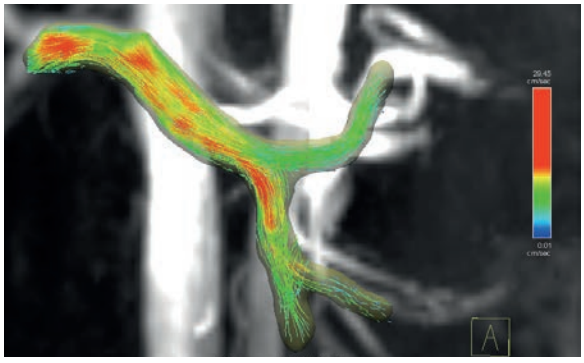

Figure 1. PV flow post-meal

References

1. Roldan-Alzate et al, *J Mag Reson Imaging*,42(4) 1009-1017, 2015
2. Stankovic et al, *Radiology*, 262(3):862-873, 2012
3. Lycklama A Nijeholt et al, *J Hepatol*, 26(2):298-304, 1997

Reduction of Flow Jets following Lumbar Puncture in Patients with Pulsatile Tinnitus

Henrik Haraldsson, Joseph Leach, Evan Kao, Megan Ballweber, Cynthia Chin, David Saloner, Matthew Amans

University of California San Francisco

Purpose: Pulsatile Tinnitus (PT) is the perception of a pulsatile "whooshing" sound in sync with the heart beat that can have a variety of causes. The condition is commonly associated with disturbed blood flow caused by vascular irregularities, and symptoms may be altered by changing the flow conditions (e.g. applying pressure to the neck or by performing a Valsalva maneuver). PT can be caused by idiopathic intracranial hypertension (IIH) that is thought to be related to stenoses in the transverse sinuses of these patients[1]. Draining CSF to lower the intracranial pressure in IIH via lumbar puncture (LP) may temporarily alleviate PT[2]. The aim of this study is to investigate the changes in flow in transverse sinus stenoses before and after LP and compare these to changes in PT symptoms.

Methods: 10 patients with PT suspected to be caused by IIH underwent MRI immediately pre- and post-LP. The MRI examination included pre-LP MRA and pre- and post-LP flow acquisitions (2DFlow at the sigmoid sinuses and 4Dflow of the sinuses). The patients rated symptoms pre- and post-LP on a scale from 0 (no sound) to 10 (corresponding to the sound of a train passing by). The 4DFlow data was postprocessed by: 1) contouring the ipsilateral sinuses, 2) extracting the centerline of the lumen, 3) creating transluminal cut-planes along the centerline, and 4) extracting the peak velocity of the cut-planes along the sinuses.

Results: Six of the patients had both, 1) PT symptoms at the pre-LP examination, and 2) an ipsilateral flow jet (velocity>0.5 m/s) revealed by the pre-LP 4DFlow (see Figure 1). Five of these patients had their symptoms alleviated by the LP, whereas for one it was exacerbated. The six patients had a mean reduction in their PT intensity of 3.8 ($p<0.05$), and a mean reduction of peak velocity of 0.34m/s ($p<0.05$). The decrease in PT intensity correlated with the relative decreased ipsilateral peak velocity ($r=0.91$, $p<0.05$). No significant change was seen in the ipsilateral flow rate (16ml/min, $p=0.39$), and no correlation was seen between change in peak velocity and the change in flow rate ($r=0.47$, $p=0.34$).

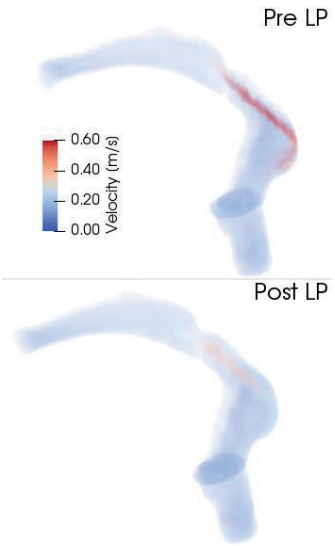

Figure 1: A patient with a flow jet (pre-LP) that is reduced after the intervention (post-LP).

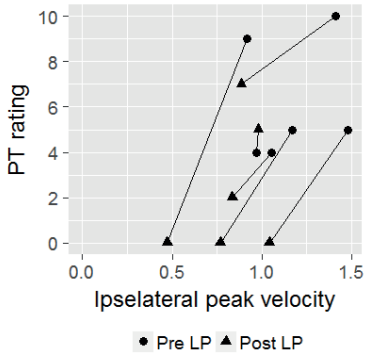

Figure 2: Changes in PT symptom score and ipsilateral peak velocity.

Discussion: Our results show a correlation between the relative reduction of the ipsilateral flow velocity and the alleviation of PT for patients undergoing LP. Somewhat counter-intuitively, a reduction in flow jet velocity is seen without a concomitant decrease in ipsilateral flow rate, likely indicating local changes in the sinus geometry caused by a reduction in intracranial CSF pressure.

References:

1. Boddu S, Dinkin M, Suurna M, et al. Resolution of Pulsatile Tinnitus after Venous Sinus Stenting in Patients with Idiopathic Intracranial Hypertension. PLoS One 2016;11:e0164466

2. Harvey RS, Hertzano R, Kelman SE, et al. Pulse-synchronous tinnitus and sigmoid sinus wall anomalies: descriptive epidemiology and the idiopathic intracranial hypertension patient population. Otol Neurotol 2014;35:7-15

Augmenting 4D Flow MRI in Cerebral Aneurysms with High-resolution PIV and CFD Data

S.M. Rothenberger[1], M. Brindise[2], S. Schnell[3], D. Saloner,[4] Michael Markl[3], P. P. Vlachos[1,2] and V.L. Rayz[1,2]

[1]Biomedical Engineering, Purdue University; [2]Mechanical Engineering, Purdue University; [3]Radiology, Northwestern University School of Medicine; [4]Radiology and Biomedical Imaging, University of California San Francisco.

Purpose: Hemodynamic forces affecting progression and rupture of cerebral aneurysms can be assessed in vivo with 4D Flow MRI which provides time-resolved, three-directional velocity fields [1]. The limited spatiotemporal resolution and dynamic range of velocities can hinder the accuracy of 4D Flow MRI in relatively small cerebral aneurysms with intermittent flow. Image-based modeling, e.g. Computational Fluid Dynamics (CFD) simulations or Particle Image Velocimetry (PIV) Measurements, are capable of superior resolution, however reliability of modeling results depends on various assumptions. Our previous reports showed that 4D Flow MRI can provide boundary conditions for patient-specific CFD models, which in turn can resolve flow structures not detected by imaging. In this study, we evaluate both computational and imaging approaches in comparison to volumetric PIV and in vitro 4D Flow measurements conducted in 3D-printed flow phantoms.

Methods: 4D Flow MRI and MRA data were acquired for two cerebral aneurysm patients, one studied at the Northwestern University School of Medicine and the other at UC San Francisco Vascular Imaging Research Center. MRA data was used to generate patient-specific vascular geometries for both CFD simulations and in vitro experiments. The inlet and outlet flow conditions required for the models were determined from the 4D Flow MRI data. The numerical simulations were carried out using a finite-volume solver Fluent. The mesh density for CFD was varied from 0.4 mm to 50 um in order to ensure accurate representation of the velocity field. A high-resolution 3D printer was used to build the replicas of the aneurysmal geometries, which were then used to fabricate “negative” flow phantoms from clear silicone. A flow loop was constructed for PIV and in vitro 4D Flow MRI experiments using a gear pump, generating the inlet flow waveforms extracted from *in vivo* imaging. A mixture of water and glycerin was used to match blood viscosity and index of refraction for PIV. *In vitro* 4D Flow MRI measurements were obtained on a 3T SIEMENS Magnetom scanner using a dual-venc sequence developed at Northwestern University [2]. Time-resolved volumetric PIV measurements were acquired for two phantom models using four cameras.

Results: In order to determine the spatial and temporal resolution required for the intra-aneurysmal flow fields, CFD simulations with various mesh density and time steps were carried out. Numerical solutions obtained on subsequently refined meshes indicated that the spatial resolution of 0.15 mm and the time interval of ~2 ms provide sufficient accuracy of the computational results. The maximum velocity values in the aneurysm changed by 2% between 0.2 mm and 0.15 mm meshes, while only changing by 0.5% between 0.15 mm and 0.10 mm. A similar spatiotemporal resolution was attained in volumetric PIV experiments. In comparison, the resolution of the *in vivo* 4D Flow data was in the order of 1mm in space and 40 ms in time. A comparison of the velocity fields acquired with different modalities is shown in Figure 1. The CFD, in addition to providing high resolution, is not affected by noise which ensures mass conservation and accuracy of flow-derived metrics, e.g. vorticity and shear stress. The in vtiro 4D Flow model provides higher resolution due to scalability of the phantom and increased time of the scan.

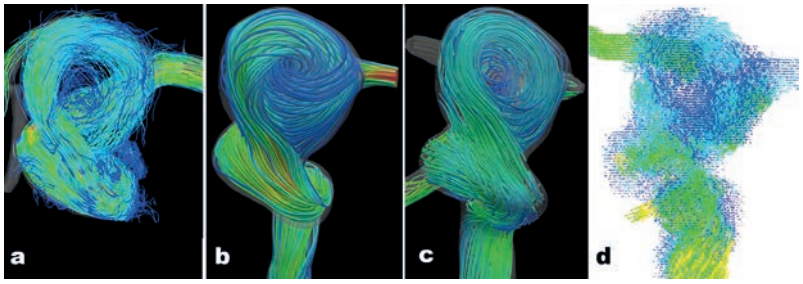

Figure 1 Velocities obtained with (a) in vivo 4D Flow MRI; (b) CFD and (c) in vitro 4D Flow MRI and (d) PIV

Discussion: Comparison of various flow quantification modalities demonstrated the advantages and limitations of each approach. While no gold standard method is available for assessing the flow in cerebral aneurysms, the results obtained with 4D Flow MRI, CFD and PIV can be verified and validated in controlled *in vitro* experiments. MR imaging of the flow phantoms is not affected by the patient’s movements or limited time of the acquisition, while the CFD of the phantom flow is independent of the assumptions of wall compliance, viscosity of the fluid, and inlet and outlet flow rates. Acquiring both lower resolution in vivo 4D Flow MRI and higher resolution in vitro 4D Flow and volumetric PIV, allows to determine the uncertainty of 4D Flow MRI. This in turn, affects the uncertainty of the derived hemodynamic forces. In a clinical setting, it is not practical to manufacture a flow model and carry out high-resolution flow measurements for each aneurysm patient, but once the uncertainty of the 4D Flow is established, it can be augmented with numerical models providing high-frequency flow structures to be combined with low frequency structures detected by in vivo 4D Flow MRI.

References: [1] Schnell S, Ansari SA, et al. Three-dimensional hemodynamics in intracranial aneurysms: influence of size and morphology. J Magn Reson Imaging, 2014. [2] Schnell S, Ansari SA, et al. Accelerated dual-venc 4D flow MRI for neurovascular applications. J Magn Reson Imaging, 2017

Title: Preoperative 4D Flow Analysis of Renal Cell Carcinoma

Carson A. Hoffman[1], E. Jason Abel [2], Oliver Wieben[1,3], and Christopher J. Francois[3]
[1]Department of Medical Physics, University of Wisconsin, Madison, WI, [2]Department of Urology, University of Wisconsin Madison, WI [3]Department of Radiology, University of Wisconsin Madison, WI

Purpose

Renal cell carcinoma (RCC) frequently invades and obstructs the Inferior Vena Cava (IVC), which can cause the redistribution of flow and collateral vessel development. Knowledge on the individual vascular anatomy and hemodynamics of the vessels including collaterals prior to intervention may improve surgical planning. . For example, the additional preoperative information could influence the way IVC reconstruction and vessel ligation is conducted, with potential reductions in both, surgical time and patient bleeding. In this pilot study, we investigated the use of 4D flow MRI for added presurgical information by providing anatomical coverage and qualitative and quantitative flow information over a large imaging volume.

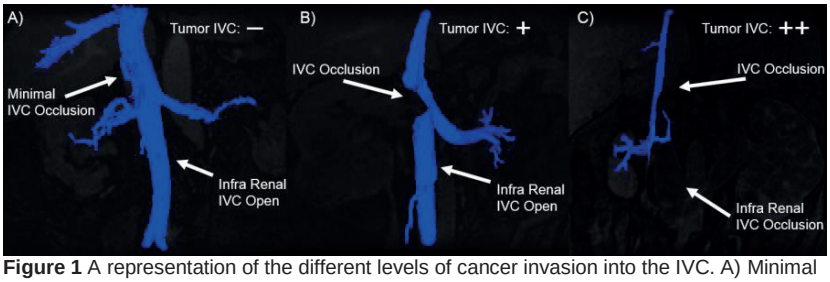

Figure 1 A representation of the different levels of cancer invasion into the IVC. A) Minimal to no cancer invasion:'-'. B) Large cancer invasion with lower IVC open, '+' C) Large cancer invasion with occluded lower IVC: '++'.

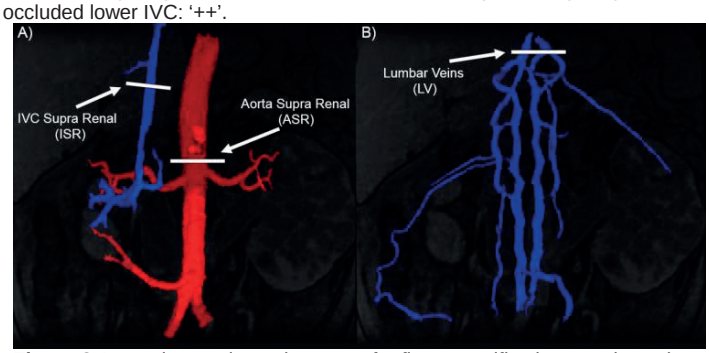

Figure 2 Approximate plane placement for flow quantification are shown by the white lines. A) Includes two planes measuring the arterial and venous blood supply to the kidney's and lower body. B) Quantify flow in the lumbar veins when visible.

Methods

Eleven RCC patients participated in the study. Imaging was performed on 1.5T and 3T clinical scanners (GE Healthcare) using 4D flow MRI with an undersampled radial acquisition (PC-VIPR[1]). Imaging parameters included: image volume: 32x32x32 cm, isotropic spatial resolution = 1.25 mm; VENC = 60-120 cm/s; scan time: ~10 min. The arterial and venous vasculature was segmented semi-automatically (Mimics Materialize, Leuven, Belgium) from the time averaged PC MR angiogram (Figure 1). The level of IVC invasion and occlusion was visually assessed on the venous PC MR angiogram (Figure 1).. Three arterial and venous flow measurements were conducted using in house macros developed for Ensight (CEI, Apex, NC): Aorta SupraRenal (ASR), IVC SupraRenal (ISR), and Lumbar Veins (LV) shown in Figure 2. The LV flow measurement is the total flow of all detectible lumbar veins. The venous to arterial flow ratios were computed with and without the inclusion of lumbar venous return as a measure of collateral flow. One patient was scanned both pre- and post- treatment.

TABLE 1 – Renal Flow Measurements (ml/sec)

Age	Sex	Tumor Side	ASR	ISR	LV	ISR/ASR	(ISR+LV)/ASR	Tumor IVC
70	M	L	39.52	50.66	4.79	1.28	1.40	–
58	M	L	28.70	36.60	ND	1.28	1.28	–
84	M	R	38.36	38.16	ND	0.99	0.99	–
58 (pre-treatment)	M	L	45.22	60.73	ND	1.34	1.34	–
58 (post - treatment)	M	L	32.40	32.70	ND	1.01	1.01	–
47	F	L	30.34	20.20	12.05	0.62	0.99	+
63	M	R	43.70	37.30	6.61	0.85	1.00	+
50	M	R	34.82	26.48	6.67	0.76	0.95	+
63	M	L	33.73	11.40	17.51	0.34	0.86	++
52	M	L	31.70	10.64	15.95	0.34	0.84	++
68	M	R	48.99	32.06	9.03	0.65	0.84	++

ASR - Aorta SupraRenal ,ISR - Inferior Vena Cava Supra Renal, LV - Lumbar Vein Total, ND - Not Detectable
Symbols : – No to minimal tumor in the IVC, + Tumor in the IVC with open Infra IVC, ++ Tumor in the IVC with Occluded Infra IVC

Table 1 Patient data is from eleven patients with RCC. All of the measurements reported are taken prior to treatment of the cancer except for one.

Results

The results are summarized in Table 1. The lumbar veins were detectable and large enough for flow analysis in seven out of the eleven cases. The average lumbar flow showed an increase with the level of IVC invasion category from (-) 0.958 ml/sec, (+) 8.44 ml/sec (++) 14.16 ml/sec. Three of the four pre-treatment(-) cases had an ISR/ASR value greater than 1 ranging from 1.28-1.34. Six of the seven cases with detectible lumbar veins had an ISR/ASR ratio below 1 ranging from 0.34 – 0.85. The addition of LV to the ISR/ASR ratio resulted in average values closer to 1 (+) 0.98 (++) 0.85. The PC angiograms showed little to no difference between the single pre- and post- treatment case, but did show a change in the ISR/ASR value from 1.34 to 1.01 respectively.

Conclusion

4D flow MRI can acquire preoperative geometric and hemodynamic vessel information in RCC patients. The venous to arterial ratio are a means to quantify collateral flow and may correlate to treatment decisions. Comprehensive preoperative knowledge of the patient specific collateral vascular network and flow and invasion of the IVC as demonstrated in this work may enable surgeons to better plan for their treatment approaches such as grafting or ligation of major vascular structures. Future work will include additional post-treatment cases to help establish an additional metric to monitor patient recovery.

References: [1] Johnson, K. M. et al Magnetic Resonance in Medicine. 2008; 60(6), 1329-1336.

Modeling to Better Understand Bolus Shaping Effects in Contrast-Enhanced MRA

Jeffrey H. Maki[1], Toshimasa J Clark[1] and Gregory J. Wilson[2]
1 - University of Colorado, Department of Radiology, Aurora, CO, USA; 2 – Bayer, Whippany, NJ

Introduction: High resolution 3D contrast-enhanced MR angiography (CE-MRA) acquires k-space during the 1st pass of an intravenously injected gadolinium-based contrast agent (CA). The evolution (or 'profile') of the contrast bolus during acquisition, if non-constant, leads to blurring and loss of spatial resolution. Previous work, including the TIP[1] (Tailored Injection Profile) technique (test bolus to calculate optimal bolus) and an analysis of the modulation transfer function (MTF) for different bolus types[2] has demonstrated this effect is real and relevant to MRA, and suggests slower or diluted boluses for improved image quality, particularly at 3T and for longer acquisition durations (T_{acq}), such as with carotid MRA.

This work attempts to extend a modeling formalism to 3D anthropomorphic phantoms in attempt to better understand how different bolus shapes/durations effect the actual images as may be perceived by the interpreting physician. This entails being able to identify blurring effects in different sized and oriented vessels with any type of contrast bolus and MR parameters – something that cannot be easily performed in the clinic.

Injection Type	Test Bolus Injection Profile	Full Bolus Injection Profile
Standard (NS)	1 ml @ 1.6 ml/s	Remaining Vol @ 1.6 ml/s
Diluted, Single-phase (DS)	2 ml @ 2 ml/s	38 ml @ 1.6 ml/s
Diluted, Bi-phasic (DB)	2 ml @ 2 ml/s	9 ml @ 3.3 ml/s, 29 ml @ 1.4 ml/s
Diluted, Tailored (DT)	2 ml @ 2 ml/s	TIP

Methods: Recent work examined four injection strategies[3], the latter two of which were specifically designed to give ~ 20 sec plateau (**Table**: 10 subjects each - "standard" injection [NS], 3 variants of diluted contrast (to 40 mL) – single phase [DS], biphasic [DB], and tailored [DT] – all gadobenate 0.1 mmol/kg [Bracco]) by collecting signal intensity (SI) vs time using a 100 s time-resolved 3D SPGR acquisition with CE-MRA mimicking parameters: TR = 3.5 ms, TE = 1.5 ms, flip angle = 30°, FOV = 400 x 248 x 64 mm^3, voxel volume = 2 x 2 x 8 mm^3. Data from each group of 10 subjects were normalized to pre-contrast SI and time-shifted to align contrast arrival, after which non-parametric curve fitting was performed using a smoothing spline technique.

CT data from a silicone abdominal aorta phantom (Shelley Medical) was digitally manipulated to provide a high resolution, high contrast essentially binary model consisting of vascular structures and lower signal background. This was input into a flexible Matlab (Mathworks) program developed to: a) convert the image to the desired MR resolution/FOV, b) Fourier transform the input image into k-space, c) determine the temporal order of k-space acquisition (centric ordering), d) evolve the vascular SI per any arbitrary input bolus profile (e.g. NS, DS, DB, DT) and correctly apply this modulation to k-space, and e) transform the 'bolus corrupted' image back into image space for visualization. Modeling was performed to simulate 3T renal MRA; FOV 400 x 400 x 64 mm^3, TR/TE 4.0/1.5 ms, phase SENSE = 4, T_{acq} 22 s. Further steps include outputting data to DICOM for viewing at a 3D workstation. Analysis consists of MPR images for artifacts and line profile analysis.

Results: The fitted curves for the different bolus types are shown in **Figure 1**. These curves are used for input into Matlab. Note all of the diluted profiles have longer plateau periods than "standard" injection without much signal loss, and provide a good basis for the Matlab modeling. Evaluation of differences between the different injections demonstrate differences relative to injection profile, most pronounced between "standard" and the longer diluted strategies. These will be discussed.

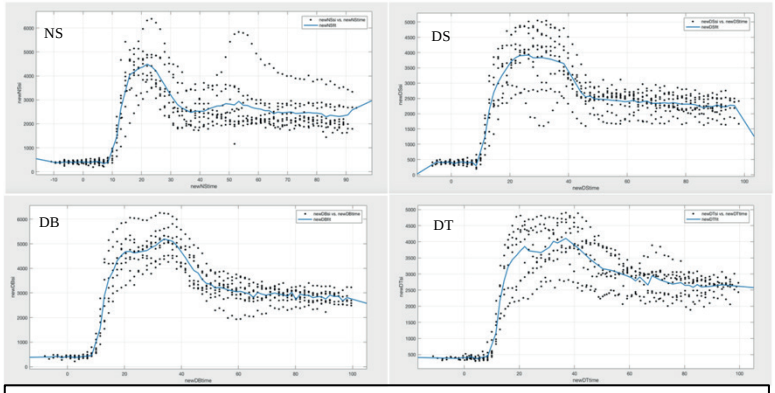

Figure 1. N=10 normalized and time-shifted data for each injection type, blue solid line representing non-parametric fit for each. Note relatively short peak for "standard" NS injection (top left) without significant signal gain.

Discussion: Intelligently crafted injection profiles provide a longer enhancement plateau, providing more uniformity during k-space acquisition and therefore less blurring while costing minimal, if any decrease in peak signal intensity. Anatomic modeling taking into account different MR acquisition parameters, contrast bolus profiles, and ultimately vascular territories can be extremely helpful in understanding and optimizing acquisition strategies and visualizing effects on clinical images. It may also prove useful for analyzing other types of MRA such as time-resolved MRA using view sharing.

References:

1. Wilson GJ, Maki JH. J Magn Reson Imaging (2016) 44(6):1664-72.
2. Clark TJ, Wilson GJ, Maki JH. Magn Reson Med (2016) 78:357–69.
3. Maki JH and Wilson GJ. 28th SMRA Scientific Meeting, Stellenbosch, South Africa. September 2017.

Next Generation Gd-Free T_1 MRI Contrast Agents for Angiography: High Relaxivity, Remarkable Stability and Tunable Pharmacokinetics

Hanlin Liu[1,2], Piryanka Sasidharan[1,2], Xiao-an Zhang[1,2,3]*

[1]Department of Chemistry, University of Toronto, [2]Department of Physical & Environmental Science, and [3]Department of Biological Sciences, University of Toronto Scarborough, 1265 Military Trail, Toronto, ON M1C 1A4, Canada

Purpose: Gadolinium based contrast agents (GBCAs) play a pivotal role in contrast enhanced MRI, but their scope of application in vascular imaging has been largely restricted due to the intrinsic limitations. First, free Gd(III) ion is toxic, but most GBCAs, including those with cyclic ligands, are kinetically labile towards transmetallation, and thus can release free Gd(III) in vivo, causing Gd-deposit in the brain and other tissues, as well as the rare but severe side effect: nephrogenic systemic fibrosis (NSF). Second, most commercial GBCAs have low sensitivity (measured as T_1 relaxivity, or r_1), especially at high clinical field of 3 T, and the required high dose increases the toxicity risk. Finally, after the market withdrawal of Gadofosveset (Ablavar), the first clinically approved blood-pool agent (BPA), the remaining GBACs all have nonoptimal pharmacokinetics for MRA: their rapid extravasation decreases the vascular selectivity and half-life. In fact, the vascular retention needed for MRA contradicts the fast renal clearance required for safety, which is a dilemma for the design of Gd-based BPA. Our goal is to develop Gd-free BPA, with high biocompatibility, stability and relaxivity, as well as tunable pharmacokinetics optimized for different MRA applications.
Methods: We chose manganese(III) porphyrin (MnP) as our basic building block.[1] Unlike Gd, Mn is a biocompatible micronutrient, and can be tightly bound to the rigid porphyrin ligand as a +3 oxidation state complex, chemically distinct from the labile Mn^{2+} CAs such as MnDPDP (Teslascan). Certain water-soluble MnPs, such as MnTPPS, was reported with anomalously high T_1 relaxivity (r_1).[2] To further improve the r_1 at clinical fields (1-3 T), molecular parameters, including tumbling rate, number of paramagnetic centres, and water-accessibility, were optimized through structural modifications.[1] A hydrophobic binding unit is attached to gain adjustable affinity with human serum albumin (HSA) (Fig. 1a), and consequently, the desired vascular retention.[3] Flexible synthetic strategies were established for the preparation of diverse MnP structures.[1] The relaxivity was evaluated by nuclear magnetic resonance dispersion (NMRD) profiles using variable field relaxometry. The stabilities were tested against low pH and metal ions known to cause transmetallation with GBCAs, and monitored by UV-vis absorption and HPLC. The interactions between MnPs and HSA were monitored by optical spectroscopies, including circular dichroism (CD), UV-vis and fluorescence.[4] The pharmacokinetic properties were examined in rodent models and monitored by 3T clinical MRI scanners.[3]
Results & Discussions: A series of new MnPs, including monomers and dimers (n = 1 or 2, Fig 1A) were designed and synthesized. All MnPs exhibit higher r_1 at clinical fields, in contrast to GBCAs. Specifically, at 3 T, the r_1 of most small MnP monomers is above 8 $mM^{-1}S^{-1}$, twice as sensitive as typical small GBCAs. In comparison with Gadofosveset, which displays a large r_1 increase upon binding to HSA, owing to slower tumbling, our dimeric MnPs show comparable r_1 at 1 T (~30 $mM^{-1}S^{-1}$); at 3 T, the r_1 of Gadofosveset-HSA complex drastically decreases to 9.7 $mM^{-1}S^{-1}$, whereas selected MnP-dimers keep the molar r_1 above 20 $mM^{-1}S^{-1}$ (Fig 1B). New MnPs also exhibit remarkable stability: no demetallation or transmetallation was detected after incubation of MnP at low pH and/or with excess of metal ions, including Mg, Ca, Cu, Fe and Zn at different temperature for up to three weeks. Under similar conditions, transmetallation was observed for GBCAs, including the stable ones with cyclic ligands. Depending on the structures, new MnPs achieved a range of affinities with HSA, with the dissociation constants (K_d) determined from 100s μM to 100s nM.[4] In general, large hydrophobic binding unit leads to higher affinity. The difference in HSA affinity consequently led to predictable pharmacokinetics.[3] While the high affinity MnP2 displays a long selective vesicular contrast enhancement for up to 48 hours, the non-protein binding MnTCP rapidly extravasates and cleared by kidney as an extracellular agent. Applications of the long circulating MnP2 for cardiovascular (Fig1C)[4] and lung imaging (Fig1D)[5] have also been demonstrated.

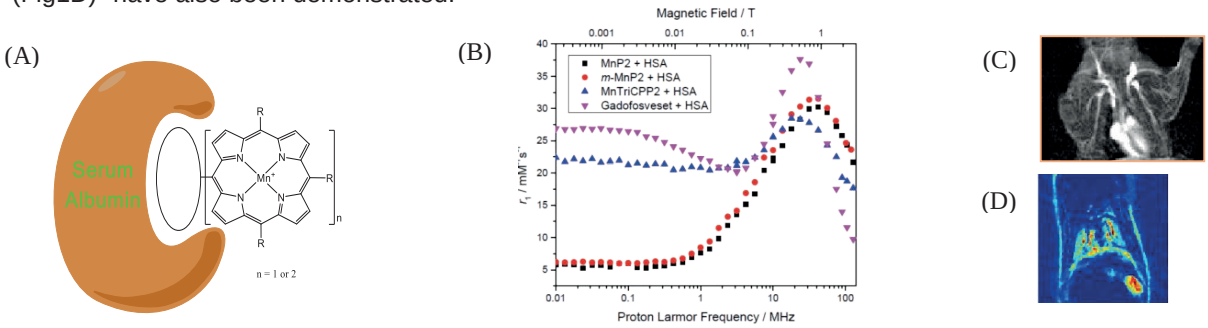

Fig.1 (A) General design of HSA-targted BPAs based on MnP; (B) NMRD profiles of slected MnPs; (3) MnP2 enhanced cardiovascular MR imaging;[4] (D) MnP2 enhanced lung imaging with ultra-short echo time.[5]

Conclusion: Through rational molecular design, novel MnPs with high T_1 relaxivity, especially at high clinical field of 3 T, remarkable stability, modulable affinity with HSA and desirable vascular retention time were acomplished, fulfil the criteria as next generation BPA. Our results have systematically demonstrated the potential of MnPs as safer and more sensitive alternatives of GBCAs.

References: [1] *J. Med. Chem.* **2014**, 57(2), 516; [2] *Magn. Reson. Med.* **1987**, 4, 252; [3] *J. Magn. Reson. Imaging* **2014**, 40(6) 1474; [4] *J. Bio. Inorg. Chem.* **2014**, 19(2), 229; [5] *Mol. Imaging* **2014**, 13(8), 7290.2014. 00027

Assessment of Pulmonary Hypertension using Time Resolved MRA and 4D flow MRI

Daniel Z Gordon[1], Michael Markl[1], Pascale Aouad[1], Jeremy Collins[1], Monica Korell[1], Roberto Sarnari[1], Benjamin Freed[2], Sanjiv Shah[2], Michael Cuttica[3], James C Carr[1]

[1]Radiology, [2]Cardiology, & [3]Pulmonary and Critical Care, Northwestern University

Purpose: To develop an optimized MRI/MRA protocol utilizing time resolved MRA and 4D flow MRI to evaluate patients with pulmonary venous hypertension (PVH), pulmonary arterial hypertension (PAH), and healthy controls. We aim to test the following hypotheses: 1. MRI bolus transit-time measurements, derived from time resolved MRA, are prolonged in pulmonary hypertension (PHTN) patients and can distinguish pulmonary arterial from pulmonary venous hypertension. 2. Hemodynamic parameters (flow, velocity) measured by 4D flow MRI at different vascular anatomic landmarks can distinguish between pulmonary arterial and pulmonary venous hypertension.

Methods: A total of 21 subjects (8 patients with PVH (defined as mPAP≥25mmHg, PCWP>15mmHg at right heart catheterization)[1], 5 patients with PAH (mPAP≥25mmHg, PCWP≤15mmHg), and 8 controls) underwent MRI incorporating time resolved MRA and 4D flow MRI. The patients with pulmonary hypertension completed the contrast-enhanced MRI within 28 days of right heart catheterization (RHC). 4D Flow measurements were made using a commercial 4D flow software prototype (Circle Cardiovascular Imaging, Calgary, Canada). Transit time analysis from time-resolved MRA was completed in a subset of 12 subjects (4 PVH, 3 PAH, 5 controls). Transit time measurements were calculated using subtracted maximum intensity projections from the time resolved MRA images on a dedicated post-processing workstation (Leonardo, Siemens Medical Solutions, Malvern, PA, USA).

Results: Early results show that peak velocity in LPA/RPA was lower in PAH group compared to PVH and normal (although only significant for RPA ($p<0.05$; Table 1). Additionally, net flow differed significantly in the right lower pulmonary vein (RLPV) and in the RPA ($p<0.005$; Table 1) for both PHTN groups compared to normals. Peak velocity RPA 4D flow data are consistent with Odagiri et al. (2016). Transit times also differed significantly among the 3 groups ($p<0.05$; Table 2, Figure 1). These transit time findings are consistent with Jeong et al. (2011).

Table 1. Peak velocity and net flow in the RPA in PVH patients, PAH patients, and controls.

	PVH n=8	PAH n=5	Control n=8	p value
Peak Velocity (cm/s)				
RPA	67.0±19.0	35.4±29.1	73.6±16.0	0.0126*
LPA	54.9±13.8	45.2±15.1	65.5±14.9	0.0699
RLPV	26.3±13.6	25.2±18.7	39.1±11.4	0.1400
RUPV	43.4±13.2	29.0±17.4	48.5±22.1	0.1716
LLPV	26.4±16.9	37.0±7.5	36.1±13.2	0.2919
LUPV	54.1±14.4	35.8±4.1	45.6±24.2	0.2161
IVC	60.1±15.7	47.4±24.7	55.1±18.8	0.5217
SVC	52.6±22.2	44.4±20.5	49.25±7.8	0.7178
Net Flow (ml/cycle)				
RPA	39.8±8.5	26.6±18.3	51.3±5.2	0.0027*
LPA	29.4±8.5	31.1±11.2	38.2±5.15	0.1045
RLPV	11.2±7.9	11.7±10.7	23.9±3.1	0.0048*
RUPV	24.5±11.2	14.4±10.1	26.2±9.4	0.1391
LLPV	9.5±8.4	12.3±4.1	14.6±3.6	0.2655
LUPV	20.1±5.9	14.1±3.1	19.9±6.6	0.1587
IVC	31.6±10.6	28.6±28.4	49.0±14.1	0.0817
SVC	21.9±11.8	17.5±11.2	23.6±4.4	0.5328

*Denotes significant values ($p<0.05$). Data are expressed as mean ± standard deviation.

Table 2. Aorto-SVC transit times (TT) between PVH patients, PAH patients, and controls.

	PVH n=4	PAH n=3	Control n=5	p value
TT(sec)	13.0±3.7	14.2±2.7	7.8±1.4	0.0156*

Figure 1. Example of transit times from a control. The peaks for each vessel were used to calculate total transit times.

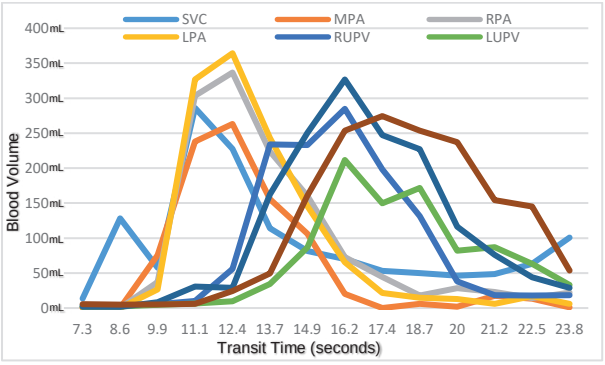

Discussion: Pulmonary arterial velocities were lower in PAH group compared to PVH/controls and transit times were longer in pulmonary HTN in general. These early findings suggest that 4D flow MRI may be able to distinguish between PAH and PVH. Work is ongoing to calculate pulmonary blood volumes, full velocity profiles and regional transit times in entire cohort.

References:

1. Freed, Benjamin H. et al. "Magnetic Resonance and Computed Tomography Imaging for the Evaluation of Pulmonary Hypertension." *JACC. Cardiovascular imaging* 9.6 (2016): 715–732. *PMC*. Web. 12 Apr. 2018.
2. Odagiri, K., Inui, N., Hakamata, A. et al. SpringerPlus (2016) 5: 1071. https://doi.org/10.1186/s40064-016-2755-7`
3. Jeong, Hyun J. et al. "Time Resolved MRA: Evaluation of Intrapulmonary Circulation Parameters in Pulmonary Arterial Hypertension." *Journal of magnetic resonance imaging : JMRI* 33.1 (2011): 225–231. *PMC*. Web. 12 Apr. 2018.

Abstract title

18F-Fluoride PET MR in valvular and coronary heart disease; A pilot investigational study

Full name(s) of all authors

Jack Andrews[1], Alastair Moss[1], Mhairi Doris[1], Tania Pawade[2], Philip Adamson[1], Gillian MacNaught[3], Christophe Lucatelli[3], David Newby[1,2] and Marc Dweck[1,2]

Author affiliations, including country, stage of training

1. Centre for Cardiovascular Science, University of Edinburgh, Chancellor's Building, Royal Infirmary of Edinburgh, 49 Little France Crescent, Edinburgh, EH16 4SB, UK

2. Edinburgh Heart Centre, Royal Infirmary of Edinburgh, 51 Little France Crescent, Edinburgh EH16 4SB, UK

3. Clinical Research Imaging Centre, QMRI, Little France Crescent, Edinburgh, EH16 4SB, UK

JA- Cardiology Registrar and Research Fellow AM – Cardiology Registrar and Research Fellow MD – Cardiology Research Fellow TP – Cardiology Registrar PA – Cardiology Consultant GM – PET-MR Physicist CL – Chief Radiochemist DN – Professor of Cardiology MD – Consultant Cardiologist

Background/Introduction Recently, hybrid PET-CT imaging has shown promise in the identification of high-risk coronary atherosclerosis and in the prediction of aortic stenosis progression.[1,2] The development of PET-MR imaging platforms has provided opportunity to combine the assessment of disease activity (PET) with detailed anatomical and functional assessments of the heart with reduced radiation exposure. While this has already shown promise in the assessment of myocardial disease [3], the value of PET-MR imaging in coronary atherosclerosis, myocardial infarction and aortic stenosis remains uncertain.

Purpose We aimed to investigate aortic valve 18F-NaF PET activity in subjects with aortic stenosis (AS) compared to those without. We also investigated 18F-NaF uptake in culprit arteries and areas of late gadolinium enhancement (LGE) in patients with recent myocardial infarction (MI). Cohort 1 consisted of patients with mild or moderate aortic stenosis (n=10). Cohort 2 consisted of patients with stable coronary disease (n=2) and those with MI and percutaneous coronary intervention within the previous year (n=13).

Methods 25 patients underwent PET-MR scanning approximately 90 minutes after injection of 125MBq (Cohort 1) or 250MBq (Cohort 2)18F-NaF. PET data was acquired in list mode for 50 minutes with a standard Dixon attenuation correction technique. Contrast-enhanced MR coronary angiography was performed following infusion of Gadolinium with delayed imaging for scar assessment. PET activity was quantified in the aortic valve, coronaries and areas of LGE by calculating standardised uptake values (SUV) and tissue to background ratios (TBR) on fused PET-MR images. Culprit arteries were identified by experienced operators during preceding invasive coronary angiography and areas of LGE were visually identified by an experienced MR reader.

Results 22 of 25 patients completed the protocol. Patients with aortic stenosis (n=9 completed) had higher aortic valve SUVmax and TBRmax (Valve SUV max/left atrial SUV mean) than those without aortic stenosis (SUVmax 1.89 +/- 0.60 vs 1.15 +/- 0.38, **p=0.001** and TBRmax 2.87 +/-0.98 vs 1.77+/-0.43, **p = 0.001,** Figure 1; graph A+B). 13/13 (100%) patients with MI had focal 18F-NaF uptake in the culprit vessel with an SUV max of 1.05 +/- 0.26 vs 0.74+/- 0.13 for the proximal referent vessel (**p = 0.002,** Fig1; graph C). Culprit mean TBR max (culprit SUV max/left atrium SUV mean) was also greater than proximal referent vessel at 1.64 +/- 0.47 vs 1.16 +/- 0.26 (**p = 0.004,** Fig 1; graph D). 11/13 patients had LGE evidence of myocardial infarction with all 11 (100%) demonstrating greater infarct than remote myocardial SUV means (0.62 +/- 0.23 vs 0.4 +/- 0.14, **p = 0.003**, Fig 1; graph E). Within areas of LGE, TBR mean (LGE SUVmean/LA SUVmean) was greater than remote myocardial mean (1.00+/-0.36 vs 0.63 +/-0.25, **p = 0.001**, Fig 1; Graph F)

Conclusion(s) PET-MR aortic valvular uptake of 18F-NaF is significantly greater in those with confirmed aortic stenosis than those without (Figure 2). 18F-NaF uptake also accurately identifies culprit arteries in those with recent MI (Figure 3). Furthermore uptake within areas of LGE was greater than that in healthy myocardium (Figure 4) suggesting tissue degeneration similar to that seen in atherosclerotic plaque abdominal aortic aneurysms. [4] The results share similarities with recently published valvular and coronary 18F-NaF PET-CT studies [1,2] and thus promote further research into the utility of cardiovascular PET-MR as a complementary hybrid imaging technique in coronary and valvular disease.

References

1. N.V. Joshi, A.T. Vesey, M.C. Williams, *et al.***18F-fluoride positron emission tomography for identification of ruptured and high-risk coronary atherosclerotic plaques: a prospective clinical trial**. Lancet, 383 (2014), pp. 705-713

2. M.R. Dweck, N.A. Boon, D.E. Newby. **Calcific aortic stenosis: a disease of the valve and the myocardium**. J Am Coll Cardiol, 60 (2012), pp. 1854-1863

3. R. Abgral, M.R. Dweck, M.G. Trivieri, *et al.* **Clinical utility of combined FDG-PET/MR to assess myocardial disease**. J Am Coll Cardiol Img, 10 (2017), pp. 594-597

4. Forsythe, RO., Dweck, MR.,McBride, OMB et al. (**18)F-Sodium Fluoride Uptake in Abdominal Aortic Aneurysms: The SoFIA(3) Study**.2018 JACC.71(5);513-523

Efficacy of gadoterate meglumine enhanced MRA in evaluating vascular diseases compared with gadobutrol enhanced MRA.

Louise Collins[1], Sydney Rabin[1], Ali Serhal[1], Pascale Aouad[1], Monica Korell[1], Jeremy Collins[1], James Carr[1]
[1]Northwestern University, Chicago, IL, United States

Purpose

Contrast enhanced magnetic resonance imaging plays an important role in the diagnosis and follow-up of patients with several different vascular pathologies such as aneurysm, dissection, stenosis, etc. (1). Both computed tomographic angiography and contrast enhanced magnetic resonance angiography are equally validated techniques for imaging patients with vascular pathologies (2). There has been increasing focus recently on use of macrocyclic gadolinium based contrast agents due to their superior safety profiles compared to linear agents. There are several macrocyclic agents now available and it is unclear how they perform in clinical practice, particularly for cardiovascular applications. The objective of this study is to demonstrate that carotid and chest MRA with gadoterate meglumine has comparable image quality and diagnostic confidence to MRA using gadobutrol.

Methods

This study was IRB approved and informed consent was obtained from all participants. The study population consisted of 20 patients presenting for routine follow-up with CE MRA of the thoracic aorta or carotid arteries. All patients underwent gadobutrol enhanced MRA as part of a routine clinical scan and returned on average 5-6 weeks later for a research gadoterate meglumine enhanced MRA. The injection rate and dose were the same for both studies. Measurements of the thoracic aortic diameters were obtained at the levels of sinus of Valsalva, Sino-tubular junction, ascending aorta, proximal arch, distal arch and distal descending aorta for both scans (according to AHA guidelines). The average diameters for each measurement were calculated and correlation was assessed by linear regression analysis. Quantitatively, SNR was calculated for the thoracic aorta at the ascending, aortic arch and descending aorta for both scans, SNR for the carotid arteries was calculated at the left and right carotid, internal carotid and vertebral arteries for both scans. These were compared using a paired two-tailed t-test ($\alpha = 0.05$).

Results

A total of 20 patients were analyzed, this included 8 patients presenting for routine follow up with CE MRA of the thoracic aorta and 12 patients presenting for routine follow up with CE MRA of the carotid arteries. Quantitatively, there was excellent agreement between thoracic aortic diameter measurements for both scans ($r^2=0.97$, $p<0.001$) at all measured aortic levels. Quantitatively, there was no significant difference in the SNR of the thoracic aorta and carotid arteries at all measured levels when comparing the clinical and research scans.

Discussion

Gadoterate meglumine enhanced MRA showed comparable image quality to gadobutrol enhanced MRA when analyzing the carotid and thoracic aorta with excellent correlation of thoracic aortic measurements.

References

1. Eric M. Isselbacher. Epidemiology of Thoracic Aortic Aneurysms, Aortic Dissection, Intramural Hematoma, and Penetrating Atherosclerotic Ulcers. Volume 260 of the series Developments in Cardiovascular Medicine pp 3-15, 2007.
2. Laura A. Freeman, Phillip M. Young, Thomas A. Foley, Eric E. Williamson, Charles J. Bruce, Kevin L. Greason. CT and MRI Assessment of the Aortic Root and Ascending Aorta. American Journal of Roentgenology. 2013;200: W581-W592. 10.2214/AJR.12.9531

Figures

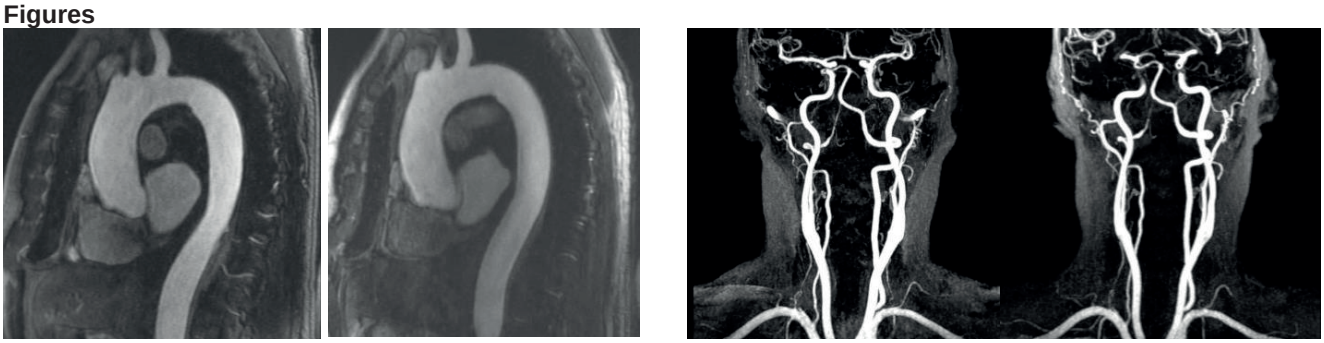

(a) (b) (c) (d)

Sagittal contrast enhanced MRA of the thoracic aorta and coronal MIP MRA of the neck using gadobutrol (a, c) and gadoterate meglumine (b, d) demonstrate comparable image quality.

Flow-MRF: a novel way of quantifying blood velocities in combination with tissue relaxation parameters

Sebastian Flassbeck[1], Simon Schmidt[1], Mark E. Ladd[1], and Sebastian Schmitter[1,2]
[1]Medical Physics in Radiology, German Cancer Research Center (DKFZ), Heidelberg, Germany,
[2]Physikalisch-Technische Bundesanstalt (PTB), Braunschweig and Berlin, Germany

Purpose:
The simultaneous quantification of blood flow velocities along with relaxometric parameters of static tissue has recently been proposed within the magnetic resonance fingerprinting (MRF) framework [1]. This technique is termed "Flow-MRF", and it allows use of very small encoding velocities (venc) of 40 cm/s and below without velocity aliasing. At the same time, T1 and T2 can be quantified, which are important parameters to characterize atherosclerosis [2], suggesting the carotids as an ideal application of Flow-MRF, particularly at high fields where higher spatial resolution is achievable. In the present volunteer study, however, we investigate Flow-MRF in the femoral artery due to the lack of a carotid coil and we make use of the high SNR provided by 7 Tesla in combination with a knee coil.

Methods:
Bipolar gradients were incorporated into a radial spoiled-SSFP-based MRF sequence to allow the modulation of the first gradient moment (m_1) during the acquisition train, as shown in Fig. 1. The same flip angle pattern as in [3] was used. m1 was varied simultaneously on all axes between -30 and 30 $mT/m \cdot ms^2$ as shown in Fig. 1c. The maximal difference in m_1 corresponds to a venc of 20 cm/s. The random nature of the m_1 pattern ensures that the minimal difference in m_1 is small (< 1 $mT/m \cdot ms^2$); thus, even high velocities (> 150 cm/s) can be correctly mapped without aliasing. During the entire MRF acquisition train, a constant TE/TR of 5.96/8.96ms was used; this decouples the quantification of velocities from the quantification of relaxation constants.
A spatial resolution of (0.8×0.8×5) mm^3 was used and the velocity vectors were reconstructed to have a temporal resolution of 45 ms (5·TR). 5 k-space interleaves per timeframe were required, resulting in a total measurement time of 84 s, which includes 5×8 s waiting periods for the magnetization to approximate thermal equilibrium. These pauses can be shortened or used to encode different slices.
The study was carried out on a whole-body 7T (Siemens Magnetom) with approval of the local ethics committee.

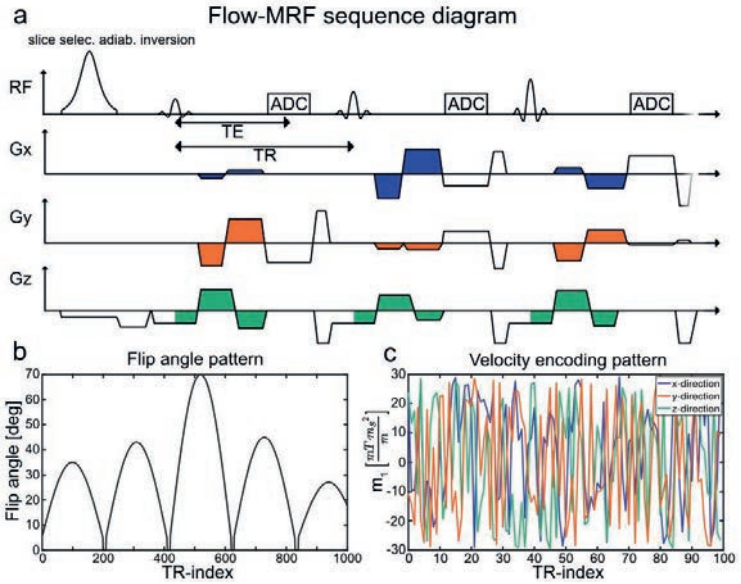

Figure 1: *a) Schematic sequence diagram. b) Flip angle pattern needed for relaxometric quantification. c) m1 pattern for velocity quantification. The colored bipolar gradients in a) apply the corresponding m1 in c).*

Results:
Figure 2 displays a summary of the information retrieved from the Flow-MRF sequence. Fig. 2a shows a magnitude image overlaid with the quantified velocities in the vessel lumen of the artery and vein. A comparison with a vendor provided phase-contrast (PC) cine is shown in Fig.2 b. The mean deviation between the two techniques is 1.3 cm/s with a peak deviation of 13 cm/s. The relaxometric maps are shown in Fig. 2 c-d. Obtained T1 and T2 in skeletal muscle (1360±50 ms and 27±5 ms) agree with literature values [4].

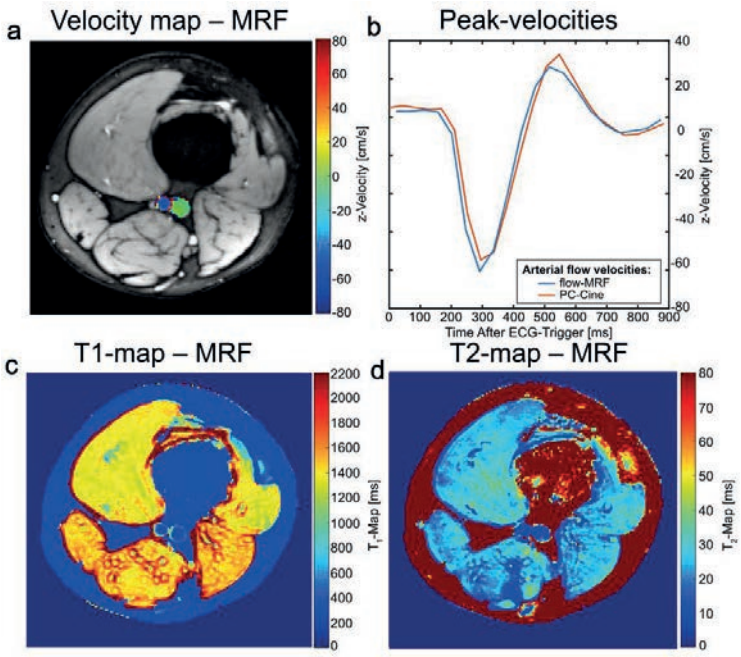

Figure 2: *a) Magnitude image overlaid with z-velocities quantified by Flow-MRF in the vessel lumen of the femoral artery and vein. b) Line plot of peak velocities in the artery over the cardiac cycle. c-d) relaxometric maps calculated with prior knowledge of an external B1 map.*

Discussion:
The quantified velocities of Flow-MRF are in good agreement with the PC-cine sequence. Residual deviations are likely linked to differences in velocity encoding time points. The relaxation times are in agreement with literature values. The heterogeneity in the T2 map is partly due to flow artifacts in the external B1 map that is presently still needed at 7T.

References: [1] Flassbeck et al. Proc 25th ISMRM 2017; [2] Hunter et al. Nature Reviews 2010. [3] Y. Jiang et al. MRM 2014; [4] Ren et al. Proc 17th ISMRM 2009

Submillisecond water excitation for flow-independent noncontrast-enhanced peripheral angiography at 3T

Nolwenn ML Levêque[1], Lionel P Arn[1], Davide Piccini[1,2], Jessica AM Bastiaansen[1]
1. Department of Radiology, Lausanne University Hospital (CHUV) Lausanne, Switzerland. 2. Advanced clinical imaging technology, Siemens Healthineers, Lausanne, Switzerland

Purpose - To develop and test a submillisecond water excitation pulse for noncontrast-enhanced angiography.

Methods - LIBRE water excitation pulses [1] were shortened to total RF pulse durations below 1ms. LIBRE pulses of such durations require a large pulse frequency offset (f_{RF}>1500Hz) [1], for which the efficiency of on-resonant water excitation (η_{WE}) decreases. The η_{WE} was obtained through Bloch simulations and verified in experiments to assign the pulse amplitude increase ($1/\eta_{WE}$) needed to achieve similar water excitation compared to a conventional 1-(180°)-1 on-resonance water excitation pulse (WE11). The actual excitation angle (α_{act}) of water can be expressed as the apparent excitation angle (α_{app}) indicated on the console times the excitation efficiency, $\alpha_{act} = \alpha_{app} * \eta_{WE}$. Experiments in a phantom containing water and fat were performed on a 3T scanner (Prisma Siemens). A 3D radial golden angle isotropic (0.9mm^3) GRE sequence [2] was used with either WE11 pulses (1.7ms duration), or LIBRE pulses with durations of 0.4ms, 0.6ms, 0.8ms and 1.0ms, with respective f_{RF} of 4610Hz, 2950Hz, 2100Hz, and 1580Hz. Acquisition parameters: TR=5ms, field-of-view 175mm^3, matrix 192^3, bandwidth 499 Hz/pixel. The apparent RF excitation angles were based on the Bloch simulations and were set to α_{WE11}=5°, $\alpha_{LIB0.4}$=48°, $\alpha_{LIB0.6}$=31°, $\alpha_{LIB0.8}$=22°, $\alpha_{LIB1.0}$=18°. Subsequently, magnetic resonance angiography (MRA) experiments were performed in legs of healthy volunteers (n=3) with the above GRE sequence preceded by a 40ms T2 preparation module and using a 0.8ms LIBRE pulse. For comparison MRA was also performed using WE11. Acquisition parameters were $TE/TR_{LIB0.8}$=2.5/5.7ms, TE/TR_{WE11}=3.0/6.6ms, α_{WE11}=12°, $\alpha_{LIB0.8}$~61°, 37 readouts per T2prep were acquired with a total scan time of 4min and a total of 12k readouts. Signal-to-noise ratios (SNR) were computed by dividing the average signal from water and fat compartments (red arrows, Fig. 1) by the standard deviation of the background noise. Maximum intensity projections were reconstructed from the acquired 3D MRA data, with exclusion of areas containing synovial fluid.

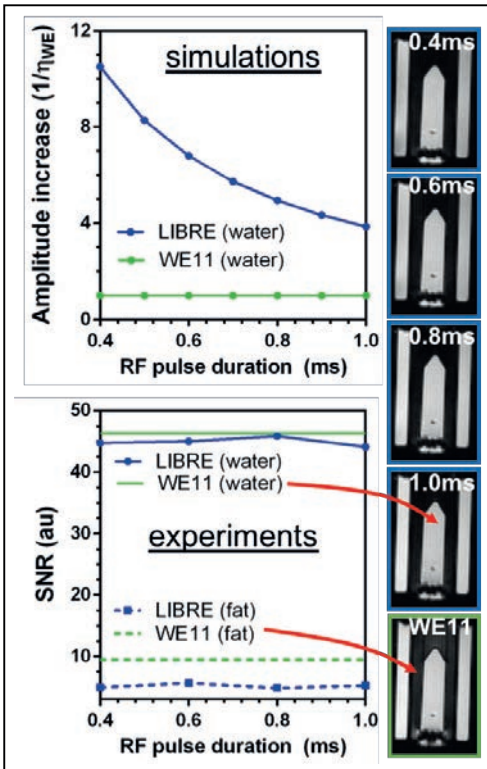

Figure 1. Amplitude correction **(top)** for different off-resonance LIBRE pulses to maintain water excitation (**bottom**).

Results - LIBRE pulses experience a decrease in water excitation efficiency (η_{WE}) of 9.5% (LIB0.4) to 25.9% (LIB1.0) compared with WE11 (Fig. 1, top). Experiments showed that increasing the pulse amplitude by $1/\eta_{WE}$ restored the water SNR (Fig. 1, bottom), while maintaining homogeneous fat suppression. In vivo, LIBRE pulses increased fat signal suppression significantly ($p<0.05$) compared to WE11 and resulted in improved vessel conspicuity (Fig. 2, red arrows).

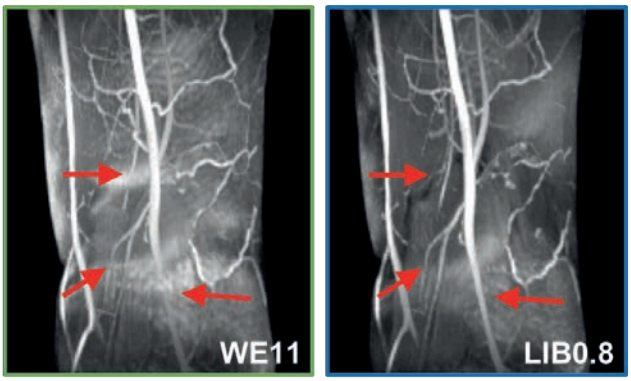

Figure 2. MIP images of a volunteer showing the comparison of 3D MRA in the leg obtained with WE11 (left) and LIBRE (right). Note the bright areas as a result of incomplete fat suppression using WE11 that hinders vessel visualization.

Discussion – Noncontrast-enhanced and flow-independent MRA was successfuly performed using submillisecond LIBRE water excitation pulses, and demonstrates promising increases in fat suppression, compared to more conventional water excitation. The use of inversion pulses [3-6] to null signals from long T1 compartments such as edema and synovial fluid was not investigated in the current study, and neither a comparison with phase contrast and time-of-flight MRA [7,8]. The current golden angle acquisition may also be further accelerated with compressed sensing to reduce scan time [9].

References - [1] Bastiaansen, MRM 79:3007-3017 (2018) [2] Piccini MRM 66:1049–1056 (2011) [3] Brittain, MRM 38:343-354 (1997) [4] Fielden, MRM 73:1026–1033 (2015) [5] Cukur, MRM 61:1533–1539 (2009) [6] Bangerter, MRI 29:1119-1124 (2011) [7] Steinberg, MRM 14:315-320 (1990) [8] Reimer, Eur Radiol 9:122-127 (1999) [9] Piccini MRM 77: 1473–1484 (2017).

Contrast Free MRI Methods for Vascular Assessment in Diabetic Lower Extremities

Jie Zheng,[1] Yongsheng Chen,[2] E. Mark Haacke, [2] Mary K Hastings, [1] Mohamed Zayed [1]
[1] Washington University School of Medicine, Missouri, Saint Louis, USA
[2] The MRI Institute for Biomedical Research, Detroit, Michigan, USA

Purpose A hallmark of peripheral arterial disease (PAD) in the setting of diabetes, is the accumulation of densely calcified, recalcitrant, occlusive disease of the tibial and pedal arteries. A radiation- and contrast-free imaging modality that can better characterize the extent of tibial and pedal arterial occlusive disease in patients with PAD and diabetes would provide great benefit to the diagnosis and treatment of this highly prevalent disease process. The objective of this ongoing study is to develop a new contrast-free-MR angiography (CF-MRA) technique without using any ECG signals and to integrate with existing microcirculation methods for the vascular assessment of lower extremities in patients with PAD and diabetes in one imaging session.

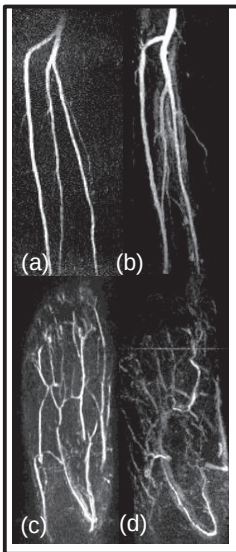

Figure 1. Examples of MRA in calf (a-b) and foot (c-d)**.** (a) and (c) were obtained from a healthy subject; (b) and (d) from a patient with diabetes and a foot wound (on the first digit - arrow). While (a) and (b) show similar patent arteries, (d) shows more diffusive arteries than (c).

Methods The new CF-MRA was recently developed and optimized for brain imaging (1). This technique allows simultaneous data collection for angiography, phase images, quantitative susceptibility mapping (QSM), and susceptibility weighted imaging (SWI) with only approximately 5-min scan of the whole brain. The sequence is a single 3D excitation interleaved rephrased/dephased multi-echo gradient-echo sequence. By subtracting the flow-dephased images from the flow-rephased images with the same echo time, a MR angiogram and venogrant (MRAV) can be created. The QSM data from the rephrased echo can be used to suppress veins on the MRAV to generate MRA. Unlike other CF-MRA, the new CF-MRA does not need ECG triggering. This is an important feature because ECG signal was not consistent in many individuals with diabetes who are overweight or obese, due to the increased subcutaneous fat and altered physiology, as well as prone to the interference by the strong magnetic field within a high field MRI system ($\geqslant$ 3T). We have performed a pilot study in healthy volunteers and patients with diabetes and foot ulcers. Each image session included both calf and foot imaging. CF-MRA was performed at rest and perfusion of one calf and one foot was performed at rest and during a standardized isometric contraction within the MRI bore. The MRI system was a 3 T trio system (Siemens Healthcare, Erlangen, Germany). The isotropic image resolution was 0.9 x 0.9 x 0.9 mm^3. The scan time for 72 mm length of calf was 6 min 14 sec and for 63 mm of foot was 4 min 15 sec.

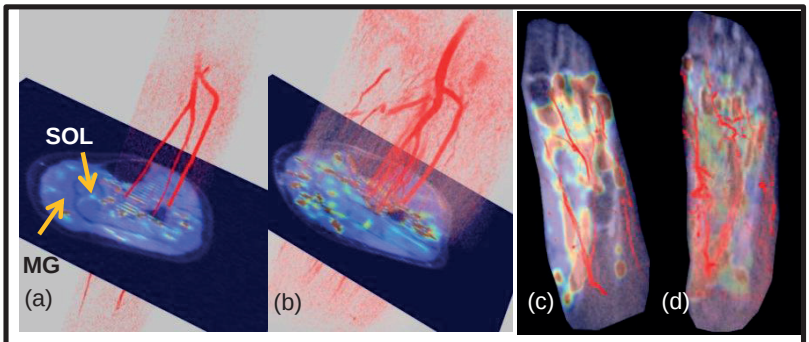

Figure 2. The display of 3D volumetric rendering of CF-MRA in a leg of healthy subject (a) and a patient (Fig. 1 (b)) with diabetes and a foot ulcer, integrating respective calf perfusion maps during an isometric exercise. The reader can view the 3D data from any angle. Both calf perfusion maps appear normal. The same type of display in feet in the same healthy (c) and patient (d) above, with perfusion maps during an isometric toe flexion exercise. MG= medial gastrocnemius; SOL= soleus

Results Figure 1 shows two sets of CF-MRA images in a foot and calf of one healthy (left) and one patients (right) with diabetes and a ulcer (big toe). While the vessels in both calves appear normal, the vessels in the diabetic foot show more diffuse and less signals compared to the healthy foot. Figure 2 shows the 3D display of integrated exercise perfusion maps and CF-MRA in the same subjects. Although the calf perfusion map of the patients with diabetes and an ulcer appear normal, relatively reduced overall exercise perfusion was observed in the patient's foot.

Discussion and Conclusion The ongoing pilot study demonstrates potentials of the new CF-MRA method for imaging arteries of lower extremities without using any ECG signals to trigger sequence for flow rephrase/dephase. Exercise perfusion distribution can be measured in the same imaging session, which is particularly important in patients with diabetes who are prone to peripheral arterial disease and perfusion deficit in their lower extremities. With the capability of simultaneous acquisitions of QSM and SWI, oxygenation images and vein images could be explored for more functional findings in this cohort of patients.

Reference. 1. Chen YS, Liu SF, Buch S, Hu JN, Kang Y, Haacke EM, Magn. Reson. Imaging, 2018, 47: 1 – 6.

Magnetic Resonance Imaging of Diabetic Feet – Going with the Flow

Jie Zheng, Mary K Hastings, Mohamed Zayed, Michael J. Mueller
Washington University School of Medicine, Missouri, Saint Louis, USA

Purpose Foot ulcers are the leading causes of hospitalization in patients with diabetes mellitus (DM). Tissue ischemia accounts for up to 50% of population with foot ulcers. Assessment of local perfusion and perfusion reserve in foot muscle is critical in understanding the status of ischemia in diabetic foot and corresponding therapeutic treatment effects. However, current clinical evaluation of pedal perfusion, such as ankle-branchial index (ABI), is indirect. The objective of this project was to use a new MRI compatible foot ergometer and develop MRI methods to characterize the local perfusion and perfusion reserve in diabetic foot with ulcers.

Methods Seven patients (age: 57±10 yrs) with diabetic foot ulcers (DM) and seven age and BMI (body mass index) matched participants without DM, foot ulcers, and history of cardiovascular diseases (non-DM) were prospectively recruited for this study. Using a new MRI compatible foot ergometer, all participants underwent MRI perfusion assessment at rest and during a standardized toe flexion exercise (**Fig. 1a**). The ergometer dynamically displayed the contraction pressures so that the participants can maintain exercise strength (**Fig. 1b**). The exercise lasted for 4 min with 20% of maximum voluntary contraction. The participants without DM were scanned twice on two different days to assess reproducibility of perfusion measurements. The measurement of local perfusion was performed using an arterial spin labeling method that was validated previously. Three slices were obtained to cover majority of foot intrinsic muscles.

Averaged perfusion maps over three slices were created using a custom-made software for all three slices (**Fig. 1d**). To facilitate the analysis of the ulcer location, a grids-eye map of perfusion with 6 segments per slice was created in a foot (**Fig. 1c,e**). To simplify quantitative analysis, the perfusion values within the medial and lateral regions of foot angiosome were calculated from respective segments, as well as perfusion values within segments immediately adjacent to a foot ulcer (peri-ulser) and segments away from a ulcer (away-ulcer). The perfusion reserve was calculated as the ratio of perfusion during flexion exercise to perfusion at rest. Bland and Altman methods were used to determine measurement repeatability and coefficients of repeatability (CRs) were calculated.

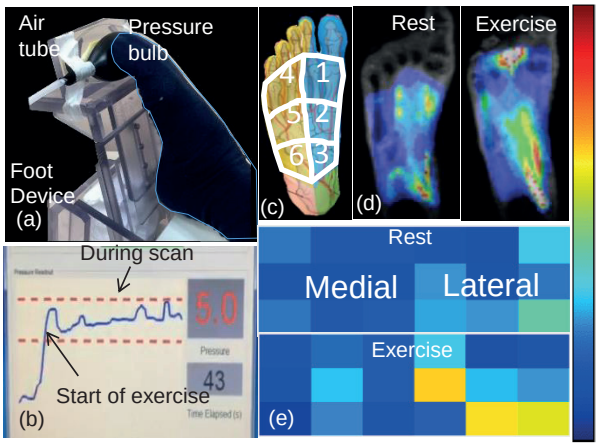

Figure 1. Photos of the foot ergometer device (a) and a screen shot of dynamic contraction pressure display (b). Angiosome of a right foot to show medial (blue) and lateral (yellow) regions that are segmented into 6 segments in one slice (c). Averaged perfusion maps over three slices of a foot in a non-DM participant at rest and during the toe-flexion exercise (d). The grid-eyes display of the entire foot perfusion distribution (e). Illustration of a grids-eye display of a total 18 segments for 3 slices. The color scale bar indicates 0 – 55 ml/min/100g.

Results The ABIs in non-DM and DM groups were 1.14±.08 and 1.12±.32, respectively. The perfusion reserves had the best reproducibility (CR in medial region: 1.6, lateral region: 0.9). The total perfusion reserve was significantly lower in DM compared to the non-DM (1.44 ± .30 versus 1.76 ± .31, *P* = .04) [**Figure 2 (a-b)**]. The exercise peri-ulcer perfusion was significantly lower (9.5 ± 3.7 ml/min/100g) than exercise away-ulcer perfusion (14.4 ± 2.9 ml/min/100g, *P* = .02). **Figure 2(c-d)** shows a foot ulcer case (arrow). The peri-ulcer exercise SMBF was 11.8 ± 5.3 ml/min/100g and SMBF reserve was 1.28. The foot ulcer of this patient healed 3 months after the MRI scan.

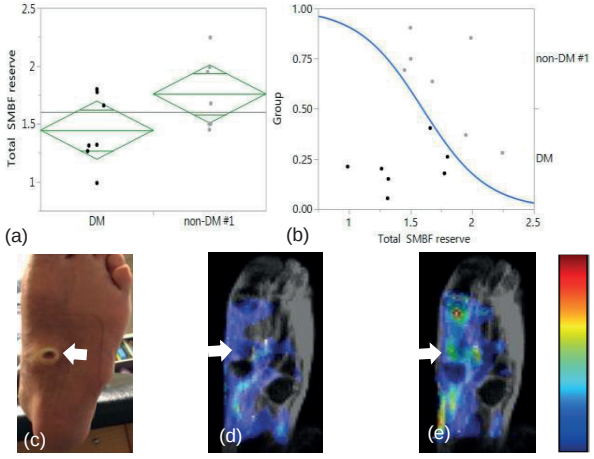

Figure 2. The 95% mean diamond plots for total perfusion reserve (a) and cumulative probability plot of the relationship between the total perfusion reserve and group membership (DM vs. non-DM) (b). The means of total perfusion reserves are significantly different between two groups. The photo of a left foot in a patient with DM and a ulcer located at the medial region. Averaged perfusion maps at rest (d) and during the toe-flexion exercise (e). The color scale bar adjacent indicates 0 – 55 ml/min/100g.

Discussion and Conclusion This pilot study demonstrated new methods for direct perfusion evaluation of feet with ulcers by contrast-free and exercise-based MRI for the first time. All patients performed the exercise study successfully and comfortably without any adverse incidents. The overall perfusion reserve in DM was significantly lower than that in non-DM. The ischemia region can be readily distinguished from normal perfused muscle region in the same foot by the assistance of grids-eye display. These methods are currently investigated with larger sample size in DM patients with foot ulcers.

Non-invasive lower limb angiography in a large health board – how low a radiation dose is achievable? Audit Update

P Douglas, G Roditi
NHS Greater Glasgow and Clyde, Scotland, UK

Purpose: Non-invasive angiography of the arterial supply to the lower limbs to identify stenotic or occlusive disease allowing planning of interventions is preferentially performed through MRA[1,2]. CTA is used where MRA is contraindicated or not tolerated. A previous 2011 audit in our health board revealed 70% of non-invasive lower limb angiography was performed using MRA and that 40% of patients who underwent CTA had no clear contraindication to MRA. Thus up to 80% of patients can be imaged with MRA. We set out to re-evaluate practise to ensure the radiation dose to our population can be kept "As Low As Reasonably Achievable" with appropriate imaging.

Methods; All non-invasive lower limb angiography performed in 2017 was evaluated including radiation dose for each patient. Where CTA was performed a determination was made as to whether this was justified according to the following previously used criteria:

- Metallic foreign body unsafe for MR
- Claustrophobia or other patient intolerance*
- Need for active monitoring (trauma, active haemorrhage, acute clinical deterioration etc)
- Dialysis or severe end stage renal failure precluding gadolinium contrast use

* Potential intolerance due to ischaemic rest pain was not considered a contraindication to MRA – it is good clinical practice that pain should be controlled to allow MRA.

Results: 1671 patients underwent angiography of the lower limbs in 2017. This marks almost a 50% increase from our first audit cycle in 2011; further analysis shows this is a year-on-year effect. Of these, 865 were MRA (51.8%) and 806 were CTA (48.2%). Of patients undergoing CTA then199 (52.1%) were justified according to the criteria above, a reduction from 60% at the first cycle. The average DLP for CTA was 1045.5 mGycm. When analysed by the origin of referrer, the proportion of MRA vs CTA shows a wide variation; outpatient clinics 76.1% MRA, inpatient wards 32% MRA and the Accident and Emergency department 4% MRA.

Discussion: The overall increase in number of patients undergoing non-invasive lower limb angiography and the proportion of CTA performed is likely to be related; changes to out-of-hours radiology service provision have resulted in a surge of additional CTA, and out-of-hours MRA is still not yet available. The trend towards CTA among in-patients is unfortunate, especially when considering that the quality of infragenitulate run-off (that is better evaluated with MRA[1,3)] is often a major factor when planning intervention in patients with critical limb ischaemia. To try and reverse this trend we propose ring-fenced in-patient MRA provision to a level commensurate with the demonstrated demand.

References

1. Young PM, Mostardi PM, Glockner JF, et al. Prospective Comparison of CAPR MRA with CTA for Evaluation of Below the Knee Runoff. Journal of vascular and interventional radiology : JVIR. 2013;24(3):392-399. doi:10.1016/j.jvir.2012.11.005.
2. Peripheral arterial disease: diagnosis and management NICE Clinical guideline [CG147] https://www.nice.org.uk/guidance/cg147/chapter/Recommendations#imaging-for-revascularisation
3. Owen, Andrew R, Iain R Robertson, Ganesan Annamalai, Giles H Roditi, Richard D Edwards, Lilian S Murray, and Jon G Moss. "Critical Lower-limb Ischemia: The Diagnostic Performance of Dual-phase Injection MR Angiography (including High-resolution Distal Imaging) Compared with Digital Subtraction Angiography." *J Vasc Interv Radiol* 20, no. 2 (2009): doi:10.1016/j.jvir.2008.10.014.

Ferumoxytol MRA in Haemodialysis Access Assessment : Pre- and Post-Surgical Findings - A Pictorial Review

A B Tan[1], S Stoumpos[1,2], P Hall Barrientos[1], M Hennessy[1], A Vesey[1], D B Kingsmore[1], R Kasthuri, P B Mark[1], A Radjenovic[2] & G Roditi[1]

1. NHS Greater Glasgow and Clyde, Scotland, UK 2. University of Glasgow

Purpose: Haemodialysis access options in renal failure patients include arteriovenous (AV) fistula, AV grafts and central dialysis catheters. The commonly used imaging modalities in planning dialysis access selection and its follow-up include ultrasonography and conventional venography, both have limitations. Contrast-enhanced cross-sectional imaging methods such as gadolinium contrast-enhanced MRA and CT angiography carry potential risks for patients with renal failure. Ferumoxytol is a superparamagnetic iron oxide nanoparticle preparation with the potential to circumvent these limitations when used for ferumoxytol enhanced MRA (FeMRA). Our aim in this pictorial review is to explain the principles of haemodialysis access methods and how FeMRA can be used to assess anatomical suitability of candidates and evaluate their post-surgical status and potentially predict access failure.

Methods: This pictorial review is based on a cohort of 50 patients enrolled in a prospective trial undergoing FeMRA as planning for haemodialysis access surgery with follow-up studies as appropriate in order to illustrate the following –

1 - The topography of the different types of haemodialysis access methods
2 - Assessment criteria in pre- & post-dialysis access creation and criteria for maturation
3 - Causes of non-maturation of dialysis fistulae and complications encountered in dialysis access surveillance
4 - The use of Ferumoxytol-enhanced Magnetic resonance angiography (FeMRA) for vessel mapping in dialysis access evaluation
5 - Correlation of FeMRA with conventional methods
6 - Technical difficulties in FeMRA performance and pitfalls encountered in FeMRA assessment

Results: An example of a radiocephalic fistula is presented in this abstract by way of illustration

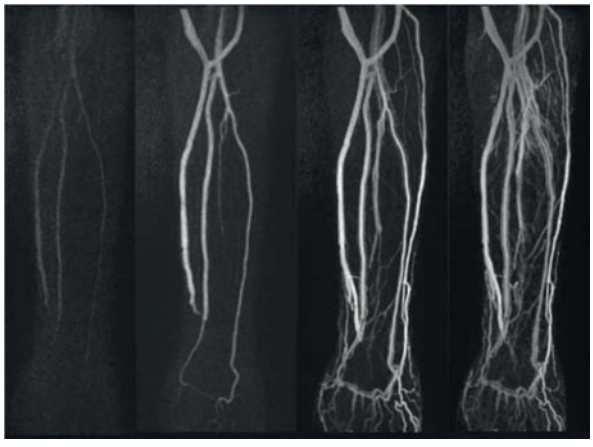

Fig 1. Dynamic Time Resolved Angiography depicting the flow of contrast through the fistula and forearm vessels over time.

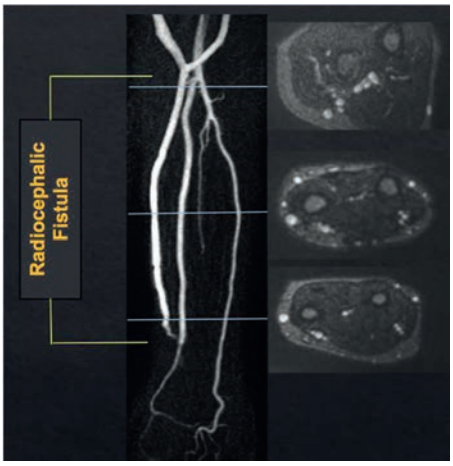

Fig 2. High resolution steady state imaging cross-sectional images at various levels through a radiocephalic fistula

Discussion: FeMRA is highly promising in the assessment of the arterial and venous vasculature both central and peripheral in a comprehensive fashion prior to and following haemodialysis access creation.

Safety profile of ferumoxytol as contrast for MR angiography in patients with chronic kidney disease

Sokratis Stoumpos[1,2], Pauline H Barrientos[3], Douglas Black[3], Martin Hennessy[3], Alex T Vesey[1], Ram Kasthuri[3], David B Kingsmore[1], Patrick B Mark[1,2], Aleksandra Radjenovic[2], Giles Roditi[3]

1. Renal & Transplant Unit, Queen Elizabeth University Hospital, Glasgow, UK
2. Institute of Cardiovascular and Medical Sciences, University of Glasgow, UK
3. Department of Radiology, Queen Elizabeth University Hospital, Glasgow, UK

Purpose: Ferumoxytol is increasingly reported as an alternative to gadolinium-based contrast agents for MR angiography (MRA), particularly for patients with chronic kidney disease (CKD). Ferumoxytol has a good safety profile[1,2], however hypersensitivity reactions have been reported leading to recommendations for a controlled intravenous infusion over at least 15 minutes. We determined immediate side effects of ferumoxytol when used as a contrast agent for MRA in patients with CKD.

Methods: A prospective cohort study investigating the utility of Ferumoxytol-enhanced MRA (FeMRA) for the assessment of vasculature in late-stage CKD (Clinicaltrials.gov identifier: NCT02997046) is currently recruiting in our centre. So far 107 FeMRA have been performed in CKD patients requiring imaging before listing for kidney transplantation or before vascular access creation for haemodialysis. A maximum dose of 3mg/kg of diluted ferumoxytol (1:5) was administered as divided controlled infusions (between 2 and 5 aliquots) at a rate of 1mL/sec and flushed by normal saline at the same rate. Patients were divided into 13 dose bands according to body weight using increments of 5kg up to a maximum dose of 300mg. Pulsed infusions were delivered with a minimum interval of 5-minutes between them to allow time for the different imaging components to be performed. The rate of infusion allowed for first–pass, dynamic and steady-state imaging components of a comprehensive angiography protocol to be performed. Patients were continuously monitored by pulse oximeter (measuring heart rate and oxygen saturation) while in the MRI scanner and had blood pressure measured before and after scanning.

Results: All patients completed their studies with no adverse events related to ferumoxytol administration. There was no significant change in the mean systolic (SBP) and diastolic blood pressure (DBP) (SBP 153±26 vs 158±24 mmHg, p=0.54; DBP 79±15 vs 78±13 mmHg, p=0.88 pre and post-ferumoxytol, respectively). The same was true for heart rate (75±8 vs 76±9 bpm, p=0.76 pre and post-ferumoxytol, respectively). Oxygen saturations remained unchanged for the duration of the scans. One patient experienced extravasation of the agent in the subcutaneous tissue as a result of poor intravenous cannulation and the scan was abandoned but there were no untoward effects from this.

Discussion: We observed no side effects of ferumoxytol when used for MR imaging in patients with impaired renal function, when approximately half the therapeutic dose is administered as controlled infusions at 1mL/sec of diluted solution.

References

1. Singh A, Patel T, Hertel J, et al. Safety of ferumoxytol in patients with anemia and CKD. *Am J Kidney Dis.* 2008;52:907–915.
2. Spinowitz BS, Kausz AT, Baptista J, et al. Ferumoxytol for treating iron deficiency anemia in CKD. *J Am Soc Nephrol.* 2008;19:1599–1605.

Title: Protocol time optimization: Institutional experience in clinically applied high-resolution intracranial vessel wall MRI

Authors: Laura Eisenmenger MD,[1] Lizhen Cao PhD,[1] Chengcheng Zhu PhD,[1] Christopher Hess MD, PhD,[1] David Saloner PhD[1] *1. University of California, San Francisco

Purpose: High-resolution intracranial vessel wall imaging (VWI) can provide valuable information not only about vascular morphology[1] but also about the presence or absence of vessel wall enhancement;[2-3] however, VWI acquisition times are often long, limiting the routine use in clinical practice. We sought to investigate the use of the VWI in routine clinical practice to evaluate not only its application within our institution, but also to optimize the imaging protocol to meet clinical needs.

Methods: A search was conducted of all studies obtained for routine clinical practice using the UCSF high-resolution intracranial vessel wall imaging protocol from 10/20/2015 through 10/19/2017. MRIs obtained for research purposes were excluded. The UCSF VWI protocol includes both pre- and post-contrast high-resolution 3D CUBE T1 weighted intracranial vessel wall images. Qualitative image quality was assessed for both pre- and post-contrast imaging using a four-point scale: 0 = non-diagnostic; 1 = vessel wall seen in part, diagnostic quality; 2 = vessel wall seen clearly in most parts, good image quality; and 3 = sharp vessel wall confidently delineated; excellent image quality. The images were also evaluated for the presence of vessel wall enhancement, detection of the vascular pathology on pre-contrast VWI alone, and detection of the vascular pathology on post-contrast VWI alone (dichotomized as either YES or NO).

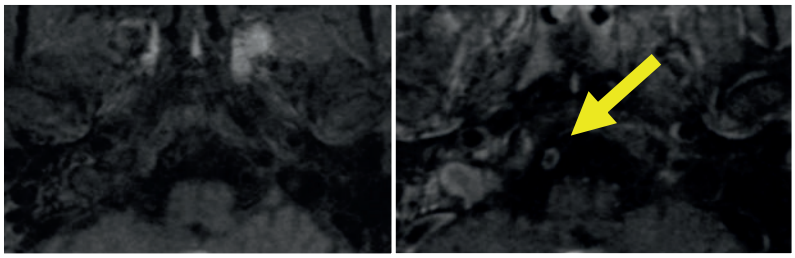

Figure 1: 75-year-old male with vertebrobasilar insufficiency. Pre-contrast high-resolution 3D CUBE T1- weighted VWIs demonstrated no significant pathology (left). However, post-contrast VWIs (right) showed right vertebral artery stenosis with enhancement of the vessel wall and atherosclerotic plaque (yellow arrow).

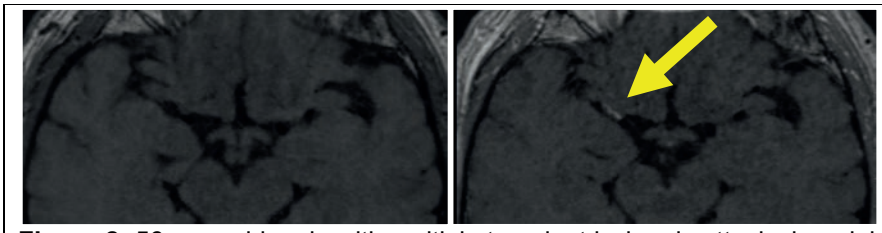

Figure 2: 56-year-old male with multiple transient ischemic attacks in a right middle cerebral artery (MCA) distribution. Pre-contrast high-resolution 3D CUBE T1- weighted VWIs showed no right MCA pathology. Post-contract images (right) showed eccentric, enhancing atherosclerotic plaque causing stenosis of the right MCA M1 segment (yellow arrow).

Results: During this 2-year period, 82 MRI examinations using the VWI protocol were obtained. Five patients had multiple examinations with 4 subjects having 2 scans and 1 subject having 5 scans. Some subjects had multiple areas of pathology yielding a total of 45 non-coiled aneurysms, 30 focal stenoses, 7 vessel occlusions, 5 coiled aneurysms, 2 pseudoaneurysms, 1 dissection, and 1 arteriovenous malformation. Eight of the examinations had no vascular pathology. There was no statistically significant quality difference between the pre- (2.75 ± 0.51) and post-contrast (2.78±0.52) VWI scans (p=0.53; paired t-test). Pre-contrast VWI detected the pathology in 62/74 MR examinations with disease. Post-contrast VWI detected the pathology in 71/74 examinations with only 3 cases not showing the pathology on the post-contrast scan (p=0.002). 81/82 of the scans did not benefit from the addition of pre-contrast imaging with one case of vertebral artery dissection showing intrinsic T1 hyperintensity on pre-contrast; however this could also be seen on the non-black blood routine T1 sequence.

Discussion: Our study found post-contrast VWI more often demonstrated the vascular pathology compared to pre-contrast VWI. We also found only one case that might have benefited from the addition of pre-contrast VWI; however, the addition of pre-contrast VWI would not have changed clinical management. This suggests that the routine use of pre-contrast VWI may not be needed to obtain the imaging necessary for diagnosis and patient management.

Conclusion: Routine use of pre-contrast VWI imaging may be unnecessary. Obtaining only post-contrast VWI would reduce acquisition times while providing the imaging necessary for diagnosis.

References:

1. Li ML, Xu YY, Hou B, et al. High-resolution intracranial vessel wall imaging using 3D CUBE T1 weighted sequence. Eur J Radiol. 2016 Apr;85(4):803-7. doi: 10.1016/j.ejrad.2016.01.014. Epub 2016 Jan 21.
2. Mandell DM, Mossa-Basha M, Qiao Y, Hess CP, et al; Vessel Wall Imaging Study Group of the American Society of Neuroradiology. Intracranial Vessel Wall MRI: Principles and Expert Consensus Recommendations of the American Society of Neuroradiology.AJNR Am J Neuroradiol. 2017 Feb;38(2):218-229. doi: 10.3174/ajnr.A4893. Epub 2016 Jul 28.
3. Mossa-Basha M, Shibata DK, et al. Added Value of Vessel Wall Magnetic Resonance Imaging for Differentiation of Nonocclusive Intracranial Vasculopathies. Stroke. 2017 Nov;48(11):3026-3033. doi: 10.1161/STROKEAHA.117.018227. Epub 2017 Oct 13.3.

A Morphology aided Diagnosis Network for Discrimination between Normal and Atherosclerotic Carotid Arteries on Black-Blood Vessel Wall MRI

Jiayi Wu[1,2], Jingmin Xin[1], Jie Sun[2], Dongxiang Xu[2], Xihai Zhao[3], Rui Li[3], Chun Yuan[2,3]
[1] Institute of Artificial Intelligence and Robotics, Xi'an Jiaotong University, Xi'an, China
[2] Department of Radiology, University of Washington, Seattle, USA
[3] Center for Biomedical Imaging Research, School of Medicine, Tsinghua University, Beijing, China

Purpose: Direct plaque imaging with black-blood (BB) vessel wall (VW) MRI has allowed for early detection of atherosclerotic changes in carotid arteries before luminal stenosis become apparent, providing valuable information for individual cardiovascular risk assessment and treatment planning [1]. Analyzing BB-VWMRI images slice by slice to identify carotid atherosclerosis will be tedious with moderate inter-reader reproducibility [2]. In this study, we propose a Morphology aided Diagnosis (MD) network to discriminate (diagnose) between normal and atherosclerotic carotid arteries on BB-VWMRI. Particularly, it is implemented by concatenating a morphology network for VW segmentation and a classification network for diagnosis, which is enhanced with the aid of morphological information from the morphology network.

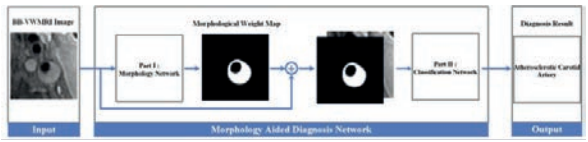

Fig. 1. The framework of the proposed Morphology aided Diagnosis (MD) network

Methods: The proposed MAD network combines the BB-VWMRI image with its morphological information (i.e., the shape of VW) to enhance the diagnosis performance. As shown in Fig. 1, the MD network includes two steps: 1) designing a morphology network to extract a weight map as morphological information from the original image, and 2) concatenating the corresponding weight map to the original image together as the multi-channel input to the classification network. As plotted in Fig. 2, in order to train a morphology network for the VW segmentation (i.e., weighting map embodying the shape information of vessel wall), we reuse the U-net [3] based network, in which a contracting path is constructed to capture context and a symmetric expansion path is built up to enable segmentation in pixel-to-pixel manner. And then, a classification network makes the final decision under multi-channel inputs as depicted in Fig. 3.

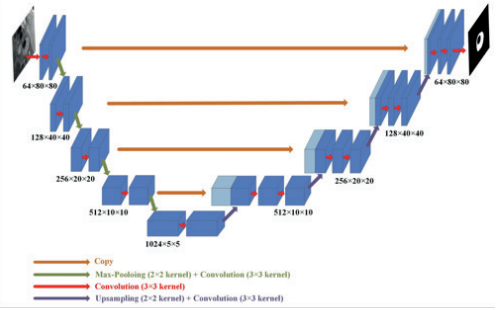

Fig. 2. The architecture of morphology network for morphological information

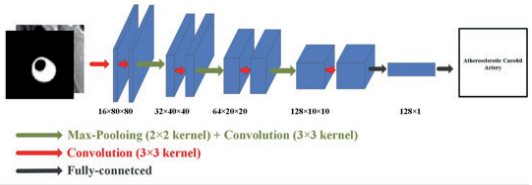

Fig. 3. The architecture of classification network for diagnosis

Dataset: The CAREII dataset is used to train and evaluate the discrimination performance of the proposed MD network. The CAREII dataset includes 1072 carotid MRI scans, which was collected from a previous multicenter cohort study on patients with recent cerebrovascular events that may or may not be of carotid origin. Each scan of this dataset includes around 16 axial slices of multiple contrast weightings, and only the T1-weighted MRI sequence of each scan is used in this study, while 965 scans are randomly used for training and 107 scans are for CAREII testing. In other words, 15117 images are prepared for training and 1375 images are used for CAREII test. In the carotid atherosclerosis diagnosis based on this dataset, type I-II lesions are indistinguishable from the normal vessel wall on MRI as demonstrated by the modified American Heart Association (AHA) [4]. Therefore, the slices with modified AHA type III-VIII lesions are defined as the atherosclerotic and the others are defined as normal in this study.

Results: In our study, an 80*80 pixels' square image lies in the manual center point of carotid artery lumen and is serves as the input of MD network. The prediction of diagnosis is evaluated with two metrics: the accuracy and the area under the receiver operating characteristic curve (AUC). Furthermore, the Pre-trained VGG16 [5] network is employed as the baseline. The proposed network is also compared with the single classification network without morphological information, shown in Fig. 3. The classification results on CAREII test dataset is shown in Table 1. Obviously, the proposed MD network has outperformed other traditional networks on test dataset. Some examples of input images from test dataset and the results obtained from our MD network are presented in Fig. 4, respectively. Meanwhile, the corresponding morphological weight map from morphology network and binary images are obtained through processing by a threshold of 0.5, and the ground truth are shown in Fig. 4. More pleasantly surprised, pixel-wise segmentation of carotid arteries vessel wall achieves 0.8607 (dice coefficient) on the test dataset.

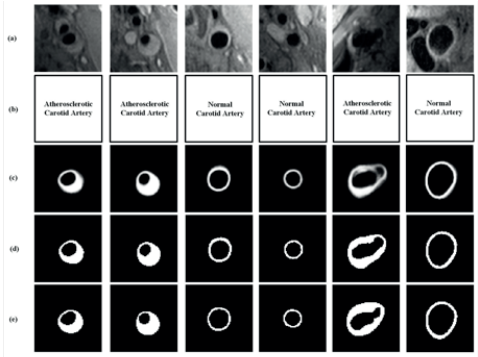

Fig. 4. Visualized images in the CAREII test dataset with our MAD network. (a) are input images. (b) are the outputs of our MAD network, namely diagnosis results. (c) are weight map from Morphological network, namely morphological information. (d) are binary images. (e) are ground truth of Morphological network.

Table 1. Comparison of diagnosis performance on CAREII test dataset. Bold is better.

Test datasets	Classification network	Accuracy	AUC
CAREII test dataset	Fine-tuning VGG16 network	70.04%	0.7269
	Single classification network	79.23%	0.8963
	Our MAD network	**88.58%**	**0.9557**

Conclusions: In this study, we proposed the so-called MAD network by utilizing BB-VWMRI image and its morphological information in the CNN to discriminate (diagnose) between the normal and atherosclerotic carotid arteries, where the weight map embodied with morphological information was derived from a morphology network, which reinforces the diagnosis performance. Different to the previous studies, which required the reviewer intervention, the proposed MAD network can automatically screen the atherosclerotic carotid arteries from the normal carotid arteries. Hence this network could be applied in the screening review to separate the normal carotid from atherosclerotic arteries.

Acknowledgements: The authors thank the participants and investigators of CAREII study.

References: [1] Zavodni, A. E., et al. Carotid artery plaque morphology and composition in relation to incident cardiovascular events: The multi-ethnic study of atherosclerosis (MESA). Radiology, pp. 271(2)-381, 2014. [2] Chu, B., et al. Reproducibility of carotid atherosclerotic lesion type characterization using high resolution multicontrast weighted cardiovascular magnetic resonance. JCMR, vol. 8, no. 6, pp. 793-799, 2006. [3] Ronneberger, O., et al. U-net: Convolutional networks for biomedical image segmentation. Proc. MICCAI. pp. 234-241, 2015. [4] Cai, J. M., et al. Classification of human carotid atherosclerotic lesions with in vivo multicontrast magnetic resonance imaging. Circulation, vol. 106, no. 11, pp. 1368-1373, 2002. [5] Simonyan, K., et al. Very Deep Convolutional Networks for Large-Scale Image Recognition. Computer Science, 2014.

An optimised subtraction approach for subtractive NCE-MRA techniques based on robust regression using the deviation angle

Hao Li[1], Shuo Wang[1], Andrew Nicholas Priest[1], Martin John Graves[1] and David John Lomas[1]
[1] Department of Radiology, University of Cambridge and Addenbrooke's Hospital, Cambridge, United Kingdom

Purpose: To develop an optimised subtraction method for Non-Contrast-Enhanced (NCE) MRA techniques, which can correct the intensity difference of background tissues between dark-blood images (DBIs) and bright-blood images (BBIs) and thereby improve the background suppression.

Methods: As shown in Fig.1, for conventional direct subtraction, the intensity value for a pixel is obtained by subtracting its intensity on DBIs from its intensity on BBIs, which is proportional to the distance between the point P(x, y) and the line of identity (green line) on the scatter map (d_1). However, the intensity of background tissue appears higher on BBIs than DBIs in most cases, which leads to residual background signal because there is still a considerable distance between the tissue and the line of identity (d_3).

In this study, a corrected regression line is obtained to replace the identity line. A robust regression model using iteratively reweighted least squares [1] is employed. Compared to the conventional ordinary least-squares regression (OLS) model, robust regression is more resistant to outliers (artery points in Fig. 1) far from model predictions. In particular, instead of using Euclidean distance (d_2), the deviation angle (θ) is used in the weighting function: $w = e^{-\theta^2}$.

The optimised subtraction approach was tested on multiple datasets including ten coronal femoral Fresh Blood Imaging (FBI)-MRA [2] datasets from five healthy volunteers, 26 coronal thoracic Flow-Sensitive Dephasing (FSD) - MRA [3] datasets (DANTE-bSSFP) from 26 healthy volunteers and ten coronal iliac FSD-MRV datasets (iMSDE-bSSFP) from seven healthy volunteers. All the images were acquired using a 1.5 T MRI system. The performance of the proposed robust regression model using the deviation angle (RRDA) was compared with conventional robust regression model using Euclidean distance (RRED) and OLS.

Results: Comparing RRDA to conventional direct subtraction, the vein, muscle and bladder to artery ratios in the femoral FBI-MRA reduced to 32.0%, 45.0% and 29.2% respectively; the artery, muscle and bladder to vein intensity ratios in the iliac FSD-MRV reduced to 92.4%, 62.2% and 70.6% respectively; the muscle and liver to artery intensity ratios in the thoracic FSD-MRA reduced to 61.9% and 82.7% respectively.

Fig. 2 shows two example results. It can be observed from B-C that the residual signal of veins (blue arrows) and other background tissue such as the bladder (yellow arrows) shown in the direct subtracted images (B) is suppressed more thoroughly in the angiogram obtained using RRDA (C). Similar results can be found in an example of a thoracic FSD-MRA shown in D-E. RRDA demonstrated robust performance in all cases, while the results using RRED were minor in some femoral FBI cases (A), and OLS was sensitive to the presence of outliers in some thoracic cases (D).

Conclusion: The optimised subtraction approach can correct the intensity difference between background tissues in BBIs and DBIs and thus improve the background suppression.

Reference: [1] Holland et al., Commun. Stat. - Theory Methods. 1977; 6(9), 813-827. [2] Miyazaki et al., J Magn Reson Imaging 2000; 12:776–783. [3] Priest AN et al., MRM 2012; 67:628–637.

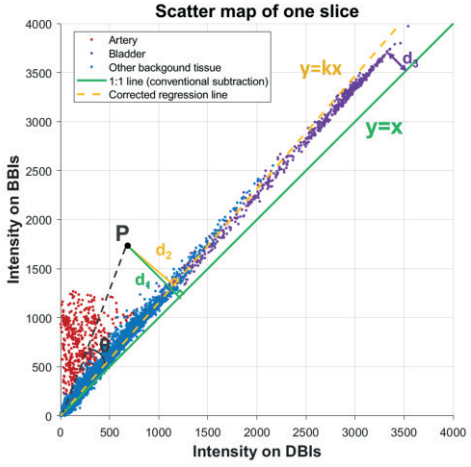

Fig.1 The scatter map of pixel intensities on DBIs and BBIs in one slice selected from a femoral FBI-MRA

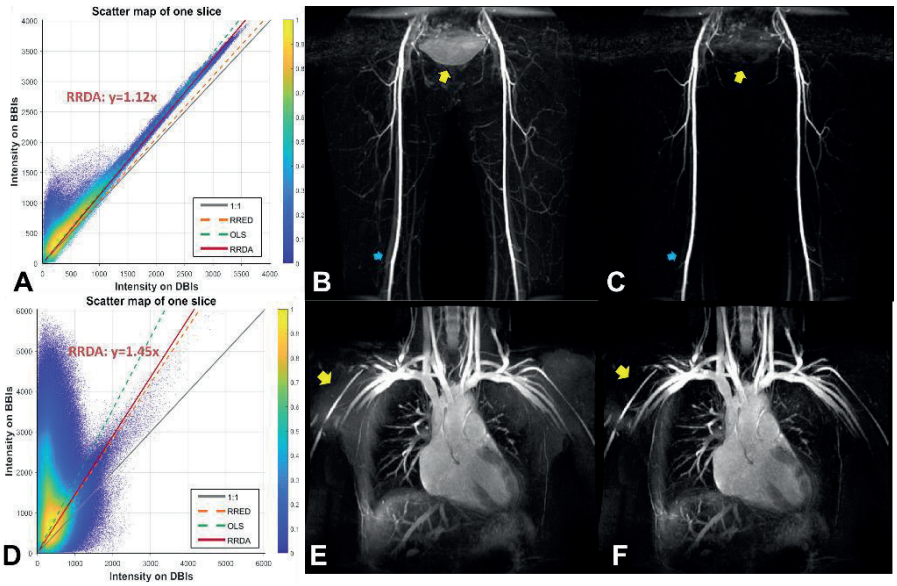

Fig. 2 Example images of femoral FBI-MRA and thoracic FSD-MRA. A and D: the scatter map with normalised density. B and E: the MIP of angiogram generated by direct subtraction. C and F: the MIP of angiogram generated by RRDA.

Simultaneous Multi-VENC Imaging with Dual-Echo Acquisition

Simon Schmidt[1], Sebastian Flassbeck[1], Mark E. Ladd[1], Sebastian Schmitter[1,2]

[1]Medical Physics in Radiology, German Cancer Research Center (DKFZ), Heidelberg, Germany, [2]Physikalisch-Technische Bundesanstalt (PTB), Braunschweig and Berlin, Germany

Purpose

Time-resolved unidirectional 2D phase-contrast (PC) MRI is a velocity imaging technique used to characterize hemodynamics in vivo. Since the velocity is obtained from a phase difference, at least two acquisitions with different first gradient moments (Δm_1) are needed, each lengthening the total acquisition time. Assuming the corresponding velocity noise to be linearly dependent on the velocity sensitivity $VENC = \pi/(\gamma|\Delta m_1|)$, low VENC values are typically desirable. Simultaneous Multi-VENC (SMV) imaging[1] excites a single slice multiple times for a single readout and thus enables the simultaneous encoding of that slice with multiple different velocity sensitivities. This allows higher temporal resolutions compared to the separate acquisition of low- and high-VENC data. However, an additional B0 map had been necessary so far to correct a phase bias within fat tissue. In this work, we combine B0 mapping with SMV by acquiring a second echo and demonstrate successful quantification in-vivo.

Methods

The excitation pulse of a standard gradient echo (GRE) sequence was replaced by three sinc-shaped pulses separated by bipolar gradients (Fig.1) in the slice direction ($TE = 9.79/6.33/3.37\ ms, TR = 16.5\ ms$). Three different first gradient moments ($23.5/11.8/0\ mT/m \cdot ms^2$) are thereby applied, corresponding to two different VENC values ($50/100\ cm/s$). Furthermore, a second echo was acquired with $\Delta TE = 3.78ms$. CAIPIRINHA[2] was applied to shift the field of view by $0\%/33\%/66\%$ for magnetization excited by the 1st/2nd/3rd pulse. Acquisition parameters: resolution = (1x1x5) mm³, FOV = 144x144 mm², cardiac triggering using ECG, 57 cardiac phases. The acquired data were separated by a slice-GRAPPA[3] algorithm using a separate GRE scan. For each cardiac phase the 6 resulting data sets (3 pulses & 2 echoes) were jointly reconstructed to determine velocities and ΔB0. Measurements targeting the femoral artery were performed at a 7T system (Siemens) with approval of the local ethics committee.

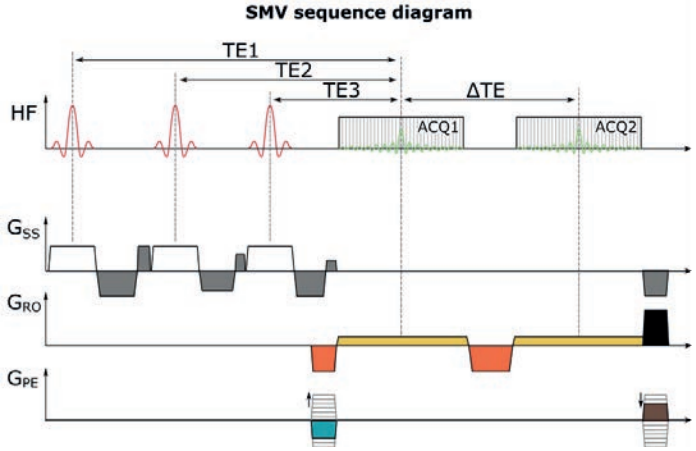

Figure 1: *Schematic sequence diagram of SMV encoding with bipolar gradients. Earlier pulses make use of all following gradients including the following slice-selection gradients to encode the velocity.*

Results

Fig. 2a-b shows the reconstructed velocity and ΔB0 map obtained from the SMV data for an exemplary cardiac phase in mid-systole. Within fat tissue, the phase bias from off-resonance effects can be separated from the velocity information, allowing correct velocity quantification in all tissues. Corresponding arterial peak velocities calculated over the entire cardiac cycle are illustrated in Fig. 2c in comparison with a standard PC-cine acquisition. Fig. 2d shows the corresponding Bland-Altman plot. The mean difference averaged over the cardiac cycle was 1.9 cm/s with a standard deviation of 0.7 cm/s.

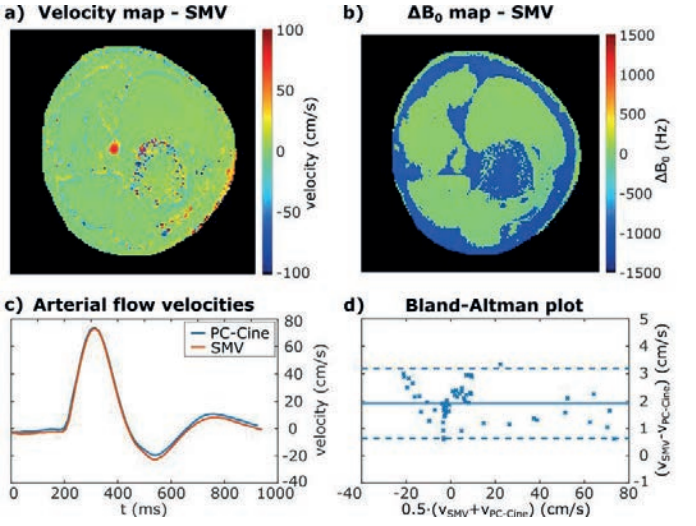

Figure 2: *a) Through-plane velocities and b) ΔB0 obtained with SMV imaging. c) Line plot of peak velocities in the femoral artery over the cardiac cycle. d) Bland-Altman plot illustrating differences between velocities obtained with SMV and PC-cine. The solid line illustrates the mean value of 1.9 cm/s and the dashed lines indicate the 95% confidence interval.*

Discussion

Acquiring a second echo enables a clear separation of phase contributions from velocities and ΔB0 within the SMV data. The echo times used in this work allow resolution of ΔB0 with a bandwidth of 3kHz, enabling correct velocity quantification within fat tissue at 7T (~1kHz offset). The quantified velocities are in excellent agreement with the PC-cine sequence and remaining differences are probably attributable to eddy currents that have not been corrected here.

References

[1] Schmidt et al.: Proc. 25th ISMRM 2017; [2] Larkman et.al.: JMRI 2001; [3] Setsompop et al.: MRM 2012

Motion-corrected coronary MR angiography and myocardial PET: initial clinical experience

Camila Munoz[1], Radhouene Neji[1,2], Karl P Kunze[3], Imran Rashid[1], Muhummad Sohaib Nazir[1], Stephan G Nekolla[3], René M Botnar[1], Claudia Prieto[1]

[1]School of Biomedical Engineering and Imaging Sciences, King's College London, UK; [2] MR Research Collaborations, Siemens Healthcare, UK; [3]Technische Universität München, Nuklearmedizinische Klinik und Poliklinik, Germany.

Purpose: Cardiac PET-MR has shown potential for the differential diagnosis and comprehensive assessment of several cardiac diseases[1]. However, image degradation due to physiological motion during long examinations remains a challenge for both imaging modalities. The purpose of this study is to demonstrate the benefits of a recently proposed respiratory motion-correction scheme for simultaneous coronary MR angiography (CMRA) and myocardial characterisation by PET[2] in different clinical contexts and with two different PET tracers.

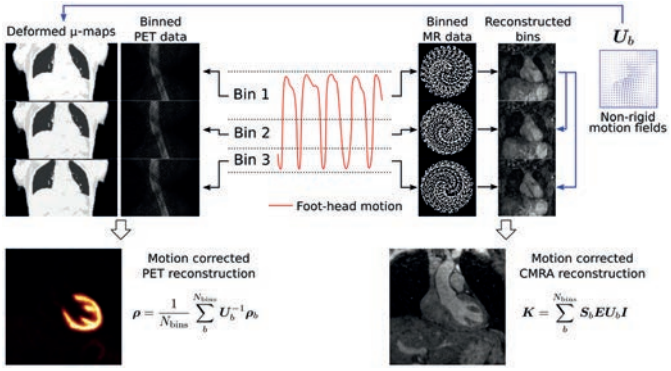

Fig1. Respiratory motion-corrected image reconstruction scheme for simultaneous whole-heart CMRA-PET.

Methods: The proposed PET-MR acquisition consists of an ECG-triggered free-breathing CMRA sequence simultaneously acquired with list-mode cardiac PET data[2]. The CMRA sequence is integrated with 2D image navigators, which are used for estimating foot-head and right-left motion of the heart in a beat-to-beat fashion. Respiratory motion fields estimated from MR data (2D image navigators and 3D data itself) are used to correct both the CMRA and PET datasets to the same reference position, so that after a short and efficient scan (no data rejection, thus 100% scan efficiency), respiratory-motion corrected co-registered PET and CMRA images are obtained (Fig1).

Fifteen patients were referred to our institutions for a cardiac PET-MR examination for different clinical indications and four are reported here in Table 1. Subjects were scanned in a 3T Biograph mMR scanner (Siemens Healthcare, Germany). The CMRA-PET data was acquired after injection of a Gadolinium-based MR contrast agent and either ^{18}F-FDG (viability or inflammation) or ^{13}N-Ammnonia (perfusion) PET tracer with the following MR parameters: resolution=1x1x2mm, FOV=304x304x96-104mm, TR/TE= 3.7/1.7ms, FA=15º, T2 preparation=50ms, fat saturation. Motion corrected (MC) and uncorrected (NMC) images were reconstructed for comparison purposes.

	Gender	Age (years)	Cardiac PET Protocol	Clinical Condition
P1	M	51	^{13}N-Ammonia Perfusion	Healthy Subject
P2	M	37	^{18}F-FDG Inflammation	Suspected Sarcoidosis
P3	M	58	^{18}F-FDG Inflammation	Chronic Total Occlusion LAD
P4	M	78	^{18}F-FDG Viability	Chronic Total Occlusion LAD

Table 1 Summary of 4 patient characteristics.

Results: Scans were successfully completed in all subjects. The average acquisition time for the PET-CMRA acquisition was 12.3±2.4 minutes. Improvements in the delineation of the left anterior descending and right coronary arteries can be observed after applying motion correction to the CMRA images (Fig2a). MC CMRA shows sufficient image quality for depicting the proximal coronary anatomy, in agreement with X-ray coronary angiography findings (Fig3, red arrow). In the cardiac PET images, motion correction enhances the visualisation of small structures such as the papillary muscles (Fig2b) and improves the delineation of myocardial defects, resulting in an improved agreement with LGE imaging (Fig3, blue arrow).

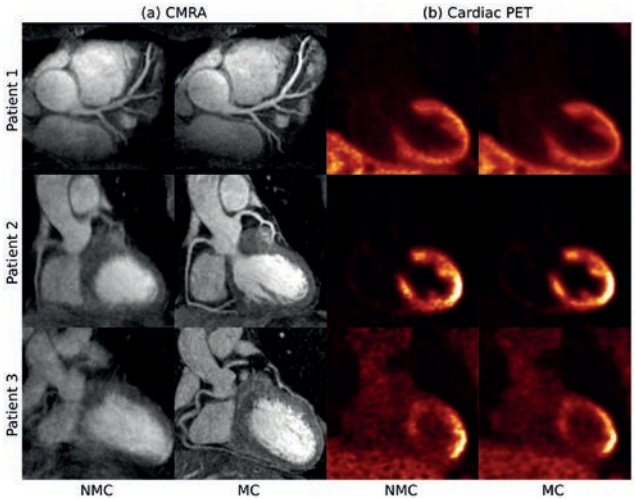

Fig2. Uncorrected (NMC) and motion-corrected (MC) (a) CMRA and (b) cardiac PET images for 3 patients. Patient 2 exhibits inadequate suppression of myocardial uptake.

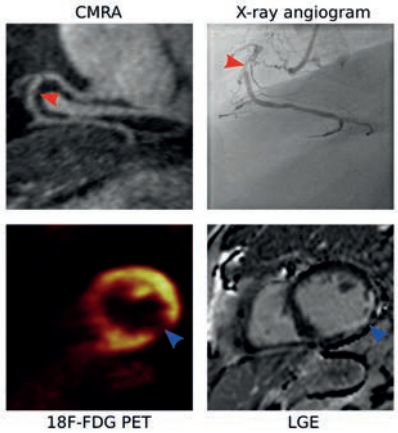

Fig3. MC CMRA and myocardial viability PET images, alongside with X-ray angiogram and LGE for Patient 4.

Discussion: We have tested a novel respiratory motion-corrected simultaneous CMRA-cardiac PET framework in a small cohort of patients with a range of cardiac pathologies and different PET tracers. For all subjects, MC CMRA allows for the depiction of both the right and left coronary arteries while MC PET shows improvement in the sharpness of the left ventricular myocardial wall and delineation of small features. The approach is robust and highly efficient, producing diagnostic images from both modalities in a short and predictable scan time, showing promise for its integration in clinical practice.

References: [1]Rischpler C, et al 2015. Semin Nucl Med 45(3):234-47. [2]Munoz C, et al 2018. MRM, 79(1):339-50.

XD-ORCCA: Optimized Respiratory-resolved 3D Cartesian Coronary MRA

Teresa Correia,[1] Imran Rashid,[1] Giulia Ginami,[1] Gastão Cruz,[1] Radhouene Neji,[1,2] René Botnar,[1] Claudia Prieto[1]
[1]School of Biomedical Engineering and Imaging Sciences, King's College London, London, UK
[2]MR Research Collaborations, Siemens Healthcare Limited, Frimley, United Kingdom

INTRODUCTION: Respiratory motion compensation remains a major challenge in free-breathing whole-heart coronary MR angiography (CMRA). 1D diaphragmatic navigator gating is commonly used to minimize respiratory motion. However, this approach leads to long and unpredictable scan times. XD-GRASP[1,2] has been recently proposed to provide respiratory-resolved 3D radial CMRA images over the whole respiratory cycle. This approach assigns the acquired data to multiple respiratory phases (or bins) and exploits Total Variation (TV) sparsity along the respiratory dimension to reconstruct the bin images. However, XD-GRASP has been shown to suffer from reduced image quality for Cartesian imaging.[3] Here, we propose a robust framework to provide high-quality respiratory-resolved Cartesian CMRA images. The proposed Optimized Respiratory-resolved Cartesian Coronary MR Angiography (XD-ORCCA) method incorporates translational motion information to increase the sparsity in the respiratory dimension. Additionally, 2D beat-to-beat translational motion information extracted from image navigators[4] (iNAVs) is used to minimize intra-bin motion. XD-ORCCA was tested on seven healthy subjects and three patients with cardiovascular disease and compared against XD-GRASP.

METHODS: Free-breathing acquisitions were performed on a 1.5T scanner (Siemens Magnetom Aera). 3D Cartesian[5] CMRA bSSFP acquisitions were performed using: coronal orientation, FOV = 320 x 320 x 80-104 mm^3, resolution = 1 x 1 x 2 mm^3 (1.2 x 1.2 x 1.2mm^3, for patients), TR/TE = 1.56/3.6ms, flip angle = 90°, T2 preparation (40ms), fat saturation, acquisition window ~100ms, acquisition time ~9-12min. For the 2D iNAV acquisition, 14 bSSFP startup echoes were used (same geometry). Patient 1) had a non-ischemic cardiomyopathy, 2) had previous stent deployment in the mid-distal segment of the right coronary artery (RCA) and 3) had sub-total occlusion of the RCA and moderate stenosis of the mid left anterior descending artery (LAD). Each undersampled bin is reconstructed using: 1) XD-GRASP and 2) XD-ORCCA. The respiratory-resolved images were obtained by solving the following optimization problems: 1) $\hat{\mathbf{x}} = \arg\min_{\mathbf{x}} \left\{\frac{1}{2}\|\mathbf{E}\mathbf{x} - \mathbf{k}\|_2^2 + \alpha \|\mathbf{x}_i - \mathbf{x}_{i+1}\|_1\right\}$ and 2) $\hat{\mathbf{x}} = \arg\min_{\mathbf{x}} \left\{\frac{1}{2}\|\mathbf{E}\mathbf{x} - \mathbf{b}\|_2^2 + \alpha \|T_i\mathbf{x}_i - T_{i+1}\mathbf{x}_{i+1}\|_1 + \beta \Psi_s(\mathbf{x})\right\}$, where $\mathbf{x}$ is the respiratory-resolved image series, $\mathbf{k}$ is the binned k-space data, $\mathbf{b}$ is the 2D translational corrected binned k-space data, Ψ_s is the 3D spatial TV function, α and β are regularization parameters, T_i is the translation transform that maps the bin image $\mathbf{x}_i$ to the reference image $\mathbf{x}_1$ (end-expiration) and $\mathbf{E}$ is the SENSE operator.

RESULTS: Reformatted respiratory-resolved images obtained with XD-ORCCA and XD-GRASP are shown in Fig. 1 for a representative healthy subject and in Fig. 2 for the three patients. In Fig. 1, images correspond to the bin that typically presents the least respiratory motion (end-expiration, phase 1) and the two bins with largest motion (phase 4 and phase 5, end-inspiration). Motion blurring is observed in XD-GRASP images, for subjects with more irregular breathing patterns. This is evident for the healthy subject and patients 1 & 2. Comparison against CT coronary angiography (CTCA) is shown in Fig. 3, showing excellent agreement for stenosis visualization. Note that a vasodilator (glyceryl trinitrate) was used for CTCA. Significant improvements in visible vessel length and sharpness were observed for XD-ORCCA in comparison to XD-GRASP for both coronaries in healthy subjects (Fig. 4).

DISCUSSION: Here, we present a robust and highly efficient respiratory-resolved motion-compensated framework for 3D Cartesian CMRA. XD-GRASP provides good-quality images in subjects with regular breathing patterns. However, motion blurring is observed in XD-GRASP images for respiratory phases with larger motion amplitudes and subjects with irregular breathing patterns. The proposed XD-ORCCA provides high-quality images for all respiratory phases, independently of the regularity of the breathing pattern.

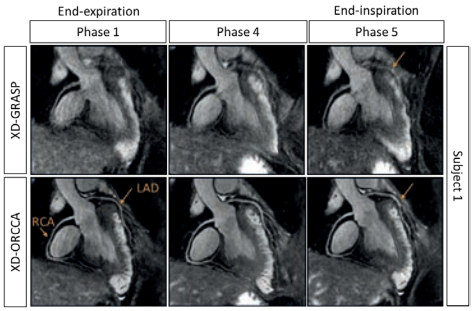

Fig 1. XD-GRASP (top) and XD-ORCCA (bottom) respiratory-resolved images (3 phases shown) for a healthy subject, showing the right (RCA) and left (LAD) coronary arteries. XD-ORCCA improves the visibility and sharpness of the coronary tree, particularly for respiratory phases that have more motion (arrows).

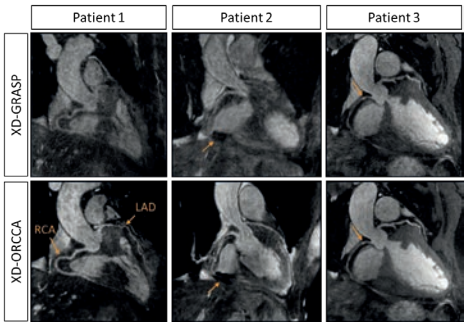

Fig 2. XD-GRASP (top) and XD-ORCCA (bottom) images (best bin), for 3 patients, showing the right (RCA) and left (LAD) coronary arteries. XD-ORCCA allows the visualization of both RCA and LAD, coronary stent in patient 2 and sub-total occlusion in patient 3 (arrows).

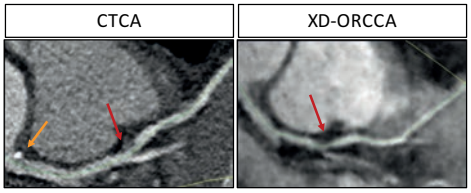

Fig 3. CT coronary angiography, CTCA, (left) and XD-ORCCA (right) images, showing the left coronary artery. Plaque calcification (yellow arrow) is visible in CTCA and stenosis is visible in both images (red arrows).

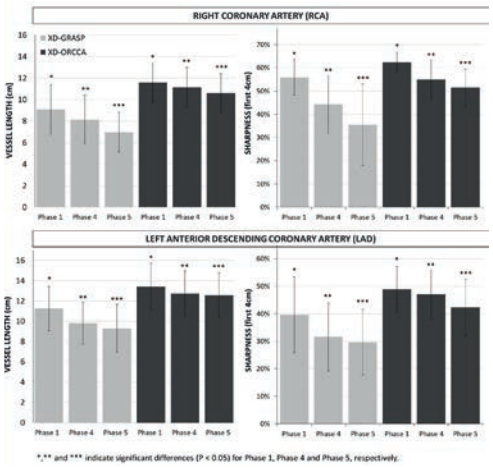

Fig 4. Metrics for seven healthy subjects for the XD-GRASP and XD-ORCCA approaches. Image quality was assessed by measuring the average visible vessel length and vessel sharpness of both coronaries.

References: 1. Feng L *et al.* MRM 2016; 75:775-788. **2.** Piccini D *et al.* MRM 2017; 77:1473-84. **3.** Feng L *et al.* ISMRM 2017; #1285. **4.** Henningsson M *et al.* MRM 2012; 67:437-445. **5.** Prieto C *et al.* JMRI 2015; 41:738-746. **Acknowledgments:** This work was supported by the following grants: EPSRC EP/N009258/1, EP/P032311/1, EP/P001009/1 and EP/P007619.

Quantitative myocardial perfusion using multi-echo Dixon for combined motion and T2* correction

Markus Henningsson[1], Alexandre Farias[1, 2], Cian Scannell[1], Adriana D.M. Villa[1], Torben Schneider[3], Amedeo Chiribiri[1]

(1) School of Biomedical Engineering and Imaging Sciences, King's College London, London, United Kingdom

(2) University of Minas Gerais State, Belo Horizonte, Brazil

(3) Philips Health Systems, London, UK

Purpose: Myocardial perfusion can be assessed using dynamic MRI during first-pass of a contrast agent. Quantitative perfusion is challenging due to (1) respiratory motion, precluding pixel wise quantification, and (2) non-linear relationship between MRI signal and contrast agent concentration. In this study, we investigate multi-echo Dixon acquisition for motion correction and arterial input function (AIF) estimation for first-pass perfusion.

Methods: *MRI acquisition:* The proposed acquisition strategy is shown in Figure 1, and consisted of spoiled gradient echo readout with three echoes per excitation pulse to enable water-fat separation using Dixon reconstruction. Imaging parameters were: Δx=2.3×2.3×10mm, FOV=360×300mm, TR/TE1/ΔTE=3.9/1.05/0.9ms, SENSE=2, partial Fourier=0.63, T_{acq}=143ms, saturation delay=100ms. The scan was performed at rest over 1 minute during free-breathing with a dual-bolus contrast injection of 0.075mmol/kg. 8 patients clinically referred for non-stress cardiac MRI assessment were recruited. *Motion correction:* Water and fat images were generated using Dixon reconstruction. The fat images were used to estimate respiratory motion using a rigid-body cross-correlation algorithm to calculate displacement and rotation for each frame. Motion correction was performed on the corresponding diagnostic water images by inverting the calculated rigid-body transformation for each frame. *AIF estimation:* For each echo, a region-of-interest was defined in the left-ventricle and T2* was estimated by fitting the mean intensity for each echo to $S(t)=S_0e^{(-TE/T2^*)}$, where S_0 is the signal without T2* decay. Example signal for the 3 echoes and T2* corrected AIF is shown in Figure 1. *Perfusion quantification:* Quantitative perfusion was estimated using Fermi model-based deconvolution to estimate myocardial blood flow (MBF). Quantification for performed using motion corrected and non-motion corrected perfusion images using the main bolus with and without T2* correction. The coefficient of variation of rest perfusion estimates was used to assess the effects of motion compensation on the homogeneity of rest perfusion values.

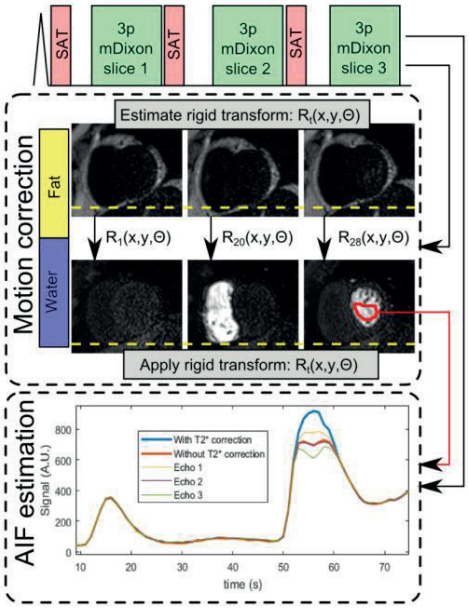

Figure 1. Multi-echo Dixon perfusion sequence, using saturation recovery. Three echoes were acquired for each slice to enable motion correction and arterial input function (AIF) estimation. The fat images were used to estimate respiratory motion for each frame to obtain rigid body motion parameters. The motion transformations were applied to the corresponding water images. A ROI in the left-ventricle was defined in the echo images, and the mean intensity at each echo was used to estimate the T2 corrected AIF.*

Results: Improved myocardial sharpness for the image averaged across the scan was obtained in all patients following motion correction. Mean MBF across all patients was 2.8±0.5ml/g/min without T2*-corrected AIF, and 2.1±0.3ml/g/min with T2*-corrected AIF. Motion correction yielded a mean coefficient of variation of 0.22±0.01, while no motion correction resulted in a coefficient of variation of 0.37±0.08. MBF for two patients, with and without respiratory motion correction are shown in Figure 2.

Discussion: Multi-echo Dixon can be used to address two of the main challenges of quantitative first-pass perfusion: respiratory motion and AIF estimation. Following water-fat separation, the fat images (which are unaffected by the contrast agent bolus) can be used to accurately track respiratory motion with simple and fast image registration techniques. The three echo images enable T2* correction of the AIF to improve quantification.

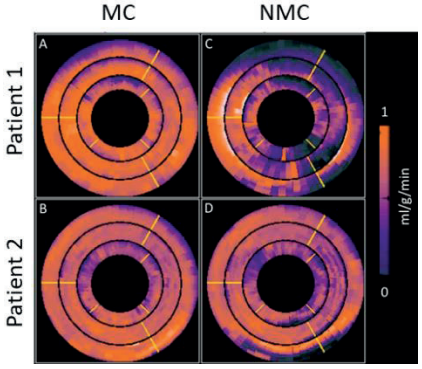

Figure 2. Quantitative perfusion maps from two patients demonstrating the effects of motion compensation in improving the quality of the results. Errors in quantification are evident as darker areas particularly at the epicardial border of each slice, which can be clearly seen in the non motion corrected (NMC) compared to the motion corrected (MC) images.

Particle swarm optimization for simultaneous T2 preparation and robust broadband fat suppression for coronary magnetic resonance angiography at 3T

Lionel P Arn[1], Ruud B van Heeswijk[1], Matthias Stuber[1,2], Jessica AM Bastiaansen[1]

1. Department of Radiology, University Hospital (CHUV), Lausanne, Switzerland; 2. Center for Biomedical Imaging, Lausanne University Hospital (CHUV) Lausanne, Switzerland

Purpose - To develop an adiabatic T_2 preparation (T_2-prep) [1] module using particle swarm optimization (PSO) [2,3] for blood-myocardium contrast enhancement and simultaneous broadband fat suppression.

Materials and Methods - The excitation and restoration pulse parameters (durations, frequency, amplitude and phase) of an adiabatic T_2-prep (Fig. 1A) [1] were optimized using PSO to develop a new adiabatic T_2-prep module (PSO-T_2-prep) that provides a large fat suppression bandwidth. Through Bloch equation simulations of the T_2-prep, the PSO minimized the following fitness function: $f = SD(Fat_{z,res} + 0.05) + SD(Wat_{z,exc}) + SD(Wat_{z,res} - 1)$, where SD means standard deviation, Fat_z and Wat_z are the fat (resonance frequency spanning from -600 to -200 Hz) and water (frequency = 0 Hz) longitudinal magnetizations, and subscripts *exc* and *res* stand for after excitation and restoration respectively. For each simulated tissue frequency, the B_1 strength was varied between 80% and 120% to search for B_1 insensitive solutions.

An ECG-triggered navigator gated 3D gradient echo imaging module was preceded by three different T_2-prep strategies: 1) the original T_2-prep, 2) the original T_2-prep with the addition of a CHESS [4] fat saturation pulse (T_2-prep+FS) and 3) the new PSO-T_2-prep. Data were acquired in healthy volunteers (N=7, age=29$\pm$4y) on a 3T MR scanner (Prisma, Siemens), using a 18 (6x3) channel chest coil. Sequence parameters: 1.4 mm^3 isotropic spatial resolution, 25 k-space lines acquired per T_2-prep, RF excitation angle 15°, TE = 1.97 ms, TR = 3.95 ms, bandwidth = 501 Hz/px, TE T_2-prep = 40 ms. The right coronary artery sharpness was measured using Soap-Bubble [5] and signal-to-noise ratio (SNR) was computed in compartments containing blood, myocardium, chest fat, and epicardial fat, in addition to blood-myocardium contrast-to-noise ratio (CNR). Noise standard deviation was computed in the background signal. Differences were tested via a Student's t-test for paired comparison, with a p-value < 0.05 considered as significant.

Results – PSO provides simple but non-intuitive modifications of pulse parameters (fig 1A) that predicts fat saturation bandwidth of 350 Hz (fig 1B, dashed arrow) for B1 strength variations from 70-120% (Fig 1B, black arrow). Compared to the T_2-prep+FS, the PSO-T_2-prep reduced chest and epicardial fat SNR by 53 % (p=0.011) and 45% (p=0.016) respectively in volunteers. No significant difference of blood SNR (p=0.51), myocardium SNR (p=0.43) and blood-myocardium CNR (p=0.61) was observed. The homogeneous suppression of fat signal increased vessel sharpness by 10.8%, although this difference was not statistically significant (p=0.11) (Fig. 2).

Discussion – Using PSO, a novel adiabatic T_2 preparation module was developed that provided robust fat suppression while preserving efficient T_2 preparation capabilities for coronary magnetic resonance angiography at 3T. Additional fat suppression such as CHESS was not needed as was previously used in a water selective T_2-prep [6].

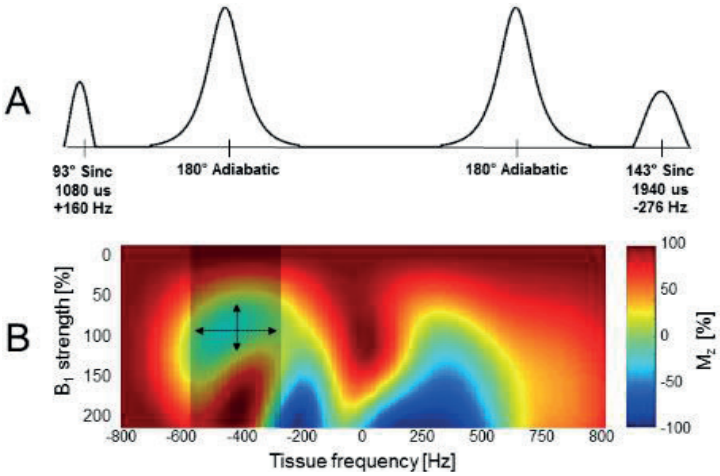

Figure 1. (A) Schematic of RF pulses used in the PSO-T_2-prep module. **(B)** Longitudinal magnetization as a fraction of the available magnetization after application of the PSO-T2-prep as a function of B1-strength and tissue off-resonance frequency. The shaded region indicates the frequencies that correspond to fat (-250 Hz to -600 Hz). The black arrows indicate the range of B1 strength where the -450Hz magnetization is within the ±10% range while the dashed arrow indicates the saturation bandwidth at B_1=100%.

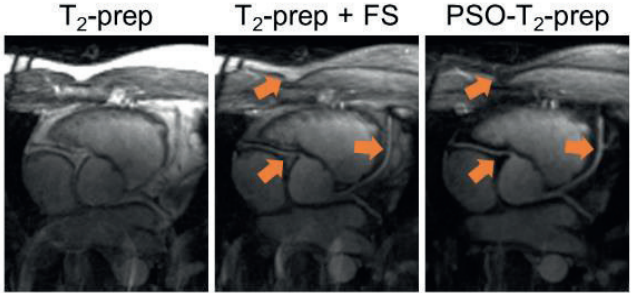

Figure 2. Representative in vivo image reformats simultaneously showing the right coronary artery, the left main, the left anterior descending coronary artery, and the left circumflex coronary artery using different fat saturation approaches. Arrows indicate locations of improved fat suppression using the PSO-T_2-prep. Images were reformatted using Soap-Bubble.

References [1] Nezafat R et al. Magn Reson Med 2006;55:858–864. [2] Kennedy J, Eberhart R, Particle swarm optimization. Proceedings of the IEEE International Conference on Neural Networks, 1995;1942–1948. [3] Clerc M, Standard Particle Swarm Optimisation. 15 pages. 2012. [4] Haase A et al. Phys Med Biol 1985;30:341–344. [5] Etienne A et al. Magn Reson Med 2002;48:658-666 [6] Coristine A et al. Magn Reson Med 2014;72:763–769.

Flexible, Semi-Projective MR Angiography using Cine FISS ASL for Combined Flow Quantification and Optimal Display of Arterial Anatomy

Robert R. Edelman[1,2], Jianing Pang[3], Ioannis Koktzoglou[1,4]

[1]Radiology, NorthShore University HealthSystem, Evanston, Illinois, United States, [2]Radiology, Feinberg School of Medicine, Northwestern University, Chicago, Illinois, United States, [3]Siemens Medical Solutions USA Inc, Chicago, Illinois, United States, [4]Radiology, Pritzker School of Medicine, University of Chicago, Chicago, Illinois, United States

Purpose: Recently, a new angiographic technique called cine FISS ASL (cFASL) was described which provides a potential alternative to phase contrast techniques for in-plane flow quantification, while enabling an efficient, visually-appealing, semi-projective display of blood flow patterns throughout the course of an artery and its branches [1]. We hypothesized that the combination of a radial k-space trajectory and cine acquisition might enable flexible trade-offs in spatial and temporal fidelity, depending on whether one wishes to optimally display arterial anatomy or measure flow velocity.
Methods: Breath-hold cFASL imaging of the coronary and renal arteries was performed in healthy volunteers at 1.5 Tesla (MAGNETOM Avanto, Siemens Healthcare, Erlangen, Germany). Each FISS module consisted of a series of 5 radial bSSFP readouts sandwiched between a pair of alpha/2 RF pulses, with gradient and RF spoiling applied between modules. Slice thickness ranged from ~3 to 36 mm, matrix = 160 to 192, FOV = 24 to 34-cm. 10 shots (i.e. number of heartbeats) were acquired per slice with 100 radial views ("high-frame rate" mode) for optimal flow velocity measurement (~12 to 35 msec per phase, 32 to 64 phases reconstructed) vs. 400 radial views ("high-quality" mode) for optimal vessel display (8 phases reconstructed). RF labeling was applied perpendicular to the aortic root for coronary MRA and through the descending aorta proximal to the vessel origins for the renal arteries.
Results: For the renal arteries, the entire length of the vessel including branches was seen in a single thick (e.g. 24-mm) slice in high-quality mode, whereas high-frame rate mode enabled measurement of in-plane flow velocity at any location along the vessel length (Figs. 1A-C). For coronary imaging, extensive vessel lengths (up to 9-cm) were visualized in each slice in high-quality mode (Fig. 1D), whereas flow velocity was measurable using frame-to-frame bolus displacement in high-frame rate mode.

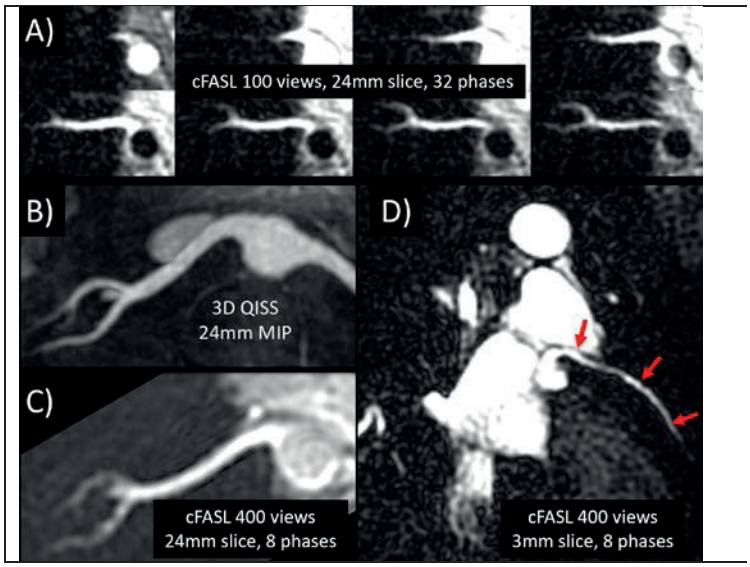

Fig. 1. *Examples of high-quality and high-frame rate modes for cFASL of the renal and coronary arteries. A) High frame-rate cFASL (8 of 32 phases shown) using 24-mm axial slice allows measurement of flow velocity in the right renal artery. B) Axial MIP from breath-hold 3D QISS MRA. C) cFASL in high-quality mode (1 of 8 phases shown) displays the entire length of the right renal artery. D) Oblique coronal cFASL in high-quality mode displays a long portion of the left anterior descending coronary artery (arrows).*

Discussion: Cine FISS ASL provides a flexible new approach for MRA that enables efficient demonstration of arterial anatomy as well as quantitative assessment of flow velocity. While the technique was applied to the coronary and renal arteries for this study, it should be readily applicable to any arterial system, including the intracranial circulation and peripheral arteries.

References: [1] Edelman RR, et al. J Cardiovas Mag Reson. 2018 Feb; 20(1):12.
Funding: NIH grants R01 HL137920, R01 HL130093, and R21 HL126015.

Altered Biventricular Myocardial Velocities in Patients During Year 1 After Heart Transplantation

Roberto Sarnari[1], Alexander Ruh[1], Julie Blaisdell[1], Ryan S. Dolan[1], Kai Lin[1], Kambiz Ghafourian[2], Jane E. Wilcox[2], Sadiya S. Khan[2], Esther E. Vorovich[2], Jonathan D. Rich[2], Allen S. Anderson[2], Clyde W. Yancy[2], James C. Carr[1], Michael Markl[1,3]

[1]Dept. of Radiology, [2]Dept. of Cardiology,[3]Dept. of Biomedical Engineering - Northwestern University, Chicago IL

Purpose: Acute allograft rejection (ACR) is a main cause of graft dysfunction and mortality during the first year after heart transplant (Tx): cellular infiltration can involve left (LV) and right ventricular (RV) myocardium during ACR episodes. Endomyocardial biopsy (EMB) is the gold standard technique for rejection monitoring at the expenses of invasiveness, cost and possible sampling errors.[1] Cardiac magnetic resonance imaging (CMR) is increasingly used as a complementary modality for post-Tx monitoring due to its capacity of acquiring a multi-parametric allograft evaluation.[2] However, altered post-Tx regional RV and LV motion compared to the normal heart and the impact of ACR episodes on RV and LV function is poorly understood. It was the aim of this study to apply CMR tissue phase mapping[3] (TPM, phase-contrast technique to measure 3-directional regional myocardial velocities) for the systematic assessment of biventricular myocardial velocities in patients during year 1 after Tx and age-matched healthy controls.

Methods: Twenty-two Tx patients (50±13 yrs, 14m) underwent a total of 44 CMR scans during the first year after Tx (8 patients had 1 scan, 9 had 2 scans, 2 had 3 scans, 3 had 4 scans). Average time of the baseline CMR after Tx was 101 ± 73 days. These 22 scans were used for comparison with 18 age-matched healthy controls (49±14 yrs, 12m). CMR was performed at 1.5T Siemens Aera/Avanto and included TPM[2,3] covering LV and RV at 3 short axis locations (base, mid, apex). Each TPM slice was acquired in a breath-hold (in-plane resolution=(2.0-2.3mm)^2; temp. resolution=20-24ms; venc=25cm/s, k-t acceleration with R=5). TPM data analysis included epi- and endocardial tracing and transformation of the acquired 3-directional velocities (v_x, v_y, v_z) in a LV/RV adapted coordinate system reflecting radial, circumferential, and long-axis motion (v_r, v_φ, v_z). Regional quantification of LV/RV velocities was based on an extended 16+10 AHA model and included the calculation of segmental systolic and diastolic peak velocities (v_r, v_z). Global biventricular velocities were calculated as average over all LV and RV segments, respectively. LV/ RV twist was quantified from the difference in circumferential velocities (v_φ) between base and apex. Based on EMB history, Tx patients presented with a total of 102 mild ACR (ISHLT grade 1R, 4.6±3.2 per patient, range 0-14) and 7 moderate ACR (grade 2R, 0.3±0.6 per patient, range 0-2) episodes. Correlations between LV/RV myocardial velocities and number of prior rejection episodes were evaluated from all 44 scans.

Table 1: Global biventricular velocities (18 controls vs. 22 Tx baseline scans)

* p<0.05, ** p<0.01		Left Ventricle		Right Ventricle	
		Controls	Tx patients	Controls	Tx patients
Peak v_r	systole	2.9 ± 0.4	3.0 ± 0.6	4.1 ± 0.9	4.3 ± 0.9
[cm/s]	diastole	-3.4 ± 1.1	-3.8 ± 1.0	-3.9 ± 1.0	-4.0 ± 0.8
Peak v_z	systole	**5.2 ± 2.1**	**4.0 ± 1.4 ***	**4.2 ± 1.3**	**3.0 ± 1.2 ****
[cm/s]	diastole	-3.8 ± 1.8	-3.9 ± 1.2	**-3.9 ± 1.3**	**-2.3 ± 1.1 ****
Peak twist	systole	2.6 ± 0.8	2.8 ± 1.0	2.8 ± 1.5	2.2 ± 1.4
[cm/s]	diastole	-3.2 ± 0.9	-3.0 ± 1.1	**-3.1 ± 1.6**	**-1.9 ± 1.0 ****

Figure 1: Long-axis peak velocities (extended 16+10 AHA model)

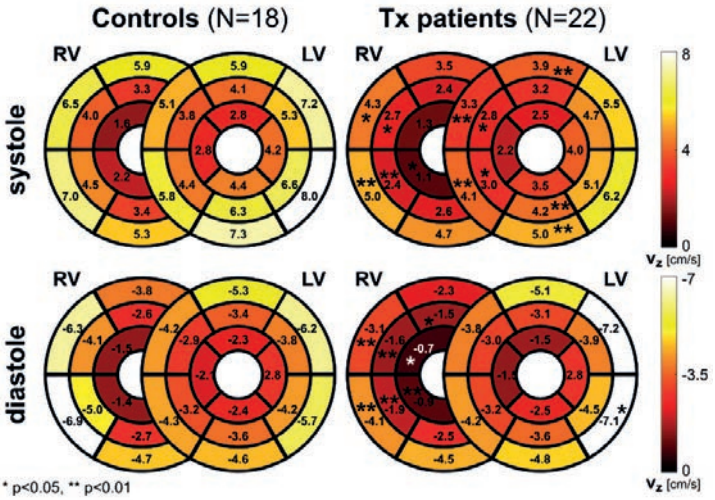

Figure 2: Correlation analysis in Tx patients between number of ACR episodes prior to CMR and myocardial velocities from 44 scans.

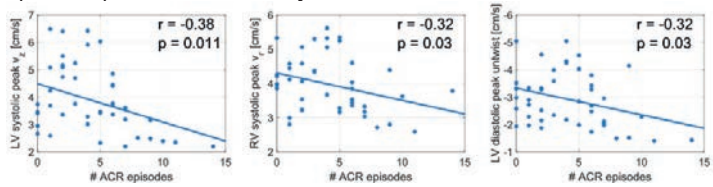

Results: As shown in Table 1, global peak velocities in Tx patients (baseline scan) were significantly reduced for LV and RV long-axis velocities during systole and for RV during diastole. RV diastolic untwisting also showed significant reduction compared to controls. At the segmental level, Tx patients showed significantly reduced biventricular systolic myocardial long-axis velocities and for RV segments during diastole (Fig 1). There were significant inverse relationships between increased number of rejection episodes and reduced LV systolic peak v_z (r=-0.38, p=0.011), RV systolic peak v_r (r=-0.32, p=0.03) and LV diastolic peak untwist (r=-0.32, p=0.03) (Fig 2).

Discussion: Long-axis peak myocardial velocities are reduced in LV and RV segments in the transplanted heart; especially, RV long-axis velocities may be a promising new parameter to monitor for transplant rejection. History of multiple rejections shows negative impact on LV and RV peak myocardial velocities and diastolic LV untwisting.

Acknowledgements: Grant support by NHLBI R01 HL 117888. **References:** 1. Costanzo MR et al. J Heart Lung Transplant. 2010;29:914-56. 2. Markl M et al. Magn Reson Med. 2013;70:517-26. 3. Jung B et al. J Magn Reson Imaging. 2006;24:1033-9.

A multimodality quantification of the influence of cardiac allograft vasculopathy on the coronary arteries and the myocardium

Ruud B van Heeswijk[1,4], Jessica AM Bastiaansen[1], Juan F Iglesias[2], Sophie Degrauwe[2], Samuel Rotman[3], Jerome Yerly[1,4], Giulia Ginami[1,5], Matthias Stuber[1,4], Roger Hullin[2]

1. Radiology; 2. Cardiology; 3. Clinical Pathology; 4. Center for Biomedical Imaging, Lausanne University Hospital (CHUV) Lausanne, Switzerland; 5. Biomedical Engineering, King's College, London, United Kingdom

Purpose - Cardiac allograft vasculopathy (CAV) occurs with a high prevalence after heart transplantation (HTx) and is a major cause of mid-term to late heart transplant failure.[1] CAV is characterized by concentric thickening of the inner layer (tunica intima) of the coronary vessel wall, which ultimately may result in reduced perfusion and oxygenation of the dependent myocardium. Unfortunately, routine X-ray coronary angiography (XRCA) diagnosis of CAV is in general limited to late-stage CAV, when treatment options are limited. The goal of this study was therefore to investigate whether the presence of CAV as diagnosed by XRCA or intima thickness as assessed by optical coherence tomography (OCT) is linked with the myocardial T_1 relaxation time or extracellular volume (ECV) by MRI, or interstitial fibrosis as assessed through histology of endomyocardial biopsies (EMB).

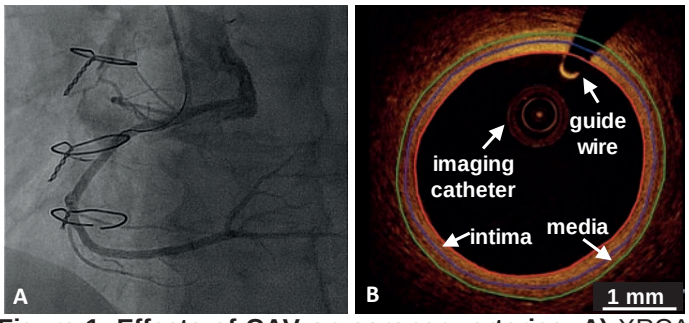

Figure 1. Effects of CAV on coronary arteries. A) XRCA does not show any significant lesions. **B)** A corresponding segmented OCT frame shows a thickened intima.

Methods - Routine XRCA and EMB as well as OCT were performed on the same day in stable HTx recipients (n=27) presenting for per-protocol control. CAV was graded on the basis of the XRCA in accordance with the ISHLT recommendations (0=not significant; 3=severe, Fig. 1A).[1] Quantification of interstitial fibrosis was based on Van Gieson's staining of the EMB (Fig. 2A) and automated image analysis. Intracoronary OCT was performed during automated pullback over 54mm at a radial resolution of 20µm and a frame density of 10frames/mm. The intima and media borders were manually traced and the ratio of the average thickness of the two layers (intima-media thickness ratio – IMTR) was calculated (Fig. 1B). Segments with atherosclerotic plaque were excluded from analysis. Pre- and post-Gadovist myocardial MRI T_1 mapping (breath-held MOLLI, Fig. 2B)[4] was performed in 2 short-axis slices at 3T (Siemens Prisma). The T_1 and ECV of the entire segmented myocardium were computed. A Student's t-test was used to establish whether the presence of CAV on XRCA is linked to differences in IMTR, EMB-based interstitial fibrosis, T_1 value, or ECV. A Pearson correlation was calculated to ascertain whether there is a link between the IMTR or fibrosis on the one hand, and the T_1 or ECV values on the other hand.

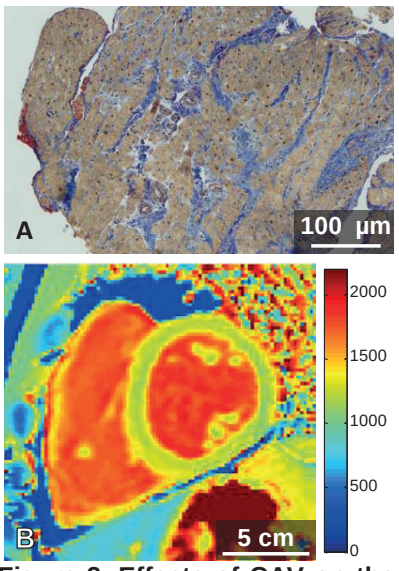

Figure 2. Effects of CAV on the myocardium. A) Histology of the EMB shows significant fibrosis (purple). **B)** A pre-contrast T_1 map with slightly but homogeneously elevated myocardial T_1.

Results – CAV was confirmed with XRCA in 4/27 patients, while 15/27 patients had IMTR>1. Both the T_1 relaxation time and ECV were significantly higher in patients with CAV (P=0.03 both). However, IMTR and fibrosis did not significantly differ between the groups with and without CAV (P>0.11). Interstitial fibrosis correlated significantly with the ECV (ρ=0.46, P=0.02) and showed a trend with the T_1 relaxation time (P=0.06), in accordance with previous reports on different cardiac pathologies.[5,6] IMTR correlated neither with the T_1 value nor ECV, but was associated with the amount of fibrosis (ρ=0.58, P=0.01).

Discussion –The present pilot study shows that T_1 values and ECV increase in HTx recipients with CAV as detected by XRCA, suggesting that MRI-based non-invasive detection of CAV has the potential to play a diagnostic role for the detection of CAV. The T_1 relaxation time is mainly influenced by the tissue water mobility, while ECV depends more directly on collagen deposition, which might explain the correlation of interstitial fibrosis with ECV. T_1 mapping enables a global assessment of the myocardium, albeit at a much lower spatial resolution than OCT, which is used to locally characterize the coronary artery wall. These differences may explain why T_1 and ECV values were not correlated with IMTR in this pilot study. However, the correlation between IMTR and EMB-based fibrosis suggests a link, which should be investigated further in a larger patient cohort. We therefore suggest that the results of this study merit evaluation in the context of a larger multicenter study.

References - 1. Mehra, J Heart Lung Transplant 2010 2. Khandhar, J Heart Lung Transplant 2013 3. Messroghli J Cardiovasc Magn Reson. 2017 4. Messroghli, Magn Reson Med. 2004 5. Fontana, J Cardiovasc Magn Reson 2012 6. S Nakamori, JACC Cardiovasc Imaging. 2017

Quantitative 4D CT DSA: A New tool for CT-guided Vascular Diagnosis and Intervention.

M Wagner*,**, Y Wu*, P Laeseke*, Y LI,* M Speidel*, S Leng#, Gabe Shaughnessy*, Fred Lee*,**,CM Strother*, and CA Mistretta*,**
*The University of Wisconsin Madison
Mayo Clinic, Rochester MN
**LiteRay Medical LLC

Purpose Modern CT scanners are capable of large volume coverage and continuous scanning at 2-3 rotations per second. Conventionally, each time point in a time-resolved CT scan is reconstructed from around 1000 projection images corresponding to ~0.33 to 0.5 seconds of data. The purpose of this work is to introduce a new X-ray CT method that makes use of the sparseness of the reconstructed objects to increase the temporal resolution for time resolved CTA (4D CT DSA), providing sufficient temporal information to allow estimation of vascular velocity and flow.
Methods The previously reported C-arm based 4D DSA technique [1] has been extended to CT where very high temporal resolution is available. This is achieved by performing a constrained back-projection to create a single 3D time frame for each projection image. Within this work, 30 3D CT volumes per second were reconstructed. Previously reported velocity and quantitation techniques [2] provided information required to extract vascular velocity and flow.
Results Color-coded flow images using the previously reported C-Arm 4D DSA technique are shown in Figure 1 where the results are compared with PC VIPR values obtained in a patient who had C-arm 4D-DSA and MRI studies.

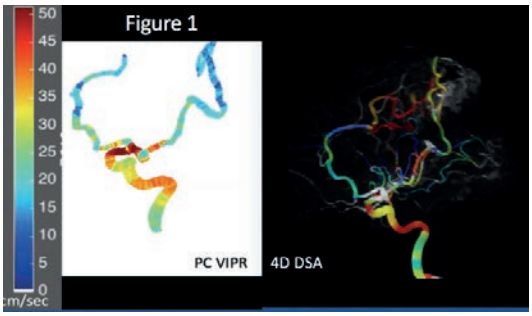

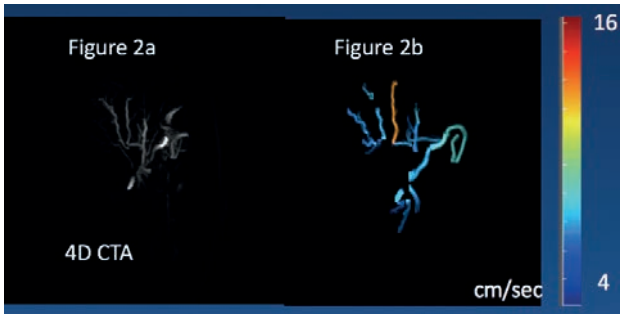

On a conventional CT scanner, results were obtained in pig hepatic arteries using intra-arterial injections and coronary arteries using the standard intravenous injection used for coronary CTA. Figure 2a shows a 4D CT DSA time frame of the hepatic arteries in a pig. Figure 2b shows corresponding color-coded velocity values. Figure 3 shows flow values in the major coronary arteries.

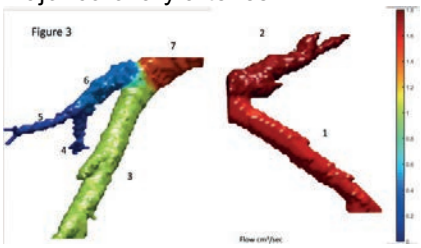

Discussion: The technique described here will be important when used in conjunction with the 250x dose reduced CT vascular fluoroscopy also reported in this conference and will enable, for the first time, CT-guided vascular interventions. At the present time, 3D anatomical information from coronary CTA studies are subjected to time consuming model-dependent CFD analysis to determine coronary flow reserve and cannot be completed while the patient is still in the scanner and available if an intervention is required. With 4D CT-DSA, flow reserve can be immediately determined from pre-and post-hyperemic injections in a model independent manner. At present time the only validation of the coronary flow determination is the continuity of flow at the bifurcations. Table 1 lists, in order, the independently measured flow values for the seven labelled branches in Figure 3. The flow is conserved to within 3% at the 4-5-6 bifurcation and 3.4% at the 7-6-3 bifurcation. This project is in its initial stage and further validation will be required.

Table 1

1	2	3	4	5	6	7
1.54	1.74	1.03	.30	.183	.47	1.45

A limitation of this study is that only non-hyperemic velocities were encountered. Hyperemic velocities in humans will be significantly higher and frame rates higher than 30 per second may be necessary. However, the technique can provide up to 2500 images per second to accommodate these higher velocities.

Synopsis The combination of 4D CT DSA and 250x dose reduced CT Fluoroscopy promises to open a new field of CT-guided vascular interventions not requiring combined CT/C-arm laboratories. There is potential for significant impact in interventional radiology and cardiology.

References **1** B Davis et.al Volumetric limiting spatial resolution analysis of four-dimensional digital subtraction angiography. J. Med. Imag. 3 (1), 013503 (January 25, 2016); 2. US Patent US2017/0076467 A1

Assessment of myocardial microvascular pathology using ferumoxytol-enhanced MRI and 3-compartment model of capillary level water exchange in patients with chronic kidney disease: comparison with healthy controls

D.Black[1], S.Stoumpos[1], M.Jerosch-Herold[2], N.R.Chatterjee[3], P.Gatehouse[4], G.Jayasekera[1], T.J.Carroll[5], D.Kingsmore[1], C.Berry[1], P.Mark[1], G.Roditi[1], A.Radjenovic[1]

[1]Institute of Cardiovascular and Medical Sciences, University of Glasgow and GGC NHS Trust, Glasgow, UK; [2]Harvard Medical School, Boston, USA; [3]Northwestern University, Chicago, USA: [4]Imperial College, London, UK; [5]University of Chicago, USA

Background: Patients diagnosed with chronic kidney disease (CKD) are not able to benefit from diagnostic imaging involving gadolinium based contrast agents (GBCA). Intravascular contrast agent ferumoxytol provides a potential alternative to GBCA for the diagnosis of cardiovascular pathologies in CKD. We have previously reported measurements of myocardial fractional blood volume and vascular-interstitial water exchange rate in a cohort of CKD patients[1]. In this report we present findings in a larger set of CKD patients and a control set of healthy volunteers.

Methods: Twenty two patients with severe CKD and eleven healthy volunteers (HV) were recruited following approval by two regional ethics boards (CKD - 14 male; median age 56 (28 - 75); BW = 77 ± 10 kg; BMI = 27 ± 6 kg/m^2; HV – 6 male, median age 30 (22 - 61); BW 88 ± 19 kg; BMI = 28 ± 5 kg/m^2).

CKD subjects were scanned on a 3T Prisma and healthy volunteers on a 1.5T Aera (Siemens Healthcare). All subjects received fractionated injections of diluted ferumoxytol (1:5), up to the maximal dose of 3mg/kg. T1 maps of the mid-ventricular left myocardium were acquired using a modified Look Locker inversion recovery method (MOLLI) before contrast and following each fractionated injection. $R1_{myo}$ and $R1_{blood}$ values (1/T1 [s^{-1}]) were recorded at each step. Three-compartment 2-exchange sites model [2] was used to estimate fractional blood volume (FBV, unit free fraction), vascular-interstitial exchange rate (k_{vi} [s^{-1}]) and their product FBV* k_{vi} (proportional to permeability surface area product (PS, [s^{-1}])). Model assumptions included a fixed extracellular volume (ECV) of 0.3 for CKD patients and a lower value of 0.25 for controls. Intracellular water lifetime of 100 ms was assumed in all subjects. Non-parametric Mann Whitney and Kruskal-Wallis tests were used to assess the differences in model parameters.

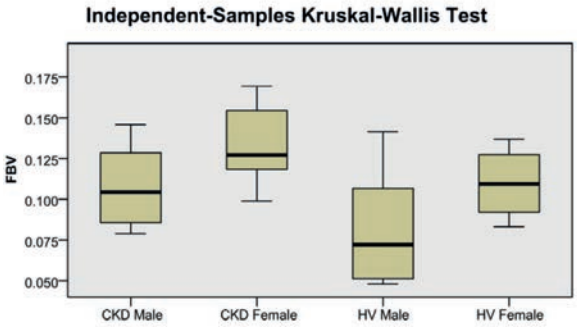

Figure 1. Myocardial fractional blood volume (FBV) is elevated in females, in both CKD and control (HV) subjects.

Results: In CKD subjects, FBV estimated using a 3-compartment model was 0.13 ± 0.03, compared to 0.09 ± 0.03 in healthy volunteers (p = 0.063).
The distribution of estimated vascular-interstitial exchange rates k_{vi} (5.9 ± 2.2 s^{-1} vs 13.8 ± 10.4 s^{-1}) and PS (0.67 ± 0.23 s^{-1} vs 1.04 ± 0.51 s^{-1}) varied significantly between CKD and HV subgroups. (Mann Whitney p = 0.029 and 0.04, respectively).

In four subject subgroups (CKD Male (n = 14), CKD Female (n = 8), HV Male (n = 6) and HV female (n = 5), there was a significant difference in FBV (Kruskall-Wallis test for differences between four subgroups: p = 0.027). There were no gender differences in other two model parameters.

Discussion: Our results suggest that patients suffering from chronic kidney disease appear to have reduced vascular-interstitial exchange rate and lower permeability surface area product than well matched healthy controls. FBV values showed no statistically significant differences between the CKD and control group, although we observed pronounced gender differences that are present both in health and disease (Figure 1). CKD patients seem to have largely preserved (if not elevated) resting myocardial fractional blood volume compared to sex-matched controls. The differences in water exchange rates between the interstitial and vascular compartment and permeability surface area product point to the possible alterations in the architecture and function of capillaries supplying the myocardial tissue in patients with CKD. Given that FBV is expected to correlate with microvascular surface area, reduced values of PS with preserved (or elevated) FBV suggest the reduction in blood vessel permeability.

Conclusion: Although our sample size is small, and two sets of data were acquired using slightly different acquisition protocols, the results presented here strongly suggest that ferumoxytol enhanced MRI has the potential to provide a unique insight into the nature of microvascular pathology in CKD and other diseases affecting myocardium, with particular relevance to mechanisms of drug delivery and monitoring effects of therapies.

References: [1] D. Black et al, Proc SMRA 2018; [2]. Spencer RGS, Fishbein KW. J Magn Reson 2000;142:120–135

Non-Contrast Enhanced Simultaneous Bright- and Black-Blood 3D Whole-Heart MRI in Patients with Congenital Heart Disease

Giulia Ginami[1], Israel Valverde[1,2], Louisa O'Neill[1], Imran Rashid[1], Radhouene Neji[1,3], Alessandra Frigiola[1], Rene M. Botnar[1], Claudia Prieto[1]

[1]*School of Biomedical Engineering and Imaging Sciences, King's College London, London, United Kingdom*
[2]*Hospital Universitario Virgen del Rocio, Seville, Spain*
[3]*MR Research Collaborations, Siemens Healthcare Limited, Frimley, United Kingdom*

Introduction: Congenital heart disease (CHD) represents one of the most common types of birth defect; with recent improvements in diagnosis and treatment, more infants presenting with CHD are expected to reach adulthood. CHD can involve different cardiac structures, including the aorta, pulmonary veins, atrial and ventricular cavities, as well as the coronary circulation. Cardiovascular MRI plays an important role in the diagnosis and follow-up of CHD; while contrast-enhanced (CE) bright-blood acquisitions are typically performed to visualize the great vessels and the coronary course, black-blood images may be preferable for the depiction of the cardiac valves as well as of the atrial and the ventricular septum. However, resolution and volumetric coverage are usually limited with these approaches due to the associated long scan times. Moreover, the reliance on intravenous administration of Gadolinium (Gd)-based contrast-agents for the CE bright-blood image is not ideal, especially for CHD patients where repeated scans are usually required to monitor progress. In this work, we present a novel non-contrast enhanced simultaneous bright- and black-blood 3D whole-heart imaging sequence for CHD assessment. Such sequence operates in free-breathing with 100% respiratory scan efficiency (no data rejection) and predictable examination time. The approach was tested in adult patients with CHD.

Methods: The proposed framework consists of a 3D whole-heart phase sensitive inversion recovery (PSIR)-like sequence for simultaneous bright- and black-blood imaging (BOOST) that is similar to that described in [1] (Fig1). In order to ensure high quality depiction of both the arterial and the venous systems, magnetization transfer contrast (MTC) is exploited here. The sequence acquires two differently weighted bright-blood volumes, MTC-IR BOOST (designed for anatomy visualization), and MTC BOOST (required for PSIR computation) both preceded by a low-resolution image-based navigator (iNAV) [2] for 2D translational respiratory motion estimation/compensation. A non-rigid motion correction strategy is exploited in order to further improve image quality [3]. MTC-IR and MTC BOOST are then combined in a PSIR reconstruction [4] to obtain a complementary and co-registered black-blood volume (PSIR BOOST). Data acquisition was performed on a 1.5T MR system (Siemens Magnetom Aera) in 6 patients (3 males, 34±15 years) presenting with CHD. Imaging parameters for the proposed 3D whole-heart Cartesian sequence [5] included: coronal orientation, spatial resolution: 1.4x1.4x2.8mm (reconstructed to 1.4mm isotropic), field of view FOV: 320x320x90-120mm, TE/TR: 1.4/3.6ms, pixel bandwidth: 1395 Hz/Pixel, flip-angle: 90°, inversion time TI: 140ms, nominal predictable acquisition time ~7min. MT-preparation consisted of 15 Gaussian pulses (flip-angle: 800°, pulse duration: 20.48ms, off-resonance frequency offset: 3000Hz, pause between pulses: 1.5ms). A T_2-prepared CE bright-blood 3D acquisition was performed with similar imaging parameters for comparison purposes after injection of 0.2 mml/kg of a Gd-based contrast agent in one case.

Results: The proposed sequence provided high quality depiction of cardiac anatomy without the need for contrast agent administration (Fig2). A sharper delineation of the pulmonary veins was obtained in comparison to the CE clinical sequence (Fig3). Effective blood signal suppression was achieved in the black-blood PSIR reconstruction.

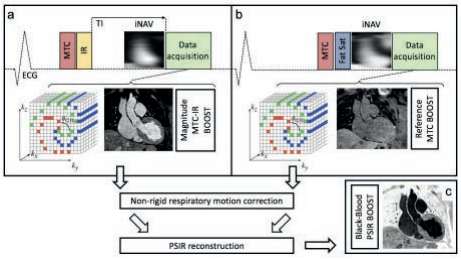

Fig.1: Two differently weighted bright-blood volumes (MTC-IR in a, MTC in b) are acquired and combined in a PSIR reconstruction to obtain a complementary black-blood volume (c).

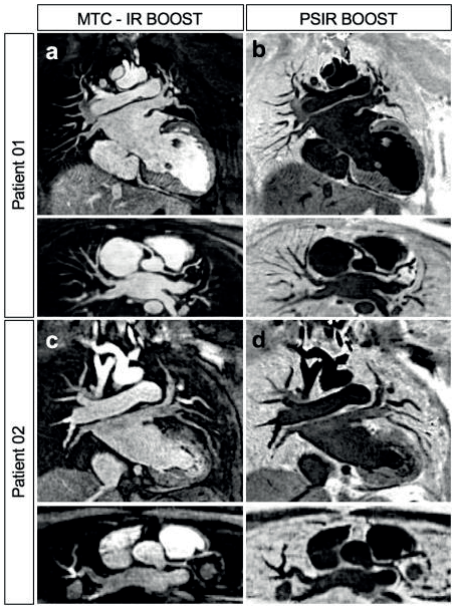

Fig.2: BOOST bright- (a,c) and black-blood (b,d) 3D whole-heart acquisitions in two patients without endogenous contrast agent.

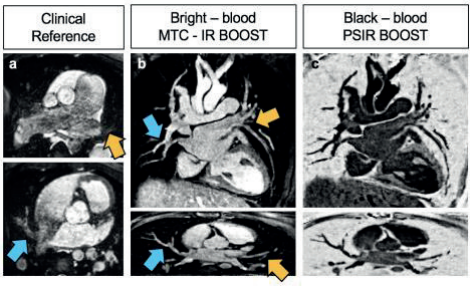

Fig.3: Despite the use of contrast agent, pulmonary veins are poorly depicted in the clinical sequence due to the use of T2-preparation (a, arrows). Conversely, BOOST provides contrast-free sharp depiction of both arteries and veins (b – bright-blood, arrows – and c – black-blood).

Conclusion: The proposed sequence provides simultaneous bright- and black-blood 3D whole-heart images and was successfully tested in a small cohort of patients with CHD. The use of MTC resulted in high-quality depiction of both the arterial and the venous system. The sequence operates without the need of contrast agent administration, which makes it particularly suitable for the monitoring of patients over time. The framework will be integrated with acceleration techniques in order to improve acquisition times and spatial resolution. This will ultimately lead to a broader clinical validation.

References: [1] Ginami G et al, MRM 2017; [2] Hennigsson M et al, MRM 2012; [3] Cruz G et al, MRM 2016; [4] Kellman P et al, MRM 2002; [5] Prieto C et al, MRM 2015.

Native T1-rho mapping: An alternative to ECV for detection of diffuse myocardial fibrosis? A Clinical Study in 219 Patients

Martijn Froeling, Csilla Celeng, Tim Leiner
Department of Radiology, Center for Imaging Sciences, Utrecht University Medical Center, Utrecht, The Netherlands

Background

T1-rho is the spin lattice relaxation time measured using a long continuous spin-lock RF pulse, which is applied aligned with the spins. Native T1-rho mapping is sensitive to low-frequency interactions between water and macromolecules and may be an attractive technique for detection of myocardial interstitial fibrosis without the need for exogenous contrast agents[1].

Materials and Methods

Between January 2015 and January 2017 we enrolled 219 patients [87 F, 132 M; mean age 48±18] referred for evaluation of suspected or known non-ischemic cardiomyopathies. The study was approved by the medical ethics committee and written informed consent was obtained from all participants. All patients underwent T1-rho mapping on a 1.5T clinical MR system (Ingenia, Software Release 5.1.7, Philips Healthcare) using the following imaging parameters: TR/TE, 3.5/1.75 ms; flip angle, 35 degrees; BW/pixel, 723 Hz; FOV, 288 x 288 mm2; slice thickness, 8.0 mm; in-plane spatial resolution: 2.0 x 2.0 mm2; SENSE parallel imaging factor 2; 8 startup echoes and spin-lock amplitude of 500 Hz. Acquisition time was 3 breath holds (approximately 45 s in total). After acquisition was completed T1-rho images were transferred to a dedicated workstation for motion correction and standardized post-processing. Results of T1-rho mapping were compared with the results of native and post-contrast T1 mapping as well as extra cellular volume fraction (ECV) measurements. Spearman correlation coefficients were calculated to determine the correlation between ECV and whole heart T1-rho values, native T1-values and post-contrast T1-values.

Results

T1-rho and ECV maps were successfully obtained in all 211 patients. 189 datasets were of sufficient quality for automatic processing. Mean T1-rho relaxation time was 64.0 ± 5.0 ms. Mean native T1 was 1094 ± 56 ms, mean post-contrast T1 was 390 ± 58 ms. ECV values ranged between 5-47%, with a mean value of 25.2 ± 8.0%]. A strong and significant correlation was found between T1-rho relaxation time and ECV fraction (Spearman coefficient: 0.63, p<0.001, figure 1). Weak correlations were found between native T1 and ECV fraction (0.31, p<0.001, figure 2), and post-contrast T1 (-0.26, p<0.01, figure 3).

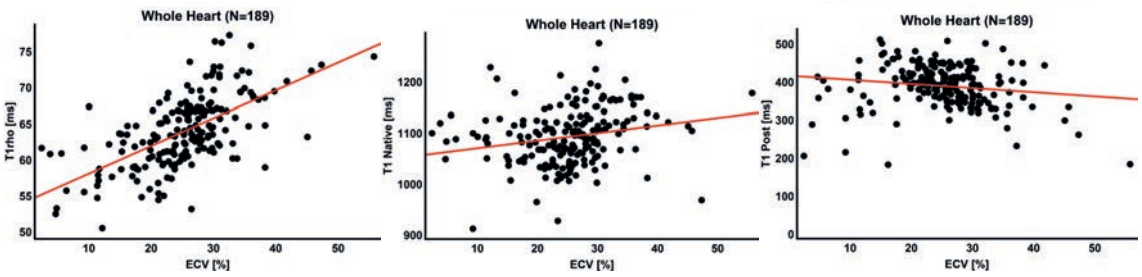

Conclusions

Native T1-rho is strongly correlated with ECV and thus provides information on diffuse myocardial fibrosis without the need for injection of contrast agents.

References

1. van Oorschot JW et al. Endogenous assessment of diffuse myocardial fibrosis in patients with T1ρ -mapping. J Magn Reson Imaging 2017 Jan;45(1):132-138.

Left ventricle in Idiopathic Pulmonary Arterial Hypertension. Longitudinal, circumferential and radial strain and dyssynchrony.

[1]G Jayasekera, [1]T Crowe, [1]A Mackenzie, [2] C McComb, [1]M Johnson, [1]C Church, [2] C Berry, [1]A Peacock*, [2]A Radjenovic*
[1] Scottish Pulmonary Vascular Unit, Golden Jubilee National Hospital, Glasgow
[2] Institute of Cardiovascular and Medical Sciences, BHF, University of Glasgow, UK

Background Pulmonary arterial hypertension(PAH) is characterised by elevated pulmonary artery pressure leading to right ventricular (RV) failure. CMR derived conventional right and left ventricular(LV) functional variables have shown to be prognostic in PAH.(1, 2) Conventionally the reduced LV Stroke volume in PAH has been ascribed to reduced preload from the failing RV but it has been suggested that functional abnormalities of the LV may be present and maybe associated with prognosis and survival. Here we examine LV strain and intraventricular dyssynchrony in Idiopathic PAH (IPAH) and their association with known markers of disease severity and survival.

Methods 56 healthy volunteers (45% male, mean age 46) and 76 patients (30% male, mean age 62) with IPAH were enrolled in the study. All subjects underwent CMR imaging and the patients underwent right heart catheterisation in addition to imaging. Pulmonary artery pressure measurements were obtained during right heart catheterisation. Feature tracking software (MEDIS, QStrain) was used to determine LV global(E_{LL}) longitudinal strain from the 4 chamber view cine images and LV global(E_{CC}) circumferential strain and LV global(E_{RR}) radial strain from a mid-ventricular short axis slice. Intraventricular dyssynchrony of the LV was determined by the standard deviation(SD) of Time to Peak(TPS) of the ventricular segments in longitudinal (Longitudinal SD-TPS), circumferential (Circumferential SD-TPS) and radial directions (Radial SD-TPS).

Results The patient group and the control group did not differ in terms of LV function measured by LVEF (65.8 vs 64.1 p=0.49). LV E_{LL} was significantly lower in IPAH patients compared to controls (-16.7 vs -23.7 p<0.001). LV E_{CC} (-29.2 vs -31.7 p=0.15) and LV E_{RR} (65.3 vs 67.0 p=0.41) were not different in the two groups. Longitudinal SD-TPS (112.2 vs 54.5 p<0.0001), Circumferential SD-TPS (74.6 vs 31.6 p<0.0001) and Radial SD-TPS (45.8 vs 14.8 p<0.0001) were higher in the IPAH group compared to volunteers. In the patient subgroup of impaired LVEF (< 55%), LV E_{CC} and LV E_{RR} was impaired than the patient group with normal LVEF (-17.4 vs -30.8 p< 0.0001, 33.7 vs 72.1 p<0.0001). Radial strain demonstrated strongest correlations with known markers of disease severity such as RVEF(r=0.65) and cardiac output (r=0.51), as illustrated in Figure 1. Radial dyssynchrony was predictive of 5 year survival (p<0.05) in IPAH patients.

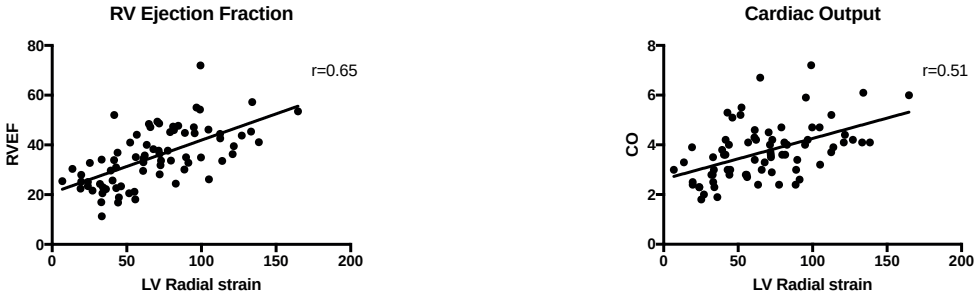

Figure 1. Correlations between LV Radial strain and markers of PAH disease severity: RV Ejection Fraction (left) and Cardiac Output (right)

Conclusion There is impaired longitudinal strain and intra-ventricular dyssynchrony of the LV in IPAH patients. In the setting of impaired longitudinal function, left ventricular systolic function is maintained by circumferential and radial contraction. In IPAH patients with impaired LV function, circumferential and radial strain is impaired in addition to longitudinal strain. Radial function of the LV may be influenced by both direct (interventricular septal bowing) and serial (reduced preload to LV) effects of the RV to the LV in IPAH patients and may provide a novel LV marker of disease severity and survival.

References [1] Peacock AJ, Vonk Noordegraaf A. Eur Respir Rev. 2013;22(130):526-34.
[2] Peacock AJ, Crawley S, McLure L, Blyth K, Vizza CD, Poscia R, et al. Circ Cardiovasc Imaging. 2014;7(1):107-14.

Cardiac Quantitative Susceptibility Mapping at 3T: a Comparison between Breath hold and Free-breathing Approaches

Yan Wen[1,2], Thanh D. Nguyen[2], Pascal Spincemaille[2], Zhe Liu[1,2], Jiwon Kim[3], Jonathan W. Weinsaft[3], and Yi Wang[1,2]
[1]Meinig School of Biomedical Engineering, Cornell University, Ithaca, NY, United States, [2]Radiology and [3]Medicine, Weill Cornell Medicine, New York, NY, United States

PURPOSE

The objective of this study was to compare cardiac QSM obtained with 2D breath-hold (2DBH) and 3D free-breathing navigator (3DNAV) approaches in healthy volunteers at 3 Tesla.

METHOD

Eight healthy volunteers were scanned with both standard 2DBH and custom 3DNAV sequences on a GE MR750 scanner running DV26 software. The imaging parameters were matched for both sequences as follows: 1stTE/ΔTE/#TE/BW = 2.3ms/3.6ms/5/±111.1kHz, acquisition matrix=192x192x20 with 75% phase FOV, slice thickness = 5 mm, views per heartbeat = 10, and parallel imaging factor = 1.5. To shorten 3DNAV scan time, partial Fourier acquisition was applied in phase and slice encoding direction with .75 factor. Each breath hold for the 2DBH approach was about 11 seconds.

The total field was obtained from the complex data using SPURS phase unwrapping[1] followed by IDEAL fat/water separation algorithm with chemical shift update[2]. Then QSM was reconstructed with Total Field Inversion Method[3] while constraining the susceptibility variations in RV and LV blood.

QSM visual quality was scored on a 3 point scale: 1= uninterpretable with excessive artifacts, 2=acceptable with moderate artifacts, and 3=excellent with minimum artifacts. Cases with image score≥2 were considered successful.

RESULTS

2DBH yielded uninterpretable QSM in 37% (3/8) of cases, primarily due to inconsistent breath-holding levels between subsequent scans. 2DBH QSM quality was excellent in 37% (3/8) and acceptable in 26% (2/8) of subjects. In comparison, 3DNAV was successfully acquired on all subjects with 63% (5/8) excellent and 37% (3/8) acceptable QSM. In the presence of slice misregistration (Fig. 1 red arrows) due to inconsistent breath-holding, 2DBH QSM map was degraded with major shadowing artifact (Fig. 1 Case 1). When the breath-holding was consistent, 2DBH provided similar QSM contrast compared to 3DNAV but with slightly reduced SNR (Fig. 1 Case 2). Overall, the average RV-to-LV susceptibility difference was $\Delta\chi$ = 213.5 ± 6.4ppb (392.5 ± 258.0 ppb if failed cases were included) for 2DBH vs. 257.8 ± 32 ppb for 3DNAV, which corresponds to ΔSO_2 = 15.3±5.8% vs. 18.8±2.4%.

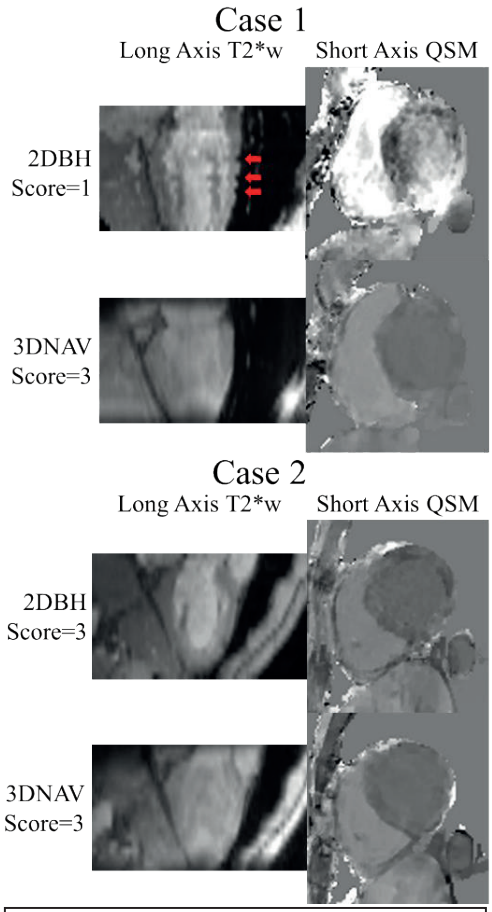

Figure 1. In case 1 where 2DBH failed due to slice misregistration (red arrows) from inconsistent breatholds, the QSM map from 2DBH was degraded by major shadowin artifact whereas the QSM map from 3DNAV remained excellent. In case 2 where both 2DBH and 3DNAV were successful, the resulting QSM maps from both approaches were excellent.

DISCUSSION

Our preliminary data showed that the ΔSO_2 obtained from the 3DNAV approach agreed reasonably well with literature value[4]. The ΔSO_2 obtained from the 2DBH approach is lower than that from 3DNAV, potentially due to a decreasing arterial blood oxygenation during the duration of the breath hold. Both 2DBH and 3DNAV can produced similar high quality QSM maps, however, the practicality of 2DBH approach suffers from its vulnerability to inconsistent breath holds. When slice misregistration occurs as the result of inconsistent breath holds, the resulting QSM may be degraded by major shadowing artifacts. The 3DNAV approach, on the other hand, eliminated the need of breath holds, therefore by-passed the problem with slice misregistration, making it a more viable option in clinical environment than 2DBH approach.

REFERENCES

1. Dong J, Liu T, Chen F, Zhou D, Dimov A, Raj A, Cheng Q, Spincemaille P, Wang Y., "Simultaneous Phase Unwrapping and Removal of Chemical Shift (SPURS) Using Graph Cuts: Application in Quantitative Susceptibility Mapping," in *Medical Imaging, IEEE Transactions on* , 2015. 34(2), 531-540.
2. Dimov A. V., Liu T., Spincemaille P., Ecanow J. S., Tan H., Edelman R. R. and Wang Y., Joint estimation of chemical shift and quantitative susceptibility mapping (chemical QSM). *Magn Reson Med*, 2015, 73: 2100–2110.
3. Liu Z, Kee Y, Zhou D, Spincemaille P, Wang Y. Preconditioned total field inversion (TFI) method for quantitative susceptibility mapping. MRM. doi:10.1002/mrm.26331
4. Barratt-Boyes, Brian G. et al. The Oxygen Saturation of Blood in the Venae Cavae, Right-Heart Chambers, and Pulmonary Vessels of Healthy Subjects. The Journal of Laboratory and Clinical Medicine , Volume 50 , Issue 1 , 93 - 106

Peak velocity across the aortic valve using same-day Doppler echocardiography and 4D flow MRI

Hyungkyu Huh[1], Menhel Kinno[2], James D Thomas[2], Michael Markl[1,3], Alex J Barker[1]
[1]Department of Radiology, Northwestern University, Chicago, IL USA
[2]Department of Cardiology, Northwestern University, Chicago, IL USA
[3]Department of Biomedical Engineering, Northwestern University, Chicago, IL USA

Purpose: Aortic valve stenosis (AS) can result in severe complications such as left ventricle hypertrophy, aortopathy and heart failure. Current guidelines recommend a combination of systolic peak velocity, mean pressure gradient and effective orifice area measurements for risk stratification. Among these parameters, peak velocity is the strongest predictor of clinical outcome[1]. Hence, precise measurement is essential for the management of patients with aortic valve disease. 2D Doppler echocardiography (Echo) is the first line test for surveillance. However, misalignment of the Doppler beamline with the transvalvular flow jet may cause peak velocity underestimation. Alternatively, 2D CINE Phase-Contrast (PC) MRI can be used to quantify aortic blood flow velocities. However, 2D CINE PC MRI is also limited by one-directional velocity encoding as well as reduced spatial and temporal resolution compared to 2D Doppler Echo. Recently, a number of studies have shown that 4D flow MRI can provide more accurate quantification of aortic peak velocities compared to 2D CINE PC MRI due to full 3D coverage of the aorta and three-directional velocity encoding. The purpose of this study was to systematically investigate aortic peak velocity measured by 2D Doppler Echo and 4D flow MRI in a cohort of 41 subjects using a same-day study design to better understand the source of errors in each modality.

Methods: Data was acquired with an average time of 3.47±1.94 hr between echo and 4D flow MRI in four different study groups: healthy volunteers ages under 50 years old (n=13, age: 30.4±7.0 years) healthy volunteers ages over 50 years old (n=22, 61.7±9.9 years), bicuspid aortic valves (BAV; n=4, age: 36.2±9.8 years, all type1 L-R fusion) and AS (n=2, moderate to severe) patients. For 2D Doppler Echo, aortic peak velocity was measured by continuous-wave Doppler following guidelines[2] (Fig.a). For 4D flow MRI, a volume of interest was selected over the entire flow jet area (Fig.b, dashed-line, $VROI_{free}$) or limited along a simulated 'beamline' along the flow jet direction and 4mm in diameter (Fig.b, solid line, $VROI_{beamline}$). The 'beamline' measurement attempted to replicate the aortic region measured with 2D Doppler Echo.

Results: As shown in Figure c, averaged peak velocity measured by 2D Doppler Echo (139.1±52.6 cm/s) was 10.5% lower than the velocity measured by 4D flow MRI within the $VROI_{free}$ (155.4±47.6 cm/s, p=0.074) and 2.25% lower than the velocity measured within the $VROI_{beamline}$ (142.3±49.3 cm/s, p=0.387) (bias [limits of agreements]: -16.4 [18.0:-50.9]cm/s and -3.3 [33.5:-40.1]cm/s, respectively). The peak velocity of healthy volunteers aged over 50 years old was always underestimated by 2D Doppler Echo compared to 4D flow MRI within the $VROI_{free}$ (Echo vs MRI: 129.2±19.6 and 154.3±19.6 cm/s, p<0.001), while no significant difference was observed for healthy volunteers aged under 50 years old (Echo vs MRI: 120.8±17.0 and 129.3±20.9 cm/s, p=0.143). In both AS patients, 4D flow MRI underestimated aortic peak velocities regardless of the VROI compared to 2D Dopper Echo (Echo: 34.0 and 36.6cm/s, MRI-$VROI_{free}$: 33.4 and 34.5 cm/s MRI-$VROI_{beamline}$: 31.5 and 34.5 cm/s). Finally, aortic peak velocity measured by 2D Doppler Echo and 4D flow MRI was similar in BAV group (Echo: 145.5±25.2 cm/s, MRI-$VROI_{free}$: 154.5±23.0 cm/s, MRI-$VROI_{beamline}$: 146.7±19.9 cm/s, p=0.3317 and 0.4743, respectively).

Discussion: 3D volumetric velocity information with 4D flow MRI queries the entire volume of interest allowing for identification of the peak velocity region with all 3 principal velocity directions encoded. Our findings indicate that peak velocity measured with 4D flow MRI was higher than 2D Doppler Echo, especially for the older aged group, due to oblique flow jets. The bias was significantly reduced in the $VROI_{beamline}$ which mimics the 2D Doppler Echo measurement, and which supports the fact that 2D beamline measurements with echo may underestimate peak velocity due to beamline misalignment. However, the higher peak velocities in the AS group were underestimated by 4D flow MRI regardless of the VROI, possibly due to lower spatio-temporal resolution of MRI. This preliminary data in the patient population requires additional study with larger numbers of patient.

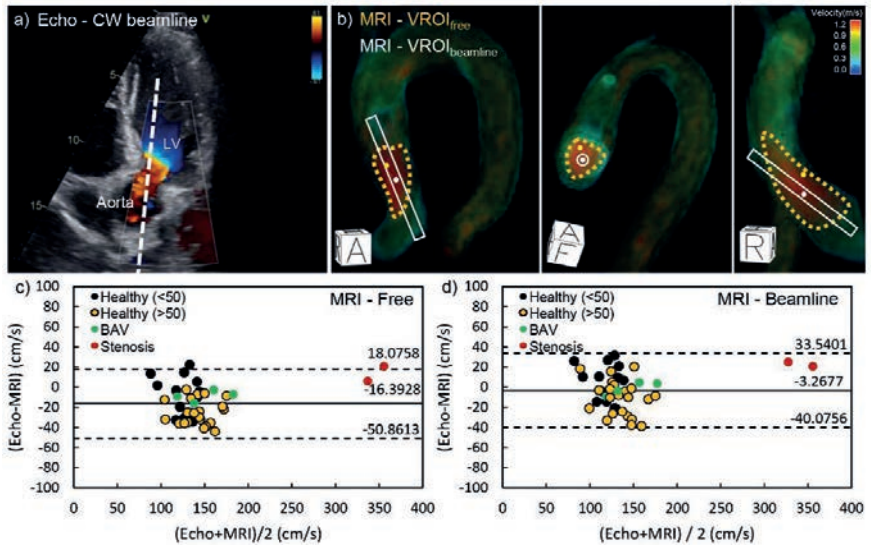

Figure a) Measurement of aortic peak velocity with 2D Doppler Echo at systole. The dashed line indicates the CW beamline. **b)** Peak velocity measurement with 4D flow MRI with different volumes of interest. The dashed-line indicates VROI around the jet while the solid line indicates a VROI restricted along the beamline. (**c-d**) Bland-Altman plot of aortic peak velocity measured by echo and 4D flow MRI by each method**.**

References: [1] Otto, Catherine M., et al. *Circulation* 95.9 (1997): 2262-2270. [2] Baumgartner, Helmut, et al. *Journal of the American Society of Echocardiography* 30.4 (2017): 372-392.

Simultaneous 3D whole-heart bright-blood anatomy and black blood wall assessment with interleaved T2prep-IR

G. Milotta[1], G. Ginami[1], G. Cruz[1], R. Neji[1,2], C. Prieto[1], R.M. Botnar[1]
[1]School of Biomedical Engineering and Imaging Sciences, King's College London; [2]MR Research Collaborations, Siemens Healthcare

Introduction: Visualization of cardiovascular anatomy plays a major role in the diagnosis, risk stratification and planning of interventional procedures both in patients with congenital and non-congenital heart disease. Conventional 2D double inversion recovery[1] (DIR) black-blood imaging techniques have been successfully used to visualize atrial, myocardial and aortic walls. However, DIR techniques provide limited volumetric coverage and are flow-dependent[1]. A 3D flow-independent approach for simultaneous lumen and vessel wall visualization (iT2prep) was recently proposed[2]. iT2prep is based on an interleaved acquisition and weighted subtraction of data with and without T2-preparation (T2prep). However, this approach remains sub-optimal as it requires subject-dependent weighted subtraction to completely null arterial blood signal. Here, we propose an interleaved T2-prepared Inversion Recovery (iT2prep-IR) approach that improves vessel wall to blood contrast and removes the need of weighted subtraction while simultaneously providing bright-blood whole-heart anatomy visualization.

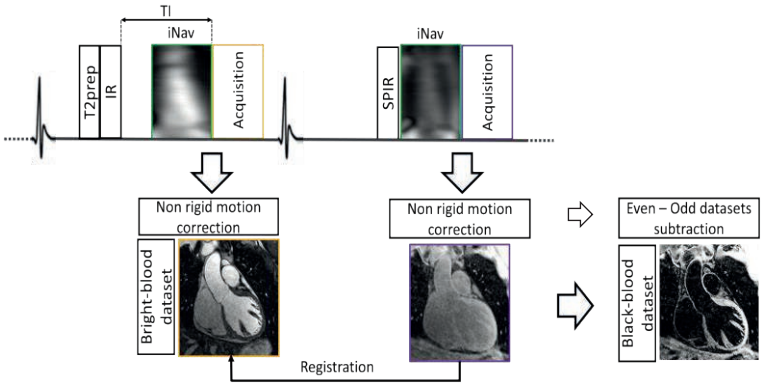

Fig1: Proposed sequence: a T2Prep-IR module is applied prior to data acquisition in odd heartbeats (bright-blood dataset) and no T2Prep-IR preparation is applied in even heartbeats. 2D-iNAVs are acquired in each heartbeat to estimate/correct SI and RL translational motion. Non-rigid motion correction is performed on the two datasets and non-rigid image alignment is performed prior to datasets subtraction (black-blood dataset).

Methods: The proposed iT2prep-IR bright-and-black-blood sequence is based on the acquisition and direct subtraction of two interleaved 3D whole-heart image datasets acquired with (odd heartbeats) and without (even heartbeats) T2prep-IR preparation as shown in Fig.1. Image-based navigators[3] (iNAVs) are acquired prior data acquisition to estimate and correct for superior-inferior (SI) and left-right (LR) beat-to-beat translational respiratory motion. Bin-to-bin non-rigid motion compensation[4] is performed independently on both odd and even datasets. Non-rigid registration is performed prior subtraction. Six healthy subjects were scanned under free-breathing in a 1.5T MR scanner (Siemens Magnetom Aera) with the proposed 3D iT2prep-IR, and with the 3D iT2prep and 2D DIR techniques for comparison. iT2prep-IR was acquired with an ECG-triggered 3D Cartesian[5] b-SSFP imaging sequence and the following parameters: resolution=1.4x1.4x1.4mm, FOV=320x320x144mm, TR/TE=3.6/1.6ms, flip-angle=90°, TI=110ms, T2Prep duration=40ms, 14 startup-echoes for iNAV. Fat suppression was achieved with a STIR-like approach in odd and with a SPIR pulse in even heartbeats, respectively. iT2prep was acquired with a T2prep length of 70ms and matching imaging parameters. DIR was acquired with a GRE imaging sequence (FA=15°, TR/TE=5.1/2.35ms, bandwidth=473Hz), 1.4mm in-plane resolution and 7mm slice thickness. Signal-to-noise and contrast-to-noise ratio of blood and myocardium (SNR_{blood}, SNR_{myoc}, $CNR_{myoc-blood}$) were computed for all acquisitions.

Results: The proposed iT2prep-IR sequence showed improved blood nulling, and thus improved atrial, myocardial and aortic wall visualization, compared to both DIR and iT2prep techniques (Figure 2). SNR_{myoc} of 80.2, 57.4, 42.1 and $CNR_{myoc-blood}$ of 33.5, 14.7 and 15.2 were computed respectively from the black-blood iT2prep-IR, iT2prep and DIR datasets. Additionally, iT2prep-IR showed higher $CNR_{blood-myoc}$ compared to the iT2prep approach in the bright-blood dataset (62.2 and 35.9 respectively).

Conclusion: The proposed iT2prep-IR sequence showed promising results in terms of blood signal nulling, SNR_{myoc} and $CNR_{myoc-blood}$ without the need of weighted subtractions. Thus, the propose approach enables aortic, ventricular and atrial wall visualization while simultaneously providing co-registered bright-blood anatomy with high $CNR_{blood-myoc}$.

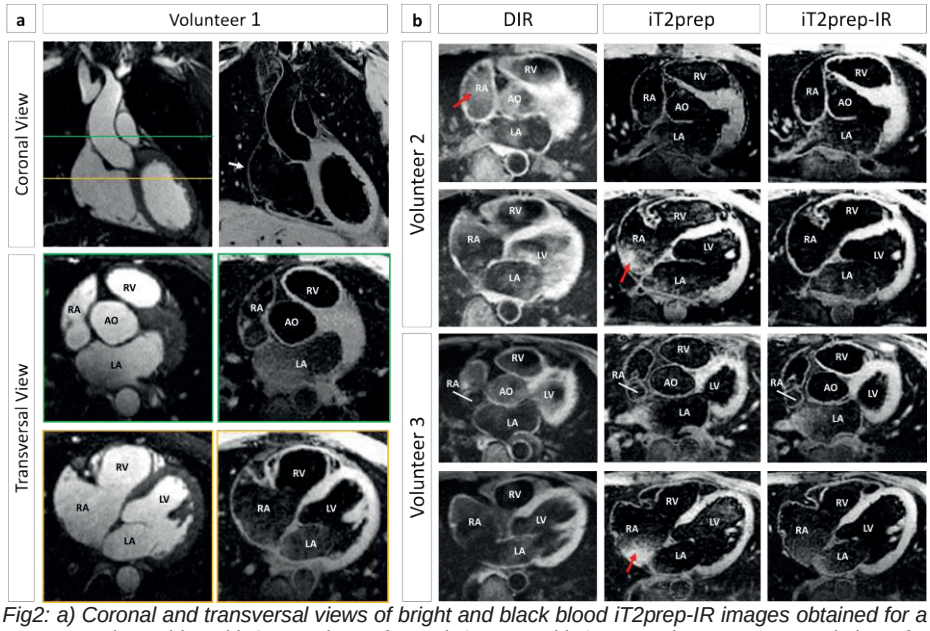

Fig2: a) Coronal and transversal views of bright and black blood iT2prep-IR images obtained for a representative subject. b) Comparison of DIR, iT2prep and iT2prep-IR in two transversal views for two subjects. iT2prep-IR shows uniform blood nulling compared to both DIR and iT2prep techniques. Aorta (AO), left and right ventricle (LV, RV) and left and right atrium (LA, RA) walls are visible. Red arrows indicate a not complete blood nulling due flow obtained with DIR and iT2prep techniques. White arrows indicate wall that are depicted with the proposed technique but not with

References: 1) Botnar et al. MRM 2001;46:848-54. 2) Andia et al. MRM 2013; 69:150-7. 3) Henningsson et al. MRM 2012; 67:437-45. 4) Cruz et al. MRM 2017; 77:1894-1908. 5) Prieto et al. JMRI 2015; 41:738-46.

Maximizing the Conspicuity and Characterizing Signal Generation of Fluorine-19 MRI for the Quantification of Inflammation in Atherosclerosis

Emeline Darçot[1], Roberto Colotti[1], Jérôme Yerly[1,2], Maxime Pellegrin[3], Anne Wilson[4], Stefanie Siegert[4], Matthias Stuber[1,2], and Ruud B. van Heeswijk[1,2]

[1]Department of Radiology, [2]Center for Biomedical Imaging (CIBM), [3]Division of Angiology, Lausanne University Hospital (CHUV); [4]Flow Cytometry Facility, University of Lausanne (UNIL).

Purpose. Fluorine-19 (^{19}F) MRI of an intravenously injected perfluorocarbon (PFC) can be used to monitor inflammation over time [1]. Injected PFCs are taken up by immune cells and transported mainly to inflammation sites and the reticuloendothelial system. In this study, we investigated two aspects of the detected ^{19}F signal in inflammation in a mouse model of atherosclerosis: 1) whether the conspicuity of regions with PFC uptake improves with the use of a wavelet denoising filter [2] during the image reconstruction, and 2) which immune cell populations take up the PFC and generate the signal.

Methods. C57BL/6 apolipoprotein-E-knockout (ApoE$^{-/-}$) mice (n=23), a model of atherosclerosis, were fed with a high-fat diet. Thirteen mice were injected intravenously with 2×200µL of perfluoropolyether (PFPE, Celsense), 1 and 2 days before an MRI scan on a 3T clinical scanner (Prisma, Siemens) with a ^{19}F/^{1}H volume coil (Rapid Biomedical). After anatomical ^{1}H imaging, ^{19}F images were acquired with an optimized 3D turbo spin echo (TSE) sequence [3] (voxel size 0.78×0.78×1mm^3, TR/TE=1070/13ms). Images were reconstructed with and without a wavelet denoising filter [4]. After ^{19}F/^{1}H image coregistration, signal thresholding using the noise floor of standard images, and plaque segmentation, the MRI-derived PFC concentration in the plaques (C_{MRI}) was calculated based on the signal intensity of each plaque (SI) relatively to an external reference with a known PFC concentration. From the segmentation, the volume of the plaques (V_{SI}) and the SI×V_{SI} product (i.e. the ^{19}F signal integral) were quantified. After imaging, all aortas were dissected and photos were taken. To characterize the aortic leukocyte populations, ten ApoE$^{-/-}$ mice were used for post-mortem imaging flow cytometry (ImageStream) [5]: five were injected with fluorescent FITC-PFPE and five were injected with non-fluorescent-PFPE as control mice. Identification and quantification of the cell populations that took up PFC was performed, and the area of PFC uptake per individual cell as well as the average uptake per cell (area×relative brightness) were calculated.

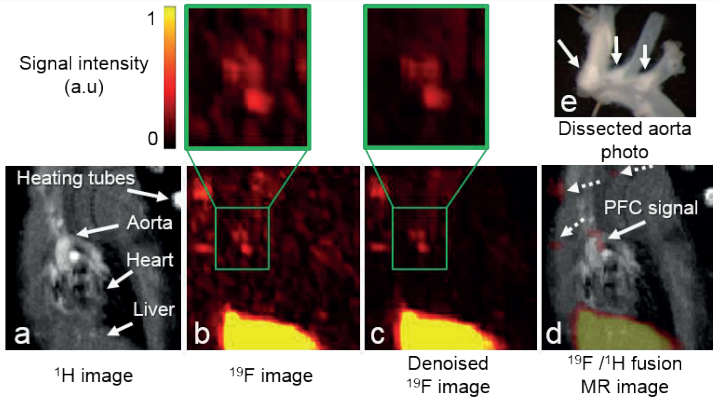

Figure 1. Detection of PFC signal in a mouse atherosclerotic plaques at 3T. a. Mouse anatomy ^{1}H image, ^{19}F images **b.** without and **c.** with application of a denoising filter, and **d.** fusion of the ^{1}H and ^{19}F denoised images, respectively. PFC signal can be observed in the aortic arch (solid arrow) and in subcutaneous fat, where the anesthetic isoflurane accumulates (dotted arrows). **e.** Dissected aorta with visible plaques in the aortic arch (white arrows).

Results. ^{19}F MR hotspots were detected in all aortas and were confirmed on matching post-mortem photos (Figure 1). Denoising led to a higher conspicuity of the hotspots (Figure 1b,c). Both C_{MRI} and V_{SI} decreased from standard to denoised reconstruction images (C_{MRI}=0.56±0.09mM vs. 0.49±0.10mM, P=0.001; V_{SI}=4.5±1.0mm^3 vs. 2.8±1.1mm^3, P<0.001, respectively). Imaging flow cytometry demonstrated that the population sizes of dendritic cells, macrophages and neutrophils that internalized PFC had a ratio of 9:1:1. The distribution of internalized PFC depended on the cell type, and resulted for dendritic cells, macrophages and neutrophils in average areas of 22.0±18.0µm^2, 4.6±4.2µm^2 and 3.7±1.8µm^2 per individual cell, respectively (Figure 2). When accounting for the relative brightness, the average PFC uptake per individual cell was at a ratio of 25.2:1.2:1.

Discussion. The denoising filter improved the conspicuity of the small plaques on the ^{19}F MR images. The decrease of the plaque volume V_{SI} due to the regularization of the denoising filter was three times stronger than the decrease of the concentration C_{MRI}, which suggests that the removed part of the signal regions was low-intensity motion blur: ^{19}F signal tends to become blurred during motion, which in this case results in extra low-intensity signal regions around the actual plaque signal. The imaging flow cytometry demonstrated that the PFC was mainly taken up by dendritic cells, followed by macrophages and neutrophils, which agrees well with previous studies [6]. In conclusion, we characterized two aspects of atherosclerosis inflammation imaging with ^{19}F MRI, which contribute to the translation of ^{19}F MRI to the clinical setting for the monitoring of small inflammation sites.

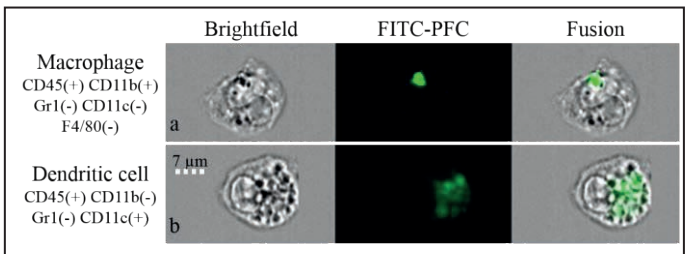

Figure 2. Microscopic visualization of a macrophage and a dendritic cell with internalized PFC nanoparticles. From left to right: brightfield (gray), FITC-PFC (green) and their fusion image, showing the variability in PFC uptake by the different cells.

References. [1] Jacoby et al., NMR in Biomed 2013; [2] Donoho et al., J Am Stat Assoc. 1995. [3] Colotti et al., Magn Reson Med. 2016; [4] Yerly et al., Magn Reson Med. 2016; [5] Basiji et al., J Immunol Methods. 2015; [6] Choi et al., Immunity 2011.

Simultaneous T1 and T2 Mapping of Plaque (SIMPLE) with T2 and Inversion Recovery Prepared 3D Radial Imaging

Haikun Qi[1], Jie Sun[2], Huiyu Qiao[1], Niranjan Balu[2], Chun Yuan[2], Huijun Chen[1]
[1] *Center for Biomedical Imaging Research, School of Medicine, Tsinghua University, Beijing, China*
[2] *Department of Radiology, University of Washington, Seattle, WA, USA*

Purpose

Previous work has established the capability of multi-contrast vessel wall MRI in differentiating plaque components in carotid arteries (1). However, due to the qualitative nature of multi-contrast imaging, plaque components are identified by comparing to the signal intensity of reference tissues, which is subjective resulting in intra-/inter-reader variability and strongly influenced by imaging parameters and coil positioning (2). Quantitative mapping of carotid vessel wall has been reported (3-5). However, these techniques will require separate scans to obtain T1 and T2 maps, which increases total scan time and is prone to misregistration errors. In this study, we aimed to develop a technique that allows simultaneous T1 and T2 mapping of carotid vessel wall with large coverage and 3D isotropic resolution.

Methods

Sequence Design: A previously described sequence for fast 3D T1 mapping (GOAL-SNAP) (5) was improved in this study to allow simultaneous T1 and T2 mapping of plaque (SIMPLE). As shown in Fig. 1a, SIMPLE is prepared with both adiabatic T2 preparation (6) with variable duration (TE_{prep}), and IR pulses (T2IR) to produce T1 and T2 contrasts. Following T2IR preparation, 3D radial sampling is adopted for isotropic acquisition, and water excitation pulse is used for fat suppression. The 3D golden angle radial order of the GOAL-SNAP sequence (5) is modified for iGOAL-SNAP to achieve uniform distribution of spokes used for reconstruction at a certain TI and TE_{prep}.

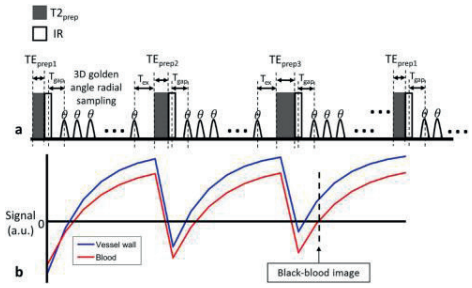

FIG.1. The schematic diagram of the T2 and IR prepared 3D golden angle radial sequence, where the three shown sequence blocks have different duration of T2 preparation.

Image reconstruction and T1, T2 fitting: Sliding window reconstruction was performed to reconstruct the T2IR image series by combining spokes of all shots with the same TI and TE_{prep}. CG-SENSE iteration (7) was used to reduce undersampling artifacts with the sensitivity maps estimated by using spokes at TI larger than 1300ms. To take into account B1 inhomogeneity, another two 3D radial SPGR images were acquired with flip angles different from SIMPLE (8). Then, five parameters including proton density, inversion efficiency, B1, T1 and T2 were estimated simultaneously by fitting the signals of the T2IR image sets and the SPGR images to the signals simulated using Bloch equation. The imaging parameters of SIMPLE and 3D radial SPGR are shown in Table 1. In this study, the temporal width for the sliding window reconstruction of the T2IR image series was set as 25 (250s/frame), resulting in 21 frames for T1/T2 fitting. Additionally, a black-blood image with near-zero luminal signal (Fig. 1b) was reconstructed to depict vessel wall (SIMPLE VW), using the KWIC method (9).

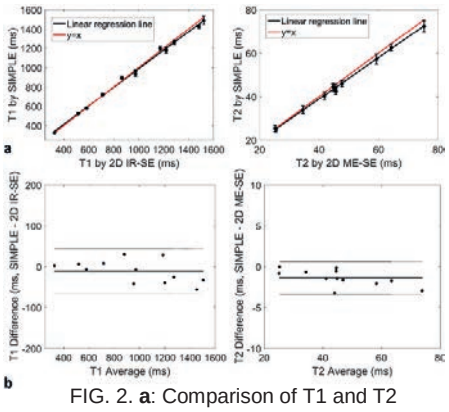

FIG. 2. **a**: Comparison of T1 and T2 measurements of phantoms between iGOAL-SNAP and 2D standard spin echo methods. **b**: Bland-Altman plots.

Table 1: Imaging parameters of SIMPLE and 3D radial SPGR scan

	FOV (mm^3)	Voxel Size (mm)	TR/TE (ms)	Flip angle	TFE factor (N)	T_{gap} (ms)	T_{ex} (ms)	Scan duration
SIMPLE	120×120×120	0.8 isotropic	10/4.0	8°	175	10 [b]	250	8min
SPGR	120×120×120	1 isotropic	10/4.0	6°/10° [a]	NA	NA	NA	45s

a: The SPGR images were acquired with 2 nominal flip angles of 6° and 10°
b: The minimum values allowed on the scanner
NA: not applicable

MR Imaging: All scans were performed on a 3T MR scanner (Philips, Achieva). First, SIMPLE was tested in phantoms with different T1 and T2 values. The standard 2D T1 and T2 mapping sequences: IR-spin echo (IR-SE) and multi-echo spin echo (ME-SE), were performed for comparison. After institutional review board approval, in vivo imaging was performed in five heathy volunteers and five patients with carotid atherosclerosis. For comparison, besides SIMPLE, MOLLI and T2prep bSSFP were performed for healthy volunteers, and the conventional multi-contrast imaging protocol (1) and SNAP (10) were performed for patients.

Results

The mean T1 and T2 values of phantoms from SIMPLE were in good agreement with 2D IR-SE and ME-SE (T1: R^2=0.99; T2: R^2=0.99, Fig. 2a). Bland-Altman plots showed the measurement bias with the average of the measurements (Fig. 2b). For in vivo imaging, the T1 and T2 of muscle in the five volunteers estimated by SIMPLE (T1: 1027±32.3ms; T2: 30.3±1.1ms) were reasonable compared with MOLLI (1012±22.1ms) and T2prep-bSSFP (31.8±2.1ms). The mean T1 and T2 values of carotid vessel wall from healthy volunteers were 1213±48.3ms and 51.1±1.7ms, respectively. Eight carotid plaques were found in the five patients. And IPH was detected in five plaques on SNAP images. Figure 3 shows an example of carotid plaque with IPH. Alternations of T1 and T2 values observed in the plaque region were in agreement with the findings on SNAP and T2-weighted images.

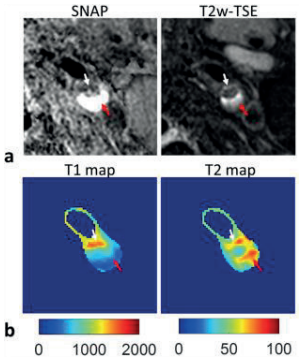

FIG. 3. T1 and T2 mapping of one plaque with IPH and fibrous tissue by SIMPLE. The red arrow indicates the IPH region, and the white arrow indicates fibrous tissue.

Discussion and Conclusions

A high spatial resolution, time-efficient, simultaneous vessel wall T1 and T2 mapping technique was developed, which showed excellent correlation in measuring T1 and T2 of phantoms with traditional 2D SE methods. Preliminary in vivo studies indicated good feasibility and great potentials of the proposed technique for comprehensive characterization of carotid plaque in a single scan. Compared with existing T1-weighted and T2-weighted techniques, SIMPLE may provide more quantitative, reproducible biomarkers of carotid atherosclerosis.

Reference

1. Cai JM, et al. Circulation. 2002;106(11):1368-1373. 2. Li FY, et al. JMRI. 2010;31(1):168-176. 3. Biasiolli L, et al. JCMR. 2013;15:69. 4. Coolen BF, et al. MRM. 2016;75(3):1008-1017. 5. Qi H, et al. Radiology. 2017;(Epub). 6. Nezafat R, et al. MRM. 2006;55(4):858-864. 7. Pruessmann KP, et al. MRM. 2001;46(4):638-651. 8. Kecskemeti S, et al. 2016;75(3):1040-1053. 9. Song HK, et al. MRM. 2000;44(6):825-832. 10. Wang JN, et al. MRM. 2013;69(2):337-345.

Vascular Deformation Mapping (VDM) for Assessment of Thoracic Aortic Growth Using Magnetic Resonance Angiography: Preliminary Results

Nicholas S Burris MD[1], Benjamin A Hoff PhD[1], Ignas B Houben MD[2], Theodorus MJ van Bakel MD[2], Himanshu J Patel MD[2]

[1]*University of Michigan, Department of Radiology,* [2]*University of Michigan, Department of Cardiac Surgery*

Purpose: Imaging surveillance plays a central role in the management of patients with thoracic aortic aneurysm (TAA). Maximal aortic diameter is the primary metric used to determine disease progression, however, confident determination of change in aortic dimensions is often not possible due to high measurement variability (±2 mm), especially when aortic growth is slow or intervals are short.[1] Vascular Deformation Mapping (VDM) is an image processing technique recently developed by our group for three-dimensional assessment of change in aortic dimensions between two studies using volumetric CTA data.[2] However, depending on the institution and indication, MRA may be the preferred modality. The purpose of this work was to establish feasibility of VDM for assessing TAA progression using MRA data.

Methods: In brief VDM analysis involves: 1) aortic segmentation at two time points, 2) non-rigid image registration with B-spline warping (MATLAB Elastix), 3) quantification of deformation using determinate of spatial Jacobian each voxel location (normalized by time interval to yield deformation rate).[2] MRA data was acquired with 3D-navigated SSFP technique (0.7 mm isotropic). To validate VDM's unitless Jacobian output, aortic circumference was measured using double-oblique technique and diameter was derived as $(\Delta d = \Delta C/\pi)$. Dimeter measurements were taken from clinical MRA reports for comparison.

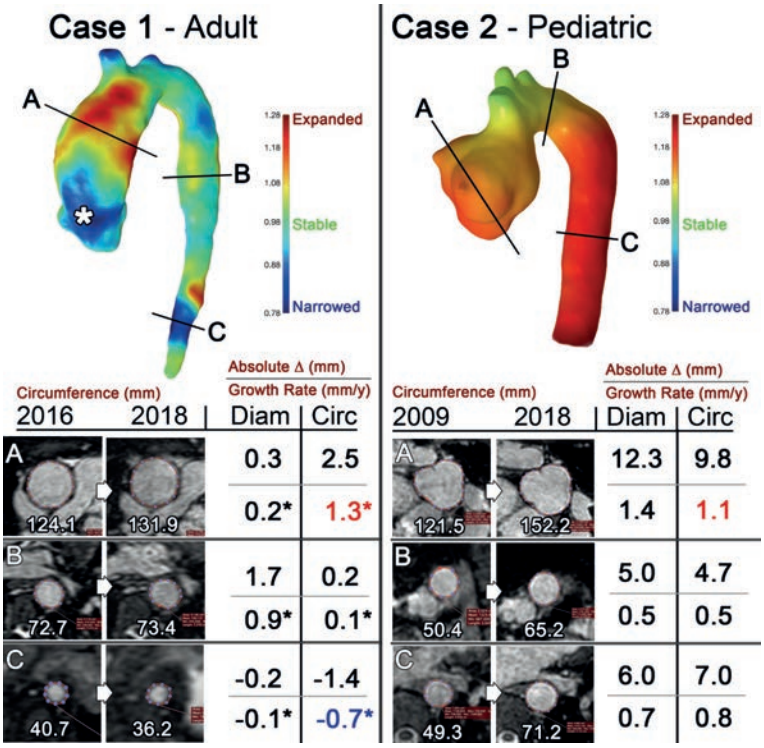

Figure: Representative VDM analyses using MRA data: Case 1- Adult patient with Takaysu arteritis, with absolute and growth rate measurements (2-year interval) at the mid-ascending (A), mid-descending (B) and distal-descending (C) levels. Case 2- Pediatric patient with dilated neoaortic root, with absolute and growth rate measurements (9-year interval) at the root (A), distal arch (B) and mid-descending (C) levels.

Results: Two clinical cases were analyzed with VDM (**Figure 1**). Case 1 is an adult patient with Takayasu arteritis and mildly dilated ascending aorta undergoing MRI/MRA surveillance (2-year interval). VDM demonstrated growth at the mid-ascending level, confirmed to be growing at 1.3 mm/year by circumference measurements, although no confident change could be detected by diameter measurements (Case 1A). The mid-descending aorta showed no significant growth by VDM (0.1 mm/year) concordant with circumference measurements, although diameter measurements yielded a 0.9 mm/year growth rate (Case 1B). Lastly, VDM depicted an area of interval luminal narrowing related to progressive Takaysu arteritis, with circumference assessment at that level showing a -0.7 mm/year rate of narrowing, however, diameter measurements did not detect a change (Case 1C). Mild motion artifact in the proximal ascending aorta resulted in artifact due to slight variations in image segmentation (Case 1, asterisk). Case 2 is a pediatric patient with history of transposition of the great arteries, status post arterial switch procedure, with dilated neoaortic root (9-year interval, 9 y/o at first study). VDM demonstrated growth moderate growth at the root (1.1 mm/year, Case 2A) and mid-descending (0.8 mm/year, Case 2C) levels, which was in agreement with diameter measurements due to the long interval and higher degrees of absolute growth. Interestingly, the aortic arch and arch vessels grew slower (0.5 mm/year, Case 2B). Spatial Jacobian values were largest in the descending aorta due to a higher degree of overall deformation at this location related to elongation in the setting of somatic growth.

Discussion: Vascular Deformation Mapping is a feasible technique for assessing three-dimensional change in aortic dimensions using MRA images from routine clinical studies. Further work is required to optimize and validate this technique, however, VDM may allow for more complete assessment of aortic growth in TAA patients undergoing MRA surveillance, and promises to allow for a more comprehensive assessment of aortic growth in pediatric patients that are experiencing both pathologic and somatic growth.

References: 1) Quint LE et al. *Int J Cardiovas Imag*. 2013; 2) Burris et al. *Tomography*. 2017.

Comparison of Qualitative and Quantitative Methods for Vessel Wall Imaging MRI Evaluation of Intracranial Atherosclerosis

MD Alexander, AH DeHavenon, DL Parker, SE Kim, JS McNally
Department of Radiology and Imaging Sciences, University of Utah, Salt Lake City, UT, USA

Purpose: As vessel wall imaging (VWI) MR techniques become more widely accepted for the evaluation of intracranial atherosclerotic disease (ICAD), standardized methods are needed to ensure reproducibility. This study compares qualitative and quantitative methods of evaluating pre- and post-contrast signal intensity of ICAD plaques.

Methods: Prospectively maintained records were retrospectively queried to identify patients undergoing VWI for analysis of new infarcts at a major academic medical center. Patients were evaluated within 14 days of original MRI demonstrating restricted diffusion. All images were acquired on a Siemens Prisma 3T MRI scanner. All reviewers were blinded to diffusion and clinical data and instructed to analyze the arterial tree to which the new infarct was referable. All reviewers evaluated the ICAD plaque deemed most likely to have caused the infarct. One reviewer rated all culprit lesions as either having or lacking enhancement following administration of intravenous contrast by comparing pre- and post-contrast T1 DANTE images. Two reviewers obtained maximum voxel signal intensity values for the plaque on T1 DANTE images both before and after the administration of gadolinium contrast. Several normal reference structures were measured to evaluate the degree of plaque enhancement. Structures normally expected to enhance were measured, including the mid infundibulum, defined as the midway point between the inferior margin of the hypothalamus and the upper margin of the pituitary gland; low infundibulum, defined as the lowest segment of the infundibulum distinguishable from the pituitary gland; choroid plexus in a lateral ventricle; cavernous sinus, measured at a site clearly intravascular as seen on post-contrast images; and muscle, measured in the temporalis muscle in tissue with signal medial to the mid-belly fibrous band. For each variable quantitatively measured, the mean of three data points were computed after obtaining the maximum single-voxel intensity values at each site of interest. Pre- and post-contrast signal intensity measurements were divided by the corresponding measurements for each of the reference structures. Enhancement was considered to be quantitatively present of the ratio of plaque to normal structure was greater than 1. Rates of enhancement as defined by the various quantitative measurements and qualitative assessment were descriptively summarized.

Results: 26 patients met inclusion criteria. Mean time to VWI after diagnosis of infarct was 7 days. Results are summarized in Table 1.

	Enhancement	No Enhancement
Qualitative (n-26)	24 (92.3%)	2 (7.7%)
Mid Infundibulum (n=23)	16 (70.0%)	7 (30.4%)
Low Infundibulum (n=25)	11 (44.0%)	14 (56.0%)
Choroid Plexus (n=26)	21 (80.8%)	5 (19.2%)
Cavernous Sinus (n=26)	14 (53.8%)	12 (46.2%)
Muscle (n=26)	26 (100%)	0 (0.0%)

Discussion: Rates of ICAD plaque enhancement vary considerably between qualitative and quantitative measures. Additionally, rates of enhancement vary among enhancement defined by comparison of several normal reference structures. Further investigation is needed to determine what constitutes true plaque enhancement and the most appropriate and reproducible method for measuring enhancement in order to achieve the highest quality data in future studies evaluating ICAD with VWI.

Cardiovascular black-blood imaging using Volume ISotropic Turbo spin echo Acquisition (VISTA) in patients with congenitalal heart disease

Markus Henningsson[1], Riad Abou Zahr[2], Gerald F Greil[2], Barbara Burkhardt[2], Animesh Tandon[2], Tarique Hussain[2]

1 Division of Biomedical Engineering and Imaging Sciences, King's College London, United Kingdom
2 Departments of Pediatrics and Radiology, University of Texas Southwestern/Children's Health, Dallas, TX, US

Purpose: Three-dimensional (3D) cardiovascular magnetic resonance (CMR) can be used for visualization of the whole heart and great vessel morphology in patients with congenital heart disease (CHD). Here, we describe a new Volume ISotropic Turbo spin echo Acquisition (VISTA) protocol for 3D black-blood CMR of the whole heart and great vessels. The main purpose of this study was to assess the feasibility of black-blood VISTA for the visualization of the whole heart and great vessels in patients with CHD. We compare the new VISTA technique to the conventional techniques for 3D morphological CMR – bright-blood 3D bSSFP.

Methods: All experiments were performed on a 1.5T Philips scanner. The VISTA sequence used a slice-selective 90° excitation pulse and non-selective refocusing pulses. The refocusing flip angles of VISTA were modulated to yield constant transverse magnetisation across the echo train for a specific T1 (880 ms) and T2 (40 ms).

Patient experiments: Patients with CHD referred for CMR examination at Children's Medical Center, Dallas, Texas, USA, were considered for inclusion. Patients were scanned with VISTA and 3D bSSFP. The VISTA parameters were: FOV = 250-350mm, 120 to 180 slices, TE_{eff} = 30 ms, TE_{sp} = 2.7 ms, voxel size = 1.3×1.3×1.3 mm, echo train length = 18 to 35 (plus 8 startup echoes), 1 average, coronal orientation, SENSE acceleration = 2 (LR). The bSSFP scan had same resolution, FOV, orientation and SENSE factor, echo time = 2 ms, echo train length = 22 to 40 (plus 10 startup echoes). Both VISTA and bSSFP were ECG-triggered to the longest cardiac rest period and used a diaphragmatic navigator with 3-7 mm gating window (dependent on patient size) and 0.6 tracking factor.

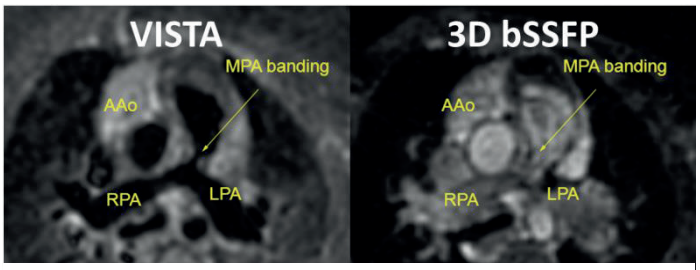

Figure 1. VISTA (left) and 3D bSSFP (right) of a 6 month old patient with a main pulmonary artery (MPA) band. The MPA is clearly seen with VISTA (arrow) but not 3D bSSFP (right) due to dephasing artifact from turbulent flow after the band.

The relative success rates of achieving a full sequential segmental diagnosis (i.e. identifying all thoracic cardiovascular elements) was compared between VISTA and bSSFP. A structure was recorded as visualized if its connections were identified and there was no image blurring affecting that structure.

Results: Twenty one patients underwent CMR (12 female). Mean age = 9.6 ± 7.4 years. The main indication for imaging was coronary anatomy (5 cases), pulmonary venous anatomy (4), aortic root anatomy (1) and complex single ventricle anatomy (3). The remaining cases received imaging for follow-up of repaired truncus arteriosus, tetralogy or transposition. In patients with CHD, 3D bSSFP failed to achieve full segmental diagnoses in all but 1 case (5 % success rate). Failure was due to dephasing artifacts of one or more pulmonary veins in 15 out of 21 cases. Three patients had poor image quality of head and neck vessels. Pulmonary arteries showed more than mild blurring in 3 cases (all with stenotic lesions causing dephasing artifacts).

In contrast, VISTA achieved full segmental diagnoses in 5 cases (23.8 % success rate). All failed cases were due to inadequate image quality of coronary origins while pulmonary vein visualization was successful in all cases. The combination of bSSFP and VISTA was able to provide the full segmental morphological diagnosis for all cases. A case where pulmonary arteries were visualized with VISTA but not 3D bSSFP (due to dephasing artifact from a pulmonary artery band) is shown in Figure 1. Example images from four patients with improved PV visualization are shown in Figure 2.

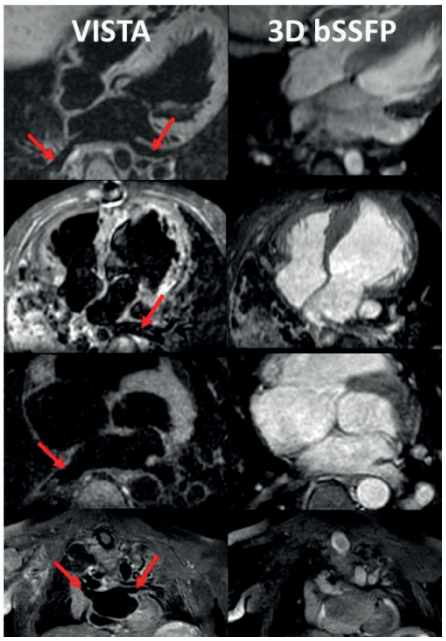

Figure 2. Example images from four patients with CHD. Red arrows mark the pulmonary veins which are well visualized on VISTA (left), but not sufficiently or not at all on 3D bSSFP (right).

Discussion: In this study, we have demonstrated the feasibility of VISTA for black-blood imaging of the whole heart and great vessels. As we have shown, VISTA offers very clear advantages in pulmonary vein imaging compared to 3D bSSFP, while 3D bSSFP provides superior coronary artery imaging. Structures that are prone to dephasing artifact in 3D bSSFP, such as stenotic lesions and pulmonary veins, tended to show good blood suppression and superior image quality using VISTA. This made the acquisition of both sequences complementary in achieving a full segmental diagnosis. With the advent of increased vigilance regarding the use of gadolinium-based contrast agents in children, clinicians may use the combination of 3D bSSFP and VISTA to achieve full segmental diagnosis and reduce the need for contrast agents.

Simultaneous Water-Fat Separation and Quantitative Susceptibility Mapping of the Carotid Artery Wall: Sequence and Processing Considerations

Pascal P R Ruetten[1], Jonathan H Gillard[1], Martin J Graves[1]
1 University of Cambridge, Department of Radiology

Purpose: Calcification and intra-plaque-haemorrhage are signs of carotid artery disease [1]. Their detection could be improved using quantitative susceptibility mapping (QSM). The presence of fat in the neck requires QSM processing to be modified. We have applied IDEAL water-fat separation, which corrects the field map required for QSM and also may help identifying the lipid-rich necrotic cores of carotid plaques [2,3,4]. In this work we investigated sequence and post-processing considerations to optimize QSM in carotid artery wall imaging.

Methods: Four volunteers were scanned on a 3T system (750, GE Healthcare Waukesha, WI) with a four-channel carotid coil (PACC, MachNet, Roden, The Netherlands) using a multi-echo gradient echo sequence: Four echoes, evenly spaced between 3.7ms, and 14.4ms were acquired. We repeated the scan with a parallel imaging factor of two (ASSET), reducing scan time from 5:43min to 2:51min. From the phase data (i) a field non-uniformity map (ΔB) of the neck was estimated using IDEAL [2,3] (ii) the background field was removed [5] (iii) and the susceptibility map was calculated via dipole field inversion[6-10]. Since the performance of the IDEAL algorithm depends heavily on the initial estimate of ΔB, we compared different values: a) 0 as suggested in literature ($\Delta B_{(a)}$) [2], b) background field, estimated from a field map calculated from all acquired echoes ($\Delta B_{(b)}$) [3,11-13], and c) background field, estimated from a field map calculated from the in-phase echoes only ($\Delta B_{(c)}$), which is a novel approach suggested by us.

Results & Discussion: Unaccelerated and accelerated datasets both produced water and fat fractions without any water-fat swaps (Fig. 1a). In areas close to the surface coils (ROI1,2,6), which contain the carotid arteries mean and standard deviation values for ΔB are similar for both datasets. In the centre of the neck (ROI3,4,5) both datasets have similar mean ΔB values but the standard deviation increased using parallel imaging. The air-tissue interfaces in the neck, cause large background fields. This leads to errors in IDEAL, when initializing ΔB to $\Delta B_{(a)}$ (Fig. 2a). The use of $\Delta B_{(b)}$ reduced some errors (Fig. 2b) but large areas of fat cause errors in the background field estimation. These can be avoided using in-phase echoes only. With an initial estimate of $\Delta B_{(c)}$ IDEAL produced reliable water and fat fractions in the entire region-of-interest (ROI) in all four cases (Fig. 2c). Therefore, QSM can be performed on the entire ROI (Fig. 3a), while in the other cases, a smaller ROI has to be drawn manually to exclude areas where the water-fat separation failed (Fig. 3b).

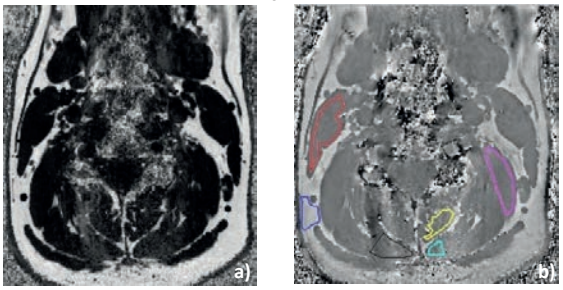

Figure 1: Fat fraction a) and ΔB b) calculated from the parallel imaging acquisition; Table compares ΔB of full and parallel imaging acquisition within the coloured regions

	Full Dataset	Parallel Imaging Dataset
ΔB ROI 1 (μ±σ)	0.02±0.05	-0.02 ±0.05
ΔB ROI 2	0.52±0.09	0.45±0.1
ΔB ROI 3	0.001±0.08	-0.016±0.16
ΔB ROI 4	-0.015±0.1	0.015±0.15
ΔB ROI 5	0.04 ±0.07	0.03 ±0.17
ΔB ROI 6	-0.004 ±0.06	-0.02 ±0.06

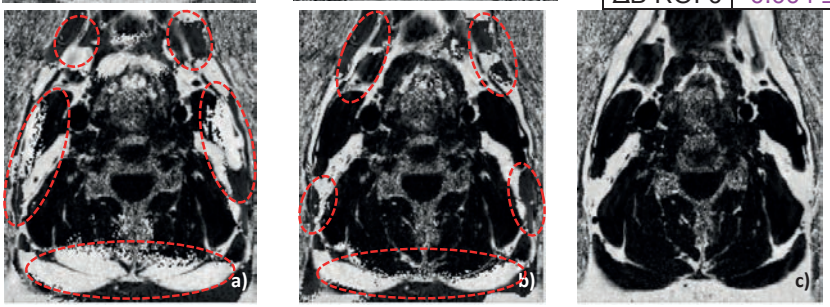

Figure 2: Fat fraction calculated with ΔB initialized to a) $\Delta B_{(a)}$, b) $\Delta B_{(b)}$, c) $\Delta B_{(c)}$ (-- indicates water-fat swaps)

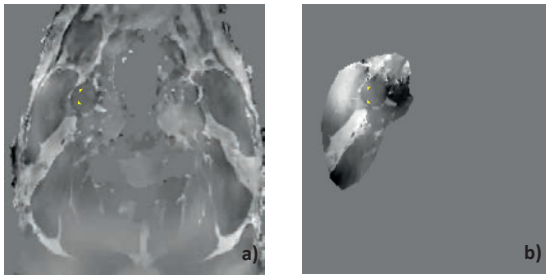

Figure 3: Susceptibility Map from a healthy volunteer with a full a) and reduced b) ROI due to IDEAL water-fat swaps ◣ indicates the carotid artery wall

References: [1]Gillard, J, et al., eds. Cambridge University Press, 2006.[2]Reeder, SB, et al. MRM 51.1 (2004): 35-45. [3]Dimov, AV, et al. MRM 73.6 (2015): 2100-2110.[4] Koppal, S, et al. MRM 78.1 (2017): 285-296. [5] Zhou, D, et al. NMR in Biomedicine 27.3 (2014): 312-319.[6]Liu, T, et al. MRM 69.2 (2013): 467-476.[7]Liu, J, et al. Neuroimage 59.3 (2012): 2560-2568.[8]Liu, T, et al. MRM 66.3 (2011): 777-783. [9]de Rochefort, L, et al. MRM 63.1 (2010): 194-206. [10]Shmueli, K, et al. MRM 62.6 (2009): 1510-1522.[11]Liu, T, et al. MRM 69.2 (2013): 467-476.[12]Kressler, B, et al. IEEE transactions on medical imaging 29.2 (2010): 273.[13]de Rochefort, L, et al. MRM 60.4 (2008): 1003-1009.[14]codes ref. in [5-13] avail. at http://weill.cornell.edu/mri/pages/qsm.html

Comparison of Multiple Normal Reference Structures for Vessel Wall Imaging MRI Sequences

MD Alexander, DL Parker, AH DeHavenon, SI Kim, JS McNally
Department of Radiology and Imaging Sciences, University of Utah, Salt Lake City, UT, USA

Purpose: To properly quantify degree of plaque enhancement on vessel wall imaging (VWI) MR sequences for the evaluation of intracranial atherosclerotic disease (ICAD), reliable references structures that normally enhance are needed. This study investigates multiple different structures that normally enhance following contrast administration to evaluate their degree of enhancement and inter-rater agreement. Validated references are important for future research that aims to better homogenize interpretation techniques in search of widely applicable results.

Methods: Prospectively maintained records were retrospectively queried to identify patients undergoing VWI for analysis of new infarcts at a major academic medical center. Patients were evaluated within 14 days of original MRI demonstrating restricted diffusion. All images were acquired on a Siemens Prisma 3T MRI scanner. Two reviewers were blinded to diffusion and clinical data and instructed to analyze the arterial tree to which the new infarct was referable. Each reviewer identified the most likely culprit lesion and obtained maximum voxel signal intensity values for the plaque on T1 DANTE images both before and after the administration of gadolinium contrast. Normal vessel was also evaluated. If a contralateral analogue with normal appearance was present, such a vessel was measured. In cases involving the basilar artery, the nearest normal segment was interrogated. Additionally, structures normally expected to enhance were measured, including the mid infundibulum, defined as the midway point between the inferior margin of the hypothalamus and the upper margin of the pituitary gland; low infundibulum, defined as the lowest segment of the infundibulum distinguishable from the pituitary gland; choroid plexus in a lateral ventricle; cavernous sinus, measured at a site clearly intravascular as seen on post-contrast images; and muscle, measured in the temporalis muscle in tissue with signal medial to the mid-belly fibrous band. For each variable measured, the mean of three data points were computed after obtaining the maximum single-voxel intensity values at each site of interest. Descriptive statistics were obtained, and Pearson's correlation coefficients calculated to evaluate inter-rater performance for evaluation of pre- and post-contrast measurements.

Results: 54 patients met inclusion criteria. Mean time to VWI after diagnosis of infarct was 7 days. Results are summarized in Table 1. Low infundibulum demonstrated the highest inter-rater agreement on pre- and post-contrast imaging. Muscle and normal vessel demonstrated high agreement on pre- and post-contrast measurements, respectively, but respective post- and pre-contrast values were poor.

	Pre-Contrast		Post-Contrast	
Structure	Mean Signal	r	Mean Signal	r
Plaque	162.5 (±42.0)	0.477	366.4 (±111.0)	0.915
Normal Vessel	112.5 (±27.8)	0.477	126.2 (±33.9)	0.709
Mid Infundibulum	159.9 (±32.0)	0.582	266.1 (±65.4)	0.586
Low Infundibulum	160.3 (±38.1)	0.798	275.9 (±71.4)	0.782
Choroid Plexus	157.4 (±38.9)	0.493	280.2 (±79.9)	0.584
Cavernous Sinus	138.4 (±38.2)	0.266	371.9 (±95.1)	0.44
Muscle	99.8 (±45.3)	0.784	134.5 (±29.2)	0.403

Discussion: To better standardize investigation of ICAD with VWI, quantitative techniques are needed. Plaque enhancement should be compared against enhancement of normal structures. In this study of several normally-enhancing structures, measurements of the low infundibulum had the highest inter-rater agreement on both pre- and post-contrast images. Such techniques merit investigation and incorporation of research using VWI to evaluate ICAD.

Vessel Wall Imaging using 3T MRI in Perforating Artery Infarction
- Difference between LSA and PPA -

Keiji Igase[1),2)], Nari Kimura[2)], Ichiro Matsubara[2)], Takanori Ohnishi[2)], Kazuhiko Sadamoto[2)]
1) Department of Advanced Neurosurgery, Ehime University Graduate School of Medicine
2) Department of Neurosurgery, Washokai Sadamoto Hospital, Matsuyama, Japan

(Introduction) Perforating artery infarction is mainly differentiated to 2 groups, lenticulo-striate artery (LSA) and prepontine paremedian artery (PPA). The injury of perforating artery results in round or oval shape of infarction in each arterial territory. Etiology of this disease is mainly related to the atherosclerosis of perforating artery itself or its parent artery. This time we observed the vessel wall in each parent artery of perforating artery infarction using 3T MRI and evaluated the deference between 2 groups.

(Methods) Consecutive 36 patients (mean age: 68.9±7.4 years old; Male 22 and Female 14) with acute infarction in the territory of perforating artery (26 in LSA and 10 in PPA groups) diagnosed by 3T MRI during 1 year (from April 2017 to March 2018) were enrolled in this study. All patients underwent 3T MRI (Discovery 750w: GE healthcare) and T1-BB CUBE image, which is one of 3D-FSE sequence created by GE healthcare, was acquired. On T1-BB CUBE image we assessed the appearance of vessel wall of parent artery, that is, middle cerebral artery for LSA and basilar artery for PPA group, where we especially observed the existence of high intensity plaque of the arterial wall. In case high intensity plaque was observed, we calculated their thickness and length.

(Results) High intensity plaque was observed in 12/36 cases, resulting in 6/26 cases of LSA group and 6/10 cases of PPA group, respectively, where there was significant difference between 2 groups in terms of existence of high intensity plaque ($p<0.05$, chi-square test). Out of 12 cases with high intensity plaque on T1-BB CUBE image mean thickness of the plaque was 1.3±0.3 mm in LSA group and 1.5±0.3 mm in PPA group, respectively, and no significant difference was observed. Meanwhile, mean length of the plaque in LSA group was 5.2±1.7 mm, that was significantly shorter than 8.3±1.3 mm in PPA group ($p<0.001$, paired T test)

(Discussion) In perforating artery infarction one-third cases exhibit high intensity plaque on T1-BB CUBE image and longer plaque formation seems to be seen in PPA cases than in LSA group. Given this result, atherosclerotic change may be prone to progress in basilar artery comparing with middle cerebral artery.

(Conclusion) A difference between 2 perforating artery groups was shown in terms of parent artery atherosclerosis. Further investigation would address the mechanism of this phenomenon and lead to some therapeutic modification.

Added Value of Femoral Artery Atherosclerosis for Determining Severity of White Matter Lesions: A 3D MR Vessel Wall Imaging Study

Xihai Zhao[1], Yang Liu[1,2], Yongjun Han[1], Maobin Guan[2], Ying Cai[3], Rui Li[1], Huijun Chen[1], Chun Yuan[1,4]

1.Center for Biomedical Imaging Research, Tsinghua University, Beijing, China; 2. Department of Radiology, Yangzhou University Affiliated Hospital, Yangzhou, China; 3. Department of Radiology, Taizhou People's Hospital, Taizhou, China; 4. Department of Radiology, University of Washington, Seattle, USA.

Purpose: Previous studies reported that carotid atherosclerosis was associated with white matter lesions (WML) [1,2]. This study sought to investigate the incremental value of femoral artery atherosclerosis for carotid atherosclerotic plaques in determining WML severity using 3D MR vessel wall imaging.

Methods: **Study sample**: The subjects were recruited from a pilot community study of CROP (Cardiovascular Risk of Old Population). The inclusion criteria are as follows: 1) age ≥ 60 years; 2) no cardiovascular symptoms within recent 6 months. **MR imaging**: All subjects underwent brain, carotid and femoral artery imaging on a 3.0T Philips MR scanner. A routine T2-FLAIR sequence was acquired to evaluate the WMLs. The carotid and femoral artery vessel wall was imaged by acquiring 3D MERGE and SNAP sequences with the following parameters: carotid imaging: 3D MERGE: FFE, TR/TE 9/4.2 ms, flip angle 6°; FOV 16×16×4 cm^3 for carotid artery and 30×40×6 cm^3 for femoral artery; spatial resolution 0.8×0.8×0.8 mm^3. 3D SNAP: FFE, TR/TE 10/4.8 ms, flip angle 11°/5°, FOV 16×16×4 cm^3 for carotid artery and 30×40×6 cm^3 for femoral artery; spatial resolution 0.8×0.8×0.8 mm^3. **Image interpretation**: The WMLs were evaluated on T2-FLAIR images and WML score > 3 was defined as severe MWLs. The morphology and presence of plaque, lipid-rich necrotic core (LRNC), and intraplaque hemorrhage (IPH) were evaluated. **Statistics**: The carotid and femoral artery plaque features were compared between subjects with WML≤3 and those with WML>3. Logistic regression and ROC analysis were used to determine the correlation between plaque features and WML>3.

Results: In total, 112 subjects (mean age, 72.0±5.6 years; 49 males) were included. Subjects with WML>3 showed significantly greater carotid wall area and femoral stenosis and higher prevalence of carotid calcification (45.2% vs. 22.2%), femoral calcification (48.8% vs. 23.5%) and LRNC (54.8% vs. 28.4%) compared to those with MWL≤3 (all p<0.05). Carotid calcification and femoral calcification, LRNC and stenosis (with 10% increment) were found to be significantly associated with MWL>3 before and after adjusted for clinical factors (OR ranged from 1.51 to 3.79, all p<0.05). ROC analysis showed, in discriminating WML>3, the AUC increased from 0.615 to 0.701 after combined femoral artery LRNC and stenosis with carotid calcification compared to carotid calcification alone and the AUC reached 0.754 after adjusted for hypertension and hyperlipidemia (Fig. 1). Fig. 2 represents a patient with femoral and carotid plaques and WML>3.

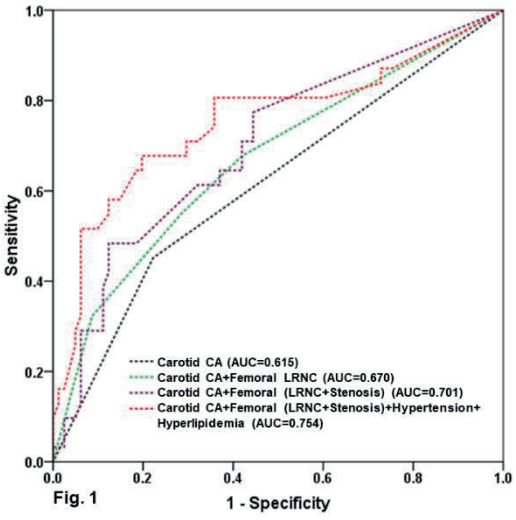

Fig. 1

Discussion and conclusions: We found that carotid and femoral artery plaque compositions, particularly calcification and LRNC were independently associated with severe WML (WML>3). Combination of femoral artery calcification and stenosis with carotid calcification had stronger predictive value for severe WML compared with carotid calcification alone. Our findings suggest that femoral artery atherosclerosis had added value for determining WML severity.

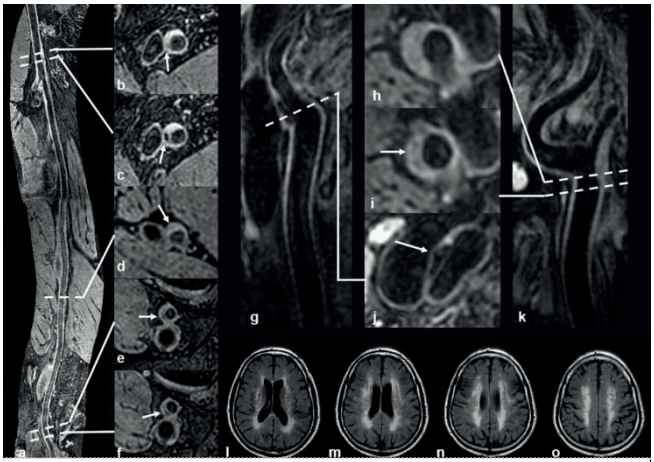

Fig. 2 Calcification (c, j) and LRNC (b, d, e, f, h, and i) in femoral and carotid arteries and the WML>3 (l-o) were seen.

References: [1] Manolio TA, et al. ATVB. 1999;19:356-65. [2] de Leeuw FE, et al. J Neurol. 2000;247:291-6.

Visualizing the Lumen and Wall of Intracranial Artery Stenosis Before and After Stenting Using High Resolution MRI Vessel Wall Imaging

Bing Tian[1], Zhang Shi[1], Xia Tian[1], Qi Liu[1], Jianping Lu[1], David Saloner[2,3]
1 Department of Radiology, Changhai hospital of Shanghai, Shanghai, China 2 Department of Radiology and Biomedical Imaging, UCSF, San Francisco, CA, USA 3 Radiology Service, VA Medical Center, San Francisco, USA

Purpose:

High resolution MRI vessel wall imaging provides important insights of assessing both vessel lumen and wall in intracranial artery stenosis disease. This study aims to compare the lumen stenosis and wall characteristics change on Vessel wall MRI imaging before and after (different time point) stenting. This would establish the method in evaluating the effect of using the stent for severe symptomatic atherosclerotic intracranial artery stenosis (≥70%).

Methods:

This was a retrospective study with patient consent. Thirty-two patients (20 male, age 55±13) underwent Wingspan stenting treatment due to intracranial artery stenosis⩾70% were included in this study between November 2011 and October 2017. Vessel wall MRI imaging(2D or 3D) was provided before and after stenting (average 354.1 days, range from 1 day to 36 months). Patients were divided into two groups(＜3 months and ⩾ 3 months) according to the time interval of vessel wall imaging after stenting. Pre and post-stenting intracranial artery stenosis was measured on post-contrast vessel wall image according to the WASID criterion. Wall characteristics was evaluated including the signal of plaque/vessel wall as well as the plaque/vessel wall enhancement, which were assigned by two neuroradiologists, respectively Plaque-to-thalamus signal intensity ratio on pre-contrast T1WI imaging was calculated to represent the signal of plaque/vessel wall. Plaque/vessel wall enhancement was compared using pre- and post-contrast T1WI vessel wall images, where the signal intensity of the plaque was compared with the signal intensity of pituitary. The degree of plaque/wall enhancement was categorized into 3 grades: grade 0 indicates no enhancement, grade 1 represents enhancement less than that of the pituitary infundibulum, and grade 2 represents enhancement equal to or greater than that of the pituitary infundibulum. Indeed, degree of stenosis, plaque-to-thalamus signal intensity ratio, plaque/vessel wall enhancement were compared between pre- and post-stenting as well as the change of different groups after stenting.

Results:

All patients got pre- and post-stenting vessel wall MRI imaging. The stent of 26 patients were placed on middle cerebral artery, and 6 were placed on basilar artery. The degree of stenosis was reduced from 86.1% ± 3.2% pre-stenting to 16.9% ± 6.5% post-stenting, which showed good consistency with DSA. The plaque-to-thalamus signal intensity ratio of post-stenting was lower than that of pre-stenting. There was no significant difference of stenosis and plaque-to-thalamus signal intensity ratio between different groups. Compared to pre-stenting imaging, the degree of plaque/wall enhancement showed no significant difference. But the plaque/wall enhancement score of ⩾3 months group was reduced more significant than that of ＜3 months group. Agreement between two reviewers were both excellent for the signal of plaque/vessel wall as well as the plaque/vessel wall enhancement.

Discussion:

Our studies showed that the degree of stenosis was reduced after stenting, which provide a useful method to demonstrate the effect of stenting regarding the lumen recanalization in patients with severe symptomatic atherosclerotic intracranial artery stenosis (≥70%). Many studies were performed to analyze the lumen of stenting including CTA and MRA. Previous methods yielded reliable results of lumen stenosis on post-stenting image due to the stent artifacts. Vessel wall MRI image showed good consistency with DSA regarding to stenosis of artery lumen after stenting. Besides the lumen recanalization, vessel wall MRI imaging also can show the wall characteristic changing after stenting. The signal of plaque and enhancement were both the important characteristic of atherosclerotic artery disease. Both the plaque-to-thalamus signal intensity ratio and plaque/vessel wall enhancement were changing significant after 3 months of stent placement, which may provide a direct method to monitor the plaque dynamic change after stent treatment.

References:

[1] Abe A, Sekine T, Sakamoto Y, et al. Contrast-Enhanced High-Resolution MRI for Evaluating Time Course Changes in Middle Cerebral Artery Plaques. J Nippon Med Sch. 2018;85(1):28-33.
[2] Shi M, Wang S, Zhou H, et al. Wingspan stenting of symptomatic middle cerebral artery stenosis and perioperative evaluation using high-resolution 3 Tesla MRI. J Clin Neurosci. 2012 Jun;19(6):912-4.

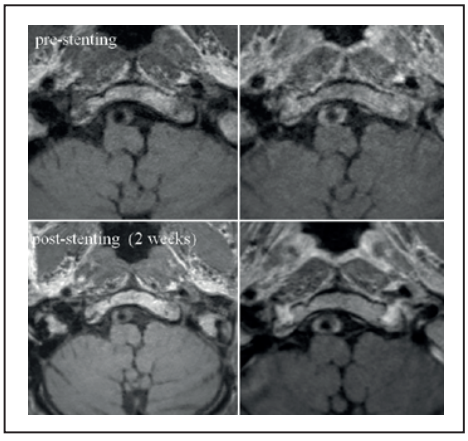

Figure 1

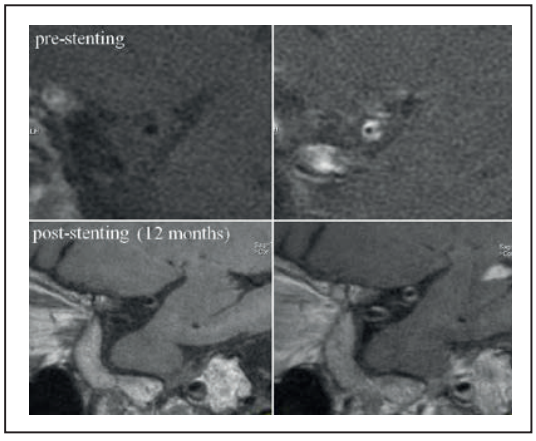

Figure 2

3D Radial Free-breathing Variable Flip Angle Whole Heart Myocardial T1 Mapping

Orhan Unal, Steve Kecskemeti, University of Wisconsin - Madison

Purpose: T_1 mapping is a promising technique to detect and quantify both focal and diffuse myocardial fibrosis at an early stage. Currently, several quantitative T_1 mapping techniques are used for assessing myocardial pathologies. Inversion recovery (IR) techniques such as MOLLI[1] are widely used due to higher precision and better reproducibility but tend to underestimate T_1 values due to heart rate dependence and range of T_1s. Each current method has its strengths and weaknesses in terms of accuracy, precision, and reproducibility. In this work, we present new, free-breathing, ECG-gated, 3D magnetization-prepared rapid acquisition gradient echo (MPnRAGE) undersampled radial and stack-of-stars (SOS) variable flip angle (VFA) techniques that are accelerated using radial k-space undersampling and are robust to transmit B_1^+ variations.

Methods: All imaging studies were performed on a 3 T scanner (GE Healthcare, Waukesha, WI) using the new techniques for myocardial T_1 quantification[2]. Inversion pulses are applied every three heartbeats and imaging is performed using an alternating VFA approach - 5° in the first heartbeat, 7° in the second, and 3° in the third. Respiratory motion is mitigated by utilizing a modified diminishing variance algorithm (DVA) with 50 % efficiency. 3D radial acquisitions were performed with FOV=25.6x25.6x25.6 cm, 2 mm isotropic resolution, flip angle=5,7,3°, BW=±62.5kHz, TR/TE=3.05/1.08 ms, acquisition window per heartbeat=200 ms, and scan time=9 min and 3D SOS acquisitions with FOV=25.6x25.6x12.8 cm, 2x2x8 mm resolution, flip angle=5,7,3°, BW=±62.5kHz, TR/TE=3.5/1.09 ms, acquisition window per heartbeat=200 ms, and scan time=6 min. Pixel-wise T_1 maps were obtained using a theoretical signal model and T_1 precision was determined from the standard deviation in a region-of-interest (ROI) over myocardium. In addition, we have also investigated the choice of flip angles and order and its effect on T_1 measurements.

T_1 Mapping Method	Mean T_1	Std Dev
Proposed 3D T1Map	565.56	6.8
2D FSE-IR	563.08	2.85
SMART1Map	564.48	7.61
MOLLI Corrected	502.36	5.13

Table 1: Mean T_1 values obtained in a uniform phantom with our new method, SMART1Map, and MOLLI are compared to reference T_1 obtained with FSE-IR.

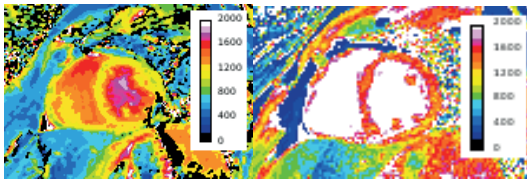

Figure 1: Mid short-axis native myocardial T_1 map of a healthy subject obtained with MOLLI (Left) and the proposed free-breathing 3D VFA IR T_1 mapping method (Right).

Results and Discussion: Table 1 shows the accuracy and precision of various T_1 mapping methods in a uniform phantom. T_1 values obtained with the proposed methods show good agreement with FSE-IR and SMART1Map[3] values and differ with MOLLI values, which are significantly lower. Note that the phantom T_1 value chosen (~565 ms) mimics expected T_1 values after Gd administration at 3T. T_1 profile across the phantom showed uniformity, due to robustness to B_1^+ variations and agreed with the FSE-IR T_1 profile. Figure 1 shows a mid short-axis native myocardial T_1 map of a healthy volunteer. Mean T_1 values for MOLLI and our 3D method are 1137±104 ms, and 1447±148 ms, respectively. While it's known that MOLLI underestimates T_1 values, it is still widely used due to its reproducibility and robustness. Our native T1 measurements in healthy subjects are closer to previously reported values at 3 T. The choice of flip angles (3,5,7 or 3,6,9) or the order (3,5,7 or 5, 7,3 or 7,5,3) studied in phantom experiments didn't have any significant effect on T_1 maps. Note that free-breathing 3D VFA IR T_1 mapping method currently utilize parallel imaging or redundant information across the inversion recovery curve. It is likely these approaches will further reduce the variance of our T_1 values. Additionally, our free-breathing 3D radial method should simplify scan prescription and reduce patient discomfort while providing whole heart coverage that accounts for transmit B_1^+ and inversion efficiency.

References:

1. Messroghli DR, Radjenovic A, Kozerke S, Higgins DM, Sivananthan MU, and Ridgway JP. Modified Look-Locker inversion recovery (MOLLI) for high resolution T_1 mapping of the heart. MRM 2004;52:141.
2. Kecskemeti S, Johnson K, Francois C, Schiebler M, and Unal O. Volumetric Late Gadolinium-Enhanced Myocardial Imaging with Retrospective Inversion Time Selection. JMRI 2013;38:1276.
3. Slavin GS, Stainsby JA. True T_1 mapping with SMART1Map (saturation method using adaptive recovery times for cardiac T_1 mapping): a comparison with MOLLI. JCMR 2013;15:3.

Low-dose time-resolved and single-phase high-resolution contrast-enhanced MRA in single session: effectiveness in detection spinal vascular diseases

Bum-soo Kim[1], Yangsean Choi[1], Borim Park[1], Na-Young Shin[1], Jinhee Jang[1], Hyun Seok Choi[1], So Lyung Jung[1], Kookjin Ahn[1]

[1]Department of Radiology, Seoul St. Mary's Hospital, The Catholic University of Korea, Seoul, South Korea

Purpose: We report effectiveness of combined low-dose time-resolved and single-phase high-resolution (HR) contrast-enhanced MRA (CE-MRA) at 3.0T in noninvasive detection and characterization of spinal vascular diseases.

Methods: We retrospectively reviewed 15 consecutive patients with a suspected spinal vascular disease. All patients underwent combined low-dose TR CE-MRA and 3D single-phase HR CE-MRA at 3T, followed by spinal DSA within 90 days. Six patients had had additional follow-up spinal MRA and DSA after treatment. The spinal lesions were analyzed for the presence and type of spinal vascular disease as well as the side, level, and number of arterial feeders.

Results: On spinal DSA, 13 patients were diagnosed with spinal dural arteriovenous fistula (dAVF, n=7), perimedullary AVF (PMAVF, n=4), spinal cord AVM (scAVM, n-=2). Two patients showed no spinal vascular abnormality. One patient with spinal dAVF which had been obliterated by surgery, developed another spinal dAVF at different level 4 years later. One patient was found with remnant extraspinal dAVF on follow-up after surgery, whereas 5 patients showed no remnant lesions on follow-ups. CE-MRA correctly detected spinal vascular lesions in 13/15 cases (87.8%). TR CE-MRA demonstrated early venous visualization and aided in proper placement of following HR CE-MRA in all patients including 2 patients with high or low level of shunt and feeding artery (Figure 1). For the detection of arterial feeder of spinal vascular diseases, HR CE-MRA correctly identified the location of the arterial feeder to within 1 vertebral level in 17/24 feeders (70.8%).

Discussion: Spinal cord MRA is useful in pre-angiographic evaluation of spinal vascular diseases, but its limited FOV hinders detection of the relatively long spinal axis in a single MRA session. In our series, low-dose (0.03 mmol/kg) injection of contrast media was sufficient to suggest the possible level of shunt by a sequential demonstration of the prominent venous sac (in spinal AVM) and the dilated perimedullary vein (Figure 1). Thus, low-dose TR CE-MRA can effectively assess arteriovenous shunts and flow patterns of venous drainage as well as test-bolus function and guidance of the placement of subsequent single-phase HR CE-MRA. In conclusion, spinal CE-MRA, with combined acquisition of low-dose TR CE-MRA and single-phase HR CE-MRA at 3 T is effective in detection of spinal vascular diseases.

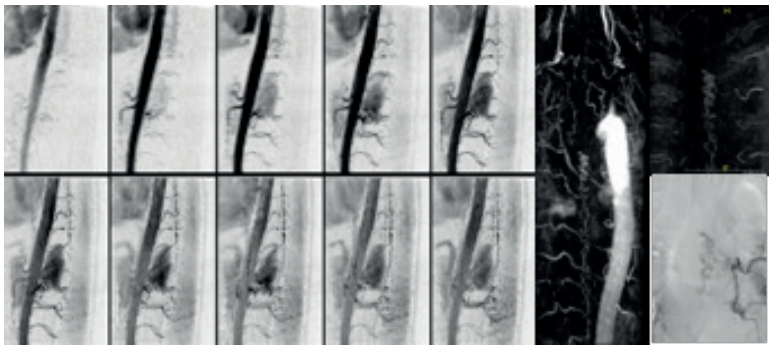

Figure 1. A 53-year-old man with spinal DAVF. TR CE-MRA (B) showed visualization of dilated perimedullary veins from the top of field-of-view. MIP images of entire FOV (C) and coronal segmental MIP image (D) of 3D single-phase HR CE-MRA revealed fistula at the left T6 level. Spinal DSA (E) confirmed spinal DAVF with shunt located at the matched level.

References: 1. Lindenholz A, TerBrugge KG, van Dijk JM, Farb RI. The accuracy and utility of contrast-enhanced MR angiography for localization of spinal dural arteriovenous fistulas: the Toronto experience. Eur Radiol 2014; 24: 2885-2894. 2. Amarouche M, Hart JL, Siddiqui A et al. Time-resolved contrast-enhanced MR angiography of spinal vascular malformations. AJNR Am J Neuroradiol 2015; 36: 417-422. 3. Ali S, Cashen TA, Carroll TJ et al. Time-resolved spinal MR angiography: initial clinical experience in the evaluation of spinal arteriovenous shunts. AJNR Am J Neuroradiol 2007; 28: 1806-1810.

Development of a targeted contrast agent for MR molecular imaging of EDB-FN

Jing-Can Qin, Nadia Ayat, Sarah Roelle, Zheng-Rong Lu
Department of Biomedical Engineering, Case Western Reserve University, Cleveland, Ohio, 44106, USA.

Purpose: MR molecular imaging (MRMI) has the potential to measure biochemical and pathological biomarkers related to life-threatening diseases, including cardiovascular diseases and cancer for early accurate disease detection and characterization. Extradomain B fibronectin (EDB-FN) is identified in both animal and human plaques and cancers. It is known that EDB-FN is involved in promoting angiogenesis, which leads to proliferation of vasa vasorum (1). It appears that the rupture of vasa vasorum is directly related to intraplaque hemorrhage and thus plaque instability. EDB-FN is highly expressed in the extracellular matrix of plaques and cancers and is a potential clinical biomarker for non-invasive characterization of these life-threatening diseases. This work is focused on development of a targeted MRI contrast agent specific to EDB-FN for early detection and characterization of cardiovascular diseases and cancer.
Methods: ZD2 peptide specific to EDB-FN was synthesized using solid phase chemistry (2,3). A targeted MRI contrast agent ZD2-N_3-Gd(HP-DO3A) was synthesized by the conjugation of ZD2 peptide with a clinical macrocyclic contrast agent Gd(HP-DO3A). The effectiveness of the contrast agent for MRMI of EDB-FN was evaluated on a 7T Bruker small animal MRI scanner with mice bearing aggressive PC3 human prostate tumor with high expression of EDB-FN and slow growing LNCaP tumor with low EDB-FN expression.
Results: ZD2-N_3-Gd(HP-DO3A) has T_1 and T_2 relaxivities of 5.44 and 7.10 $mM^{-1}s^{-1}$ at 1.4 T, and 5.53 and 7.81 $mM^{-1}s^{-1}$ at 7 T, respectively, much higher than clinical agent Gd(HP-DO3A). ZD2-N_3-Gd(HP-DO3A) produced robust contrast enhancement in aggressive PC3 tumors for at least 30 minutes post-injection and little enhancement in slow-growing LNCaP tumors at a dose of 0.1 mmol/kg. It produced 400% CNR increase in the T_1-weighted 2D spin-echo MR images of aggressive PC3 tumors as compared to CNR in LNCaP tumors.
Discussion: MRMI with a small molecular targeted contrast agent ZD2-N_3-Gd(HP-DO3A) is effective to image the expression level of EDB-FN in diseased tissues after intravenous injection at a clinical dose. Because EDB-FN expression is also associated with angiogenesis in plaques and proliferation with vasa vasorum, MRMI of EDB-FN in the plaques has the promise for detection and characterization of vulnerable plaques. Further studies will be performed to assess the potential of the targeted contrast agent for MRMI of atherosclerotic plaque.

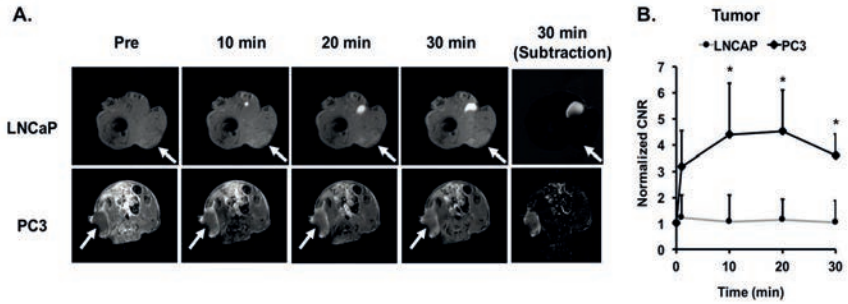

Figure 1. 2D axial MRI images of PC3 and LNCaP tumor bearing mice were taken at 10, 20 and 30 min post injection of ZD2-N3-Gd(HP-DO3A). Contrast enhancement was observed as fast as 10 min post injection in PC3 tumor bearing mice.

References:
1) Matter, C. M., et al. *Circ Res. 2004, 95*, 1225-33. 2) Li Y, et al. *Mol Pharm.* 2017, 14, 3906-3915. 3) Han Z, et al. *Bioconjug Chem.* 2017;28, 1031-1040.

Using non-contrast navigator MRA to decrease scan times of MR aorta

Michelle Walkden, Dr Sophie Willis and Dr Stephen Harden

Purpose

Our busy Cardiac MR unit scans approximately 3000 patients per year and is getting busier. Pressure on the service requires reduced scan times by optimising the imaging-sequence protocol, without compromising patient care or diagnostic utility of the subsequent images.

Free-breathing, ECG-triggered, navigator-gated 3D segmented steady state free precession (SSFP) non-contrast MRA (navigator) is used in some centres, but its diagnostic efficacy and utility is not fully explored within the literature. This sequence has long been established as an alternative imaging tool to 3D CE-MRA. When compared to the routine MR sequences and ECG gated CT angiography (considered to be the gold standard) the Navigator sequence showed the best agreement with CTA. Advances in imaging techniques have led the Navigator sequence argued by some authors, to be the MRA technique of choice for the assessment of the thoracic aorta diameters in clinical practice.

The purpose of study is to explore whether the image quality, diagnostic accuracy and utility of Free-breathing, ECG-triggered, navigator-gated 3D segmented steady state free precession (SSFP) MRA is equal to or better than HASTE and 2D SSFP cine imaging +/- contrast enhanced MRA for structural aortic disease. This would permit the shortening of the current imaging protocol in the diagnosis of thoracic aorta pathology whilst maintaining diagnostic image quality.

Method

This is a prospective examination of 50 patients, aged 18 years and over with suspected or known thoracic aortic disease, using a Siemens 1.5T Avanto scanner. All patients are being scanned using the same imaging protocol. 2 Consultant Cardiothoracic Radiologists evaluate the images in each case for image quality, artefacts and visualisation of anatomy and pathology. Both Radiologists are blinded to patient information. In order to minimise interobserver variances both Radiologists measure the aortic diameter at the mid ascending aorta, mid arch of the aorta, mid descending aorta and at the level of the diaphragm on the HASTE, sagittal oblique SSFP cines of the aorta, the Navigator and CE-MRA if performed. The radiologists also provide an opinion on whether the standard sequences provide any detail over and above that provided by the Navigator sequence and vice versa. This study will run from February to June 2018.

Results

Recruitment for this study is ongoing but so far we have 20 patients (only 1 contrast-enhanced MRA has been done). With this sample of patients the mean time for completing the navigator sequence is considerably less (5.46 mins) than the time taken to comlete the short-axis and arch cines (13.31 mins). Of the scans done the initial assessment of image quality is that the navigator is just as good.

Conclusion

The full results will be presented at the conference but our initial results suggest we can decrease the scan time in thoracic aorta patients while maintaining and in some cases better image quality.

Hemodynamics assessed with Dual-*Venc* 4D flow MRI in patients with cerebral aneurysms

Susanne Schnell[1], Maria Aristova[1], Liliana Ma[1], Alireza Vali[1], Emilie Bollache[2], Alex J. Barker[1], Michael C. Hurley[1], Matthew B. Potts[1], Babak S. Jahromi[1], Michael Markl[1], Sameer A. Ansari[1]
[1] Northwestern University, [2] Sorbonne Université, CNRS, INSERM

PURPOSE: The hemodynamics of cerebral aneurysms are new imaging biomarkers for prediction of aneurysm rupture. Previous studies showed that aneurysm morphology, flow characteristics, and vessel wall properties can be substantially different between individual patients who are considered to have similar risk of rupture according to standard clinical indicators. Hemodynamic parameters such as inflow jet patterns and wall shear stress (WSS) have been investigated in previous studies. Since blood flow velocities within a single aneurysm can differ by an order of magnitude (high inflow jets with 150cm/s vs. slow flow recirculation with 10cm/s), dual-*venc* 4D flow MRI was proposed for intracranial applications (1). This is the first study to apply dual-*venc* 4D flow MRI to patients with cerebral aneurysms.

Patient	Aneurysm location and size (mm)	Risk factors
1	Left ACA 5.5 x 5.5 x 5.5	HTN, Smoking
2	Left VA 6 x 4 x 11	HTN
3	Acomm 5.5 x 8.5 x 10	Ex-Smoker
4	Left MCA 12 x 13 x 11	HTN, HL
5	Acomm 5 x 6.5 x 6	HL
6	Right Pcomm 5 x 5 x 5	HTN, HL
7	Left ICA 9 x 10 x 10	HTN, Ex-Smoker
8	1. Left ICA 7 x 7 x 7 2. Right ICA 5 x 5 x 5	HL, Ex-Smoker
9	1. Left ICA 11 x 8 x 7 2. Right ICA 6 x 6 x 7	SLE/Collagen Vascular Disease
10	Left VA 8 x 7 x 9	None
11	Left ICA 9 x 12 x 9	HTN
12	Left VA 9 x 7 x 15	HL, Ex-Smoker

METHODS: A fully integrated dual-*venc* 4D flow MRI sequence (1) with a shared reference scan (7-point encoding) on a 3T MRI scanner (Skyra MAGNETOM, Siemens, Germany) was used in 12 cerebral aneurysm patients (66 ± 9 years old, 8 women), who presented with a total of 14 cerebral aneurysms (Table). kt-GRAPPA acceleration with R=5 was used (2) with the following average scan parameters: in-plane resolution = $(1.0\text{x}1.0\text{mm})^2$, 1.1mm slice thickness, TE/TR = 3.5/6.2ms, temporal resolution = 57ms. A combined dual-*venc* data set was reconstructed using the high-*venc* acquisition to unwrap the low-*venc* data, while maintaining the favourable velocity to noise ratio of low-*venc* data (1). Additionally, the high-*venc* data set from the same measurement was used for comparison, and considered as if acquired as single-*venc*. Based on the calculated PC-MR angiogram, intracranial vessels and aneurysms were manually segmented (MIMICS, Materialize, Belgium). Segmentations and flow data were loaded into commercial software (ENSIGHT, CEI, USA) for 3D visualization of blood flow through the intracranial vessels and aneurysms. Magnitude velocities, and WSS of all time points as well as streamlines of high-*venc* (HV) and dual-*venc* (DV) scans from the same acquisition were compared.

RESULTS: Dual-*venc* 4D flow MRI data were successfully acquired in all patients. Figure 1 shows that especially in slow flow regions, dual-*venc* streamlines were less noisy and more collinear, resulting in an improved depiction of flow patterns (increased streamline density, reduced noise along individual traces) compared to the high-*venc* acquisition. Correlation between high-*venc* and dual-*venc* velocities within aneurysms and WSS at aneurysms walls (Figure 2) demonstrates excellent agreement (velocity: R= 0.92, P<0.00001, wall shear stress: R= 0.95, P<0.00001).

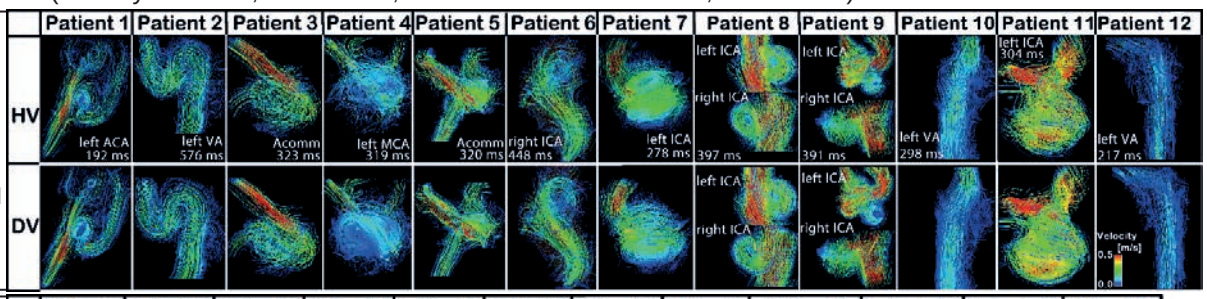

Figure 1: Blood flow visualization within aneurysms using streamlines for 1 time-point of cardiac cycle for dual- (bottom) and high-*venc* (top).

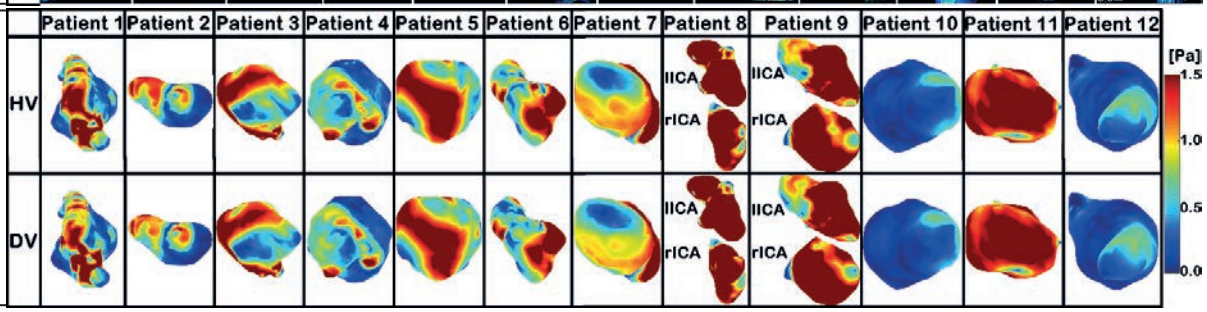

Figure 2: magnitude of WSS vectors time point of highest WSS plotted along wall of all aneurysms for dual- (bottom) and high-*venc* (top).

DISCUSSION: Assessment of hemodynamics with dual-*venc* 4D flow MRI in cerebral aneurysms demonstrated less noisy streamlines and higher sensitivity to low velocities, providing a more complete evaluation of the velocities occurring in individual aneurysms. Also, quantitative calculation of velocity and WSS showed similar results with minor differences in areas with low values. Due to its ability to detect subtle hemodynamic changes for improved aneurysm differentiation, dual-*venc* 4D flow MRI may have the potential to improve risk stratification by relating risk of rupture with differences in WSS and intra-aneurysmal 3D velocity distribution.

REFERENCES: (1) Schnell et al, JMRI 2017 (2) Jung et al, JMRI 2008

ACKNOWLEDGEMENTS: Grant support by AHA Scientist Development Grant 16SDG30420005 and NIH R01HL115828.

Quantitative Analysis of Plaque Enhancement on Vessel Wall Imaging MRI Sequences for Intracranial Atherosclerosis

MD Alexander, JS McNally, DL Parker, SE Kim, AH DeHavenon
Department of Radiology and Imaging Sciences, University of Utah, Salt Lake City, UT, USA

Purpose: Vessel wall imaging (VWI) MR techniques have provided new tools for evaluation of intracranial atherosclerotic disease (ICAD). However, techniques and interpretation can differ considerably among interpreters and sites. This study investigates quantitative methods for VWI evaluation of ICAD that can be applied to future research to better homogenize interpretation techniques and lead to more applicable results.

Methods: Prospectively maintained records were queried to identify patients undergoing VWI for analysis of new infarcts at a major academic medical center. Patients were evaluated within 14 days of original MRI demonstrating restricted diffusion. All images were acquired on a Siemens Prisma 3T MRI scanner. Two reviewers were blinded to diffusion and clinical data and instructed to analyze the arterial tree to which the new infarct was referable. Each reviewer identified the most likely culprit lesion and obtained maximum voxel signal intensity values for the plaque on T1 DANTE images both before and after the administration of gadolinium contrast. For each variable measured, the mean of three data points were computed after obtaining the maximum single-voxel intensity values at each site of interest. Additionally, degree of stenosis, presence of outward remodeling, and presence of intraplaque hemorrhage were noted. Descriptive statistics were obtained for all variables, and Pearson's correlation coefficients were obtained to evaluate inter-rater performance for evaluation of pre- and post-contrast measurements.

Results: 54 patients met inclusion criteria. Mean time to VWI after diagnosis of infarct was 7 days. Mean pre-contrast signal for plaques was 162.5 (±42.0), r=0.4772. Mean post-contrast signal for plaques was 366.4 (±111.0), r=0.915. Mean difference between post- and pre-contrast signal was 184.3 (±114.1), r=0.819. Mean stenosis was 57.7%. 34 (62.9%) demonstrated eccentric remodeling, and 2 (3.7%) demonstrated intraplaque hemorrhage; there was uniform agreement between raters on these two measures.

Discussion: As evaluation of ICAD with VWI becomes more widely accepted, standardized methods of investigation are needed to improve reproducibility and better assess impacts of these techniques on patient outcomes. The quantitative approach described in these methods demonstrates high inter-rater agreement, particularly with respect the post-contrast signal intensity within ICAD plaques. Such reproducible quantitative techniques warrant further investigation and should be implemented in future research of VWI for the evaluation of ICAD.

Highly accelerated 4D flow with compressed sensing for evaluation of aortic hemodynamics

Liliana Ma[1,2], Hyungkyu Huh[1], Kelvin Chow[1,4], Christoph Forman[5], Andreas Greiser[5], Susanne Schnell[1], Alex Barker[1], Michael Markl[1,2], Ning Jin[3]

[1]Department of Radiology, Feinberg School of Medicine, Northwestern University, Chicago, IL, United States, [2]Department of Biomedical Engineering, Northwestern University, Chicago, IL, [3]Cardiovascular MR R&D, Siemens Medical Solutions USA, Inc., Cleveland, OH, United States, [4]Cardiovascular MR R&D, Siemens Medical Solutions USA, Inc., Chicago, IL, United States, [5]Siemens Healthcare, Erlangen, Germany

Purpose: While the potential utility of 4D flow MRI has long been known, clinical applications are still limited due to the characteristically long scan times of multi-dimensional imaging. Recently, a highly accelerated, compressed sensing (CS) 4D flow framework with navigator gating and prospective ECG triggering was developed and tested in five volunteers.[1] This framework allows 4D flow imaging of the thoracic aorta in under three minutes, with inline image reconstruction on the scanner taking less than five minutes. The purpose of this study was to extend the previously described CS framework to retrospective ECG gating and to evaluate its feasibility in a realistic aortic flow phantom and a larger study cohort.

Methods: 4D flow imaging of the thoracic aorta was acquired in 16 healthy volunteers (age=43.6±17.7 years, 7M) and one bicuspid aortic valve (BAV) patient (age=71 years, F) on a 1.5T MAGNETOM Aera (Siemens Healthcare, Erlangen, Germany) using a prototype retrospectively-gated CS 4D flow sequence (TE/TR = 2.3/5.1 ms, 2 views per segment, spatial resolution = 2.4-2.5x2.4-2.5x2.4-2.5 mm^3, Venc = 1.5 m/s, 18-32 reconstructed cardiac phases) with an effective acceleration rate of R=7.7. 4D flow data were also acquired in vitro in a pulsatile, 3D-printed aortic phantom with an 80% coarctation in the descending aorta (DAo) using acceleration factors ranging from R=5.7 to 14.4 (TE/TR = 2.2/4.5 ms, spatial resolution = 2.2-2.3 mm^3, Venc = 2.2 m/s). For comparison, a conventional 4D flow sequence with R=2 GRAPPA acceleration and equivalent spatial/temporal resolution and coverage was acquired for all subjects and phantom. After background phase correction, noise filtering, and anti-aliasing, a 3D segmentation of the thoracic aorta (Mimics, Materialise, Belgium) was created based on a calculated 3D phase contrast-MR angiogram. Velocity maximum intensity projections (MIPs, fig. **1**) were used to visualize blood flow and quantify peak systolic velocities (PV) in 3 selected regions of interest (**Fig. 1a**, left): the ascending aorta (AAo), aortic arch (arch), and DAo. Nine 2D planes were placed orthogonally along the entire aorta for time-resolved evaluation of flow (**Fig. 1a**, right).

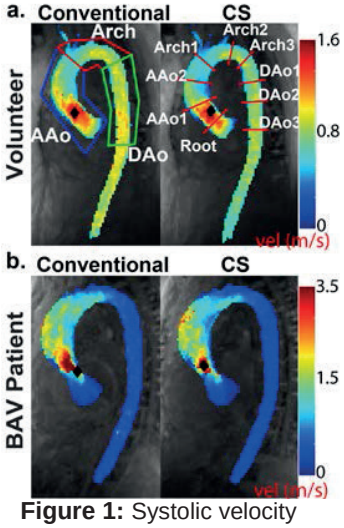

Figure 1: Systolic velocity MIPs of *a*, a representative volunteer and *b*, BAV patient.

		Phantom				Volunteers
		R5.7	*R7.7*	*R10.3*	*R14.4*	
% Change in CS Peak Flow						
Planes	*AAo1*	-3.7	-3.4	-1.2	-14.6	0.9±6.1
	Arch1	-9.1	-4.9	-7.2	-4.1	-6.8±5.4*
	DAo1	-4.2	-1.5	-17	-16.0	-8.6±4.5*
	DAo2	-5.8	1.5	-7.3	-14.2	-12.4±6.0*
% Change in CS Peak Velocity						
		-2.2	-2.4	0.8	-6.3	-8.5±8.1*

Table 1: % Change in CS Peak Flow and PV compared to conventional 4D flow in volunteer cohort and phantom at different acceleration factors (R).

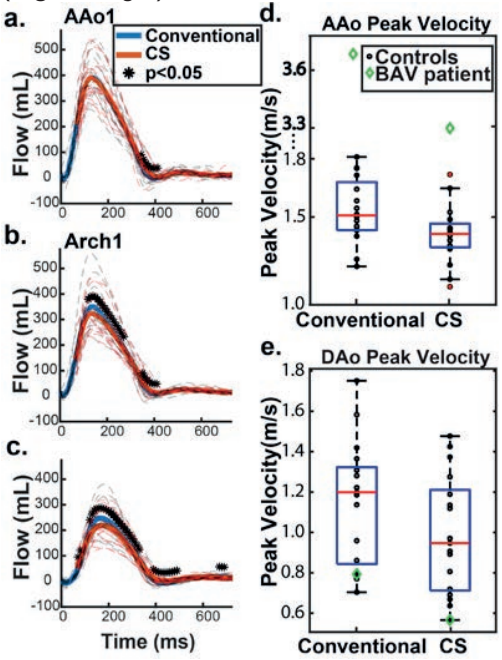

Figure 2: *a-c*, averaged and individual flow time curves of healthy volunteers interpolated to 10 ms. Black and red dotted lines represent individual conventional and CS flow curves, respectively. *d,e*, AAo and DAo peak velocities. Red lines=median, blue=25th-75th percentile.

Results: An acceleration rate of 7.7 was used in CS in-vivo acquisitions based on in-vitro analyses, where R=7.7 resulted in peak flows and velocities that were consistently comparable to conventional 4D flow (**Table 1**). Total scan time for in-vivo CS and conventional 4D flow were 1.9±0.3 min. and 7.8±3.9 min., respectively. While the MIPs and flow curves depict visually similar hemodynamics (**Fig. 1, 2**), peak velocities were significantly underestimated by CS compared to conventional 4D flow (AAo: 1.4±0.5 vs. 1.5±0.5 m/s, Arch: 1.0±0.2 vs. 1.1±0.3 m/s, DAo: 1.0±0.3 vs. 1.2±0.3 m/s, p<0.001). This relationship was also seen in the BAV patient (Conventional: AAo PV = 3.7 m/s, Arch = 1.8, DAo = 0.8 m/s; CS: AAo = 3.3 m/s, Arch = 1.5 m/s, DAo = 0.6 m/s). Peak flow in all planes except AAo1 and AAo2 was significantly lower (3.3-12.4% decrease, p<0.01, **Table 1**) in the CS acquisition. Both flow curve and peak flow analyses suggest that the % underestimation in peak flow is statistically significant past the AAo and becomes more severe in the DAo.

Discussion: This study demonstrates the clinical feasibility of highly accelerated 4D flow in a <2-minute aortic protocol with fast inline reconstruction. While CS 4D flow significantly underestimated peak velocities and peak flows at the aortic root, arch, and DAo, the percent difference in these parameters was generally within reasonable limits for in-vivo applications (< 9% for peak velocity, < 13% for peak flow, **Table 1**). Future investigations will include increased patient recruitment and CS reconstruction using different regularization weights for improved quantitative agreement between the two methods. **References:** [1] Jin, N et al. ISMRM 2018; [2] Forman, C et al. MR MatPhys 2014;

Quantitative 3D Dynamic Contrast Enhanced (DCE) MR Imaging of Carotid Vessel Wall by Fast T1 Mapping Using Multitasking

Nan Wang[1,2], Anthony G. Christodoulou[1], Yibin Xie[1], Zixin Deng[1], Bill Zhou[3], Zhaoyang Fan[1], Wei Yu[4], Debiao Li[1,2]
[1]Biomedical Imaging Research Institute, Cedars-Sinai Medical Center, Los Angeles, CA, USA, [2]Department of Bioengineering, University of California, Los Angeles, CA, USA, [3]David Geffen School of Medicine, University of California, Los Angeles, CA, USA, [4]Department of Radiology, Anzhen Hospital, Beijing, China

Introduction:

Dynamic contrast enhanced (DCE) MRI is a promising method in assessing the density and permeability of carotid adventitial vasa vasorum, which plays a significant role in the plaque inflammatory processes and disease progression[1]. However, the wide application of DCE in the evaluation of vascularity properties remains technically challenging: 1) it is hard to achieve submillimeter spatial resolution, adequate temporal resolution and entire carotid coverage at the same time, so compromises have to be made in current methods[2,3]; 2) the assumption of linearity between signal intensity and contrast agent concentration can introduce errors in kinetic modeling. In this work, we developed a Multitasking DCE MRI method with dynamic T1 mapping at 0.7 mm isotropic spatial resolution, 0.6 s temporal resolution and entire carotid vasculature coverage.

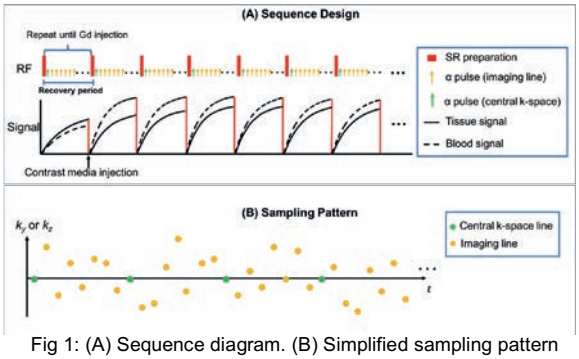

Fig 1: (A) Sequence diagram. (B) Simplified sampling pattern

Methods:

The proposed method implemented the newly developed MR Multitasking framework based on low rank tensor (LRT) model[4]. Non-selective SR preparation pulses followed by FLASH readout was designed to generate and acquire the T1 information (Figure 1A). A 3D Cartesian sampling trajectory was implemented with randomized reordering in ky and kz directions (Figure 1B). The central k-space line was collected every 8 readout lines as LRT subspace training data. In the reconstruction, image was formulated as a 3-way tensor $\mathcal{A}$ with voxel dimension $\mathbf{r} = (x, y, z)$, SR time τ, and DCE time t. Multi-dimensional correlation induces $\mathcal{A}$ to be low-rank, therefore can be factorized as $\mathbf{A}_{(1)} = \mathbf{U}\mathbf{\Phi}$. $\mathbf{\Phi}$, the weighted product of temporal basis functions describing T1 relaxation and contrast agent dynamics, is first determined from the subspace training data. $\mathbf{U}$, which contains spatial coefficients, is then recovered by fitting $\mathbf{\Phi}$ to the remainder of the sparsely sampled data.

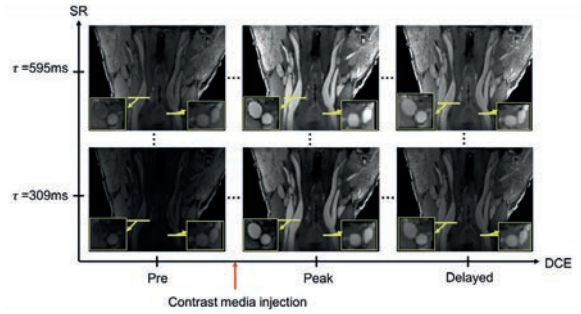

Fig 2: Representative images at different SR and DCE phases

In this study, healthy volunteers (n = 14) were scanned on a 3T Siemens Verio scanner and patients with known carotid atherosclerosis (n = 7) were scanned in Anzhen Hospital using following parameters: coronal orientation, FOV = 150x150x26 mm^3, spatial resolution = 0.7 mm isotropic, DCE temporal resolution = 595 ms, scan time = 9.8min. Gadovist (0.1 mmol/kg) was administered at the rate of 1.0 ml/sec with 20 ml saline flush. AUC, v_p and K^{trans} were evaluated for each subject

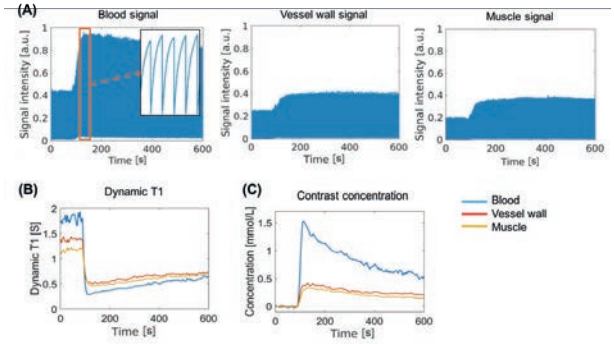

Fig 3: Real time signal evolution and dynamic T1 mapping

Results

Figure 2 shows a representative image set of Multitasking DCE at different SR recovery times and different DCE phases. Figure 3 demonstrates the real-time signal evolution of the proposed method. Figures 4 shows kinetic parameter fitting of a healthy volunteer and a patient, respectively.

Table 1 lists statistical comparison of the kinetic parameters between the control group and patient group, where significant differences were observed for all parameters.

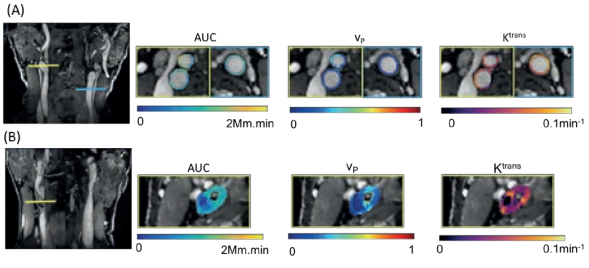

Fig 4: Parametric mapping for (A) a healthy subject and (B) a patient

Conclusion

We developed a novel Multitasking DCE method with high spatiotemporal resolution, large anatomical coverage based on dynamic T1 mapping for imaging carotid vessel wall. In vivo feasibility were demonstrated by the studies on healthy volunteers and patients with known carotid atherosclerosis. Further clinical validation is warranted.

Reference:

1 Kerwin, W. *et al. Circulation* 2003
2 Dong, L. *et al. Radiology* 2011
3 Calcagno, C. *et al. NMR Biomed* 2015
4 Christodoulou, A. *et al*. Nature Biomed Eng 2018:in press

Table 1: Statistical result of kinetic parameters

	v_p	K^{trans} (min^{-1})	AUC (mM·min)
Control	0.10 ± 0.02	0.05 ± 0.01	0.42 ± 0.12
Patient	0.13 ± 0.03	0.06 ± 0.01	0.63 ± 0.13
P value	< 0.001	0.011	0.002

Dynamic Fast Spin Echo Single Image Super-resolution Using Generative Adversarial Network

Roberto Souza[1], Mariana Bento[1,2], Richard Frayne[1]
[1]*Radiology and Clinical Neurosciences, Hotchkiss Brain Institute, University of Calgary, Calgary, AB, Canada*
[2]*Calgary Image Processing and Analysis Centre, Foothills Hospital, Calgary, AB, Canada*

Purpose: Stroke is a common cause of death in the developed world. Stroke risk from carotid artery atherosclerosis can be assessed through the trifecta of lumen stenosis, wall composition, and carotid wall distensibility. In this work we focus on carotid distensibility, which has been previously measured by Computed Tomography angiography at an in-plane resolution of 0.2 mm x 0.2 mm.[1] MR techniques to achieve this resolution would require long acquisition times, increased susceptibility to motion resulting in an infeasible technique. A possible alternative is to explore the usage of single image super-resolution (SR) techniques. Our proposal is to apply a SR generative adversarial network (SR-GAN) [2] to cine fast spin echo (FSE) [3] images.
Methods: We trained the SR-GAN having the same architecture and loss functions as proposed in Ledig *et al.*[2] using 50 cine FSE image datasets at an in-plane resolution of 0.5 mm x 0.5 mm. The low-resolution images used for training were generated by downsampling the original cine FSE images by a factor of 4. The original images were retained and used as the ground truth for assessment. Two Cine FSE datasets not seen during the training were used for testing the algorithm using as evaluation metrics: normalized root mean squared error (nRMSE), peak signal to noise ratio (pSNR) and structural similarity (SSIM).[4] We compared the SR-GAN results with second- and third-order spline interpolation and a convolutional neural network (CNN) approach having the same architecture as the SR-GAN generator using mean squared error as the loss function. Intra-rater variability of the common carotid artery lumen manual segmentation was assessed by having two different experts segmenting both the low-resolution (0.5 mm^2) and the super-resolved (0.25 mm^2) for one of the test datasets. The Dice coefficient score was computed for each slice and a Wilcoxon signed-rank test was used to assess statistical significance.
Results and Discussion: The average results on the test set are summarized in Table 1. The SR-GAN outperformed both spline interpolations in all metrics and outperformed the SR-GAN generator in the nRMSE and pSNR metrics. The adversarial component of the SR-GAN makes its results less smooth compared to the other methods (Figure 1). The intra-rater dice agreement in the low-resolution images was of 91.31 ± 0.03 and in the super-resolved images was 93.68± 0.02. The difference was statistically significant (p-value < 0.01) according to the Wilcoxon signed-rank test.

Table *1*. Summary of the results (average ± standard-deviation) computed on the test set.

Metric	2-order spline	3-order spline	CNN	SR-GAN
nRMSE	0.151 ±0.051	0.160 ± 0.058	0.099 ± 0.020	**0.095±0.018**
pSNR (dB)	30.246 ± 1.176	29.823 ± 1.381	33.606 ± 0.863	**33.983±0.733**
SSIM	0.969 ± 0.002	0.967 ±0.002	**0.983±0.002**	0.981±0.002

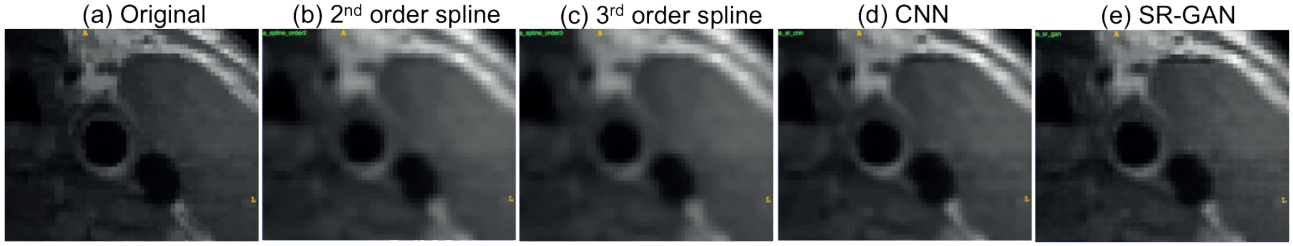

Figure 1. Sample results. (a) Original, (b) 2nd order spline, (c) 3rd order spline, (d) CNN, and (e) SR-GAN.

Conclusions: This study showed how to obtain SR dynamic FSE images. The results indicate that it can potentially improve carotid lumen segmentation measurements and reduce intra-rater variability. The framework is generic and can be extended to other images and SR scale factors. In future work, we intend to use these super-resolved images to get accurate carotid distensibility maps.

References:

1. Hameeteman, K., *et al*., *Automatic carotid artery distensibility measurements from CTA using nonrigid registration.* Medical Image Analysis, 2013; **17**: 515-524.
2. Ledig, C., *et al*., *Photo-realistic single image super-resolution using a generative adversarial network.* arXiv preprint, 2016.
3. Boesen, M.E., *et al.*, *Fast spin echo imaging of carotid artery dynamics: FSE of carotid artery dynamics.* Magnetic Resonance in Medicine, 2015; **74**: 1103-1109.
4. Wang, Z., *et al*., *Image quality assessment: from error visibility to structural similarity.* IEEE transactions on image processing, 2004; **13**: 600-612.

Deep Learning for Automated Reference-Free Image Quality Assessment of Whole-Heart Magnetic Resonance Images

Piccini D*[1,2], Demesmaeker R*[1,3], Heerfordt J[1,2], Yerly J[2,4], Masci PG[5], Van De Ville D[3], Richiardi J[1,2], Kober T[1,2,6], and Stuber M[2,4]

[1]Advanced Clinical Imaging Technology, Siemens Healthcare AG, Lausanne, Switzerland, [2]Department of Radiology, University Hospital (CHUV) and University of Lausanne (UNIL), Lausanne, Switzerland, [3]Center for Neuroprosthetics/Institutes of Bioengineering and Electrical Engineering, EPFL, Lausanne, Switzerland, [4]Center for Biomedical Imaging (CIBM), Lausanne, Switzerland [5]Division of Cardiology and Cardiac MR Center, University Hospital of Lausanne (CHUV), Lausanne, Switzerland, [6]LTS5, École Polytechnique Fédérale de Lausanne (EPFL), Lausanne, Switzerland, (*Equal contribution)

PURPOSE. Image quality (IQ) is a central metric in all branches of medical imaging. Usually, IQ is assessed visually, by a human expert, or measured with one or more mathematical quantitative metrics: e.g. signal-to-noise ratio or conspicuity of anatomical structures. One of the main challenges in this context is to be able to automatically produce numerical values that can directly correlate with the expert visual perception. Moreover, a fast and reliable IQ assessment may become especially important when iterative reconstruction algorithms are involved, as is the case with compressed sensing (CS) [1,2], and where image quality should improve at every iteration. The purpose of this work was therefore: (a) to develop a fully automated algorithm that quantitatively gauges the quality of a specific subset of medical images by employing a deep convolutional neural network that mimics human perception of image quality, and (b) to show that such algorithm can be used to monitor the progress of respiratory motion-resolved CS reconstruction of the heart.e come ti s

METHODS. A total of N=424 patients were randomly selected within a clinical database of 3D isotropic whole-heart MR imaging volumes (1mm isotropic spatial resolution). All scans were acquired on a 1.5T clinical MR scanner (MAGNETOM Aera, Siemens Healthcare, Erlangen Germany) using a prototype respiratory self-navigated sequence [3,4]. A reference standard IQ grading was established on all datasets by one expert reader using a 5-point image quality scale (0 = worst / 4 = best) similar to that proposed in [5], but with steps of 0.5. A deep convolutional neural network (DCNN) was designed and trained to achieve fully automated IQ assessment. Two-dimensional patches extracted from the isotropic volumes were used as input. The DCNN was composed of 4 convolutional layers followed by 3 fully connected layers. A final regression layer combined the implicit image features into a single quantitative IQ value on a continuous scale. The database was split into distinct training (N_{tr}=324) and test (N_{te}=100) sets with similar grade and gender distributions. The training set was first split into three equal parts for hyperparameter optimization using cross-validation and then used as a whole to train the best network. An optimizer minimized an anti-biasing L_1 loss function compensated for the non-uniform grade distribution. Finally, the patch quality grades were combined into a single grade using the mean of the patch grades in each patient. The network's performance was computed and visualized as a boxplot of the network's quality estimation against the expert reference. Correlation coefficients, linear regression and weighted kappa statistics were calculated. The network performance was compared with the inter-observer variability (a second expert graded the N_{te} datasets). Furthermore, a few randomly selected k-space datasets corresponding to patients from the test set of the network were reconstructed using a 4D respiratory-resolved reconstruction [6]. Reconstruction was performed with four respiratory phases using the XD-GRASP algorithm [2]. The DCNN was used to compare the quality of intermediate imaging volumes at subsequent iterations and to assess the differences in IQ among the different reconstructed respiratory phases. The resulting IQ evolution as assessed by the network was visually compared with the evolution of the mathematical objective function used by the CS algorithm.

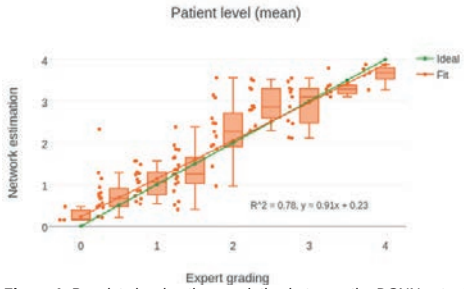

Figure 1. *Boxplot showing the correlation between the DCNN output and the reference expert grading on the test set (Nte = 100). Orange dots represent the grades of individual datasets.*

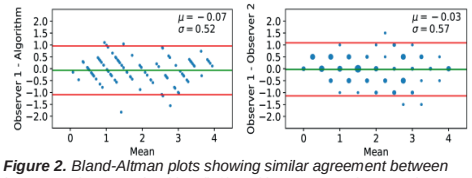

Figure 2. *Bland-Altman plots showing similar agreement between human and DCNN algorithm (left) and between two human observers (right). The DCNN algorithm outputs grades on a continuous scale.*

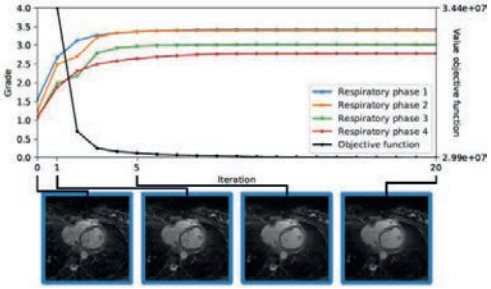

Figure 3. *The improvement in image quality during iterative CS reconstruction (grade) can be detected by the DCNN algorithm as seen from the increased quality grade over the iterations.*

RESULTS. A boxplot of the network's patient grade output against the reference standard is shown in Fig. 1. The L_1 anti-bias was 0.39, the Pearson correlation r^2=0.78 and the weighted kappa score 0.67. The agreement between the DCNN and the reference was similar to the inter-observer agreement (Fig. 2). Figure 3 displays the IQ evolution as a function of the specific iteration number during CS reconstruction for one representative dataset in a direct comparison with the objective function (normalized for visual comparison). A clear increase in estimated image quality is visible as the reconstruction progresses and the four respiratory phases do not converge to the same IQ grade.

DISCUSSION. An automated image quality assessment algorithm employing a deep convolutional neural regression network was described, optimized, trained, tested, and validated. Applied to clinical 3D cardiac MR images, it has been shown that the algorithm is able to replicate human image quality assessment with accuracy that lies within the bounds of the inter-observer variability. The visual correlation of IQ as assessed by the neural network and the objective cost function applied to the compressed sensing reconstruction seems to confirm that in general the mathematical features of the latter provide a reasonable quantitative measure of perceived image quality for our particular application.

References: [1] Lustig M, et al. MRM 2007; 58:1182-1195. [2] Feng L, et al. MRM 2016; 75:775-788. [3] Piccini D, et al. MRM 2012; 68:571-579. [4] Piccini D, et al. Radiology 2014; 270:378-386. [5] McConnel MV, et al. AJR 1997; 168:1369-1375. [6] Piccini D, et al. MRM 2017; 77:1473-1484.

Identification of high-risk intracranial atherosclerotic plaque features in intracranial atherosclerosis: initial experience using a radiomic approach by high resolution MRI

Zhang Shi[1], Chengcheng Zhu[2], Jianping Lu[1], Qi Liu[1]

1. Department of Radiology, Changhai Hospital, Shanghai, China

2. Department of Radiology and Biomedical Imaging, UCSF, San Francisco, CA, USA

Purpose: Intracranial atherosclerotic disease (ICAD) is a major cause of ischemic cerebrovascular events worldwide. High-resolution magnetic resonance imaging (HR-MRI) has been used to characterize intracranial plaque. This study aims to evaluate a quantitative radiomic approach based on HR-MRI to differentiate symptomatic intracranial artery plaque from asymptomatic plaque.

Methods:

Study population: This study retrospectively analyzed 158 patients with middle cerebral artery (MCA) and basilar artery (BA) stenosis underwent HR-MRI between September 2013 and October 2016. Patients were scanned with T1 and T2 weighted imaging, and T1 imaging following Gd contrast injection (CE-T1).

Imaging analysis: Atherosclerosis plaques from MCA and BA were extracted as the region of interest (ROI) for quantitative evaluation. The stenosis value, plaque area/burden, lumen area, intraplaque hemorrhage (IPH), contrast enhancement ratio and 109 quantitative radiomic features were extracted and compared between symptomatic and asymptomatic patients. Radiomics features including intensity, shape based feature and textures were analyzed. Textures includes gray level cooccurence matrix (GLCM), gray level run length matrix (GLRLM) and gray level size zone matrix (GLSZM). [1]

Statistical analysis: Normality test was performed for each variable. Univariate analysis was applied first to find possible variable that was associated with symptoms. Student t-test or two-sample Wilcoxon test was used if the variable was/was not normally distributed. P-values <0.05 were considered as statistical significant. To further quantify the texture features, supervised machine-learning methods were applied to classify symptomatic and asymptomatic plaques. Features in each sequence were selected during statistical analysis, those were set as input for the random forest training features. The classification performance of the features of each imaging sequence was compared. Multi-variate logistic analysis and a random forest model were used to evaluate the diagnostic performance.

Results: Smoking (odds ratio [OR]=2.724; 95%CI,1.200-6.183), IPH (OR=11.340; 95%CI, 1.441-89.221) and enhancement ratio (OR=6.865; 95%CI, 1.052-44.802) were independently associated with symptomatic plaques. The combined smoking, IPH and enhancement ratio had an area under the curve (AUC) of 0.714 for identifying symptomatic plaques. Radiomic features in T2, T1 and CE-T1 images were associated with symptomatic plaques, whose AUC respectively are 0.801,0.835 and 0.846. The combined all radiomic approach had a significantly higher AUC of 0.953. Combination of all features reached an AUC of 0.976, with accuracy of 87.4%. (Figure-1)

Discussion: Radiomic analysis of intracranial artery plaque on HR-MRI accurately distinguished between plaques in patients who were symptomatic and plaques in patients who were asymptomatic. The highest accuracy was achieved by combining radiomic features with traditional assessment of clinical and morphological features.

Key words: intracranial arteriosclerosis; magnetic resonance imaging; radiomics

References:[1.] Aerts, Hugo JWL, et al. Nature communications (2014).

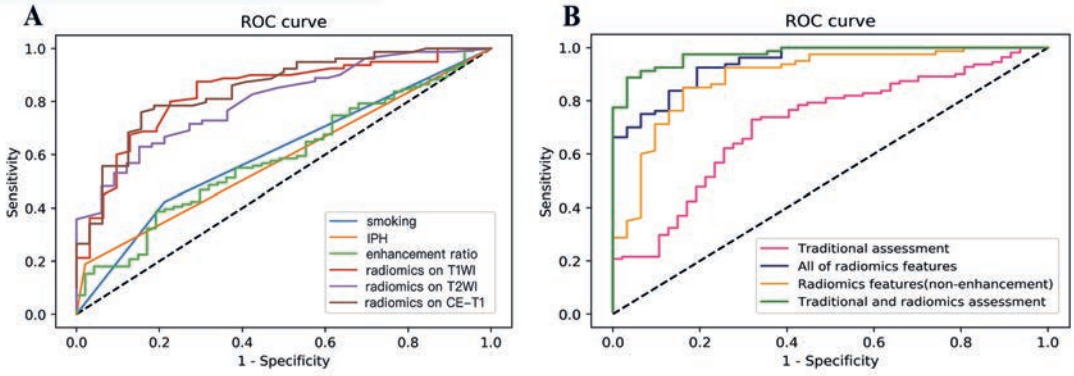

Figure-1: ROC curves to differentiate acute/sub-acute symptomatic and asymptomatic plaques. The curves on the left (A) shows the diagnostic performance of each independent parameters. The curves on the right (B) shows diagnostic performance of the combined traditional/radiomics model and a model combination of all features. Radiomic features had significantly higher AUC values compared with traditional features (p=0.01).

Carotid Artery Localization and Lesion Detection on 3D-MERGE MRI through Online Learning

Li Chen[1], Huilin Zhao[2], Niranjan Balu[3], Xihai Zhao[5], Rui Li[5], Jenq-Neng Hwang[1], and Chun Yuan[3]

[1]Electrical Engineering, University of Washington, Seattle, WA, United States, [2]Department of Radiology, Renji Hospital, School of Medicine, Shanghai Jiao Tong University, Shanghai, China, [3]Radiology, University of Washington, Seattle, WA, United States, [5]Biomedical Engineering, Tsinghua University, Beijing, China

Purpose: 3D Motion Sensitized Driven Equilibrium prepared Rapid Gradient Echo (3D-MERGE) [1] black blood MRI can image the carotid vessel wall with high isotropic resolution in a short 2-minute scan thus ensuring patient compliance and diagnostic image quality (becoming available in clinical MRI scanners). However, to make it applicable for a rapid high-risk lesion screening purpose, fully automated analysis tools on 3D-MERGE are needed. An automated method to flag locations of atherosclerotic lesions can help reduce radiologist workload and improve screening for atherosclerotic lesions. Identification of atherosclerotic lesions using deep learning may provide a better solution, but the expenses of human labels become the limitation. Therefore, the goal is to develop an automatic carotid lesion detection method from 3D-MERGE MRI using an online learning method for training a neural network to overcome the limitation on labeling.

Methods ***Study sample***: 3D-MERGE MRI of 134 subjects from a Carotid Atherosclerosis Risk Assessment (CARE II) study [2] were collected with IRB approval and informed consent. Images with unclear vessel wall boundary or artery out of scan area were excluded (34 subjects). ***MR imaging***: 3D-MERGE MRI was performed on a 3T Philips MR scanner with: TR/TE=10.35/4.87, Acquired resolution =0.7mm isotropic (interpolated to 0.35mm isotropic). ***Image pre-processing***: 3D-MERGE images were resampled in axial direction with isotropic resolution of 0.4mm. Vessel wall region was emphasized using an image filter and saved as additional channel with original image. ***Online learning***: Yolo V2 neural network [3] was trained subject by subject under an experienced radiologist supervision. This training differed from batch learning methods where labels are ready before model training (long time for a 3D isotropic dataset). An experienced radiologist marked the artery region and identified lesion occurrence subject by subject along with the neural network training process (workflow shown in Figure 1). Bounding boxes were drawn closely encompassing common/internal carotid artery on both artery sides for each slice (Figure 2), then were used as labels for Yolo V2 [3] to learn the location and lesion occurrence given whole image slices without region of interests. The trained model was then used to predict new unlabeled subjects for the radiologist to correct mistakes. Radiologist corrected results were then added into training set for later round of training. This process was repeated until all subjects were classified.

Results: Through each round of training, the radiologist needed fewer corrections as the prediction performance gradually improved. The slice-based lesion location sensitivity was 825/929=88.8%, precision was 825/1440=57.3% (Prediction example in Figure 3) at the last round of training on a separated test set of 20 subjects.

Discussion and Conclusion: Fast and fully automated localization and detection of carotid lesion is important for high-risk lesion screening among a large population. In this study, using online learning method, with minimum amount of time for human to create labels, a fully automatic lesion localization and detection model was trained on 3D-MERGE MRI. After 3D MERGE scans, without any human intervention, the neural network model is able to identify the accurate location of common/internal carotid arteries on both sides and the slices with possible lesions with total time from scan to results in under 3 minutes.

Acknowledgement: We gratefully acknowledge CARE-II Investigators and support of NVIDIA Corporation.

Figure 1 (Left) Workflow for online training used in this study. Figure 2 (Right top) Label tool used by radiologist. Normal artery labeled in red bounding box, abnormal artery with lesion labeled in blue bounding box. Figure 3 (Right bottom) Example of prediction results (location identified by bounding boxes with artery type and confidence)

Reference: [1] N. Balu, et.al, Magn. Reson. Med, 2011. [2] X. Zhao, et.al. BMJ, 2017. [3] J. Redmon, et.al, arXiv, 2016.

Deep Learning meets Compressed Sensing: Image Quality-Regularized Coronary MRA

John Heerfordt[1,2], Robin Demesmaeker[2,3], Jérôme Yerly[1,4], Tobias Kober[1,2,5] Matthias Stuber[1,4], Davide Piccini[1,2]

[1]Department of Radiology, University Hospital (CHUV) and University of Lausanne, Switzerland; [2]Advanced Clinical Imaging Technology, Siemens Healthcare AG, Lausanne, Switzerland; [3]Center for Neuroprosthetics/Institutes of Bioengineering and Electrical Engineering, EPFL, Lausanne, Switzerland; [4]Center for Biomedical Imaging (CIBM), Lausanne, Switzerland; [5]Signal Processing Laboratory 5 (LTS5), EPFL, Lausanne Switzerland

Purpose: Compressed Sensing (CS) has gained considerable attention in recent years as a means of improving image quality in Coronary Magnetic Resonance Angiography (CMRA) (e.g. [1], [2]). Usually, norms of sparsifying transforms such as finite differences or wavelet decomposition are used to regularize the image reconstruction. Here, we propose the use of a fundamentally different type of regularization, which exploits a Deep Learning (DL) model that explicitly estimates image quality. We hypothesize that the conventional sparsifying transform in an existing CS framework can be substituted by such an image quality based regularization. In contrast to image reconstruction techniques relying completely on DL (e.g. [3], [4]), our approach is easily integrated into conventional CS reconstruction.

Methods: We exploited a recently reported DL model [5] that has been trained and validated to estimate image quality using hundreds of human-graded whole-heart datasets. The image quality estimates from the model are incorporated into the reconstruction problem as a regularization term (Figure 1). The model can be differentiated numerically, which enables computation of both the image quality estimate $\boldsymbol{Qx}$ and the gradient of the image quality with respect to the image $\boldsymbol{\nabla Qx}$ (Figure 2). Hence, the reconstruction problem can be solved with standard gradient-based optimization methods. For validation, whole-heart datasets from six healthy volunteers acquired after informed consent on a 1.5T clinical MRI (MAGNETOM Avanto, Siemens Healthcare, Erlangen, Germany) with a prototype 3D radial bSSFP sequence [6] using navigator-gating and ECG-triggering were used. Reconstructions of all volunteer datasets were performed for several degrees of undersampling (20%, 15%, 10% and 5% of the radial Nyquist limit [7]) using gridding, conventional CS with spatial total variation (TV-CS) and our proposed Image Quality-regularized Compressed Sensing (IQ-CS). The regularization weights were manually tuned for the original amount of data (i.e. 20%) to balance noise and regularization artifacts. In all cases, the density compensation function was adjusted according to the undersampling to suppress noise. Reformats of the reconstructed images were compared quantitatively using the vessel sharpness [8] of the Right Coronary Artery (RCA) as an endpoint. Paired sample t-tests with Bonferroni correction were used for comparisons with $p < 0.05$ considered statistically significant. Moreover, the types of undersampling artifacts resulting from TV-CS and IQ-CS were assessed visually.

Results: Both IQ-CS and TV-CS provided significantly sharper vessels than the gridding reconstructions when data corresponding to 10% and 5% of the Nyquist limit were used (Figures 3 and 4). However, for the undersampling degrees of 15% and 20%, the sharpness was similar for most reconstructions (Figure 4). Visually, TV-CS and IQ-CS yielded different types of artifacts (Figure 5). Spatial TV generated its typical patchy artifacts, while IQ-CS overamplified certain small regions with high intensity and created structured noise. Nevertheless, IQ-CS produced visually sharper images than TV-CS at the highest degree of undersampling (Figure 3, right column).

Discussion: We have demonstrated that image quality estimates from a DL model can be used as a regularization term in CS reconstruction of CMRA images. In addition, our results suggest that the associated reconstruction problem is well-conditioned enough to consistently obtain desirable solutions. The technique appears to be promising for obtaining well-delineated coronary arteries, particularly at high degrees of undersampling. Since this new type of regularization can easily be combined with conventional sparsifying transforms, approaches investigating such combinations will be the subject of future work. Additional efforts are also needed to investigate the technique's limitations in terms of acceleration factors and generalization to different acquisition schemes and organs of interest.

References:

[1] Akcakaya M, IEEE TMI 2011, 30(5):1090–1099 [2] Bonanno G, PloS One 2014, 9(8) [3] Wang S, ISBI 2016, pp. 514-517 [4] Schempler J, http://arxiv.org/abs/1703.00555v1, 2017 [5] Demesmaeker R, ISMRM Workshop on Magnetic Resonance Imaging of Cardiac Function 2017, New York City, USA [6] Piccini D, MRM 2011, 66(4):1049–1056 [7] Nielles-Vallespin S, PhD Thesis at University of Heidelberg, 2004 [8] Etienne A, MRM 2002, 48(4):658–666

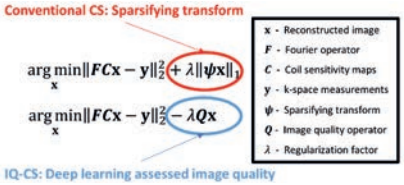

Figure 1. Reconstruction formulations using conventional CS and IQ-CS. The sign difference reflects that we want to maximize the image quality in IQ-CS (with maintained convexity).

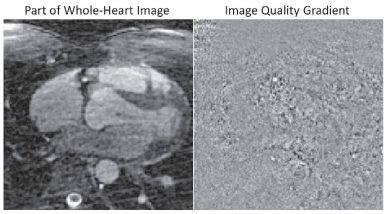

Figure 2. Image and corresponding quality gradient obtained from the DL model indicating how the image should be changed to improve the image quality.

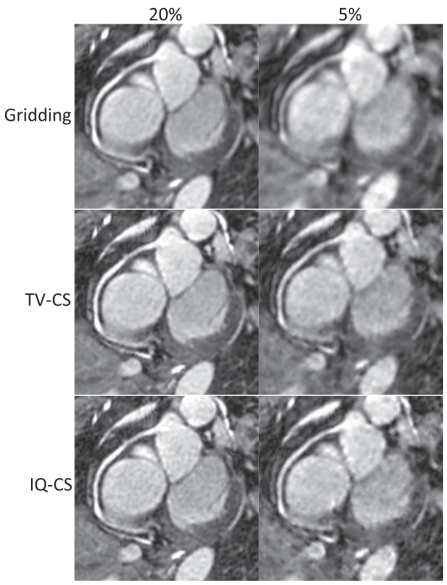

Figure 3. Example reformats for different reconstructions and varying undersampling levels.

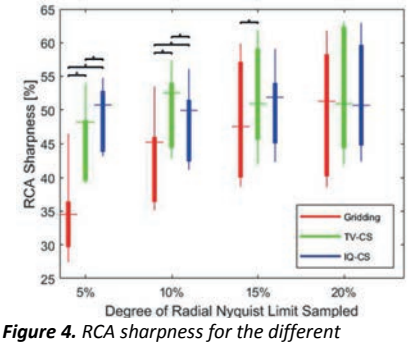

Figure 4. RCA sharpness for the different reconstructions and varying undersampling.

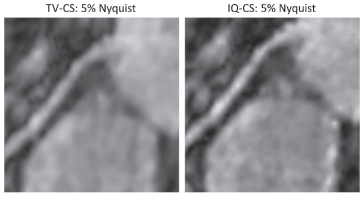

Figure 5. Undersampling artifacts of reformats.

Clinical Feasibility of High-Resolution Prospective Compressed Sensing Time-of-Flight Angiography at 7 Tesla

Patrick Liebig[1,2], Christian Meixner[3], Peter Speier[2], Christoph Forman[2], Bernhard Hensel[1], Manuel Schmidt[4], Michael Uder[3], Arnd Dörfler[4], Sebastian Schmitter[5], Armin M. Nagel[3], Robin M. Heidemann[2]

[1]Centre of Medical Physics, Friedrich-Alexander Universität Erlangen-Nürnberg, [2]Siemens Healthineers, Erlangen, Germany, [3]Institute of Radiology, Friedrich-Alexander Universität Erlangen-Nürnberg (FAU), Erlangen, Germany, [4]Institute of Neuro-Radiology, Friedrich-Alexander Universität Erlangen-Nürnberg, Erlangen, Germany, [5]Physikalisch-Technische Bundesanstalt (PTB), Braunschweig und Berlin, Germany

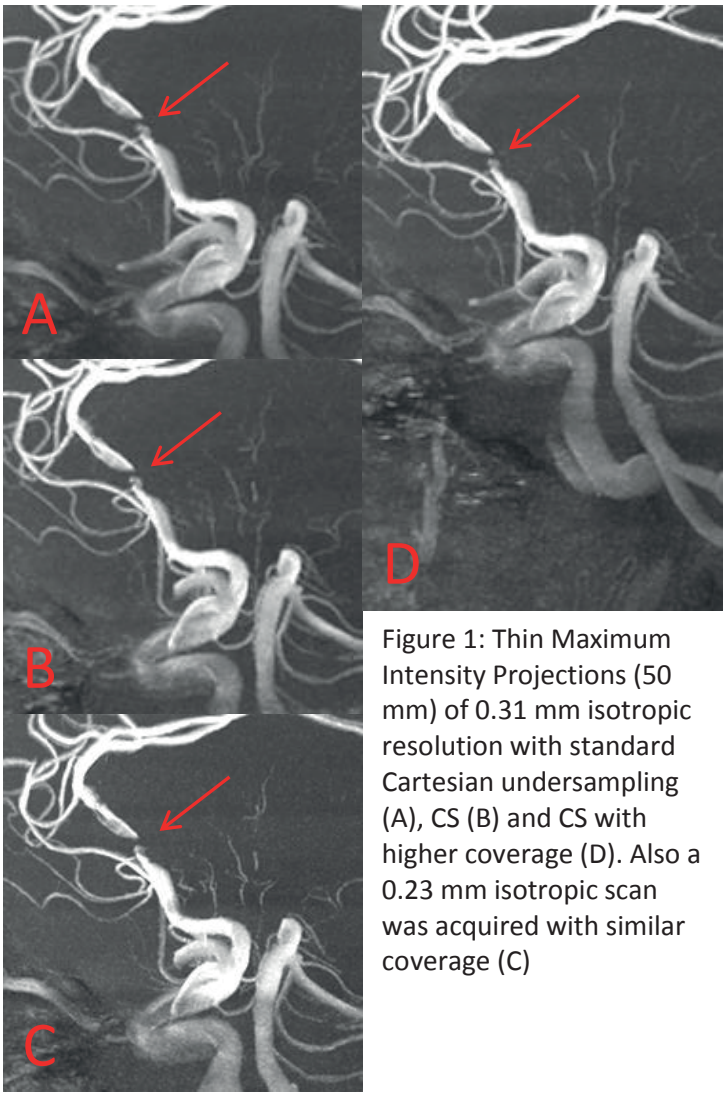

Figure 1: Thin Maximum Intensity Projections (50 mm) of 0.31 mm isotropic resolution with standard Cartesian undersampling (A), CS (B) and CS with higher coverage (D). Also a 0.23 mm isotropic scan was acquired with similar coverage (C)

Purpose: It has been shown, that Time-of-Flight (TOF) angiography at 7 Tesla enables spatial resolutions of up to 150 µm [1]. However, high resolution angiography is limited by long acquisition times of half an hour that are impractical for clinical use. Commonly, a lower resolution than possible or less coverage than necessary is used. In this study, we test the feasibility of high-resolution Compressed Sensing (CS) TOF at 7 Tesla in a clinical setting for the first time.

Methods: Data were acquired on a clinical 7 Tesla MR scanner (MAGNETOM Terra, Siemens Healthcare GmbH, Germany) equipped with a 32ch Rx, 1Tx Head coil (Nova Medical, USA). We implemented a prototype 3D TOF Gradient Echo sequence that acquires the data on a variable-density Poisson disk in the two phase-encodes. The reconstruction was implemented within the MR scanner's reconstruction framework making use of the Graphical Processing Unit [2]. Variable-rate-selective excitation (VERSE) was implemented to reduce SAR of the venous saturation [3]. Prior to acquiring patient data, protocol optimization has been performed on 20 volunteers to obtain good contrast and find an optimal sampling distribution and acceleration factor. The scan time gained due to employing CS was used to achieve either a higher resolution or a larger coverage.

Results: Figure 1 shows Maximum Intensity Projections (MIP) of 50 mm thickness. The stenosis was clearly identified in all acquisitions (shown by arrows).
The acquisition time could be reduced by 41% with CS acceleration or the coverage could be increased by 41%. The reconstruction of all acquisitions was completed 4 minutes after the end of the last scan.
Further scanning was possible during the reconstruction itself.

Protocol Parameters	Standard TOF (A)	Fast CS (B)	High Resolution CS (C)	Higher Coverage CS (D)
FOV (ROxPE) [mm]	220 x 174	220 x 174	220 x 174	220 x 174
Isotropic resolution	0.31 mm	0.31 mm	0.23 mm	0.31 mm
Nominal Flip Angle	20	20	19	20
Slabs/coverage [mm]	4/59.2	4/59.2	4/63.9	7/101.1
Acceleration factor	PAT 3, PPF 6/8	8	12	8
Acquisition time	12:29	7:20	12:07	12:49

Discussion: CS TOF has been tested on lower field strength for clinical feasibility [4]. The goal of the present study was to achieve very high acceleration factors at 7 Tesla, enabling high resolution TOF angiography in clinically acceptable scan times. This could be achieved with CS acceleration, while keeping the reconstruction time in a reasonable time frame. Future work will focus on a broader use of our CS TOF at 7T for various diseases, such as cerebral vasculitis, stenosis, arteriovenous malformations and aneurysms, respectively.

References: [1] Mattern et al. MRM doi:10.1002/mrm.27033, [2] Natsuaki et al. ISMRM 2014 #941, [3] Schmitter et al. MRM 68(1):188-197 (2012), [4] Yamamoto et al. PLoS ONE 13(1): e0189493 (2018)

High Resolution Time-of-Flight Angiography of Human Brain at 7 Tesla with VERSE Saturation and Compressed Sensing

Christian R. Meixner[1], Patrick Liebig[2,3], Peter Speier[2], Christoph Forman[2], Bernhard Hensel[3], Manuel Schmidt[4], Michael Uder[1], Arnd Dörfler[4], Robin M. Heidemann[2], Sebastian Schmitter[5], Armin M. Nagel[1]

[1]Institute of Radiology, Friedrich-Alexander Universität Erlangen-Nürnberg (FAU), Erlangen, Germany; [2]Siemens Healthineers, Erlangen, Germany; [3]MSBT, Friedrich-Alexander Universität Erlangen-Nürnberg; Institute of Neuro-Radiology, Friedrich-Alexander Universität Erlangen-Nürnberg, Erlangen, Germany, [5]Physikalisch-Technische Bundesanstalt (PTB), Braunschweig und Berlin, Germany

Purpose:

3D Time-of-Flight (TOF) angiography substantially benefits from ultra-high magnetic field strengths (e.g. 7 Tesla) due to increased Signal-to-Noise Ratio (SNR) and improved contrast [1]. However, high-resolution TOF MRI at 7 Tesla suffers from long acquisition times (TA) and SAR constraints, especially if venous saturation is employed. To address these issues, Variable-Rate Selective Excitation (VERSE)-Pulses were implemented for the venous saturation (RF_{SAT}) and prospective Compressed Sensing (CS) was applied to accelerate the acquisition.

Materials and Methods:

All measurements were conducted on a 7T MR system (MAGNETOM Terra, Siemens Healthcare GmbH, Erlangen, Germany) using a 32-channel Rx/ 1Tx head-coil (Nova Medical, Wilmington, Massachusetts, USA). A gradient echo TOF sequence was modified to perform venous saturation using VERSE pulses [2]. Data were acquired on a variable-density Poisson disk with a Gaussian density distribution (Fig. 1). Subsequently, the images were recovered by a CS reconstruction algorithm [3]. This was implemented online within the manufacturer's reconstruction framework, with the possibility to additionally use a GPU.

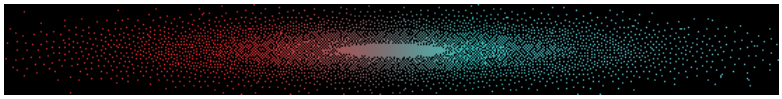

Figure 1: CS sampling pattern in the phase encoding plane with linear reordering from red to blue

Three different protocols were used (Table 1). The common parameters were: nominal flip angle=20°, TR=24ms, TE=5.44ms, Bandwidth=118Hz/px, VERSE factor=0.25 (RF_{SAT} amplitude was reduced to 25% [2]), RF_{SAT} flip angle=60°.

To analyze the TOF data, images were co-registered and 40mm thick transversal maximum intensity projections (MIPs) were created. 100 cross-sections covering 50% of the MIPs (25% up and down from the center) were compared, regarding to the number of vessels normalized to those of the standard TOF protocol (a).

Results:

Figure 2 shows exemplary MIPs of the three different protocols. Image quality of the fast CS-TOF (b) is similar to the conventionally accelerated TOF (a), even though TA is 43% shorter. The high-resolution CS-TOF (c) resolves more vessels, although TA is still 27% shorter. Table 1 shows the number of vessels and confirms the visual impression of the images.

Sequence	(a)	(b)	(c)
Voxel size (isotropic)	0.31mm	0.31mm	0.25mm
Slabs	4 à 17.4mm	4 à 17.4mm	4 à 18mm
Acceleration	GRAPPA 3, Partial Fourier 6/8	CS 7.2	CS 8.8
TA	14:14min	8:04min	10:26min
No. Vessels	100%	114±24%	150±35%

Table 1: Sequence Parameters and Results

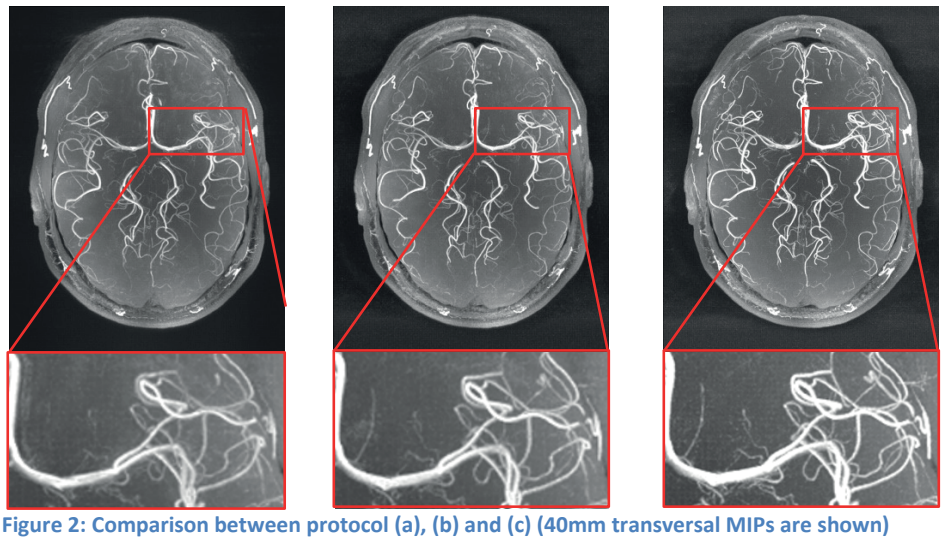

Figure 2: Comparison between protocol (a), (b) and (c) (40mm transversal MIPs are shown)

Discussion:

Here we accelerate TOF acquisitions with CS to almost halve the acquisition time without visible loss of image quality. The gain in time can be invested to increase the resolution resulting in an improved vessel dipiction. Reconstruction time for the data sets is still in a reasonable limit, enabling the clinical use. Future work will include the use of parallel transmission [4] to address B1+ inhomogeneities and motion correction [5].

References:

[1] Maderwald et al. MAGMA 21:159-167 (2008); [2] Schmitter et al. Magn Reson Med. 68(1):188-197 (2012); [3] Natsuaki et al. ISMRM 2014 #941; [4] Schmitter et al, Invest Radiol. 49(5):314-25 (2014); [5] Mattern et al. Magn Reson Med. doi:10.1002/mrm.27033

Intracranial Vessel Wall Segmentation on 3D black-blood MRI using Convolutional neural network

Hao Liu[a], Dongye Li[a,b], Xuesong Li[c], Qiang Zhang[a], GuanHua Wang[a], Kewei Chen[a,d], Xihai Zhao[a], Huijun Chen[a]

[a] CBIR, Department of Biomedical Engineering, School of Medicine, Tsinghua University, Beijing .[b] Capital Medical University, [c] School of Computer Science and Technology, Beijing Institute of Technology, Beijing, China, [d] The High School Affiliated to Renmin University of China, Beijing

Target audience: Image segmentation， deep learning

Purpose: Intracranial artery atherosclerosis is a major cause of stroke[1]. However, manually segmenting intracranial artery vessel wall is laborious. Thus, in this study, we proposed an automatic intracranial artery vessel wall segmentation framework using a 3D convolutional neural network (CNN) to find the centerline of the intracranial artery from SNAP [2] images and a 2D CNN to segment the final lumen and outer-wall contours on the cross-sectional 2D slices perpendicular to the centerline generated from 3D T1 VISTA [3] images.

Methods: Fig. 1 shows the flowchart of the proposed framework. First, intracranial SNAP images of 90 subjects with semi-automatic lumen segmentation[4] with manual correction were used to train a 3D U-Net model [5] to segment the lumen of intracranial artery. To save the GPU memory, the training data was comprised of 8 cubes of the corner and another cube was randomly cropped from the data. The final segmentation results can be merged to a big cube using the segmented corner cubes. The SNAP images of another 10 subjects were used as test set for the 3D lumen segmentation. The mean Intersection over Union (Mean IU) value was used to evaluate the performance of 3D lumen segmentation. Then, the 2D segmentation of intracranial artery vessel wall were carried out in another 50 patients with both intracranial SNAP and VISTA images. First, the trained 3D U-Net before was used to segment the intracranial artery lumen from SNAP images automatically. Then, the lumen centerlines generated with a skeleton algorithm [6] were mapped to the 3D VISTA images after the registration between SNAP and VISTA using FLIRT[7]. Thus, the 2D cross-sectional slices perpendicular to the centerline can be acquired using multi-planar reformation. The lumen and outer-wall contours were drawn manually on these cross-sectional slices. The manual segmentation and VISTA images of 45 randomly selected cases were sent to a pre-trained 2D Dense-Resnet model[8,9]. Finally, 5 cases were utilized to test the performance of 2D vessel wall segmentation using Mean IU. The quantitative parameters to evaluate the intracranial vessel wall, including the maximum thickness, mean thickness, lumen area, and vessel wall area, were compared between automatic and manual segmentations using correlation coefficient.

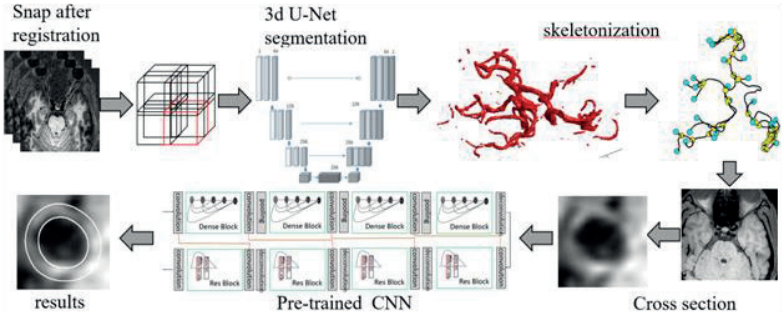

Figure1. The flowchart of the proposed framework.

Results and Discussions: The mean IU of the 3D lumen segmentation using the proposed 3D U-Net model was 0.90. The mean IU of the 2D vessel wall segmentation using Dense-Resnet was 0.94. Both suggest the good agreement between the automatic and manual segmentation. Fig. 2 shows four typical 2D-crosstional slices with similar segmentation results using the automatic and manual methods. Fig. 3 shows the scatter plot of the vessel wall max thickness, mean thickness, lumen area and vessel wall area. The high correlation coefficient of these quantitative parameters were found between automatic and manual segmentation (max wall thickness: r=0.90, p<0.001; mean wall thickness: r=0.95, p<0.001; lumen area: r=0.99, p<0.001; mean wall thickness: r=0.96, p<0.001;).

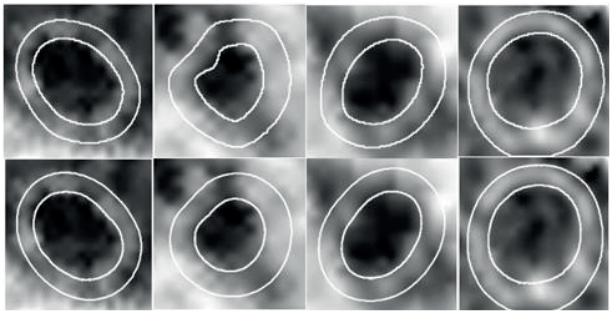

Figure2. First row: manual segmentation, Second row: the results of the proposed method.

Conclusions: In this study, a framework to automatically segment the intracranial artery vessel wall using VISTA and SNAP images were proposed. The results shows high IU and high correlation coefficient of quantitative parameters between automatic and manual segmentation. Thus, the proposed CNN based automatic segmentation framework has the ability to accurately segment intracranial artery vessel wall.

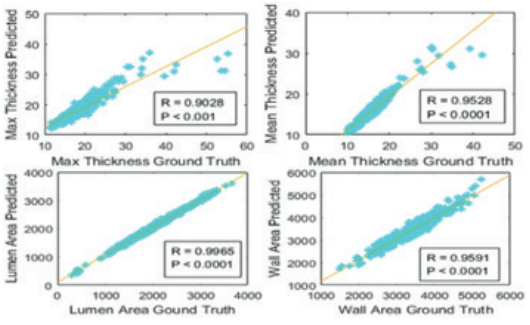

Fig.3. Scatter plots to compare the max wall thickness, mean wall thickness, lumen area and vessel wall area between the manual and proposed method.

Reference:1. Bogousslavsky et al. Stroke 19.9 (1988): 1083-1092 2. Wang et al. MRM 69.2 (2013): 337-345 3. Crowe et al. JMRI 17.5 (2003): 572-580 4. Chen, Li et al. MRM(2017). 5. Çiçek et al. Springer 6. Ta-Chih Lee et al. ICVGIP, 56(6):462–478, 1994 7. Jenkinson et al. NeuroImage, 17(2), 825-841, 2002. 8. Huang et al. arXiv:1608.06993 (2016) 9. He, Kaiming, et al.CVPR. 2016.

Network-based 4D Flow MRI quantification in healthy neurovasculature and arteriovenous malformation

Maria Aristova[1], Alireza Vali[1], Sameer Ansari[2], Ali Shaibani[2], Tord Alden[3], Michael Markl[1], Susanne Schnell[1]
[1]Northwestern University, [2]Northwestern Memorial Hospital, [3]Lurie Children's Hospital

Purpose: Existing studies have investigated normative age-dependent intracranial flow[1], but systematic evaluation of the impact of common variants[2] of the Circle of Willis (COW) architecture on flow distribution in the arterial and venous circulation is lacking. The goal of this work is to systematically assess this impact via network analysis, exploiting the improved velocity dynamic range and SNR of dual-*venc* 4D flow MRI for accurate quantification of arterial and venous cerebral hemodynamics. We also test the feasibility of comparable network analysis in arteriovenous malformations (AVM), which affect the total amount of flow to the brain and the distribution of extranidal flow[3].

Table 1. Scan parameter means (ranges); flip angle=15°. All healthy and 3 AVM subjects were scanned at 3T (Skyra: Siemens, Germany); 1 AVM at 1.5T (Aera: Siemens).

	Isotropic resolution [mm each direction]	TR [ms]	TE [ms]	Time frames	Low VENC [cm/s]	High VENC [cm/s]
Healthy (n = 21)	1.0 (0.8-1.6)	6.7 (4.2-7.4)	3.9 (2.6-4.4)	13 (6-25)	48.6 (44 - 90)	122.9 (100-200)
AVM (n = 4)	1.4 (1.2-1.9)	6.1 (6.0-6.2)	3.4 (3.3-3.5)	15 (9-17)	46.4 (44-50)	100.0 (100-100)

Figure 1. Preprocessing with dedicated tools (Matlab: Mathworks, USA) included (A) noise and phase offset correction of velocity data (time-averaged pathlines shown in cm/s; visualization: Ensight, CEI, USA), (B) phase-contrast angiogram (PCMRA) segmentation, (C) centerline extraction, placement of 2D quantification planes 1mm apart along each vessel, (D) vessel network identification and presentation as FDNG.

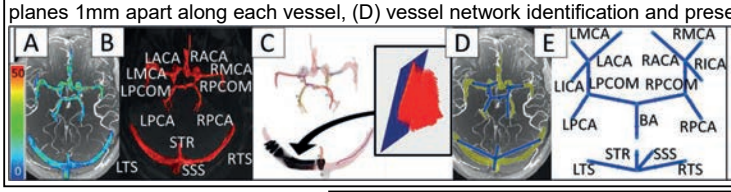

Arteries: ICA- internal carotid, MCA- middle cerebral, ACA- anterior cerebral, PCA- posterior cerebral, BA- basilar, PCOM- posterior communicating. Venous sinuses: TS- transverse, SSS-superior sagittal, STR- straight. L/ R: left/right paired vessels.

Methods: Dual-*venc* 4D Flow MRI scans were collected as in Table 1 for 21 healthy subjects (age 44±18 years, 9 female) and 4 AVM cases (age 8-68 years, 2 females: 2 frontal, 1 temporal, 1 bithalamic). For each subject, a flow distribution network graph (FDNG) stored median flow among all planes in each vessel as an edge of a directed graph (Figure 1). Healthy subject datasets were assigned to groups based on graph isomorphism, which reflects COW architecture. Classification of architecture was based on high spatial resolution time-of-flight (TOF) reads from two experienced radiologists. Each group FDNG shows mean flow per vessel normalized by total inflow to the head. In AVM cases we compute the flow ratio of nidus vs. brain parenchyma. For paired vessels (e.g. left/right transverse sinus) asymmetry index is computed as $\left|\frac{Left-Righ}{Left+Right}\right|$.

Figure 2. For each of the most common COW architectures in our sample, a representative subject network graph (blue) is superimposed on the PCMRA (yellow) and axial TOF maximum intensity projection. Within-group standardized FDNG colors show mean vessel flow as percentage of total inflow over group. Total inflow: sum of internal carotid and basilar arterial flow. Parenchyma flow: sum of flow in ACAs, MCAs and PCAs.

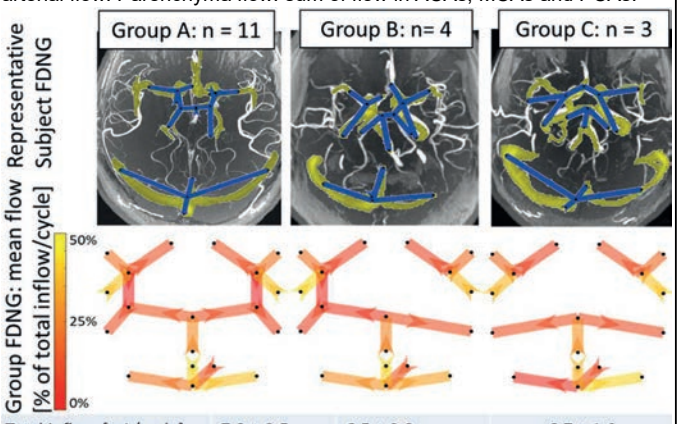

	Group A: n = 11	Group B: n= 4	Group C: n = 3
Total inflow [mL/cycle]	7.3 ± 0.5	6.5 ± 0.9	6.7 ± 1.0
Parenchyma / total [%]	90 ± 22	70 ± 19	61 ± 15
Asymmetry index: MCAs	0.14± 0.20	0.04± 0.03	0.08± 0.06
Asymmetry index: TSs	0.42± 0.29	0.46± 0.28	0.79± 0.17

Results: The control cohort yielded 5 network variant groups; 3 had at least 3 subjects: A (both PCOMs present, n=11), B (left PCOM only, n=4), C (no PCOMs, n=3). Presence/ absence of communicating (PCOM) or fetal PCAs distinguished all variants in this cohort including 3 excluded subjects with unique networks. Figure 2 shows representative individual FDNGs and group means. Left and right TS were more asymmetric than MCA in all groups ($p< 10^{-4}$), consistent with the known predominance of asymmetric venous drainage[4]. No significant difference was observed between groups in total inflow, MCA or TS asymmetry or parenchymal/ total ratio, though mean TS asymmetry trended higher in group C (p=0.07). In most AVM cases, nidal flow was comparable to parenchymal flow, and overall inflow was higher than controls; p=0.004.

Figure 3. For each AVM case, the FDNG shows median flow [mL/cycle] in each vessel. AVM inflow: sum of flow leaving feeding arteries; parenchymal inflow: non-feeding arteries.

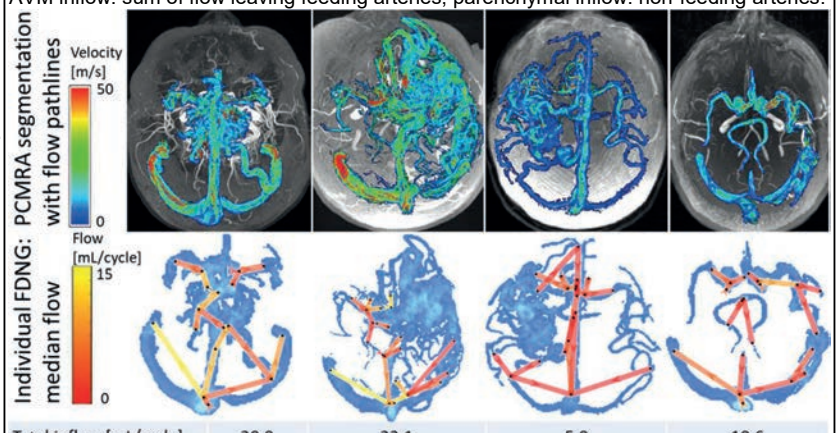

Total inflow [mL/cycle]	20.8	23.1	5.8	10.6
Parenchyma / total [%]	35	52	65	82
AVM:parenchyma ratio	2.1	1.3	2.1	0.1

Discussion: FDNGs provide a schematic format to visualize and quantitatively compare variants in COW architecture. 4 AVM cases demonstrate application of this concept to complex architectures and show flow distribution consistent with flow diversion to the nidus. These provide a basis for future studies to standardize data presentation and analysis in an expanded AVM cohort.

References: [1] Wu C. et al. JAHA 2016; 5(1):e002657.
[2] Hakim A. et al. J Neuroimaging 2018; 28:14-35.
[3] Homan R. et al. Arch Neurol. 1986; 43(8):779-785.
[4] Ayanzen, R.H. et al. AJNR 2000; 21(1):74-78.

Association between Cerebrovascular Large Artery Atherosclerosis and Cerebral Perfusion

Hualu Han[1], Runhua Zhang[2], Gaifen Liu[2], Dongye Li[1], Ying Cai[3], Huiyu Qiao[1], Xihai Zhao[1]

1.Center for Biomedical Imaging Research, Tsinghua University, Beijing, China; 2. Department of Neurology, Beijing Tiantan Hospital, Capital Medical University, Beijing, China; 3. Department of Radiology, Taizhou People's Hospital, Taizhou, China

Background and Purpose: Cerebral small vessel disease (CSVD) characterized by lacunar infarcts and white matter lesions is a leading cause of cognitive decline and functional loss in the elderly. During the process of CSVD, the decline of microcirculation perfusion, such as cerebral blood flow (CBF), in the parenchyma may occur prior to ischemic lesions. **This study aims to investigate the relationship between large artery atherosclerosis and CBF using pCASL imaging in asymptomatic adults.**

Methods: ***Study sample***: The subjects were recruited from an imaging-based community study of CAMERA which is investigating the cerebrovascular disease risk in the asymptomatic adults. ***MR imaging***: All recruited subjects underwent brain and cerebrovascular imaging on a 3T Philips MR scanner to acquire the following sequences: pCASL: labeling duration 1650 ms, post labeling delay 1575 ms, 2D EPI readout with 90° excitation RF pulse, number of averages 15, background suppression; T2-FLAIR: routine parameters; MERGE: FFE, TR/TE 9/4.2 ms, flip angle 6°, FOV 16*16*4 cm^3, spatial resolution 0.8*0.8*0.8 cm^3; T1-VISTA: TFE TR/TE 700/21 ms, FOV 20*20*4.5 cm^3, spatial resolution 0.6*0.6*0.6 cm^3. ***Image analysis***: The quantitative CBF map, referring to FLAIR, was sketched manually and divided into anterior and posterior circulation territories and periventricular white matter region. The 3D T1-VISTA and MERGE images are analyzed to identify the presence/absence of cerebrovascular atherosclerotic plaque which is defined as eccentric wall thickening in the arterial wall. ***Statistical analysis***: Independent *t* test was used to compare the differences in CBF between subjects with and without cerebrovascular plaque. Logistic regression was utilized to determine the correlation between presence of cerebrovascular plaque and CBF before and after adjusted for confounding factors (age, gender, BMI, smoking, diabetes, hypertension and hyperlipidemia).

Results: Of 134 recruited subjects (54 males; age, 56.2±12.8 years), 61 (45.5%) had plaques in intracranial and/or carotid arteries. The CBFs in anterior and posterior circulation territories were significantly reduced in subjects with cerebrovascular plaque than those without (Fig. 1). Cerebrovascular plaque was significantly associated with the first tertile of CBF of anterior circulation territory (OR, 2.62; 95%CI, 1.25-5.49; p=0.011) and posterior circulation territory (OR, 3.50; 95%CI, 1.64-7.48; p=0.001), but not with periventricular white matter (OR, 1.72; 95%CI, 0.83-3.56; p=0.144), respectively. After adjusted for confounding factors, all these associations showed statistically significant (all p<0.05). Fig. 2 represents example for the CBF of subjects with vs. without cerebrovascular plaque.

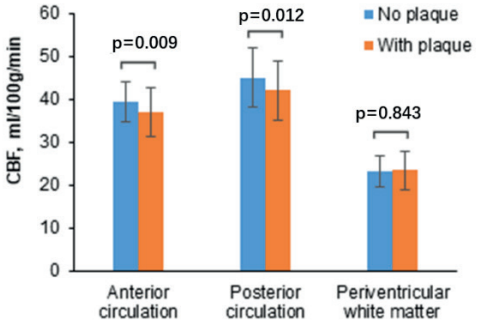

Fig 1: Comparison of CBFs between subjects with and without cerebrovascular plaque.

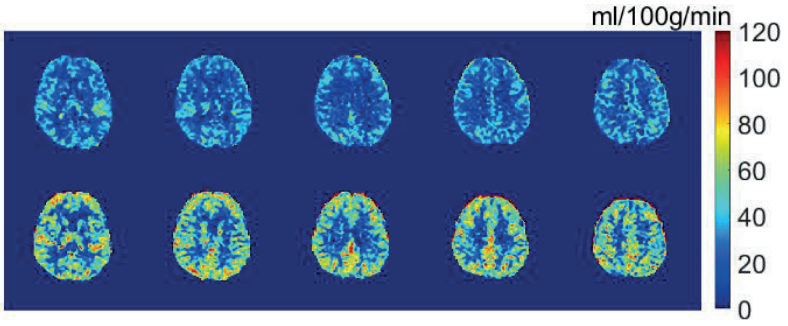

Fig 2: The CBF maps for subject with (upper row) and without cerebrovascular atherosclerotic plaque (lower row).

Discussion and Conclusions: We found that there was significant association between cerebrovascular atherosclerotic plaques and the decline of microcirculation perfusion measured by CBF, particularly the anterior and posterior circulation territories. However, this trend cannot be seen in the territory of periventricular white matter which may be due to the difficulties of pCASL in this region[4]. **The findings of our study suggest that cerebrovascular large artery atherosclerosis might be an effective indicator for early changes of CSVD**.

References: [1] Pantoni L, et al. Lancet Neurol. 2010;9:689-701; [2] van der Veen PH, et al. Stroke. 2015;46:1233-8. [3] de Leeuw FE, et al. J Neurol. 2000;247:291-6. [4] van Gelderen P, et al. MRM. 2008;59:788-95.

Assessment of the Hemodynamic Impact of Intracranial Atherosclerosis Disease

Alireza Vali[1], Maria Aristova[1], Sameer A. Ansari[1], Shyam Prabhakaran[2], Michael Markl[1], Susanne Schnell[1]

[1]*Radiology, Northwestern University, Chicago* [2]*Neurology, Northwestern University, Chicago*

Purpose: Patients with symptomatic intracranial atherosclerotic disease (ICAD) have a high risk of stroke recurrence. Hemodynamic compromise distal to the stenosis is a risk factor for recurrent stroke[1]. However, the current standard by which ICAD lesions are evaluated is percentage of lumen narrowing, or degree of stenosis, not reflecting the hemodynamic significance of the disease. Measurement of hemodynamics and new lesion characteristics based on flow quantification could improve disease management and aid risk stratification. Flow measurement in the cerebrovascular network can be achieved non-invasively with dual-*venc* 4D flow MRI[2]. To fully utilize 4D flow MRI data for ICAD patients, blood flow and velocities need to be quantified throughout the complex network of cerebral vessels[3], which can be tedious and prone to observer variability. To address these limitations, an automated flow analysis tool was developed and used to quantify flow rate (FR) and peak velocity (PV) allowing examination of the flow redistribution in the cerebral arterial network. Furthermore, pressure drop and resistance across the stenosis were estimated as new metrics that may enable better characterization of the hemodynamic significance of ICAD.

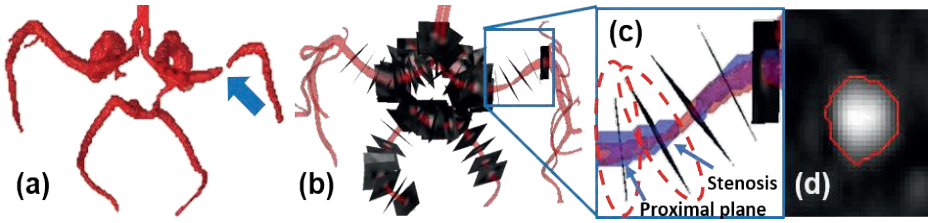

Figure 1: (a) PCMRA showing stenosis, (b) 2D cutplanes on the registered TOF, (c) planes used for pressure loss calculation (blue: PCMRA, red: TOF), (d) lumen region based on segmentation of TOF

Methods: Intracranial *k-t* GRAPPA accelerated dual-*venc* 4D flow MRI (TR/TE=6/3.2, FA=15°, voxel size= 1.1x1.1x1.1mm, venc=50/100) and time-of-flight (TOF) MRI (voxel size= 0.25x0.25x0.5mm) were acquired on a 3T scanner (Skyra or Prisma, Siemens, Germany) in 20 healthy volunteers (12M, 43±18Y) and 5 symptomatic ICAD patients (3F, 60±13Y): subjects 1-3 diagnosed with moderate (50-70%) and subjects 4 and 5 presented with severe (>70%) stenosis in right middle cerebral artery (MCA). Following noise, aliasing and phase offset correction, a 3D phase-contrast MR angiogram (PCMRA) was created. An automated flow analysis tool was developed which can perform the steps presented in Figure 1. First, to accurately identify the location of stenosis and lumen wall, the TOF was registered to the 4D flow MR images. Then, 3D centerlines of the major arteries in the Circle of Willis were extracted, and multiple evenly spaced 2D perpendicular planes per vessel segment were placed. At each 2D analysis plane, the lumen region was determined based on TOF, and vessel cross-sectional area, PV, and FR were calculated. The impact of ICAD on flow redistribution in the cerebral arterial network was characterized by asymmetry indices: the ratios of FR and PV between affected and non-affected brain hemispheres. The local hemodynamic impact of ICAD was assessed using resistance of the diseased vessel as $R = \Delta P/Q$ where Q is flow rate and ΔP is pressure loss due to stenosis estimated using the Bernoulli equation: $\Delta P = 4V^2\,(1-(EOA/A)^2)$ where V and EOA are PV and area at stenosis location respectively and A is the vessel cross-sectional area proximal to stenosis (Figure 1c).

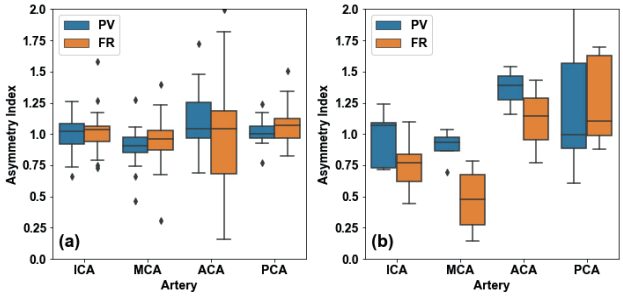

Figure 2: Asymmetry indices of FR and PV for (a) healthy control and (b) MCA ICAD patients

Results: Figure 2a shows FR and PV asymmetry indices for the healthy cohort with a median close to 1. Based on a paired *t*-test (or Wilcoxon signed rank if not normally distributed) both the FR and PV in pairs of left/right ICA, MCA, ACA, and PCA were similar (α=0.05) indicating normal symmetric blood flow distribution to left and right sides of the brain. In contrast, the median asymmetry indices of FR and PV for ICAD patients indicated highly asymmetric flow redistribution (Figure 2b). The FR in MCA and ICA on the affected side was smaller than non-affected side (median asymmetry index < 1) and there was an increase in FR and PV in ACA and PCA on the affected side compared to the non-affected side (median asymmetry index > 1). The estimated pressure gradient and resistance across the stenosis are summarized in Table 1, which show an increase in resistance with FR asymmetry index in these patients. Due to the severity of the lesion in subject 5, the affected MCA was shown as occluded in the MRI therefore hemodynamics could not be evaluated.

Table 2: FR asymmetry index, pressure gradient and resistance in affected vessel for MCA ICAD patients

#	MCA FR Asymmetry Index	Pressure gradient (mmHg)	Resistance (mmHg.s/ml)
1	0.78	0.94	1.35
2	0.64	3.04	1.85
3	0.31	3.02	2.45
4	0.14	0.79	1.32

Discussion: Cerebral dual-*venc* 4D flow MRI coupled with an efficient flow analysis of the major intracranial arteries demonstrated symmetric flow between hemispheres in healthy controls. Presence of ICAD resulted in asymmetric flow redistribution in the patient cohort, which showed a trend with flow resistance variation in the diseased vessel. More data is required to characterize the relationship between asymmetry of flow and resistance of the stenosis. However, it is noteworthy that although patients 1-3 were all classified as moderate (50-70%) stenosis, the FR asymmetry index and resistance were different among the subjects and could constitute new metrics to improve risk stratification of ICAD patients.

References: [1] Arenillas Stroke 2011,42:S20; [2] Schnell et al. JMRI 2017,46:102; [3] Wu et al. AJNR 2017,38:515

Automatic Segmentation of Carotid Vessel Wall in Multi-Contrast Blackblood Images using Deep Learning

Jifan Li[1], Shuo Chen[1], Xihai Zhao[1], Chun Yuan[1,2] and Rui Li[1]
1Center for Biomedical Imaging Research, Department of Biomedical Engineering, School of Medicine, Tsinghua University, Beijing, People's Republic of China
2Vascular Imaging Laboratory, Department of Radiology, University of Washington, Seattle, WA, United States

Purpose:

It is of crucial importance to estimate whether there is an atherosclerosis in carotid artery through the information of carotid vessel wall images. However, it is time-consuming and subjective for radiologists to segment the carotid vessel wall in multi-contrast MR images. In this work, we aimed to develop an automatic approach for segmentation of carotid vessel wall in multi-contrast blackblood images based on U-net network.

Methods:

Our data set includes 1,098 subjects (16 locations per subject, and totally 17,568 locations) with institutional review board approval. Each location has four contrasts[1] (T1, T2, TOF and MPRAGE) with 256*256 in image size. All data were viewed by experienced radiologist using CASCADE[2]. Out of the 1,098 subjects, we used 660 for training, 219 for validating and 219 for testing. The segmentation of carotid vessel wall in multi-contrast MR images was formulated as a pix-wise binary classification problem with the U-net network[3] (Figure 1). In particular, we made four copies of the first convolution layer in the original U-net network and connected each MRI sequence image with one copy. Then we merged the results of these four convolution layers by summation. In addition, we flipped the image horizontally at 0.5 probability level and cropped the image randomly as data augmentation in the training procession, which avoided overfitting. To obtain the best segmentation threshold, the ROC curve was leveraged. To evaluate the results of carotid vessel wall segmentation, the sensitivity, specificity and pixel accuracy were used.

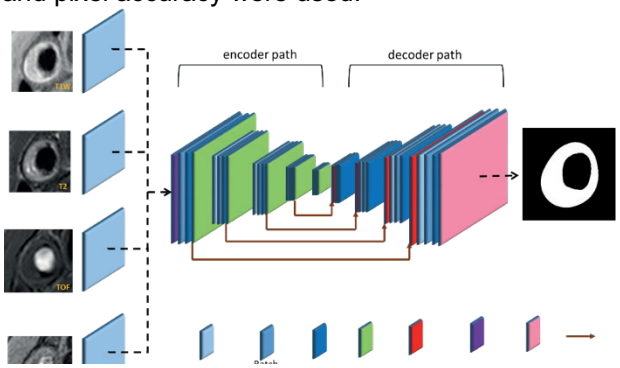

Figure 1: The architecture of fine-tuning U-net network in our model.

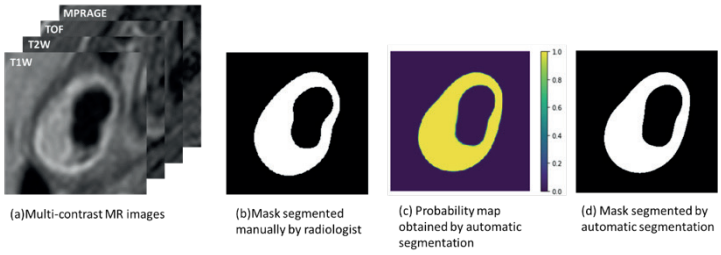

Figure 3: The segmented results of carotid vessel wall.

tissue	sensitivity	specificity	pixel accuracy
carotid vessel wall	0.973	0.963	0.972

Table 1: The quantitative evaluation.

Results:

Figure 2 shows the ROC curve in the experiment. The best threshold is 0.001107. Figure 3 shows the segmented results of carotid vessel wall in multi-contrast images. Probability map was generated at the pixel level. The probabilities of vessel wall area are almost 1.0 and background area are almost 0.0. Figure 4 shows the quantitative evaluation of models trained with sensitivity, specificity and pixel accuracy. All evaluation values are larger than 0.96.

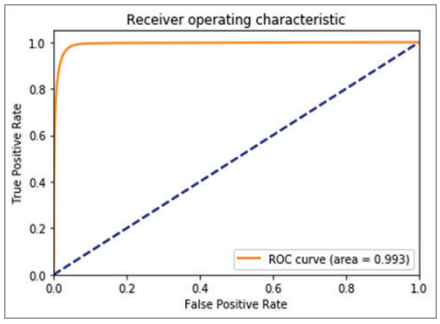

Figure 2: ROC curve

Discussion:

In this work, we proposed an automatic segmentation algorithm of carotid vessel wall in multi-contrast blackblood images based on a fine-tuning U-net neural network. Through copying first convolution layer four times and summing them together, the U-net model could be utilized on the multi-contrast MR images. The concatenate layer between encoder path and decoder path made high resolution of output images.

References:

1. Yuan, C., et al., In Vivo Accuracy of Multispectral Magnetic Resonance Imaging for Identifying Lipid-Rich Necrotic Cores and Intraplaque Hemorrhage in Advanced Human Carotid
Plaques. Circulation, 2001. 104(17): p. 2051-2056.
2. D Xu, WS Kerwin, T Saam, M Ferguson, and C Yuan. Cascade: Computer aided system for cardiovascular disease evaluation. In Proc ISMRM, page 1922, 2004.
3. Ronneberger O., Fischer P., Brox T. (2015) U-Net: Convolutional Networks for Biomedical Image Segmentation. In: Navab N., Hornegger J., Wells W., Frangi A. (eds) Medical Image Computing and Computer-Assisted Intervention – MICCAI 2015. Lecture Notes in Computer Science, vol 9351. Springer, Cham

Utility of Combining PET and MR Imaging of Carotid Plaque: Review and Early Experience

Vesey AT, Kaczynski J, Dweck MR, Newby DE
Department For Cardiovascular Science, Edinburgh University

Introduction

Hybrid positron emission tomography (PET) and magnetic resonance imaging (MRI) scanning platforms are now commercially available and offer unique advantages over other imaging modalities when assessing carotid plaque. By harnessing the versatility and soft tissue imaging capabilities of MRI to the sensitivity and biomolecular flexibility of PET, detailed multiparametric plaque characterization is possible. Multisequence carotid MR provides validated parameters of plaque risk(1) and can also image downstream neural tissue. The 18F-FDG(2) and 18F-Fluoride(3,4) PET isotopes have been shown to highlight inflamed and actively calcifying plaque. Putting the two techniques together may provide a unique “one stop” comprehensive plaque assessment.

We aim to present a review of this technology as applied to carotid imaging as well as our early experience.

Methods and Results

We conducted a review of the literature. We contacted vendors and research centres performing vascular hybrid PET/MRI in order gather data and provide a summary of the current status of the field.

We are recruiting patients who have experienced recent stroke (and controls) into an observational cohort study using carotid PET/MRI. Multi-sequence carotid MR (3D TOF, CE-MRA and 2D T1, T2, PD) was performed. 18F-Fluoride PET was synchronously obtained, reconstructed and fused with the various MR data. We present our early experience with case examples that demonstrate the advantages and challenges of this technique (see figure below).

Conclusion

PET/MRI shows promise for multi-parametric carotid imaging and our early experience supports this. However, proving cost-effectiveness and overcoming some technical challenges will be necessary before widespread clinical adoption can be seriously contemplated.

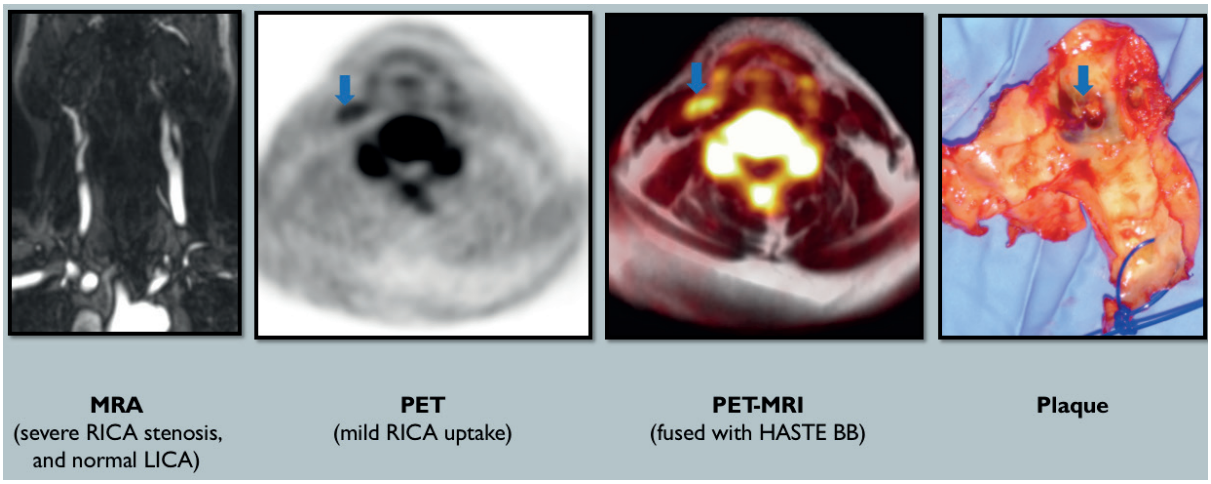

1. Saam T, Hatsukami TS, Takaya N, Chu B, Underhill H, Kerwin WS, et al. The Vulnerable, or High-Risk, Atherosclerotic Plaque: Noninvasive MR Imaging for Characterization and Assessment. Radiology. 2007 Jul;244(1):64–77.
2. Rudd JHF. Imaging Atherosclerotic Plaque Inflammation With [18F]-Fluorodeoxyglucose Positron Emission Tomography. Circulation. 2002 May 20;105(23):2708–11.
3. Vesey AT, Jenkins WSA, Irkle A, Moss A, Sng G, Forsythe RO, et al. 18F-Fluoride and 18F-Fluorodeoxyglucose Positron Emission Tomography After Transient Ischemic Attack or Minor Ischemic Stroke. Circulation: Cardiovascular Imaging. 2017 Mar 14;10(3):e004976.
4. Irkle A, Vesey AT, Lewis DY, Skepper JN, Bird JLE, Dweck MR, et al. Identifying active vascular microcalcification by (18)F-sodium fluoride positron emission tomography. Nature Communications. 2015;6:7495.

Safety for the Off-label Use of Ferumoxytol as an MR Contrast Agent: Early Results from the FeraSafe Multi-Center Registry™

Kim-Lien Nguyen,[1,2] Rola Saouaf,[3] Cynthia K. Rigsby,[4] Lindsay M. Griffin,[5] Mark A. Fogel,[6] Kevin K. Whitehead,[6] Mark L. Schiebler,[5] Peng Hu,[1] David E. Newby,[7] J. Paul Finn[1]

[1]Department of Radiological Sciences, David Geffen School of Medicine at UCLA, Los Angeles, CA, USA; [2]Division of Cardiology, David Geffen School of Medicine at UCLA and VA Greater Los Angeles, CA, USA; [3]Department of Radiology, Cedars-Sinai Medical Center, Los Angeles, CA, USA; [4]Department of Medical Imaging, Ann & Robert H. Lurie Children's Hospital of Chicago, IL, USA; [5]Department of Radiology, University of Wisconsin, Madison, WI, USA; [6]Division of Cardiology, Children's Hospital of Philadelphia, Philadelphia, Pennsylvania, USA; [7]British Heart Foundation Centre for Cardiovascular Science, University of Edinburgh, Edinburgh, UK

Purpose: Ferumoxytol is a superparamagnetic iron oxide nanoparticle approved since 2009 for treatment of iron deficiency anemia in chronic kidney disease and since 2018 for patients with normal renal function. Because of its long intravascular half-life and high MR relaxivity, ferumoxytol supports clinical applications well beyond those possible with extracellular contrast agents.[1, 2] Since March 2015 however, a U.S. Food and Drug Administration (FDA) "black-box" warning has been in effect, based on reports of hypersensitivity reactions during the post-marketing surveillance period for therapeutic use. Although single-center diagnostic safety experience has been reported, the FeraSafe Multi-Center Registry™ was established to pool multi-center safety data and to offer dynamic context for the safe and appropriate use of ferumoxytol for MRI. We aim to summarize our early multi-center registry safety experience.

Methods: The FeraSafe Multi-Center MRI Registry™ was created using the REDCap platform.[3] In this HIPAA-compliant and IRB-approved study, safety data for ferumoxytol-enhanced (FE) MRI exams between 2011-2018 from five academic medical centers across the U.S. and three in the United Kingdom (U.K.) were pooled and analyzed. Feraheme® (AMAG Pharmaceuticals, Waltham, MA) was used at centers in the U.S. and Rienso® (Takeda Italia, Italy) was used in the U.K. Ferumoxytol was diluted and administered as boluses (prior to FDA warning in 2015) and subsequently as slow infusions to a typical dose of 4mg/kg. Both first-pass and steady state image acquisitions were performed. Severity of adverse events were categorized as mild, moderate, severe, life-threatening, or death. Adverse events were classified as unrelated, possibly related, or definitely related to ferumoxytol administration. Mean arterial blood pressure, heart rate, and pulse oximetry were reviewed. Renal function was determined from plasma creatinine levels.

Results: Between 2011-2018, a total of 1294 ferumoxytol injections were administered for diagnostic purposes in 1221 human patients (age range: 1 day-96 years, 820 male) at five academic centers in the U.S. (n=709) and three academic centers in the U.K. (n=512). Sixty patients received multiple ferumoxytol injections. More adults (941/1221, 77%) than children (280/1221, 23%) received ferumoxytol. A total of 148 (12%) patients had immature renal function (age < 3.5 years); 54 (5%) patients had end-stage renal disease and were on dialysis. *No ferumoxytol-related severe or life-threatening adverse events occurred*. There were six mild (n=2 hypotension, n=2 nausea, n=1 nose pruritus and dry cough, n=1 hypertension and headache) and one moderate (n=1 back pain, flushing, nausea) adverse events that were either possibly related or definitely related to ferumoxytol administration. Two patients received supportive care: intravenous fluid (hypotension, n=1, 30 y.o. pregnant F with hypotension) and diphenhydramine (dry cough, n=1, 15 y.o. F with failed renal transplant). One 30 y.o. F with repaired Tetralogy of Fallot developed back pain and flushing with no change in vital signs, which resolved immediately after cessation of ferumoxytol. The predominant off-label indication for ferumoxytol was vascular assessment in patients with renal insufficiency. In those with documented vital signs at the time of this analysis (n=128), changes in mean arterial blood pressure, heart rate, or pulse oximetry were not statistically significant ($p>0.05$).

Discussion: Early experience from the FeraSafe Multi-Center Registry™ suggests that the off-label use of ferumoxytol for MRI /MRA has a very low incidence of adverse events in a closely monitored setting. More extensive experience and investigation will better define the risk /benefit profile across a spectrum of clinical applications and disease states and establish best practices. If the current safety trajectory is maintained, ferumoxytol may be the vanguard for a new class of agents to complement the extracellular GBCAs.

Acknowledgements: The authors thank attendees at the Ferumoxytol Working Group meeting in Toronto, Canada (2015 ISMRM). We also thank Dr. Takegawa Yoshida, Ms. Nikhita Kathuria, and Ms. Fiona Wee for their assistance.

References:

1. Finn JP, Nguyen KL and Hu P. Ferumoxytol vs. Gadolinium agents for contrast-enhanced MRI: Thoughts on evolving indications, risks, and benefits. *J Magn Reson Imaging*. 2017 Sep;46(3):919-923.
2. Bashir MR, Bhatti L, Marin D, et al. Emerging applications for ferumoxytol as a contrast agent in MRI. *J Magn Reson Imaging*. 2015 Apr;41:884-98
3. Harris PA, Taylor R, Thielke R, et al. Research electronic data capture (REDCap)--a metadata-driven methodology and workflow process for providing translational research informatics support. *J Biomed Inform*. 2009;42:377-81.

Ferumoxytol-Enhanced MRI for Intramyocardial Vascular Reactivity Mapping: Early Pre-Clinical Results

Kim-Lien Nguyen[1,2,3], Jiaxin Shao[1,3], Vahid K. Ghorati[1,3], J. Paul Finn[1,3], Peng Hu[1,3]

[1]*Diagnostic Cardiovascular Imaging Laboratory, Department of Radiological Sciences,* [2]*Division of Cardiology,* [3]*Physics and Biology in Medicine Graduate Program, David Geffen School of Medicine at UCLA, Los Angeles, CA, USA*

Purpose: Perfusion is important for organ vitality. In the myocardium, perfusion is dependent on both blood flow and blood volume. The intramyocardial blood volume (MBV) represents the fractional blood volume of the intravascular space within a unit volume of myocardial tissue.[1] Because ferumoxytol has high r1 relaxivity and a long intravascular half-life,[2] we hypothesize that ferumoxytol-enhanced (FE) MRI may enable mapping of the MBV. We aim to evaluate the vasodilator-induced variation in myocardial FE T1 signal as a surrogate for dynamic change in the MBV of normal swine.

Methods: In this ARC-approved study, four healthy Yorkshire swine (33-52 kg) underwent FE-MRI at 3.0T under general anesthesia (Figure 1A). We induced coronary vasodilation with 4-minute cycles of adenosine infusion (200-400 mcg/kg/min) pre- and post-ferumoxytol infusion (4mg/kg). During each cycle of adenosine-on and adenosine-off, we acquired myocardial T1 maps using 5-(3)-3-(3)-3 MOLLI. Using in-house T1 fitting algorithms that account for heart rate variations,[3] we generated myocardial T1 maps and derived T1 values from regions of interest drawn in the mid interventricular septum of short axis FE T1 maps. Vascular reactivity was defined as the FE T1 response during adenosine-on (coronary vasodilation) vs adenosine-off (return to baseline coronary vascular tone).

Results: No adverse events occurred and vital signs were stable throughout the adenosine infusion and FE-MRI exam. Myocardial T1 signal differential between pre- and post-ferumoxytol was -48.5%±6.4%. The adenosine-induced native T1 response as reflected by the slope between baseline and peak adenosine was less robust when compared to FE T1 response (3.0±0.6ms/min vs -35.3±16.1ms/min, p=0.03). During the two post-ferumoxytol adenosine-on cycles, the FE T1 values steadily shortened due to adenosine-induced vasodilation and increasing MBV. During adenosine-off cycles, FE T1 values increased towards values at rest. For adenosine 200-300 mcg/kg/min, the FE T1 shortened (decreased) 10.2±5.4% from baseline. For 400 mcg/kg/min dose, the FE T1 shortened >15% (swine #4). Of note, the increase in native T1 from baseline to peak adenosine was 0.7±0.2%.

Discussion: Ferumoxytol, as a potent intravascular contrast agent, sensitizes the T1 signal to changes in the MBV as reflected by vascular reactivity and substantially amplifies the intramyocardial vascular T1 estimate. Additional work in models of varying myocardial perfusion is needed to better characterize the T1 response in normal vs pathologic states.

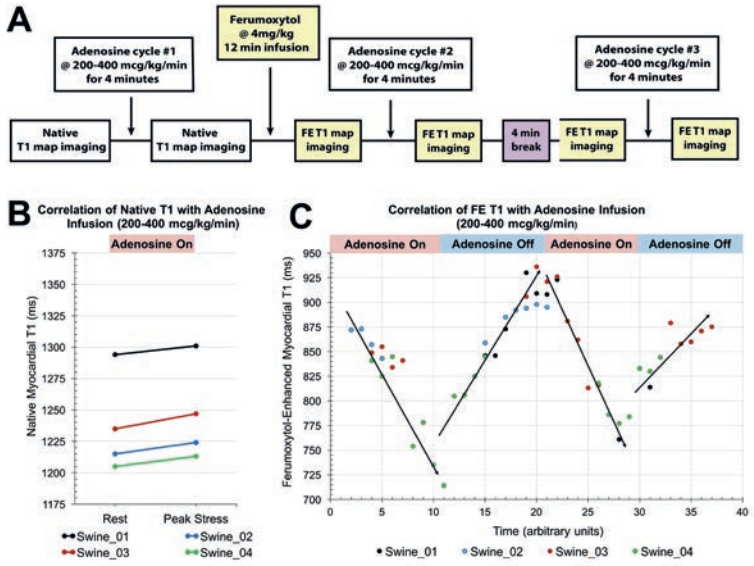

Figure 1. Ferumoxytol-enhanced (FE) MRI T1 myocardial blood volume mapping. FE-MRI T1 mapping protocol at 3.0T with one adenosine cycle pre- and two adenosine cycles post-ferumoxytol (A). Four healthy swine underwent successful myocardial T1 mapping without adverse events and vital signs were stable throughout the exam. Correlation of in vivo myocardial native T1 (B) and FE T1 (C) responses at baseline and peak adenosine infusion (200-400 mcg/kg/min) using healthy swine models are shown. The adenosine-induced native T1 response as reflected by the slope between baseline and peak adenosine was less robust when compared to FE T1 response (3.0±0.6ms/min vs -35.3±16.1 ms/min, p=0.03).

Funding: This work is supported by funding from the Radiological Sciences Exploratory Research Program, David Geffen School of Medicine at UCLA, Los Angeles, CA, USA.

REFERENCES

1. Le DE, Jayaweera AR, Wei K, Coggins MP, Lindner JR and Kaul S. Changes in myocardial blood volume over a wide range of coronary driving pressures: role of capillaries beyond the autoregulatory range. *Heart*. 2004;90:1199-205.
2. Finn JP, Nguyen KL, Han F, Zhou Z, Salusky I, Ayad I and Hu P. Cardiovascular MRI with ferumoxytol. *Clin Radiol*. 2016;71:796-806.
3. Shao J, Nguyen KL, Natsuaki Y, Spottiswoode B and Hu P. Instantaneous signal loss simulation (InSiL): an improved algorithm for myocardial T(1) mapping using the MOLLI sequence. *J Magn Reson Imaging*. 2015;41:721-9.

CT angiography (CTA) vs ferumoxytol-enhanced MR angiography (FeMRA) for the assessment of potential kidney transplant recipients

Sokratis Stoumpos[1,2], Pauline H Barrientos[3], Douglas Black[3], Martin Hennessy[3], Alex T Vesey[1], Ram Kasthuri[3], David B Kingsmore[1], Patrick B Mark[1,2], Aleksandra Radjenovic[2], Giles Roditi[3]

1. Renal & Transplant Unit, Queen Elizabeth University Hospital, Glasgow, UK
2. Institute of Cardiovascular and Medical Sciences, University of Glasgow, UK
3. Department of Radiology, Queen Elizabeth University Hospital, Glasgow, UK

Purpose: Conventional vascular imaging techniques are problematic in chronic kidney disease (CKD) patients due to associated risks, invasiveness and imprecision[1]. CT angiography (CTA) is the traditional imaging technique used to assess the vasculature of patients with CKD before being wait-listed for transplantation. Ferumoxytol originally developed as a MRI contrast agent and currently licensed for iron-deficiency anaemia[2], still has excellent potential in assessing the vasculature.

Methods: This was a comparative prospective cohort study of CTA versus Ferumoxytol-enhanced MRA (FeMRA) for the assessment of the aortoiliac vasculature in kidney transplant candidates. Patients with CKD undergoing CTA as part of pre-operative kidney transplant candidacy assessment were enrolled from the Glasgow Transplant Unit. FeMRA using 3mg/kg body weight of Ferumoxytol as intravenous contrast agent was performed in addition to CTA. We also used a proton density-weighted, in-phase (PDIP) 3D stack-of-stars gradient-echo pulse sequence (StarVIBE), to detect vascular calcifications in similar way to CT using contrast-free techniques. Head-to-head comparisons of lumen diameter, calcification, and signal intensity at predefined vascular sections were performed. Arterial and venous vasculature were assessed with both techniques by two readers and interclass correlation coefficient (ICC) was performed to assess intra and interobserver repeatability. For continuous variables, mean differences (and CI) were estimated and Bland-Altman plots of interobserver variability were created. For all comparisons, steady-state images were used using thin slab MIP reformats. Images were analysed using the Horos image viewer (Version 3, LGPL-3.0).

Results: 25 patients with CKD had CTA and FeMRA performed on the same day. There was excellent intra and interobserver agreement (between 0.85 and 0.95 for all measurements). CTA identified more foci of calcification compared with StarVIBE but this was not significant (Figure 1). Overall, FeMRA was found to overestimate lumen diameter of the examined vessels by 1.2mm (95% confidence interval [CI]: 0.07, 0.16) compared to CTA. Qualitative lumen depiction in the venous vasculature was superior with FeMRA.

Discussion: FeMRA combined with StarVIBE was comparable to CTA for assessment of lumen diameter, calcification and signal intensity in the abdominopelvic arterial vasculature of CKD patients due for transplant listing with the significant advantage of improved venous depiction. We assume the differences in calcification and lumen diameter are related to blooming artifact in CTA.

References:

1. Parfrey PS, Griffiths SM, Barrett BJ et al (1989) Contrast material induced renal failure in patients with diabetes mellitus, renal insufficiency, or both. A prospective controlled study. *N Engl J Med* 320:143–149
2. Adkinson NF, Strauss WE, Macdougall IC, Bernard KE, Auerbach M, Kaper RF, Chertow GM, Krop JS (2018) Comparative safety of intravenous ferumoxytol versus ferric carboxymaltose in iron deficiency anemia: A randomized trial. *Am J Hematol* 93(5):683-690

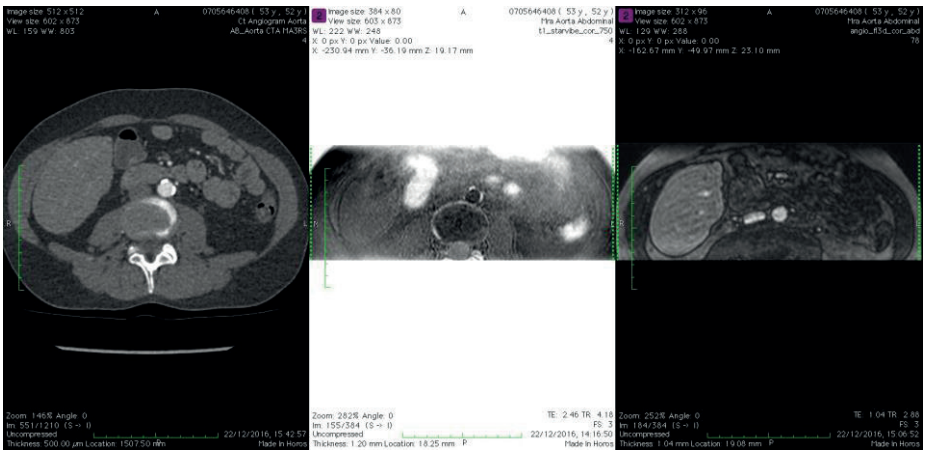

Utility of Ferumoxytol-enhanced 3-Dimensional Magnetic Resonance Imaging in the assessment of carotid atheroma inflammation

Ammara Usman[1], Jianmin Yuan[1], Andrew Patterson[1], Umar Sadat[2], Ilse Patterson[1], Martin Graves[1], Jonathan H Gillard[1]

[1]Department of Radiology, University of Cambridge, United Kingdom
[2]Department of Vascular Surgery, Cambridge Biomedical Campus, United Kingdom

Background:
Stroke is a leading cause of cardiovascular-related mortality and long term disability worldwide. Ischemic stroke constitutes two-third of them with carotid atherosclerosis being a predominant cause. The transition of the non-vulnerable to the vulnerable state of atheroma is governed by underlying immune-mediated-inflammation and related neovascularization that drive forward atherosclerosis disease process, with macrophages being the key cellular mediators.

Aims:
Ultra-small superparamagnetic iron oxide (USPIO)(Ferumoxtran-10)-enhanced MRI has shown to be a useful modality to image activated macrophages in vivo, which are principally responsible for atheroma inflammation. Recently Ferumoxtran-10 has been replaced by Ferumoxytol. This study determined the feasibility and the optimum imaging time-window to detect maximal quantitative signal change post-Ferumoxytol infusion using 3D black-blood T_2* and T_2 mapping sequences.

Methods:
Ten patients with carotid artery disease underwent high resolution MR imaging of their carotid arteries at 1.5T. Imaging was performed before and at 24, 48, 72 and 96h post USPIO (Feraheme, Takeda, Canada) infusion. USPIO uptake was evaluated by quantitative relaxometry maps indicating the difference in T_2* ($\triangle$ T_2*) and T_2 ($\triangle$ T_2) between baseline and post-USPIO MR imaging using 3D DANTE SWAN and iMSDE black-blood sequences respectively.

Results:
A significant quantitative decrease in ($\triangle$ T_2* 10.4 [3.5 -16.2]ms^{-1} ; $p < 0.001$) and ($\triangle T_2$ 13.4[6.2 -18.9] ms^{-1} ; p= 0.001) was observed at 48 hrs following the Ferumoxytol infusion. A positive correlation was also observed between T_2 and T_2* at 48 hours post-USPIO infusion (Spearman's r=0.492, p=0.039).

Conclusions:
This study demonstrated the feasibility of Ferumoxytol-enhanced MR Imaging in the assessment of carotid atheroma inflammation with 48hrs as the suitable post USPIO imaging window.

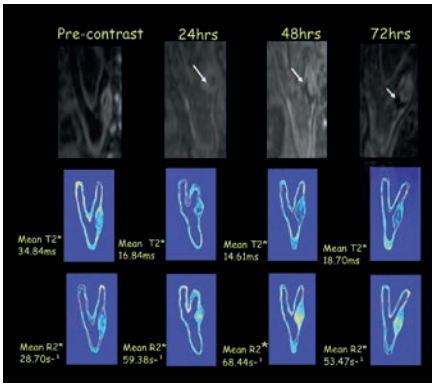

**The Fig shows ICC atheroma with relative decrease in T_2*and increase in R_2* from baseline, to 24hrs, 48hrs and 72hrs post USPIO infusion on T_2*w sequence (max T_2* decrease and increase in R_2* values at 48hrs)*

3D high resolution Black Blood(BB) Multi-Echo(ME) T2* Imaging Technique for Quantitative Superparamagnetic Iron Nanoparticle Uptake into Intracranial Atherosclerosis

Seong-Eun Kim[1], Adam de Havenon[2], J Scott McNally[1],
Bradley D Bolster, Jr[3], Gerald S Treiman[3], and Dennis L Parker[1]

[1]UCAIR, Department of Radiology and Imaging Sciences, [2]Department of Neurology, University of Utah, [3]Siemens Healthcare, [4]Department of Veterans Affairs, VASLCHCS

Purpose: Intracranial atherosclerotic disease (ICAD) is one of the most common causes of ischemic stroke in the world[1], and has a high rate of stroke recurrence. Post-gadoliniun enhancement in ICAD may be related to endothelial dysfunction or breakdown or secondary to plaque inflammation[2,3]. Delayed ferumoxytol imaging allows intravascular clearance with retention in the macrophages present in vulnerable atherosclerotic plaque[4]. We developed a 3D BB ME T2* imaging technique to allow quantitative ferumoxytol imaging on delayed scans by measuring T2* in ICAD.

Method: The 3D BB ME T2* imaging sequence was implemented with a quadruple inversion recovery (QIR) preparation[5] and segmented spoiled fast low angle shot (FLASH) readout. MRI was performed on patients with known ICAD using a Siemens Verio 3T MRI scanner with 20 channel head coil. 3D ME T2* images were acquired before (baseline) and 72 hours after ferumoxytol injection (72h delay). The imaging parameters for T2* were: resolution=0.6x0.6x1.0 mm^3, TI_1/TI_2=300/200 ms, TE_{min}/ TE_{max} /TR =2.8/27.2 /800ms, and ΔTE=3.4ms with 8 echoes. T2* maps were created and displayed using homemade software.

RESULTS:
Figure 1 shows results from a 79 year old female patient who was found to have multiple acute infarcts in the left MCA distribution. A CTA MIP (a) shows severe left MCA M1 segment stenosis. 3D SPACE shows PGE in a left MCA stenotic plaque (white arrow) (b). T2* images with TE of 16.2 ms are shown on Fig 1e (baseline) and Fig 1f (72h delay). Baseline T2* imaging shows no T2* signal in the left M1 plaque (white arrow, Fig 1c). However, the 72 h delayed T2* image shows hypointense signal (white arrow, Fig 1d). The 72h delayed T2* map shows a lower T2* value corresponding to the T2* signal enhanced area. The black arrows on T2* maps show that the ferumoxytol uptake after 72h post injection can be quantified by the difference in T2* values measured from baseline and 72h delayed scans. Mean T2* values of baseline and 72h delayed on the left M1 plaque were measure as 57.27±9.25 ms and 25.23±6.15 ms, respectively.

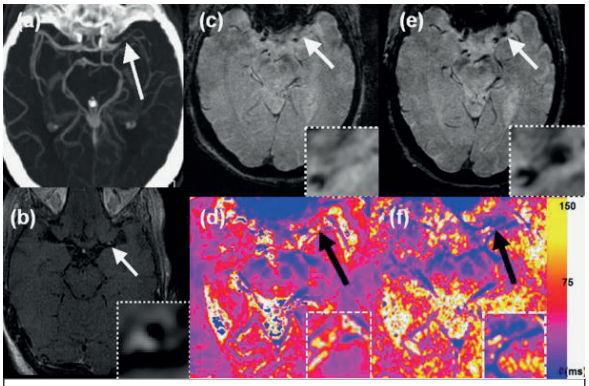

Fig 1. CTA MIP (a), 3D DANTE SPACE PGE (b), baseline T2* weighted image (c) and T2 * map (d), and 72h delayed T2* weight image (e) and T2* map (f). White arrows indicate the PGE and stenosis.

DISCUSSION: Previous studies of iron nanoparticle uptake have used 2D techniques, which are adequate for larger caliber arteries, larger plaques and more linear segments such as the carotid6,7. For the unique challenges inherent to ICAD, we developed a 3D BB ME T2* sequence that has excellent blood suppression. When a relatively thin slab (48 mm) is used with 3D acquisition and QIR preparation, we found good blood suppression on 72h delay MRI. Delayed ferumoxytol T2* imaging has been used for semi-quantitative measurement of uptake, but it can easily over- or under-estimate the uptake caused by the differences in subject and coil positioning between baseline and delayed scan which can influence the T2* signal intensities. To minimize those factors, R2*(1/T2*) can be used to assess the localization and amount of uptake more directly and with high sensitivity.

REFERENCES:
1. de Havenon A, et al. Neurovascular Imaging 2016;2(10).
2. Celletti FL, et al. Nature medicine 2001;7(4):425.
3. Libby P,et al. Circulation 2002;105(9):1135.
4. Alam SR, et al. J Cardiovasc Magn Reson2015;17:1
5. Yarnykh VL, et al. Magn Reson Med. 2002;48(5):899.

4D Flow MRI of the Uterine and Ovarian Vessels in the 2nd Trimester in Healthy Subjects

Philip A. Corrado[1], Dinesh M. Shah[2], Oliver Wieben[1,3]

Departments of Medical Physics[1], Maternal-Fetal Medicine[2], and Radiology[3], University of Wisconsin-Madison.

Purpose: Inadequate vascular remodeling during pregnancy is linked to complications including preeclampsia and fetal growth restriction[1]. The uterine arteries and uterine branches of the ovarian arteries provide oxygenated blood to the uterus and placenta during pregnancy (Figure 1). There is diagnostic value in assessing total uterine blood flow early in pregnancy, but conventional assessments using Doppler ultrasound focus on the uterine arteries alone and have limitations. Initial attempts with 2D PC MRI have struggled with scan plane placement[2]. We recently demonstrated the use of 4D flow MRI for placental flow assessment in the rhesus macaque[3], and here we expand this work to measure total uterine blood flow in a longitudinal human study at early and mid-2nd trimester.

Methods: Twenty healthy, pregnant women were scanned at two time points: (1) 14-16 weeks and (2) 20-22 weeks of gestation. All 4D flow scans were performed on a clinical 1.5T scanner (MR450W, GE Healthcare) with a 3D radially undersampled trajectory (PC VIPR[4], TR=5.9-6.1ms, TE=2.6ms, FOV=36x36x24cm^3, acquired spatial resolution=1.25mm isotropic, VENC=60cm/s, scan duration=10-12min) with retrospective respiratory gating (55% efficiency). Visibility was assessed for 8 vessel segments (uterine and ovarian arteries and veins) in the PC angiogram. Flow rate and vessel cross-sectional area were measured in visible vessels at multiple locations along the vessel and average values were reported.

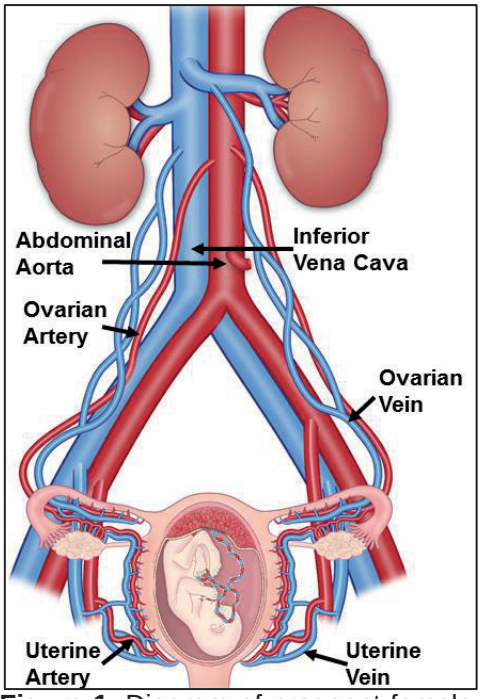

Figure 1: Diagram of pregnant female abdominal vascular anatomy.

Results: 4D flow scans were successfully completed for all 40 scans. Figure 2 shows a streamline visualization of flow in a 21-week subject with both uterine arteries and the right ovarian artery and vein visible. Table 1 summarizes the number of scans in which a given vessel was visible (N), along with mean flow and area measurements in the uterine and ovarian arteries and veins (sum of left + right vessels shown).

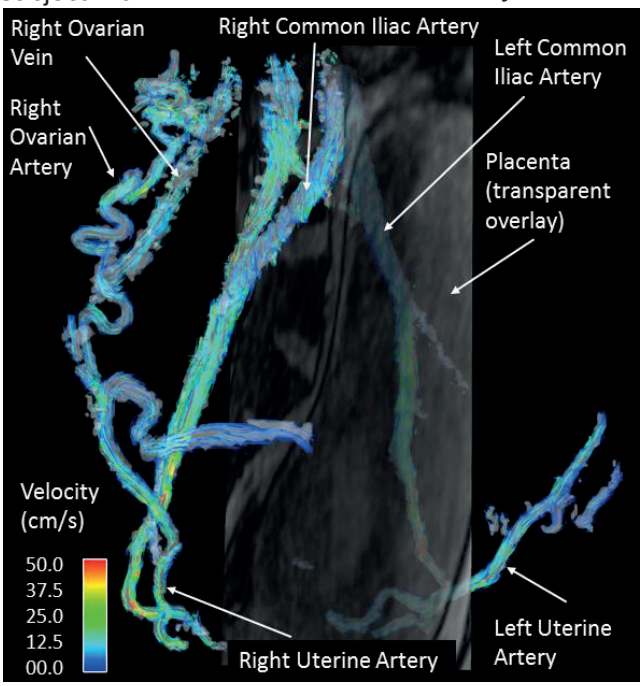

Figure 2: Streamline visualization of flow in the maternal vasculature with a semi-transparent magnitude image slice overlaid showing the uterus and placenta.

Discussion: 4D flow MRI via PC VIPR in the uterine arteries was feasible at both 14-16 weeks and 20-22 weeks gestation, while vessel visualization was less consistent for uterine veins and ovarian arteries and veins, and was worse at 14-16 weeks than at 20-22 weeks for ovarian vessels. This is consistent with our prior findings in rhesus macaques that the uterine arteries deliver most of the oxygenated blood to the uterus[3]. Flow in the ovarian vessels varied more between the subjects than flow in the uterine vessels and was higher on average at 20-22 weeks than 14-16 weeks, suggesting ovarian artery contributions to uterine flow in pregnancy are significant in some subjects, possibly related to placentation site. Future work will investigate total blood flow and blood flow changes as potential predictors of pregnancy complications.

References: **1.** Degner K, et al. Reprod Sci. 2016;1-9. **2.** Pates JA, et al. Magn Res Imag 2010; 28:507–510. **3.** Corrado PA, et al. SMRA 2017. **4.** Johnson KM, et al. MRM. 2008;60(6):1329-1336. **Acknowledgements**: NIH awards NICHD U01HD087216, TL1TR002375, and GE Healthcare for support.

Table 1	Uterine						Ovarian					
	Arteries			Veins			Arteries			Veins		
Gest. weeks	N	Flow (mL/min)	Area (mm^2)	N	Flow (mL/min)	Area (mm^2)	N	Flow (mL/min)	Area (mm^2)	N	Flow (mL/min)	Area (mm^2)
14-16	17	195±76	80±57	6	137±116	38±19	4	106±62	28±8	4	118±109	30±15
20-22	17	188±71	80±64	3	173±45	31±11	7	245±194	40±25	9	295±162	66±48

Simultaneous quantitative assessment of cardio-renal perfusion and glomerular filtration rate using dual-bolus dynamic contrast-enhanced magnetic resonance imaging

M. Lee[1], S. Sourbron[2], R. Woodward[1], K. Brooksbank[1], D. Black[1], P. Hall-Barrientos[1], C. Berry[1], P. Mark[1], G. Roditi[1], N. Sattar[1], A. Radjenovic[1]

[1]Institute of Cardiovascular and Medical Sciences, University of Glasgow and GGC NHS Trust, Glasgow, UK;
[2]University of Leeds, Leeds, UK

Background: Multi-organ microvascular pathology is present in a range of highly prevalent diseases, most notably hypertension and type 2 diabetes. Clinical MRI studies are limited to the assessment of a single organ, as despite its non-invasiveness and versatility, MRI acquisition times tend to be too long to allow acquisition of complex datasets for quantitative analysis of microvasculature at multiple sites. With the introduction of highly accelerated acquisition methods, multi-organ MRI protocols for quantitative tissue characterisation are on the cusp of becoming ready for employment in clinical trials. Here we present initial results obtained using an interleaved dynamic contrast-enhanced-MRI (DCE-MRI) sequence, designed as a part of a comprehensive cardio-renal clinical MRI protocol aimed at investigating the mechanism of action of a sodium-glucose co-transporter 2 inhibitor (empagliflozin).

Methods: Saturation recovery prepared, ECG-triggered, single-shot gradient echo sequence was adapted to capture transverse aortic plane at the level of the main pulmonary artery (for arterial input function, AIF), mid-ventricular short-axis plane through the left ventricle and "kidney-coronal" plane within each RR interval. To avoid the effects of signal saturation during peak contrast enhancement and enable simultaneous measurement of capillary blood flow in both myocardium and kidneys, as well as glomerular filtration rate, two boluses of Gd-DTPA were administered: 30 and 90 seconds after the start of acquisition (0.025 mmol/kg of Gd-DTPA, followed by a 20 ml saline flush at 3 ml/s injection rate). Three patients (2 female, age range 40-58) who were referred for a diagnostic CMR scan for evaluation of cardiomyopathy (n = 3) provided written informed consent to take part in this research study. Scanning was performed on a 3T clinical MRI system (Prisma, Siemens Healthcare).

Results All three acquisitions yielded high quality data for quantitative analysis. A representative example of cardiac and renal DCE components is presented in Figure 1 (left panel), and right panel illustrates AIF derived from the third (transverse) plane.

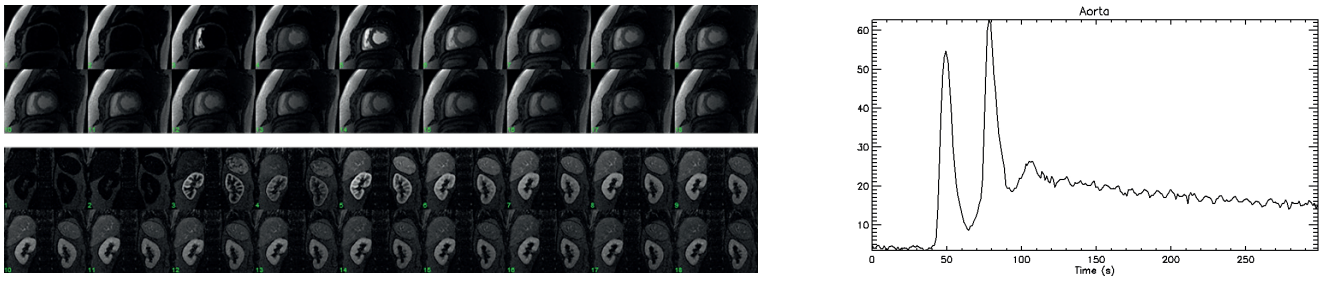

Figure 1. An illustration of interleaved cardiac and renal DCE-MRI time series and dual bolus AIF (descending aorta).

Quantitative analysis of DCE-MRI datasets was performed using PMI software[1]. Examples of renal and cardiac quantitative plasma flow maps are presented in Figure 2, alongside an example of a DCE-MRI curve derived from total kidney parenchyma, fitted to a 2-compartment filtration model. Additional motion correction method, implemented within PMI[2] was applied to the kidney slice and provided excellent motion correction.

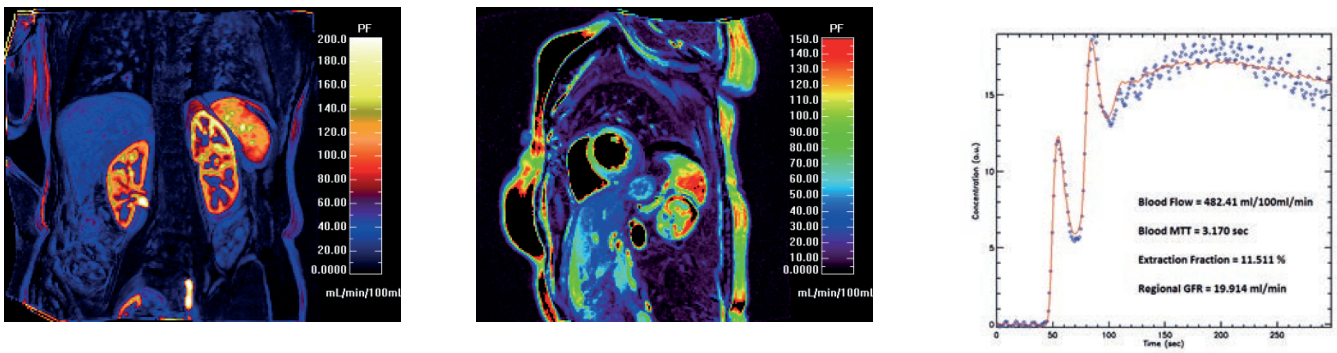

Figure 2. Quantitative maps of renal and myocardial plasma flow, and an example of renal ROI DCE-MRI data fitted to a 2-compartment filtration model.

Conclusion: We demonstrated feasibility of interleaved, single acquisition assessment of myocardial and renal perfusion, as well as glomerular filtration rate. Data acquired in three initial patients was of uniformly high quality and quantitative analysis provided results in agreement with literature values.

References: [1]. S. Sourbron et al. ESMRMB 2009. [2] D. Flouri, et al. M. ISMRM 2017.

Comparison of renal split function using 1.5T DCE-MRI and Nuclear Medicine

SL Chang [2], P Hall Barrientos[1], BA Johnston[1], MR Lopez-Gonzalez[1],G Roditi[2]
[1]Department of Clinical Physics and Bioengineering, [2]Department of Radiology,
NHS Greater Glasgow and Clyde, Scotland, U.K

Purpose

Pre-operative radiological assessment of living renal donor traditionally involves 2 different imaging techniques: multidetector computed tomography (MDCT) for renal anatomy and nuclear medicine (NM) for renal function. In recent years, Dynamic Contrast Enhanced MRI (DCE-MRI) has been gaining popularity as a potential substitute for it could assess renal anatomy as well as renal function. Clinical relevant parameters can be quantified using tracer kinetic models to estimate, blood flow, blood volume, mean transit times and glomerular filtration rate. Our aim in this study is to compare the accuracy of the split renal function of DCE-MRI by taking nuclear medicine DMSA/MAG3 Tc-99m scan result as reference.

Methods

Datasets were obtained from 70 potential renal donors who underwent both DCE-MRI and DMSA/MAG3 Tc-99m Nuclear Medicine test. Patients were scanned in a 1.5 T Siemens Aera and Avanto MRI system. DCE-MRI was performed using a fast low angle shot (FLASH) sequence continuously sampling of 3D volumes. 64 volumes were obtained in 255 s, TE/TR= 1/190 ms; FoV=420 mm; matrix=124x128; slice thickness= 8 mm.

Kidney volumes were calculated from post contrast vibe sequences using the threshold segmentation tool on Osirix 3.8.1. The kidney function was evaluated using the software PMI 0.4[1]. A ROI-based two-compartment renal filtration model was applied for quantification of four single kidney parameters which include blood volume, blood transit time, tubular flow and tubular transit time. Two observers, who were blinded to the NM results, measured the kidney volumes and function. Statistical analysis was performed using paired t-test and Bland-Altman plots.

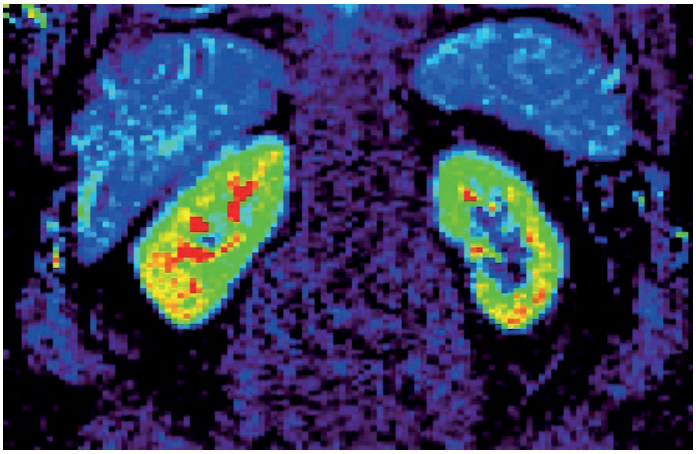

Figure 1. Example of PMI result to determine GFR.

Results

The DCE-MRI measurements were analysed and the renal split functions were derived. Based on the results of 70 potential donors, there were no significant differences between nuclear medicine and MRI split function results ($p = 0.09$, bias 2 ± 14.4 %).

Discussions

According to the result, DCE-MRI is a reliable tool for renal split function measurement in addition to renal anatomy assessment. The next stage of the study is to evaluate the feasibility of DCE-MRI Glomerular Filtration Rate (GFR) measurements in comparison with nuclear medicine GFR.

References: [1]PMI: Platform for Research in Medical Imaging. S. Sourbron, A Biffar, M. Ingrisch, Y Fierens, R Luypaert. ESMRMB 2009.

Use of k_Z-Space for Providing Sub-Millimeter Through-Plane Resolution in 2D Multislice Imaging

S Kargar, EA Borisch, RC Grimm, *A Kawashima, EG Stinson, SJ Riederer
Mayo Clinic, Rochester MN USA; *Mayo Clinic, Scottsdale AZ USA

Purpose: The goal of this study is to modify two-dimensional (2D) multi-slice acquisition and reconstruction to permit sub-mm through-plane spatial resolution. Current slice thicknesses in multislice MRI are typically no smaller than 1.7 mm.

Method: The basis of the new method is to perform the image reconstruction in k_Z-space. Acquisition is done using slices with modest slice-to-slice overlap. The acquired data are next transformed along the slice direction (Z) into k_Z-space where we then precisely account for the slice profile created by the RF excitation and for the k_Z sampling effects caused by the slice-to-slice spacing. We have tested the new method on 2D multi-slice images of a resolution phantom, an SNR phantom, and in vivo T2-weighted spin-echo (T2SE) prostate MRI. Images were acquired in one orientation (e.g. sagittal) and performance assessed in reformats in a different orientation (e.g. axial). Typical acquisition parameters were 3.2 mm slice thickness and slice increment of 0.8 mm (75% overlap) and 1.6 mm (50%). Inversion problems due to zero crossing while compensating for the slice profile were addressed by Tikhonov regularization.

Results: Reconstructions for 0.8 and 1.6 mm slice increments show improved resolution vs. the case of abutting slices (spacing = slice thickness = 3.2 mm) with zero padding. Similar results were observed in the prostate phantom and in vivo prostate images. Reduction of the regularization parameter provides improved modulation with some increased noise. Use of 0.8 mm slice increment provided clear visualization of the 0.5 lp/mm resolution pattern, confirming the desired sub-mm performance. Sagittal reformats from axial acquisitions of the prostate are competitive with direct sagittal acquisition.

Discussion: Super-resolution methods, in which a set of low resolution images is reconstructed to provide a high resolution set, have been widely studied in MRI [1]. However, virtually all methods are based on reconstruction in the spatial domain [2]. The method presented here is different in that the input data, comprised of typically 50-100 slices, are first transformed to k_Z-space. The acquisition uses incremental slice spacing [3]. The method is expected to be applicable to 2D multislice imaging in general, including potential application in MRA [4].

References: [1] Van Reeth E, Concepts in MRI 40A:306 (2012); [2] Irani M, CVGIP 53:231 (1991); [3] Greenspan H, Magn Reson Img 20:437 (2002); [4] Koktzoglou, Magn Reson Med 79:683 (2018)

Comparison of GFR measurements using 1.5T DCE-MRI and Nuclear Medicine

MR Lopez-Gonzalez[1], SL Chang [2], BA Johnston[1], P Hall Barrientos[1],G Roditi[2]
[1]Department of Clinical Physics and Bioengineering, [2]Department of Radiology,
NHS Greater Glasgow and Clyde, Scotland, U.K

Purpose

Dynamic Contrast Enhanced MRI (DCE-MRI) has been used for renal function characterisation. Clinical relevant parameters can be quantified using tracer kinetic models to estimate, blood flow, blood volume, mean transit times and glomerular filtration rate. The aim of this study is to compare the accuracy of the DCE-MRI renal function with Nuclear Medicine (NM) 51Cr-EDTA GFR estimation as gold standard, in a population of healthy living kidney donors.

Methods

Datasets were obtained from 24 donors who underwent DCE-MRI and all Nuclear Medicine tests. Patients were scanned in a 1.5 T Siemens Avanto and Aera MRI system. DCE-MRI was performed using a fast low angle shot (FLASH) sequence continuously sampling of 3D volumes. 64 volumes were obtained in 255 s, TE/TR= 1/190 ms; FoV=420 mm; matrix=124x128; slice thickness= 8 mm.
Kidney volumes were calculated using the segmentation tools on Osirix 3.8.1 and on an Extended MR workspace Philips, using a combination of threshold and manual segmentation techniques. Kidney function was evaluated using the software PMI 0.4 (1). A ROI-based two-compartment renal filtration model was applied for quantification of the four single kidney parameters of blood volume, blood transit time, tubular flow and tubular transit time. Two observers measured kidney volumes and GFR values and were blinded to the NM results. Analysis was carried out using mean coefficients of variation (CV), paired t-test and Bland-Altman plots.

Results

Kidneys volumes were measured using two different types of software (Philips workspace-method 1 and Osirix method 2) and the results were compared. Additionally, two observers measured kidney volumes and calculated GFR using the standard volume of kidneys as 200 cm^3 and the individual volumes measured.

Inter-observer variations of the kidney volumes using method 1 and 2 were obtained using the two way ANOVA for method 1 ($F[47,192]=522$, $P<0.001$) for method 2 ($F[47,192]=16.2$, $P<0.001$). Although, ICC for method 1 and 2 were 0.802 (95% confidence interval 0.493 and 0.901, lower and upper bound) and 0.916 (95% confidence interval 0.882 and 0.940, lower and upper bound), respectively. Although there were significant inter-observer variations of the kidney volumes for both measurements using two different software. However, there is high interclass correlation coefficient demonstrated by both observers in this study.

The DCE-MRI measurements were analysed and single kidney GFR was derived. SK-GFR values were obtained using a standard kidney volume of 200ml and using the values obtained from the Philips software. Based on the results of 24 donors there were significant differences between NM GFR and MRI GFR ($p = 0.0337$, bias = 17 ± 76 ml/min). This was also seen between NM GFR and MRI GFR 200 ml ($p <0.0001$, bias = 56± 69 ml/min).

Discussions

MRI has overestimated GFR when compared to NM. This was mainly due to the resulting perfusion image were not motion corrected. The next stage of the study is to perform GFR measurements on motion corrected images.

References: [1]PMI: Platform for Research in Medical Imaging. S. Sourbron, A Biffar, M. Ingrisch, Y Fierens, R Luypaert. ESMRMB 2009.

Bright venous and/or sinus signals on arterial spin labeling MRI for identifying cerebral venous thrombosis, comparing with MRA findings

Dong Woo Park, Tae Yoon Kim, Hanyang University Guri Hospital, South Korea

Purpose; Cerebral venous thrombosis is often challenging to detect on conventional MR and MR angiographic examinations, of which early diagnosis is essential to improve its prognosis. The purpose of this study is to evaluate the value of bright venous and/or sinus signals on arterial spin labeling (ASL) MR imaging for identifying cerebral venous thrombosis, comparing with MR angiographic findings.

Methods; ASL MRI of 12 patients who were diagnosed as cerebral venous thrombosis based on clinical manifestation as well as conventional MRI and MR angiography with/without cerebral angiography, were retrospectively analyzed for bright venous and/or sinus signals.

Results; Bright sinus signals on ASL MRI were detected in all 12 patients, all located proximal to sinus thrombosis. In addition, bright sinus signals were also detected distal to sinus thrombosis in 11 patients, which often extended to the jugular bulb. Meanwhile, bright venous signals on ASL MRI were detected only in 3 patients, which accompanied venous dilatation on conventional MRI. Susceptibility vessel sign and high FLAIR signal were revealed in 11 (91.7%) and 9 (75%) patients, respectively. Therefore, bright sinus signal had higher sensitivity for identifying cerebral venous thrombosis than the susceptibility vessel sign and high FLAIR signal.

Discussion; Bright venous and/or sinus signals from excessively accumulated labeled protons could be demonstrated in the vein and/or sinus proximal to thrombus, in spite of postlabeling decay. Additionally, decreased cerebral perfusion pressure from venous hypertension could contribute the development of abnormal fistulous venous channels carrying labeled protons (1). Meanwhile, labeled protons could traverse partially thrombosed venous channel to reach up to jugular bulb. The sensitivity of bright venous and/or sinus signals for identifying cerebral venous thrombosis was higher than other thrombosis signs (1,2).

Conclusions; Bright venous and/or sinus signals on ASL MRI could provide important diagnostic clue for identifying cerebral venous thrombosis. This technique could contribute to improve the prognosis of cerebral venous thrombosis.

References:

1. Kang JH, Yun TJ, Yoo RE, Yoon BW, Lee AL, Kang KM, Choi SH, Kim JH, Sohn CH, Han MH. Bright sinus appearance on arterial spin labeling MR imaging aids to identify cerebral venous thrombosis. Medicine. 2017;96(41)

2. Yoo RE, Yun TJ, Rhim JH, et al. Bright vessel appearance on arterial spin labeling MRI for localizing arterial occlusion in acute ischemic stroke. Stroke 2015;46:564–7

Results of Contrast Enhanced Magnetic Resonance Angiography (MRA) of the Hand – A Retrospective Evaluation

Carola Huber[1], Andrea Obernosterer[2], Manuela A. Aschauer[1,3]
[1] Medical University of Graz, Austria; [2] Division of Angiology, Department of Internal Medicine;
[3]Division of Neuroradiology, Vascular and Interventional Radiology, Department of Radiology

Purpose: Description and evaluation of MRA examinations of the hand and a comparison of the digital subtraction angiography (i.a.-DSA) with the MRA.
Methods/Patients: Between 2009 and 2017 MR angiography of the hand was performed in 131 patients (female: 68, male: 63, average age: 46,5 years). Conventional MRA was done with a separate evaluation of the contrast-arrival time. TWIST-MRA was conducted without timing-sequence.
Results: High-performance 3-Tesla-MR imaging gradient systems and high-quality receiver coils allow the acquisition of arterial-phase images following intravenous administration of contrast agents. Early venous overlay was seen in patients with tissue loss and/or inflammation as well as in patients with arterio-venous malformations. The differentiation between vasospastic disorders, e.g. Raynaud's disease, and other vaso-occlusive conditions requires invariably the use of vasodilators. The high-temporal resolution of the TWIST-sequence mainly avoids the early venous-overlay and allows more precise diagnoses.
For diagnostic purpose a DSA examination was never required after the MRA. A detailed consideration and inquiry of source images is unavoidable to confirm a diagnosis. Therefor MPR was used in most cases (s. Fig. 2).
Discussion: The DSA persists as the gold-standard, but there are disadvantages compared to the MRA. MRA should be the first method in diagnostic algorithm. To be able to fully depict pathologies of the vascular supply of the hand the MRA should be performed including T1 and T2 weighted images.

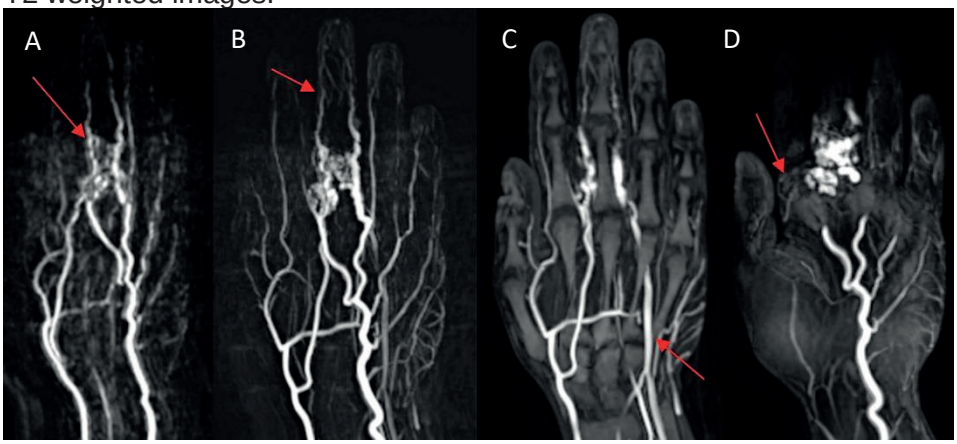

Fig.1: Arterio-venous malformation; TWIST-Sequence; arterial (a); early venous (b), equilibrium phase (c); source image with small feeder (d)

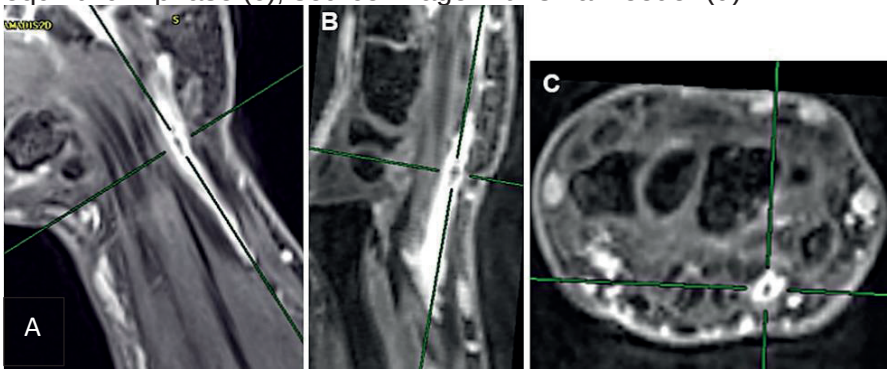

Fig. 2: Thrombus A. ulnaris sin.; coronal, sagittal and transversal imaging

References: This work contains parts of – Dissertation of Carola Huber
please ask manuela.aschauer@medunigraz.at

Fractional flow reserve in the femoral arteries derived through computational fluid dynamics: a non-invasive diagnostic tool for stenotic diseases

S. Skopalik[1], A. Radjenovic[2], G. Roditi[2], P. Hall Barrientos[4], J. Matthews[3], P. Mark[2], W. Stuart[4], M. C. Paul[1*]
[1]School of Engineering; [2]Institute of Cardiovascular & Medical Sciences, University of Glasgow, G12 8QQ, UK
[3]Canon Medical Research Europe Ltd, [4]Queen Elizabeth University Hospital, Glasgow, Scotland
Email: s.skopalik.1@research.gla.ac.uk ; *Manosh.Paul@glasgow.ac.uk

Introduction: Fractional flow reserve (FFR) is considered to be the current "gold standard" for assessing the severity of coronary stenotic diseases [1], however it is not yet tested at assessing diseases in other arteries. FFR is the ratio between the maximum achievable blood flow in a stenotic artery and the theoretical maximum achievable blood flow in the same artery in the absence of stenosis, during maximum hyperaemia [2]. Furthermore FFR measurement is costly and is associated with certain risks: it requires drug administration, specialist equipment, an operating room and a medical team [3]. Nevertheless, FFR is a good and relatively simple index of predicting the severity of a stenosis which makes it desirable to test this principle in other vessels, such as the femoral arteries.

Purpose Computational fluid dynamics (CFD) combined with high quality medical imaging data can be a viable alternative to catheter derived pressure measurements for FFR calculation. In addition CFD analysis can be useful in predicting blood flow conditions and stenosis severity in a wider range of blood vessels in which catheter measurement may not be possible. To test this, in-silico measurement of FFR in femoral arteries has been the main focus of this study. The use of primarily open-source software has also been identified as one of the goals of the study to reduce diagnostic costs.

Method: The method starts with a 3D DICOM vascular dataset of the patient in which the blood vessels of interest are identified and a surface model is generated as shown in Figure 1(a) using VMTK (www.vmtk.org). A 3D computational mesh is then generated and imported into a CFD software STAR-CCM+ (Siemens PLM, 2017) or OpenFoam (https://www.openfoam.com/), where simulations are performed with varying boundary conditions. Blood is modelled as a Newtonian fluid with density of 1060 kg/m^3 and dynamic viscosity of 4 mPa·s [4]. Velocity is defined at the inlet and pressure is set at the outlet. Steady state (constant velocity) and transient (pulsatile) boundary conditions were tested.

Results and Discussion: Figure 1(b) shows velocity plots on a cut surface plane though the model. Velocity profiles obtained from CFD appear realistic. Inspection of the pressure field, however, shows that it is strongly dependent on the boundary conditions. For example appropriate model needs to be used to take into account the rest of the cardiovascular system which is not otherwise represented in the 3D model. Furthermore, parameters such as vessel length, number of outlets and proximity of the outlets to the inlet also showed to have an influence on the pressure field. This emphasised that in order to use CFD derived FFR as a reliable diagnostic measure, special care needs to be taken when choosing the boundary conditions. Therefore further studies will seek to establish the optimal type of boundary conditions, with special focus on patient specific values, as well as to apply the method to a wider range of vessels.

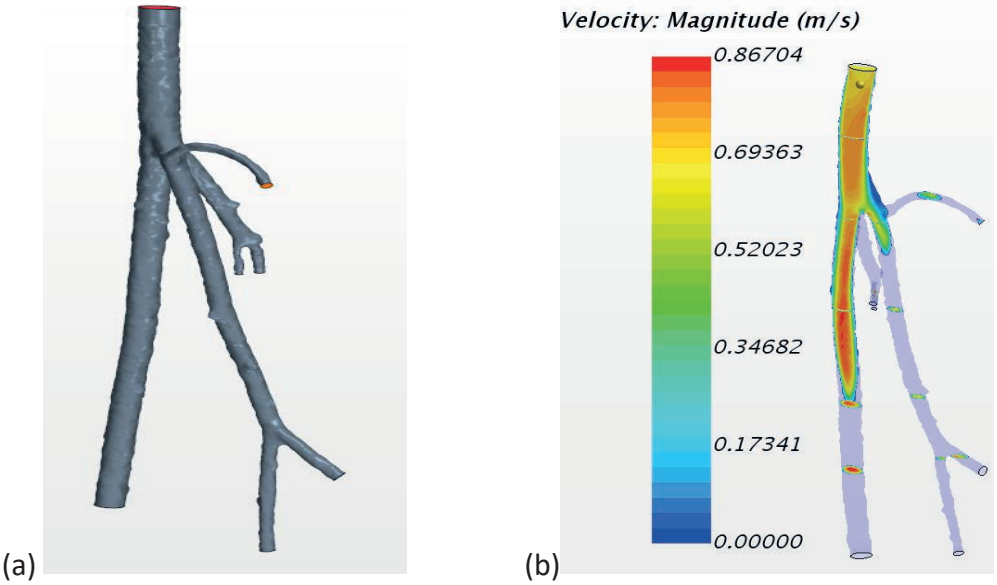

Figure 1: Femoral artery modelling process: (a) Reconstructed 3D surface, (b) Velocity contours on a cut plane

References:

1. Morris, P.D., et al., *"Virtual" (Computed) Fractional Flow Reserve: Current Challenges and Limitations.* JACC: Cardiovascular Interventions, 2015. **8**(8): p. 1009-1017.
2. Berry, C., et al., *Fractional flow reserve versus angiography in guiding management to optimize outcomes in non-ST-elevation myocardial infarction (FAMOUS-NSTEMI): rationale and design of a randomized controlled clinical trial.* Am Heart J, 2013. **166**(4): p. 662-668 e3.
3. Min, J.K., et al., *Noninvasive Fractional Flow Reserve Derived From Coronary CT Angiography: Clinical Data and Scientific Principles.* JACC: Cardiovascular Imaging, 2015. **8**(10): p. 1209-1222.
4. Linge, F., M.A. Hye, and M.C. Paul, *Pulsatile spiral blood flow through arterial stenosis.* Computer Methods in Biomechanics and Biomedical Engineering, 2014. **17**(15): p. 1727-1737.

Experimental Assessment of MEDIC and ToF Imaging Accuracy

MacDonald C.[1], Hellmuth R.[3], Priba L.[2], Ross R.[2], Houston J. G.[1,2]

[1] Ninewells Hospital and Medical School, University of Dundee, Dundee, UK
[2] NHS Tayside Clinical Radiology, Ninewells Hospital, Dunde, UK
[3] Vascular Flow Technologies, Dundee, UK

Introduction

Recently, many studies have been performed using MRI to create 3D models of blood vessels for numerical simulations of haemodynamics. Metrics analysed in these studies are generally functions of vessel radius, thus results are sensitive to vessel lumen depiction. A range of MRI sequences have been used to capture 3D anatomical data, such as steady-state free precession [1], black-blood [2], and Time-of-Flight [3]. However, there are not many cases assessing the egality of lumen depiction between MRI sequences. The purpose of this study was to determine if the Multi-Echo Data Image Combination (MEDIC) and Time-of-Flight (ToF) MRI sequences provided equal vessel lumen depiction.

Methods

Images of a series of phantoms using both ToF and MEDIC sequences were aquired on a 3T Mangeton (Siemens, Germany) scanner. The phantoms consisted of plastic tubes of 2 mm, 3 mm and 5 mm in diameter fixed either as a straight line or as a U-bend inside the same PVC box, which provided fiducial points. The flow rate was adjusted to the tube diameter to provide average velocities of either 0.5 m s^{-1} or 1 m s^{-1} over the phantom cross-section. 3D MRI datasets were post-processed to create 3D models using a contour lofting method in Simvascular [4]. Agreement between the ToF and MEDIC sequences weas analysed using Bland-Altman methods, and graphical depiction of differences. The effect of tube diameter and flow velocity on lumen depiction was assessed for each sequence.

Results and Discussion

Good inter-sequence agreement was observed in the straight tubes, which indicates that either scanning method can be used for imaging of small vessels. However, lower flow-velocity (0.5 m s^{-1}) in the straight tubes caused an underestimation of area when imaged with both MEDIC and ToF. This underestimation was consistently higher for the ToF sequence. Scanning of the U-bend geometry is underway. Once completed, U-bend geometry will allow exploration of the effect of out-of-plane flow, which is common in anatomies such as the surgical anastomosis for haemodialysis fistulas.

References

[1] J. Alastruey, N. Xiao, et al. On the impact of modelling assumptions in multi-scale, subject-specific models of aortic haemodynamics. *Journal of The Royal Society Interface*, 2016. ISSN 1742-5689.

[2] Y. He, C. M. Terry, et al. Serial analysis of lumen geometry and hemodynamics in human arteriovenous fistula for hemodialysis using magnetic resonance imaging and computational fluid dynamics. *Journal of Biomechanics*, 2013. ISSN 00219290.

[3] M. Sigovan, V. Rayz, et al. Vascular Remodeling in Autogenous Arterio-Venous Fistulas by MRI and CFD. *Annals of Biomedical Engineering*, 41(4):657–668, apr 2013. ISSN 0090-6964.

[4] A. Updegrove, N. M. Wilson, et al. Simvascular: An open source pipeline for cardiovascular simulation. *Annals of biomedical engineering*, 45(3):525–541, 2017.

Evaluate the Characteristics of Spontaneous Intracranial Artery Dissection using High Resolution MRI Vessel Wall Imaging

Bing Tian, Xia Tian, Zhang Shi, Qi Liu, Jianping Lu
Department of Radiology, Changhai hospital of Shanghai, Shanghai, China

Purpose:

High resolution MRI vessel wall imaging provides important insights of assessing both vessel lumen and wall in intracranial artery stenosis disease. This study aims to evaluate the characteristics of spontaneous intracranial artery dissection on high resolution MRI vessel wall imaging.

Methods:

This was a retrospective study with patient consent. Thirty-four patients (7 female, age 50±14) with approved spontaneous intracranial artery dissection(DSA and clinical diagnosis) were scanned on a 3T Siemens Skyra scanner with pre- and post-contrast 3D T1-weighted SPACE (0.5mm isotropic). A high resolution CE-MRA was performed following the pre-contrast SPACE sequence. Immediately following the CE-MRA, the SPACE sequence was repeated. Patients were divided into two groups based on the artery change on CE-MRA as stenosis(occlusion) group and dilatation group. The characteristics of spontaneous intracranial artery dissection were evaluated including the location of dissection, double lumen, intimal flap, intramural hematoma(an area of hyperintense signal intensity on pre-contrast SPACE images in the vessel wall), Intraluminal contrast enhancement(an area of intraluminal contrast enhancement on post-contrast SPACE images), and artery wall enhancement(degree of enhancement was assessed based on a visual grading system as follows: grade 0, similar to that of normal vessel walls; grade 1, greater than that of grade 0 but less than or similar to that of muscle; and grade 2, greater than that of muscle). The characteristics of spontaneous intracranial artery dissection were compared between two groups. Patients clinical symptom and brain parenchyma lesion(ischemic or hemorrhage) were also evaluated and compared.

Results:

Thirty patients' dissection located on the posterior circulation. There were 16 patients in stenosis group and 18 patients in dilatation group. More patients in dilatation group showed double lumen and intimal flap. Intramural hematoma and intraluminal contrast enhancement were more frequency seen in stenosis group. There was no significantly different of artery wall enhancement between the two groups.

Discussion:

Spontaneous intracranial artery dissection always show stenosis/occlusion or dilation on traditional angiography images such as computed tomography angiography (CTA), magnetic resonance angiography (MRA), and digital subtraction angiography(DSA). The definite diagnostic criteria of spontaneous intracranial artery dissection is the presence of an intimal flap and a double lumen[1]. However, in cases without a definite dissection sign, precise diagnosis may not be easy to achieve. Patients with lumenal dilatation and intramural hematoma may be misdiagnosed as intracranial aneurysm. Compared to luminal angiographic techniques, high resolution magnetic resonance imaging is more helpful to the diagnosis and differential diagnosis the dissection from other vascular pathologies such as atherosclerosis or aneurysm[2]. Intraluminal contrast enhancement and artery wall enhancement, which is suggestive of intraluminal thrombus formation, is strongly correlated with ischemic symptoms in patients with spontaneous cervical artery dissection[3]. In this study, we divided patients into two groups according to the traditional angiography images(CE-MRA), and compared the characteristics of high resolution magnetic resonance imaging between two groups. The results of our study may be helpful to understand the lumen and wall change of different type of spontaneous intracranial artery dissection shown on luminal angiographic techniques.

References:

[1] Uemura M, Terajima K, Suzuki Y, et al. Visualization of the Intimal Flap in Intracranial Arterial Dissection Using High-Resolution 3T MRI. J Neuroimaging. 2017 Jan;27(1):29-32.
[2] Jung SC, Kim HS, Choi CG, et al. Quantitative Analysis Using High-Resolution 3T MRI in Acute Intracranial Artery Dissection.J Neuroimaging. 2016 Nov;26(6):612-617.
[3] Coppenrath E, Lenz O, Sommer N, et al. Clinical Significance of Intraluminal Contrast Enhancement in Patients with Spontaneous Cervical Artery Dissection: A Black-Blood MRI Study. Rofo. 2017 Jul;189(7):624-631.

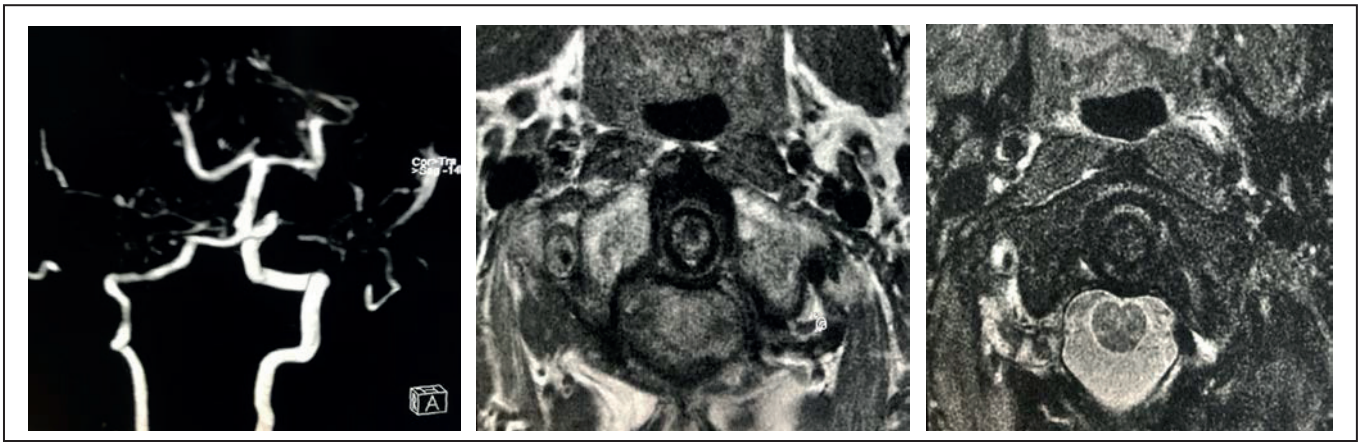

Design of a phantom to validate the accuracy of 4D flow MRI velocity measurements and derived bio-markers

Marco Castagna[1,2], Félicien Bonnefoy[2], Jean-Michel Serfaty[1,3], David Le Touzé[2]
[1]Institut du thorax, INSERM UMR 1087, CNRS UMR 6291, Nantes, France
[2] LHEEA research department, École Centrale Nantes, Nantes, France
[3]Imagerie cardiaque et vasculaire diagnostique, CHU Nantes, Nantes, France

Purposes. *4D Flow MRI* enables 3D measurements of blood velocity, and the computation of velocity-derived biomarkers, such as wall shear stress, pressure mapping, pulse wave velocity, and vortex features. Unfortunately, it presents some limitations related to its spatial resolution, limiting the investigations in small vessels and the computation of velocity-derived characteristics[1]. The purpose of this work is to devise and manufacture a *Mock Circulation Loop* (MCL), which includes a vascular phantom under pulsatile flow conditions. In vitro 4D Flow MRI validation will be carried out with the MCL, comparing the results of velocity and wall shear stress (WSS), with those obtained with *Laser Doppler Velocimetry* (LDV), which has been employed to validate 4D Flow MRI investigations in cerebral artery and aneurysm models[2].

Methods. The MCL is composed by a pulsatile programmable MRI-compatible gear pump (CardioFlow5000, Shelley Medical Imaging Technologies), connection pipes, a vascular phantom, a reservoir. During MRI investigations, a plastic box rounding the phantom contains agarose gel to mimic the human body (Fig.1). The working fluid is composed by a 0.6:0.4 (in weight) water-glycerol mixture and was selected to mimic blood's physical properties, while the phantom was designed as a squared Plexiglass (PMMA) channel (25x25x345mm) to easily allow LDV measurements. To plan them, a computational fluid dynamics study was performed. Since the geometry of the system is axial-symmetric, the fluid is homogeneous and Newtonian, the flow is pulsatile, and the walls are rigid, Womersley's approach[3] can be employed and thus incompressible Navier-Stokes momentum equation simplifies as

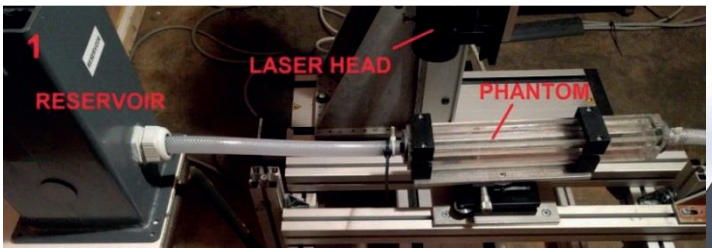

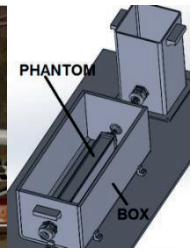

Eq.1 $$\frac{\partial^2 v_z(x,y)}{\partial x^2}+\frac{\partial^2 v_z(x,y)}{\partial y^2}-\frac{i\rho\omega}{\mu}v_z(x,y)=\frac{\nabla_z p(t)}{\mu} \qquad \text{with} \qquad \frac{\nabla_z p(t)}{\mu}=\frac{A+Be^{-i\omega t}}{\mu}$$

where v_z,$\nabla_z p$ are the velocity and pressure drop axial components respectively, and ρ,μ the density and viscosity of the fluid. A second-order finite difference scheme was employed to compute a numerical solution (Fig.2) for Eq. 1, considering a discretization step size $h = 1.25 \cdot 10^{-4}$ mm, $\omega = 2.4166$ rad $\cdot s^{-1}$, $\rho = 1.098$ g $\cdot cm^{-3}$, $\mu = 3.45$ cP, $A = -37.6959$ Pa $\cdot m^{-1}$, and $B = -636.8250 + 37.6959i$ Pa $\cdot m^{-1}$. WSS (Fig.3) was calculated as

Eq. 2 $$\overrightarrow{WSS}=\frac{\partial\vec{v}}{\partial\vec{n}}\Big|_{wall}\cdot\vec{n}=\frac{\partial\vec{v}}{\partial\vec{x}}\Big|_{wall}\cdot\vec{x} \qquad \text{or} \qquad \overrightarrow{WSS}=\frac{\partial\vec{v}}{\partial\vec{y}}\Big|_{wall}\cdot\vec{y}$$

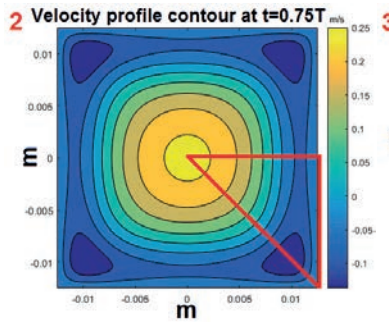

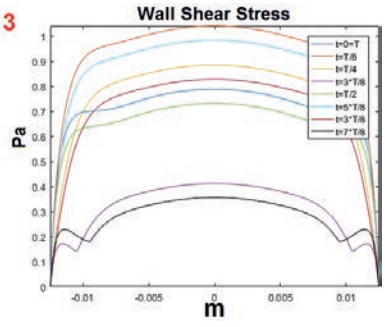

Considering the symmetry of these results, LDV measurement points will be allocated on one eighth of the total section (Fig.2, in red), which is a slice positioned 200 mm downstream the entrance, to prevent effects of the inlet and outlet. Snell's law was employed to calculate displacements of the laser head, taking into account refraction at the interfaces among the exterior air (n=1.00), the PMMA window (n=1.49), and the internal fluid (n=1.38). MRI investigations will be performed with a 4D Flow sequence, with a 2.2 mm isometric spatial resolution, 30 acquisition phases, and no contrast agent.

Results and Discussion. The experimental set-up was successfully designed and manufactured. The experimental campaign will take place in the following weeks and first results will be presented at the conference. Future developments of the present work include the development of rigid and compliant, geometrically more accurate vascular models under physiological pressure and flow conditions, to set a more realistic scenario for 4D PC MRI validation.

References

1. Dyverfeldt P et al. 4D flow cardiovascular magnetic resonance consensus statement. JCMR 2015; 17(1): 72.
2. Hollnagel DI et al. Comparative velocity investigations in cerebral arteries and aneurysms: 3D phase contrast MR angiography, laser Doppler velocimetry and computational fluid dynamics. NMR Biomed. 2009; 22(8): 795-808.
3. Womersley JR. Method for the Calculation of Velocity, Rate of Flow and Viscous Drag in Arteries when the Pressure Gradient is known. J. Physiol. 1955; 127(3): 553–563.

Contrast-enhanced Magnetic Resonance Angiography (ce MRA) in Evaluation of Vascular Stents - Ability of Assessment and Artefacts in Dependence of Stent Material and Field Strength

Retrospective in Vivo Study

Manuela A. Aschauer [1, 3], Stephanie Petutschnig[1], Andrea Obernosterer [2, 1]
[1] Medical University of Graz, Austria; [2] Division of Angiology, Department of Internal Medicine;
[3]Division of Neuroradiology, Vascular and Interventional Radiology, Department of Radiology

Purpose: Our major focus was to assess the openness and visibility of the stent lumen and to quantify upcoming artefacts in ce MRA. In addition, any further artefacts which occurred during the assessment were evaluated dependent on stent material and field strength.
Patients and Methods: Assessed are ce MRA and MRA images of 361 patients with 672 stents in pelvis and/or lower limb arteries from 1997 to 2015 in our hospital (36 different stent types from 12 manufacturers) with 1,5 or mostly 3 T SIEMENS® System. The key data of this study are signal intensity before, in and post stent, type of stent and the stent's period of use.
Results: The openness of the stents was assessed easily in most cases with our routine sequences including a high resolution sequence with 1mm THK in the stent area. The occurrence of artefacts and thus also a more accurate assessment of upcoming in-stent stenosis varied strongly dependent on stent material, primary dilatation diameter of stent, extension of stent in stent areas (if more than one stent was implanted with overlap) and time passed between implantation and examination via ce MRA. The field strength used played a rather secondary role. Source images and MPR reconstructions were necessary in all patients.
Discussion: MRA should be the first method in diagnostic algorithm also in patients with peripheral vascular stents and PAOD. Knowledge of the stent type prior to the examination can facilitate the interpretation of images.

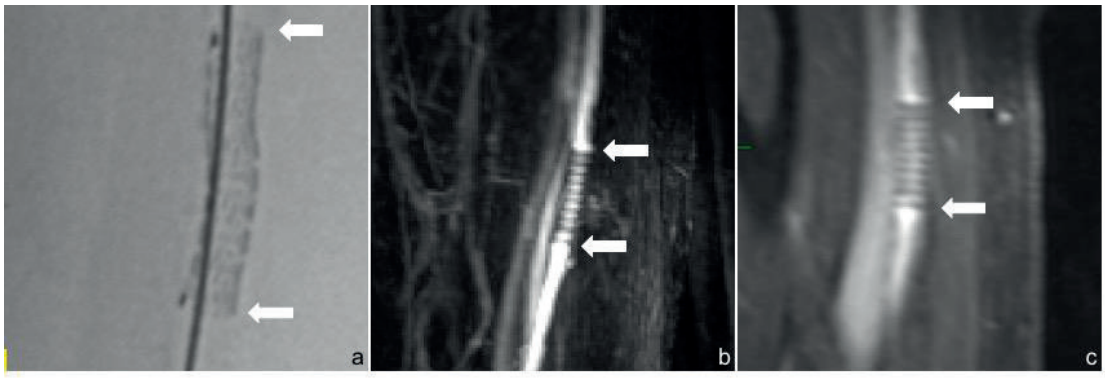

Fig.1: Example of MARIS® stent (a) during implantation; (b) source image with open stent, no stenosis; (c) source image of HR sequence

References: This work contains parts of – Dissertation of Stephanie Petutschnig;
Please ask manuela.aschauer@medunigraz.at

Diffusion-weighted MRI of acute lower extremity deep vein thrombosis

Zeynep Nilüfer Tekin MD[1], Ali Türk MD[2], Özlem Saygılı Prof[3].

Medeniyet University Göztepe Training and Research Hospital[1] ,Radiology, Acıbadem Bakırköy Hospital[2], Radiology,Acıbadem University[3], Radiology, Istanbul, Turkey.

Purpose: Diffusion-weighted imaging (DWI) based on molecular diffusion due to the thermal energy of free water, has become an increasingly routine part of clinical magnetic resonance imaging (MRI). By its unique soft tissue contrast mechanism benefits from the differences in the motion of water molecules, DWI offers a spectrum of anatomical and clinical applications, ranging from lesion detection and characterization to response evaluation in multiple organs and for multiple tumors [1, 2]. Lower extremity deep venous thrombosis (DVT) is a common disease with high morbidity and mortality in both community and hospital care [3].Doppler Ultrasound (US) is a primary non-invasive, safe simple, substantially accurate and cost-effective diagnostic tool used for the diagnosis of DVT. Even if MRI is not commonly used in DVT, the applicability to whole body imaging as a fast method, especially in diffusion weighted sequences, and technological advances in fat saturation pulse sequences and surface coils [4] leaded us to apply it as an alternative method in selected cases.The study aims to evaluate efficiency of DWI and apparent diffusion coefficient (ADC) value in the diagnosis of acute DVT of the lower extremities.

Methods: In a two- year period, 34 patients (18 females; mean age: 54.5 years, age range: 25-90 years) having typical clinical presentation of acute onset DVT were prospectively evaluated with Doppler US by an experienced radiologist. At the same day, magnetic resonance imaging (MRI) was performed on a 1.5-T scanner, using axial T1,T2 weighted, gradient echo and diffusion-weighted imaging with ADC mapping. ADC values were measured by two radiologists separately and the remained sequences of MRI were evaluated with the consensus of the same both radiologists.

Results: Recently operated 8 (23.5%) patients composed of 34 patients. Doppler findings were detected as positive in 15 (44.1%), negative in 18 (52.9%), suspicious in 1 (2.9%) of the patients. Among the patients with restricted diffusion, target signs (peripherally hyperintens, santrally hypointense) were detected in Gradient echo sequence in 7 (63.6%) out of 11.The mean ADC value of the patients with thrombosis was calculated as $1.1x10^{-3}mm^2/s$ whereas $2.7x10^{-3}mm^2/s$ in the patients without acute thrombosis.The ADC value of the acute thrombosed deep veins were significantly lower than the normal deep veins ($p<0.01$) (Fig. a-e).

Discussion : DVT is an emergency pathology with a high risk of morbidity and mortality. Doppler US imaging is user depended technique, however differantiating the restricted diffusion on DWI is extremely easy even by the inexperienced radiologists or physician assistant. Bendick PJ et al [5] revealed that results of the doppler examination should be questioned when there is a suspicion of thrombus in the deep veins of the calf. In their study comparing doppler ultrasound and contrast venography in 112 patients, they found 21 false-negative and nine false-positive results obtained by doppler. Among 21 false-negative results, there were 13 patients with thrombi isolated to the veins of the calf and 2 patients' examinations interpreted incorrectly by inexperienced personnel. Among 9 false-negative examinations, there were 3 patients with chronic disease interpreted as acute thrombosis, 3 patients' results interpretated of weak signals in the calf as thrombosis, 2 patients with weak signals due to obesity and 1 patient with excess doppler probe pressure distorting venous flow. Our study suggests that combined DWI with gradient echo sequences is able to distinguish acute deep vein thrombosis. Lower extremity MRI with these sequences may contribute to diagnosis of DVT, especially for those patients with thickened and edematous lower extremities which impedes the optimal visualisation and evaluation of deep venous system ultrasonographically.

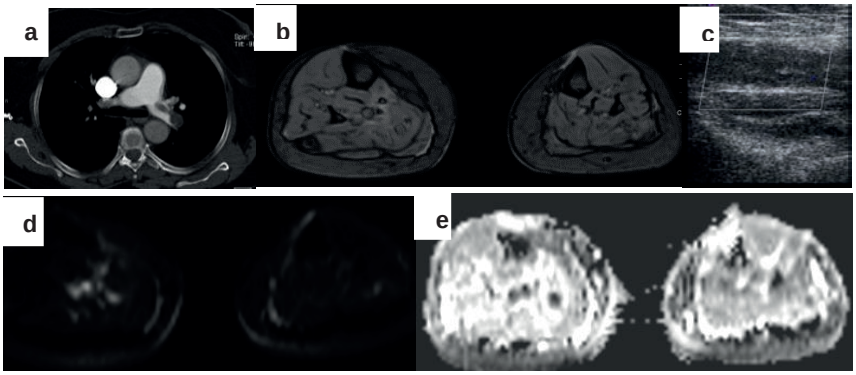

Fig.a. Axial contrast enhanced CT showing pulmonary embolism.

Fig.b-e demonstrated acute thrombosis isolated to the deep veins of the right calf in gradient echo sequences, second look Doppler US, DWI and ADC mapping,respectively

References: 1.Moore WA et al. AJR Am J Roentgenol, 2014;202(5):995-1006. **2.** Rosenkrantz AB et al. J Magn Reson Imaging. 2011;33(1):128-35. **3.** Michiels JJ et al. World J Crit Care Me. 2015;4(1):29-39. **4.** Kwee TC et al. Eur J Radiol. 2009;70(3):409-17. **5.** Bendick PJ et al. Am Surg.1983;49(6):320-3.

Influence of Intracranial Aneurysms on Volume Flow Rate Measurement using Magnetic Resonance Fluid Dynamics

Takashi Mizuno[1, 2], Haruo Isoda[1, 3], Takashi Izumi[4], Tetsuya Tsukada[4], Roshani Perera[1], Shyunsuke Tajima[1], Yoshiaki Komori[5], Yasuo Sakurai[2], Shinji Naganawa[6, 3]
[1]Department of Radiological and Medical Laboratory Science, Nagoya University Graduate School of Medicine, Aichi, Japan
[2]Department of Radiological Technology, Nagoya University Hospital, Aichi, Japan
[3]Brain & Mind Research Center, Nagoya University, Aichi, Japan
[4]Department of Neurosurgery, Nagoya University Graduate School of Medicine, Aichi, Japan
[5]Siemens Healthcare K.K., Tokyo, Japan
[6]Department of Radiology, Nagoya University Graduate School of Medicine, Aichi, Japan

Purpose: Time averaged volume flow rates (TAVFRs) measured by magnetic resonance fluid dynamics (MRFD) should be consistent between the upstream and downstream regions of intracranial aneurysms, but we found lower TAVFRs downstream of aneurysms. The purpose of this study is to confirm whether the lower downstream TAVFR measured by MRFDs increased after flow diverter (FD) placement and to investigate factors that may have caused the lower pre-FD TAVFR measurement.

Methods: Ten patients with giant aneurysms located between cavernous segment and clinoid segment underwent MR imaging with a 3.0 T MR scanner before FD placement. After FD placement, seven out of the ten patients underwent the same MR sequences again. Using MRFD analysis, TAVFRs were obtained upstream [lacerum segment (C3)] and downstream (ophthalmic segment (C6), communicating segment (C7), proximal M1 segment and distal M1 segment) of the giant aneurysms. Values were then normalized using the TAVFRs from C3 (Normalized TAVFR). The relationship between the difference of TAVFR at C3 and C6 and the degree of vortex flow in the aneurysm was evaluated. Aspect ratio, dome neck ratio, neck parent artery ratio, average velocity in aneurysm, inflow velocity and inflow volume were calculated, and Pearson's correlation coefficients between each value and TAVFR difference were investigated.

Results: TAVFRs in the aneurysmal side where parent artery stenosis occurred were lower than those in the normal side in both pre-FD and post-FD placement for all patients (Fig. 1A). Normalized TAVFRs at C6 in the aneurysmal side were lower than those in the normal side before FD placement, but similar after FD placement (Fig.1B). In addition, before FD placement, vortex flows were visible in the aneurysms that had large TAVFR differences. TAVFR difference had a positive correlation with the average velocity in the aneurysm and with the inflow volume at the aneurysm neck.

Conclusion: The presence of the intracranial aneurysm lowered the downstream TAVFR. After FD placement the difference between the downstream and upstream TAVFR decreased. The lower pre-FD TAVFR values may be affected by flow velocity in and the amount of blood flow passing through the aneurysms.

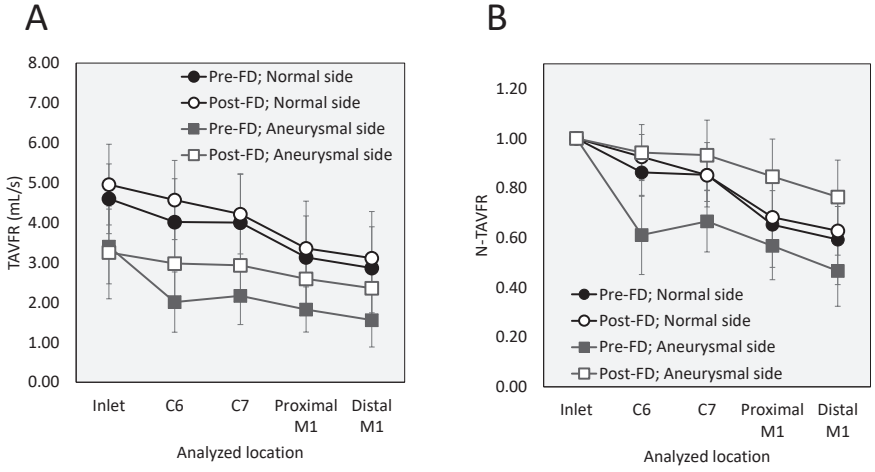

Fig 1. Comparison of TAVFR and Normalized TAVFR in bilateral side with and without aneurysms before and after FD placement
TAVFR, time averaged volume flow rate; FD, flow diverter

Contrast enhanced MRA in Thoracic Outlet Syndrome: Indications and Technical Considerations (Poster)

1st Author	Eddie Soh Po Tao
2nd Author	Tay Mei Fang
3rd Author	Tan Tee Meng
Doctor-In-Charge	Leong Sum
Institution	Singapore General Hospital

Purpose:

Discuss our experience and principles of MRA for Thoracic Outlet Syndrome including optimal parameter settings and unique postural manoeuvres.

Methods:

To conduct a literature review and present on the technical considerations and parameters used in contrast-enhanced MRA in Thoracic Outlet Syndrome in comparison to our departmental practice using a 3 Telsa Siemens Skyra. Retrospective review of all contrast-enhanced MRA in Thoracic Outlet Syndrome was performed from January 2015 to December 2017. Scans findings would be used for analysis.

Results:

The unique postural manoeuvres of arms up, and arms down MRA has proven to be useful in determining the presence and degree of vascular compression and associated complications in the thoracic outlet.

Discussion:

Based on our early experience, Contrast-Enhanced MRA in Thoracic Outlet Syndrome is feasible. With unique advantages relative to CT Angiogram, such as use of non-ionising radiation and lower contrast injection volume. Its superior soft tissue delineation also allows for better assessment of all the anatomic spaces in diagnosis of neurogenic Thoracic Outlet Syndrome.

References:

Aralasmak, A., Cevikol, C., Karaali, K., Senol, U., Sharifov, R., Kilicarslan, R., & Alkan, A. (2012). MRI findings in thoracic outlet syndrome. *Skeletal radiology*, *41*(11), 1365-1374.

Klaassen, Z., Sorenson, E., Tubbs, R. S., Arya, R., Meloy, P., Shah, R., Shirk, S. & Loukas, M. (2014). Thoracic outlet syndrome: a neurological and vascular disorder. *Clinical anatomy*, *27*(5), 724-732.

Raptis, C. A., Sridhar, S., Thompson, R. W., Fowler, K. J., & Bhalla, S. (2016). Imaging of the patient with thoracic outlet syndrome. *Radiographics*, *36*(4), 984-1000.

Use of Time Resolved Imaging of Contrast Kinetics (TRICKS) MRA sequences in complex arteriovenous malformation (AVM) assessment – pictorial review

Mark Lewis FRCR, Paul Malcolm FRCR; Norfolk and Norwich University Hospitals NHS Trust

TRICKS MRA allows for the 3D acquisition of large volumes with excellent spatial and temporal resolution. Due to the complex nature and highly variable anatomy of AVMs, the ability to acquire volumetric data over time makes detailed assessment of the vasculature possible, giving a similar level of detail to direct digital subtraction studies but with additional information of the relationships with the surrounding structures and minimising the use of ionising radiation. This technique allows for number and origin of main arterial feeders to be counted, as well as directly assessment of the nidus and categorisation of the drainage into the deep and superficial veins which is essential for deciding on suitable treatment. Using appropriate software the volume can be manipulated to be viewed at any angle and the contrast phase to be advanced in a step wise manner allowing assessment throughout the cardiac cycle. This review aims to demonstrate the clinical utility of this technique in assessment of peripheral and central AVMs.

Preferred presentation

Poster

Keywords

Time Resolved Imaging of Contrast Kinetics, TRICKS, MRA, arteriovenous malformation, AVM

Authors

Mark Lewis FRCR

Paul Malcolm FRCR

Acknowledgement of Sponsors

The Society for Magnetic Resonance Angiography would like to express its gratitude to all 2018 sponsors, without whom this years event would genuinely not have been possible. The Gold Sponsors are as follows -

Gold Sponsors

Bayer - Gold Sponsor
Bayer AG's Radiology unit is a global leader in developing and manufacturing contrast agents used in X-ray, computed tomography (CT) and magnetic resonance imaging (MRI), as well as injection systems for diagnostic and therapeutic medical procedures in CT, MRI and cardiovascular and peripheral vascular disease.
http://www.radiology.bayer.com www.bayer.com

Bracco - Gold Sponsor
Bracco Imaging S.p.A., part of the Bracco Group, is one of the world's leading companies in the diagnostic imaging business. Headquartered in Milan, Italy, Bracco Imaging develops, manufactures and markets diagnostic imaging agents and solutions that meet medical needs.
Bracco Imaging offers a product and solution portfolio for all key diagnostic imaging modalities: X-ray Imaging (including Computed Tomography-CT, Interventional Radiology, and Cardiac Catheterization), Magnetic Resonance Imaging (MRI), Contrast Enhanced Ultrasound (CEUS) and Nuclear Medicine through radioactive tracers. The diagnostic imaging portfolio is completed by several medical devices and advanced administration systems for contrast imaging products in the fields of radiology.
The Company operates in over 100 markets worldwide, either directly or indirectly, through subsidiaries, joint ventures, licenses and distribution partnership agreements.
To learn more about Bracco Imaging, visit www.braccoimaging.com

LIFE FROM INSIDE

Gold Sponsors

GE Healthcare US - Gold Sponsor
GE Healthcare provides transformational medical technologies and services that are shaping a new age of patient care. Our broad expertise in medical imaging and information technologies, medical diagnostics, patient monitoring systems, drug discovery, biopharmaceutical manufacturing technologies, performance improvement and performance solutions services help our customers to deliver better care to more people around the world at a lower cost.
http://www3.gehealthcare.com/en/global_gateway

Guerbet United States/France - Gold Sponsor
Guerbet is a pioneer in the contrast agent field, with 90 years' experience, and is the only pharmaceutical group dedicated to medical imaging worldwide. It offers a comprehensive range of X-Ray, Magnetic Resonance Imaging (MRI) and Interventional Radiology and Theranostics (IRT) products, along with a range of injectors and related medical devices to improve the diagnosis and treatment of patients. To discover new products and ensure future growth, Guerbet invests heavily in R&D, spending around 9% of its sales each year. Guerbet (GBT) is listed on Euronext Paris (Segment B – Mid Caps) and generated €776 million in revenue in 2016. For more information about Guerbet, please visit www.guerbet.com

Gold Sponsors

Philips - Gold Sponsor
Enabling better health and better care at lower cost Philips is a leading health technology company focused on improving people's lives across the health continuum – from healthy living and prevention, to diagnosis, treatment and home care. Applying advanced technologies, and deep clinical and consumer insights, Philips delivers integrated solutions that improve people's health and enable better outcomes. Partnering with its customers, Philips seeks to transform how healthcare is delivered and experienced. The company is a leader in diagnostic imaging, image-guided therapy, patient monitoring and health informatics, as well as in consumer health and home care.
https://www.philips.com/global

Siemens Healthineers - Gold Sponsor
Responsibility, excellence and innovation have been the basis for Siemens' success for over 160 years. Siemens Magnetic Resonance innovates to advance human health – in every hospital or practice or lab or university. Whether you are just beginning to work with MRI or you are at the forefront of research.
https://www.healthcare.siemens.com/

Other Sponsors

Arterys

Arterys was founded in 2011 to facilitate the global advancement of medicine through data, artificial intelligence and technology. The company was the first to receive FDA clearance for cloud-based medical image analysis product with Artificial Intelligence.

Circle Cardiovascular Imaging Inc.

Circle Cardiovascular Imaging develops highly accurate, versatile, robust, and intuitive cardiovascular post-processing software for the viewing and analyzing of CMR and CCT images. Circle's role in clinical and research settings maximizes patients' achievable benefit by enabling healthcare providers to complete effective and precise analysis. Excellence in cardiovascular imaging and patient care is our highest priority.

Heart Imaging Technologies

WebPAX/Precession, a web browser based work flow solution for cardiovascular MRI and CT, includes structured reports, HL7 messaging for orders/results, and single-click sharing for second opinions, referring physicians, or multi-center research.

Medis Medical Imaging Systems

Medis is a leading provider of post-processing software for the quantification of cardiovascular images across MR, CT, IVUS and Angiography modality. Medis solutions are CE marked and FDA 510(k) market cleared.

PIA Medical

Precision Image Analysis (PIA) is an innovator in medical image post-processing for research and clinical applications. This service encompasses most imaging modalities, including cardiac magnetic resonance (CMR) and cardiac computed tomography (CCT).

Meeting Endorsement

British Society of Cardiovascular Imaging

The BSCI is a multi-modality cardiac imaging society reflected in our scientific meetings, which enables us to discuss and compare different imaging techniques. The objectives of the society are to:

- Promote the highest standards of practice of cardiac imaging in the UK
- Promote education, training and the dissemination of scientific evidence in all aspects of cardiac imaging
- Advise the Royal College of Radiologists and the British Cardiovascular Society on cardiac imaging
- Nurture and evolve the links between the cardiology and radiology communities

bsci.org.uk

Society for Cardiovascular Magnetic Resonance

The principal international, independent organization committed to the further development of CMR through education, quality control, research, and training.

scmr.org

University of Glasgow

The University of Glasgow is the fourth-oldest university in the English-speaking world and one of Scotland's four ancient universities having been founded in 1451.

https://www.gla.ac.uk/explore/meetglasgow/inspiring/

Social Events

Tuesday Reception

The Hunterian Museum
https://www.gla.ac.uk/hunterian/

Welcome Address by Prof Julie Brittenden
Professor of Vascular Surgery, University of Glasgow
R&D Director NHS Greater Glasgow & Clyde

The Hunterian located in the same building as our conference is Scotland's oldest public museum and home to over a million magnificent items ranging from meteorites to mummies and Mackintosh. Within this diverse collection you will find astounding artefacts, amazing art and an astonishing array of animal life.

Wednesday Evening Dinner

Kelvingrove Art Gallery & Museum
http://www.glasgowlife.org.uk/museums/kelvingrove/

Music from Nicholas Lauener, Scottish Conservatoire

Social Events

Thursday Evening Dinner & Ceilidh

Old FruitMarket
Candleriggs, Merchant City, Glasgow G1 1NQ

Tutored Glengoyne Malt Whisky Tasting
Ceilidh Dance with music by Jiggered

Friday Evening Dinner with Magic at Oran Mor

https://oran-mor.co.uk/

Dinner with Magic Circle member and close-up table magician Billy Reid
President's Address: The State of the SMRA - Richard Frayne

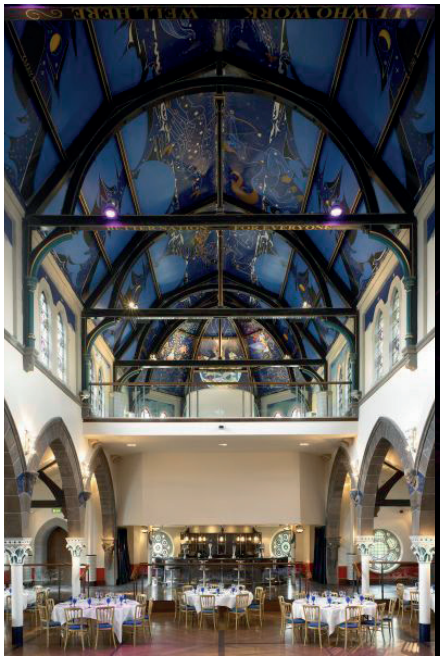

Maps For Evening Venues & Directions

Wed 29th Evening Venue

Directions - Glasgow University G12 8QQ to Kelvingrove Art Gallery & Museum G3 8AG
Approx. 13 minute walk
Exit university campus onto University Avenue and turn right
Walk to bottom of hill and turn right onto Kelvin Way,
Walk almost to end of Kelvin Way
Turn right just before the bowling green and turn into the Kelvingrove Art Gallery grounds.

Thu 30th Evening Venue

Directions - Glasgow University G12 8QQ to Old Fruit Market G1 1NQ.
Quickest route = Taxi Cab - 15 mins
Walking = approx 55 mins
Subway + walk - under 30 mins
- Hillhead Subway to Buchanan Street station then walk 9 minutes via Queen Street and Ingram Street

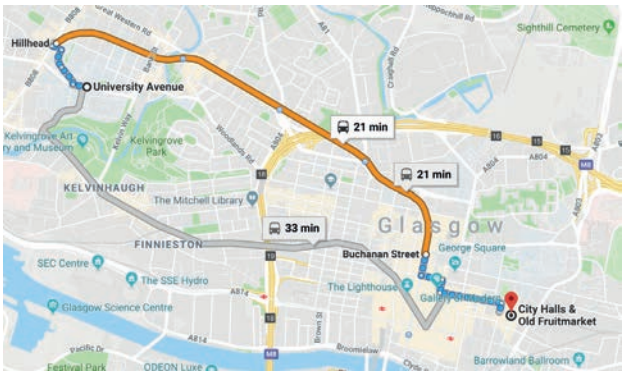

Fri 31st Evening Venue

Directions: Glasgow University G12 8QQ to Oran Mor G12 8QX
Approx 12 minute walk
Exit university campus onto University Avenue and turn left
Cross road at first set of traffic lights and follow road round past the Boyd Orr building down to large junction
Turn right at junction onto Byres road and walk straight to the end of Byres Road and Oran Mor is on your right (opposite Hilton Grosvenor Hotel)

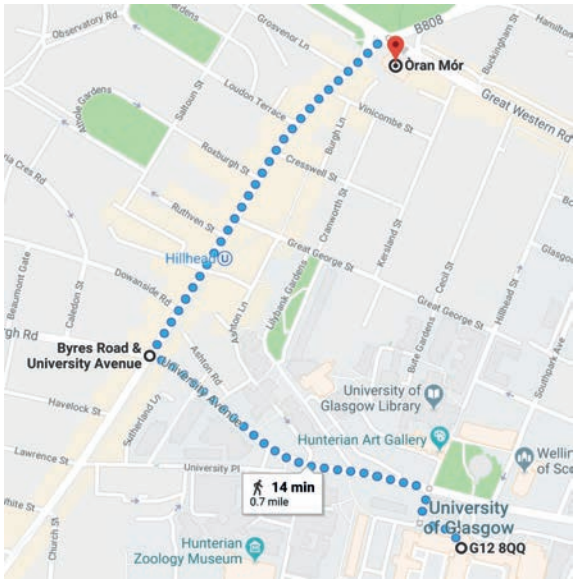

Guest Program

Wednesday 29th August

Glasgow City Tour (09:00 - 16:00)

A guided tour departing from the Hilton Grosvenor in the West End of Glasgow. Travel to Glasgow's Riverside via the Kelvingrove Museum then on to Pollock Country House, Glasgow Cathedral and via the Merchant City to the Lighthouse in the city centre.

Thursday 30th August

Edinburgh Tour (09:00 - 16:00)

A tour departing from the Hilton Grosvenor in the West End of Glasgow. Travel to Edinburgh the capital city to visit Edinburgh Castle, then tour the New Town and Holyrood Palace.

Friday 31st August

Loch Lomond & Glengoyne Tour (07:45 - 16:10)

Departing from the Hilton Grosvenor in the West End of Glasgow travel to Balloch where you will board a water bus taking you across Loch Lomond to the pretty village of Luss. Subsequently travel to Glengoyne Distillery for a tour plus Whisky & Chocolate tasting.

Optional Saturday Tour

Saturday 1st September

Loch Lomond National Park & Stirling (09:00 - 19:15)

Departing Glasgow, we'll head to the Kelpies - 30-metre-high horse head sculptures that are a monument to horse powered heritage and form a gateway at the eastern entrance to the Forth & Clyde canal. From the Kelpies, we'll travel onwards to Stirling Castle, one of the largest and most important in Scotland atop Castle Hill, surrounded on three sides by steep cliffs. We will explore the castle then after lunch the next stop is Kilmahog Woollen Mill where you'll hopefully be able to meet some of the famous Highland Cows. Then onwards via the stunning Dukes Pass to the beautiful village of Aberfoyle lying at the southern edge of the West Highland Fault in the Lomond & Trossachs National Park, with Loch Ard , Loch Chon, Loch Arklet and Loch Lomond all lying to the West, Loch Katrine, Loch Achray and Loch Venacher to the North and the Lake of Menteith, Scotland's only "lake" lying to the East. From Aberfoyle, we'll head to our Mystery Stop. There will then be a stop at Glengoyne Distillery for a photo opportunity before the return to Glasgow.

Registration is at - https://event-wizard.com/SMRA2018StirlingCastleTour/0/register/

Itinerary

Time	Location
09:00	Depart Hilton Grosvenor
10:00	Arrive Kelpies (1hr 40min stop)
11:00	Kelpies Tour (30min tour)
12:10	Arrive Stirling Castle (2hr 15min) Lunch & Attraction stop
14:30	Depart Stirling Castle
15:00	Arrive Kilmahog (15min Photo Stop)
15:15	Depart Kilmahog
16:15	Arrive Aberfoyle (30min stop)
16:45	Depart Aberfoyle
17:15	Arrive Mystery Stop (1hr Stop)
18:15	Depart Mystery Stop
18:25	Arrive Glengoyne Distillery (15 min Photo Stop)
19:15	Arrive Hilton Grosvenor

Announcement of 2019 Meeting – Nantes, France

SMRA 2019 Nantes

Society for Magnetic Resonance Angiography

society4mra.org

31st Annual Conference

An extraordinary voyage (n° 31)
in the city of Jules Vernes

August 28-30, 2019
Nantes, France

Pre-Conference
Educational Workshop
Tuesday, August 27

Organizers: Jean-Michel Serfaty & Philippe Douek
President: Michael Markl